ENGINEERING TISSUE MICROENVIRONMENT-INSPIRED ELECTROSPUN FIBROUS SCAFFOLDS FOR INTERVENTION OF DISEASE PROGRESSION

ZHANG QIANG

PhD

The Hong Kong Polytechnic University

2022

The Hong Kong Polytechnic University
Department of Biomedical Engineering

Engineering Tissue Microenvironment-Inspired Electrospun Fibrous Scaffolds for Intervention of Disease Progression

ZHANG Qiang

A thesis submitted in partial fulfilment of the requirements for the degree of Doctor of Philosophy

November 2021

Certificate of Originality

I hereby declare that this thesis is my own work and that, to the best of my knowledge and belief, it reproduces no material previously published or written, nor material that has been accepted for the award of any other degree or diploma, except where due acknowledgement has been made in the text.

_____ (Signed)

ZHANG Qiang (Name of student)

Abstract

Increasing studies have demonstrated the complex and dynamic tissue microenvironment (TME) may not only significantly alter the disease progression, but also affect the implanted scaffolds' properties and their *in vivo* treatment response. Electrospinning, as a versatile scaffold preparation technique, has many advantages like simple and feasible process, and ability to produce an ultrafine and continuous fibrous membrane with large surface areas and controllable diameters from nano- to micro-scale range, as well as the ease of functionalization for various purposes. Currently, by loading drugs or combining with other techniques or strategies, electrospinning-derived scaffolds have been widely used to modulate TME to intervene in disease progression. In the proposed three projects of this dissertation, we exploited electrospinning as the main fabrication approach and developed a series of intelligent scaffolds according to the implantation microenvironment of tendon and pancreatic cancer (PC) tissues to suppress tendon adhesion formation, promote tendon healing, and prevent PC recurrence, respectively.

Specifically, for the first project, inspired by the increased expression of matrix metalloproteinase-2 (MMP-2) in the exterior area of the injured tendon site, we designed and prepared a MMP-2 triggered stimuli-responsive drug delivery system. To regulate cell behaviors on a long-term basis, the gene was used as the cargo to intervene in disease progress. Here, extracellular signal-regulated kinase-2 (ERK-2)-siRNA was adopted as the therapeutical agent and incorporated into the gelatin methacryloyl (GelMA) nanogels by water-in-oil (W/O) nano-emulsification technique. Then, the siRNA-loaded GelMA nanogels were encapsulated into poly-L-lactic acid (PLLA) fibers by simple blending electrospinning. The resultant siRNA-laden electrospun membrane showed controllable morphology/architecture, superior swelling, degradation, and mechanical properties. Most importantly, the loaded siRNA could be released on-demand from the membrane in response to the MMP-2 and maintain its biofunction to transfect into cells and block the targeted ERK2 expression, thus

suppressing fibroblast adhesion, growth, and proliferation *in vitro*, while attenuating peritendinous adhesion formation *in vivo*. This project presents a promising approach exploiting a composite nanogel-incorporated membrane scaffold as both a physical barrier to prevent extrinsic cells invasion and a smart drug delivery vehicle to realize on-demand siRNA release, cooperatively suppressing the adhesion formation during tendon healing.

For the second project, inspired by the accumulated reactive oxygen species (ROS) and aggravated inflammation reaction during the early tendon healing stage that may affect the tendon repair outcomes and later adhesion formation, a Janus dual-layer membrane patch was developed, in which the inner layer was the multi-functional electrospun hydrogel patch (MEHP), while the outer layer was the PLLA fibrous membrane. The MEHP was prepared by blending electrospinning of zinc oxide (ZnO) and GelMA, followed by reinforcement with tannic acid (TA) solution treatment to form a secondary hydrogen-bond-mediated network in the polymer matrix. Such simple but delicate material combination rendered the MEHP with outstanding mechanical and adhesive properties, good biocompatibility, superior anti-oxidative, anti-inflammatory, and anti-bacterial properties as well as pro-healing effects, which showed huge potential as a novel and efficient therapeutical platform for tendon healing. Taking advantage of the good adhesive properties, Janus patch could be easily fabricated by directly attaching MEHP to PLLA physical barrier membrane. The resultant Janus patch exhibited hierarchical structure and integrated biofunctions, which could prevent adhesion formation while creating a favorable microenvironment for tendon repair. This project provides a proof-of-concept demonstration of regulating tendon healing phases: that is, mitigating oxidative stress and inflammatory reaction during the early inflammatory phase, while directing tendon regeneration and preventing adhesion at the later repair and remodeling phases. We envision that our Janus membrane patch will have great clinical potential as a novel bio-scaffold to improve tendon healing.

For the third project, inspired by the presence of bacteria, e.g., *Gammaproteobacteria*,

in the PC microenvironment that may reduce the chemotherapeutic efficacy of gemcitabine (GEM) by converting GEM into the inactive form (20,20-difluorodeoxyuridine), an anti-bacterial and anti-cancer system was proposed. Such system was prepared by first blending electrospinning of GEM and PLLA to obtain GEM-loaded PLLA nanofibrous membranes. Subsequently, a two-step TA-mediated silver (Ag) NP reduction strategy was exploited to in-situ form Ag NPs onto the GEM-loaded PLLA fiber surface. Such scaffold exhibited excellent mechanical performances and appropriate GEM release profile, suggesting the feasibility as a local drug delivery system to be implanted at the tumor resection site during the surgical operation for PC treatment. Moreover, such electrospun membrane could avoid the adverse reactions of intravenously administered GEM and display a combination of short- and long-term anti-tumor performance. Combined with synergistic anti-tumor and anti-bacterial effects of Ag NPs anchored onto the fiber surface, we envision that such composite membrane holds great promise as a therapeutical platform to address the issue of chemotherapy drug resistance caused by bacteria in the pancreatic microenvironment and synergistically improve the therapeutical efficacy of cancer recurrence after surgery.

In conclusion, pursuant to the microenvironmental characteristics of corresponding tissues, we developed a series of intelligent electrospun fibrous scaffolds with different biofunctions, aiming to reverse the adverse microenvironmental factors to ultimately intervene in the disease process and improve treatment outcomes.

List of Publications

Journal Papers

1. **Zhang Q**, Yang YH, Yildirimer L, Xu TP, Zhao X. Advanced technology-driven therapeutic interventions for prevention of tendon adhesion: design, intrinsic and extrinsic factor considerations. Acta Biomater. 2021, 124: 15-32.
2. **Zhang Q**, Sitoa L, Mao M, He JK, Zhang YS, Zhao X. Current advances in skin-on-a-chip models for drug testing. Microphysiological Systems. 2018, 2(4):1-7.
3. Yang YH, **Zhang Q (co-first author)**, Xu TP, Zhang HY, Zhang M, Lu L, Hao YF, Fuh JYH, Zhao X. Photocrosslinkable nanocomposite ink for printing strong, biodegradable and bioactive bone graft. Biomaterials. 2020, 263: 120378.
4. Zhang F, **Zhang Q (co-first author)**, Lia XY, Huang N, Zhao X, Yang ZL. Mussel-inspired dopamine-Cu^{II} coatings for sustained in situ generation of nitric oxide for prevention of stent thrombosis and restenosis. Biomaterials, 2019, 194: 117-29.
5. Yang YH, Xu TP, **Zhang Q (co-first author)**, Piao Y, Pan BH, Zhao X. Biomimetic, stiff and adhesive periosteum with osteogenic-angiogenic coupling effect for bone regeneration. Small. 2021, 17(14): 2006598.
6. Yildirimer L, **Zhang Q (co-first author)**, Cheung J, Chu K, He Y, Yang M, Zhao X. Engineering three-dimensional microenvironments towards *in vitro* disease models of the central nervous system. Biofabrication, 2019, 11(3), 032003.
7. Bei HP, **Zhang Q**, Lam CH, Yuen HY, Kuang S, Zhao X, Petite miracles: insight into the nano-management of scarless wound healing, Drug Discovery Today, 2021, accepted.
8. Chen ZY, **Zhang Q**, Li HM, Wei Q, Zhao X, Chen FL, Elastin-like polypeptide modified silk fibroin porous scaffold promotes osteochondral repair. Bioactive Materials. 2020, 6(3): 589-601.
9. Guo F, **Zhang Q**, Jiang H, He Y, Li M, Ran JJ, Lin J, Tian LW, Ma L. Dietary potato intake and risks of type 2 diabetes and gestational diabetes mellitus. Clinical Nutrition, 2021. 40(6): 3754-3764.
10. Guo F, Do V, Copper R, Huang Y, Zhang P, Ran JJ, **Zhang Q**, Tian LW, Fu ZR. Trends of temperature variability: which variability and what health implications. Science of the Total Environment. 2021. 144487.
11. Ma Y, He P, Xie W, **Zhang Q**, Wang M, Feng Y, Pan J, Zhao X, Pan G. Dynamic colloidal photonic crystal hydrogels with self-recovery and injectability. Research. 2021, 9565402.
12. Tu QF, Zhao X, Liu S, Li XY, **Zhang Q**, Yu H, Xiong KX, Huang N, Yang ZL, Spatiotemporal dual-delivery of therapeutic gas and growth factor for prevention of vascular stent thrombosis and restenosis, Appl. Mater. Today, 2020, 19, 100546.

13. Bei HP, Yang YH, **Zhang Q**, Tian Y, Luo XM, Yang M, ZHAO X. Graphene-based nanocomposites for neural tissue engineering. Molecules, 2019, 24(4):658.
14. Ji X, Yan Y, Sun T, **Zhang Q**, Wang Y, Zhang M, Zhang H, Zhao X, Glucosamine sulphate-loaded distearoyl phosphocholine liposomes for osteoarthritis treatment: combination of sustained drug release and improved lubrication. Biomaterials Science, 2019, 7, 2749-2728.
15. Shen XH, Tu QF, Liu YW, **Zhang Q**, Zhao X, Maitz MF, Qiu H, Huang N, Yang ZL. A facile metal-phenolic-amine strategy for dual-functionalization of blood-contacting devices with antibacterial and anticoagulant properties. Materials Chemistry Frontiers, 2019, 3, 265-275.
16. **Zhang Q**, Bei HP, Zhao MN, Dong ZF, Zhao X. Shedding light on 3D printing: printing photo-crosslinkable constructs for tissue engineering. Biomaterials, under revision.
17. **Zhang Q**, Luo Y, Liang B, Suo D, Lv S, Wang Yi, Zhao X. An anti-bacterial and anti-cancer fibrous membrane with multiple therapeutic effects for prevention of pancreatic cancer recurrence. Materials Science and Engineering: C, under review.
18. **Zhang Q**, Ma K, Lam CH, Bei HP, Liu Y, Yang X, Zhao X. Micro-and nano-environment dual-modulated anti-tendon adhesion barrier membranes. Materials & Design, under review.
19. A bio-inspired adhesive and robust Janus patch with anti-oxidative, anti-inflammatory, and anti-bacterial performances for tendon repair. In preparation.

Books

1. Piao Y, Bei PH, Tam A, Yang YH, **Zhang Q**, Yang M, Zhao X. “Calcium Phosphate Nanoparticle-Based Systems for Therapeutic Delivery” in “Theranostic Bionanomaterials”. Editor. Wenguo Cui and Xin Zhao. Elsevier. (2019) 147-164.

Acknowledgements

First of all, I would like to give my sincere gratitude to my supervisor, Dr. Xin Zhao, for her invaluable advice, sustained encouragement, and continuous support throughout my Ph.D. study. It was under the Dr. Zhao's patient guidance that I came into contact with the tissue engineering and grew to like this research direction, ultimately transferring from the field of Preventive Medicine to Biomedical Engineering. As her PhD student in PolyU, I was affected deeply by her intelligence and passion in pursing academic goals as well as the enthusiasm and optimism for daily life. This will also continue to inspire me to overcome all sorts of hurdles and to be a better researcher in my future academic career.

Then, I would like to thank all my colleagues, Dr. Yuhe Yang, Dr. Yu Tian, Dr. Mao Mao, Mr. Yun Piao, Mr. Bo Liang, Mr. Shang Lv, Miss. Quanjing Mei, Miss. Mengna Zhao, Miss. Jingdong Rao, Mr. Ho Pan Bei, Mr. Tianpeng Xu, Mr. Bo Liang, Mr. Yu Liu, Mr. Hanbai Wu, Mr. Hengze You, Mr. Hung Pak Ming, Mr. Le Duong Hien Thong, Mr. Wu Ho Kan, William, Mr. Chun Hei Lam, Mr. Yuen Andy, Mr. Huaqian Liu, Mr. Gordon Hung, Mr. Wu Ho Kan, and Miss. Di Suo for their constructive suggestions and valuable assistance to my research work during my three years' PhD study. In particular, I would give my thanks to Mr. Shang Lv for helping with gemcitabine release test, to Miss. Di Suo for helping with anti-bacterial test, to Mr. Chun Hei Lam for helping with electrospun fiber characterization, to Mr. Bo Liang for helping with pancreatic cancer project, to Mr. Yu Liu for helping with cell transfection experiments, and to Mr. Kui Ma from Orthopedics and Sports Medicine Center of Nanjing Medical University for helping with animal experiments of the first project, to Mr. Xinda Ge for providing RAW 264.7 cell lines, to Mr. Yang Luo from Southwest Jiaotong University for helping with animal experiments of the third project. Altogether, thanks to all group members for creating such a warm and harmonious atmosphere, and it is my great honor to work in such great group.

Besides, I would express my thanks to technical staff from Department of Applied Biology and Chemical Technology (ABCT), university research facility in material characterization and device fabrication (UMF), university research facility in life sciences (ULS), university research facility in chemical and environmental analysis (UCEA) for their help in use of research facilities.

Lastly and most importantly, I would like to give my heartfelt thanks to my parents and wife Fang Guo for their selfless love, understanding and support throughout my life.

Table of Contents

Certificate of Originality I
Abstract II
List of Publications V
Acknowledgements VII
List of Abbreviations XII
Chapter 1 Introduction 1
1.1 Principle, process, and parameters of electrospinning 2
1.2 Drug-incorporating strategies in electrospinning 4
1.3 Release mechanisms of drugs from electrospun scaffolds 7
Chapter 2 Development of MMP-responsive siRNA-laden fibrous membranes for prevention of tendon adhesion 9
2.1 Introduction 9
2.1.1 Tendon tissue healing microenvironment 9
2.1.1.1 Tendon structure and composition 9
2.1.1.2 Biology and pathology of tendon healing 11
2.1.2 Current strategies to prevent tendon adhesion 15
2.1.3 Motivation and objective 22
2.2 Methodology 27
2.2.1 Materials 27
2.2.2 Preparation of siRNA-laden GelMA nanogels 27
2.2.3 Characterization of siRNA-laden GelMA nanogels 29
2.2.4 Preparation of GelMA nanogel-embedded fibrous membranes 31
2.2.5 Characterization of GelMA nanogel-embedded fibrous membranes 31
2.2.5.1 Physical characterization of the fibrous membranes 31
2.2.5.2 Biological characterization of the fibrous membranes 33
2.2.6 *In vivo* anti-tendon adhesion studies 36
2.2.6.1 Animal experiment 36
2.2.6.2 Macroscopic assessment 36
2.2.6.3 Histological analysis 36
2.2.6.4 Immunohistochemical assessment 37
2.2.6.5 Biomechanical evaluation 37
2.2.6.6 Western blot analysis 37
2.3 Results and Discussion 37
2.3.1 Characteristics of siRNA-laden GelMA nanogels 37
2.3.2 Characterization of GelMA nanogel-embedded fibrous membranes 53

2.3.3 *In vitro* MMP2-responsive siRNA release from the fibrous membranes .60
2.3.4 *In vitro* biological effects of fibrous membranes.....63
2.3.5 *In vivo* biological effects of fibrous membranes 71
2.4 Summary.....75
Chapter 3 Development of bio-inspired adhesive and robust Janus patch with multi-biofunctions for tendon repair.....77
3.1 Introduction.....77
3.2 Methodology.....80
3.2.1 Materials.....80
3.2.2 Preparation of the MEHP 80
3.2.3 Characterization of the MEHP 81
3.2.3.1 Physical characterization of the MEHP 81
3.2.3.2 Tissue adhesion performance assessment 82
3.2.3.3 Mechanical performance evaluation.....82
3.2.4 Biocompatibility assessment 83
3.2.5 Anti-oxidation assessment.....83
3.2.6 Anti-inflammation and anti-bacterial assessment.....84
3.2.7 Promoting effects on tendon healing.....86
3.2.8 Construction and characterization of Janus patch 86
3.2.9 Animal study design 86
3.2.10 Gross evaluation.....87
3.2.11 Histological analysis.....87
3.2.12 Immunohistochemical examination 88
3.2.13 Gene expression of inflammatory markers 88
3.3 Results and discussion 89
3.3.1 Characterization of the MEHP 89
3.3.2 Mechanical and adhesive strength of the MEHP 106
3.3.3 Cell viability and proliferation 111
3.3.4 Anti-oxidation effects 113
3.3.5 Anti-inflammation effects..... 118
3.3.6 Anti-bacterial and pro-healing effects 119
3.3.7 Construction of the dual-layer membrane scaffold 122
3.3.8 *In vivo* tendon regeneration potential 125
3.4 Summary.....129
Chapter 4 Development of anti-bacterial electrospun fibrous scaffolds for pancreatic cancer therapy 131
4.1 Introduction.....131

4.1.1 Brief introduction of pancreatic cancer 131
4.1.2 The landscape of pancreatic tumor microenvironment 132
4.1.3 Current strategies to intervene the pancreatic cancer progression 136
4.1.4 Motivation and objective 139
4.2 Methodology 141
4.2.1 Materials 141
4.2.2 Preparation of anti-bacterial and anti-cancer fibrous membrane 141
4.2.3 Characterization of the fibrous membrane 142
4.2.4 *In vitro* GEM release 143
4.2.5 Biocompatibility test 143
4.2.6 Cell morphology observation 144
4.2.7 Cytotoxicity of GEM-loaded membrane 144
4.2.8 Anti-bacterial test 144
4.2.9 Residual tumor model 145
4.2.10 Histological examination 146
4.3 Results and Discussion 146
4.3.1 Characterization of the electrospun fibrous membrane 146
4.3.2 Characterization of gemcitabine release profiles 151
4.3.3 *In vitro* biocompatibility 152
4.3.4 Anti-cancer effects 157
4.3.5 Anti-bacterial effects 160
4.4 Summary 164
Chapter 5 Conclusions and recommendations for future work 166
5.1 Major findings and conclusion 167
5.2 Recommendations for future work 169
References 172

List of Abbreviations

Abbreviation	Full name
ADSCs	Adipose-derived stem cells
Ag	Silver
bFGF	Basic fibroblast growth factor
BMP	Bone morphogenetic proteins
BMSCs	Bone mesenchymal stem cells
CAFs	Cancer-associated fibroblasts
Col-1	Collagen type I
Col-3	Collagen type III
ECM	Extracellular matrix
EE	Encapsulation efficiency
DCM	Dichloromethane
DMF	N,N-Dimethylformamide
ERK	Extracellular signal-regulated kinase
GAGs	Glycosaminoglycans
GEM	Gemcitabine
GelMA	Gelatin methacryloyl
HA	Hyaluronic acid
HFIP	Hexafluoro-2-propanol
IL	Interleukin
iPSCs	Induced pluripotent stem cells
MDSCs	Myeloid-derived suppressive cells

MMPs	Matrix metalloproteases
NPs	Nanoparticles
NSAIDs	Non-steroidal anti-inflammatory drugs
PDGF	Platelet-derived growth factor
PC	Pancreatic cancer
PCL	Polycaprolactone
PGs	Proteoglycans
PLGA	Poly(lactic-co-glycolic acid)
PLLA	Poly-L-lactic acid
ROS	Reactive oxygen species
Scx	Scleraxis
T2DM	Type II diabetes mellitus
TA	Tannic acid
TAMs	Tumor-associated macrophages
TGFβ	Transforming growth factor beta
TME	Tissue microenvironment
Tnmd	Tenomodulin
TSPCs	Tendon stem/progenitor cells
VEGF	Vascular endothelial growth factor
W/O	Water-in-oil
ZnO	Zinc oxide

Chapter 1 Introduction

Tissue microenvironment (TME) is defined as the small-scale environment which comprises the tissue-specific immune and non-immune cells (e.g., fibroblasts and endothelial cells) and their concomitant non-cellular constituents (e.g., cytokines, extracellular matrix [ECM], and growth factors) [1]. These components in TEM interact with each other and collectively form a multifaceted regulatory network to assist the maintenance of organ homeostasis. Previous studies have demonstrated that TME is not only critical for native tissue/organ development, but also essential for the progression of diseases [2, 3]. In the field of biomedical engineering, electrospinning as a facile and widely-used technique which can yield ECM-like electrospun scaffold, proves a multifunctional tool to intervene tissue healing and disease progression through modulating the TME [4, 5]. Electrospinning enables to prepare ultrafine and continuous fibers using either organic or inorganic materials [4]. The resultant electrospun membrane scaffold has a high surface area and aspect ratio, and shows a highly controllable structure (e.g., fiber thickness or pore diameter) and modified physical properties (e.g., mechanical performance) [4]. Under this umbrella, this chapter opens with an extensive introduction of the cutting-edge electrospinning technique regarding its principle, process, parameters, and drug incorporation patterns as well as the associated drug release profile from electrospun scaffolds.

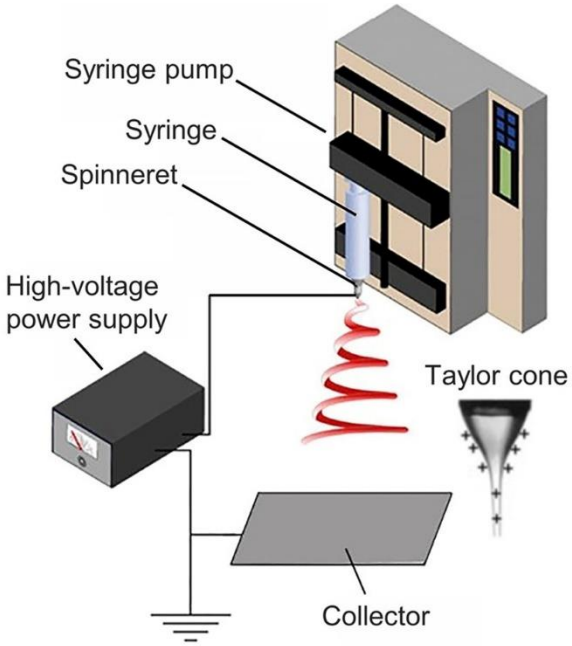

Figure 1-1. Schematic illustration of a conventional electrospinning setup and various factors influencing the resultant electrospun scaffolds. Reproduced with permission from [10]. Copyright 2019, American Chemical Society.

1.1 Principle, process, and parameters of electrospinning

During the electrospinning, the fine polymeric fibers are generated from a precursor solution driven by a strong electrostatic force [6]. The electrospinning system is commonly comprised of three components: a high-voltage generator, a syringe equipped with a needle and pump of appropriate size, and a meta collector (**Figure 1-1**) [7]. The strong electrostatic force between the needle and collector is induced by the high-voltage supplier. At the beginning of electrospinning, the precursor solution forms a hemisphere at the needle tip, which subsequently turns a Taylor cone upon application of a high voltage. With the increase of electrical potential, the precursor solution overcomes the surface tension and yields a jet fiber that is then deposited onto the metal collector. Despite the above-mentioned simple concept, many parameters such as polymeric precursor solution and process deployed and the ambient conditions (e.g., humidity and temperature) would influence the electrospinning system and further the resultant fibrous membrane [8]. The preparation of precursor solution for electrospinning requires appropriate choice of materials and solvents. The electrospun

precursor solution should possess appropriate viscosity, electrical conductivity, and surface tension. The materials for electrospinning should possess suitable glass transition temperature, solubility, molecular weight, and molecular weight distribution. Currently, the commonly used materials include natural and synthetic polymers as well as their combinations [6]. In general, the natural polymers (e.g., collagen, gelatin, elastin, and silk) are used due to their excellent biocompatibility and bioactivity which can mimic the native tissue components, while the synthetic polymers (e.g., poly-L-lactic acid [PLLA], polycaprolactone [PCL], and poly(lactic-co-glycolic acid) [PLGA]) are used because of their good mechanical properties and relatively slow degradation, which can provide a long-term mechanical support for tissue regeneration [4]. Besides, a suitable solvent is another crucial factor for successful electrospinning. The electrospun solvent must meet the following two basic requirements: 1) it can dissolve the polymeric materials to a relatively high concentration; 2) the solvent should evaporate fast so as to maintain the resultant electrospun fibrous structure. As a result, the solvent properties like vapor pressure, polarity, and surface tension significantly affect the electrospinning process. Currently, the organic solvent such as hexafluoro-2-propanol (HFIP), dichloromethane (DCM), acetone, ethanol, chloroform, and N,N-Dimethylformamide (DMF) are commonly adopted for electrospinning. Some specific solvent mixtures like chloroform/acetone or ethanol/DCM are also used to dissolve the polymer. Nevertheless, when selecting the solvent for electrospinning, its toxicity should be carefully concerned which may compromise the bioactivity of encapsulated cargoes such as cells, drugs, or biomaterials.

Electrospinning is a versatile technique, of which the parameters can be readily modulated so as to produce fibers of needed diameter and morphology, and thus the electrospun membrane with desired performance [6]. The basic modifiable parameters for electrospinning include precursor solution properties (e.g., concentration, conductivity, and surface tension), equipment settings (e.g., electric tension, tip size, tip-to-collector space, and flow velocity), and the surrounding environmental conditions (e.g., temperature and moisture) [9, 10] (**Figure 1-2**). For example, increase

of voltage, conductivity, and/or needle tip-to-collector distance usually causes decreased fiber diameter. Through adjusting those arguments, the diameter of the resultant electrospun fibers can range from nanometers to micrometers. Increasing the molecular weight of precursor solution or flow rate of syringe would produce fibers with larger diameters. Besides, by using different nozzle designs or multi-component co-electrospinning technique, fibers of different morphology can also be obtained. For instance, coaxial nozzle is often designed for preparation of fibers with core-shell structure, while different NPs like mesoporous silica NPs and hydroxyapatite NPs have also been incorporated to obtain fibers with hierarchical structure [4]. It is worth mentioning that different from the laboratory electrospinning setup that can produce fibrous membranes with a limited size, the industrial electrospinning, by reasonable design (such as multiple jetting needles), has allowed for large-scale fabrication of membranes with desirable area. Altogether, electrospinning possesses many advantages including simplicity, cost effectiveness, and easy to scaled-up fabrication, therefore showing great potential for application in biomedical engineering.

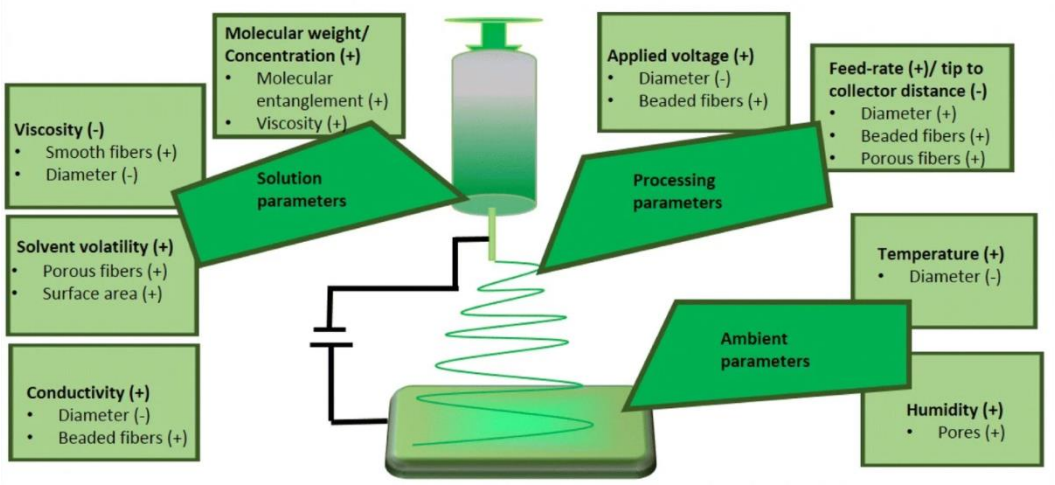

Figure 1-2. Schematic showing the various electrospinning parameters that influence the morphology of the resultant nanofibers. Reproduced with permission from [9]. Copyright 2018, Springer.

1.2 Drug-incorporating strategies in electrospinning

Currently, many commercial electrospun nanofiber-based products have been put

forward such as HealSmart™ (PolyRemedy), Mimetix® scaffold (Electrospinning Company), NeoDura™ (Medprin Biotech GmbH), and ResQFoamTM (Arsenal Medical). These scaffolds have been widely used in clinic to promote tissue repair and/or regeneration (e.g., skin, bone, and dental tissues, etc.). To further improve the therapeutical efficacy, various therapeutic agents including chemical drugs and biologicals (e.g., protein and nucleic acid) have been incorporated into the electrospun membrane scaffolds [4]. The current drug-loading strategies can be classified as surface modification, direct blending, emulsion, and coaxial electrospinning (**Figure 1-3**) [4]. As for surface modification, the drugs are physically or chemically deposited onto the surface of electrospun fibers. Through such loading technique, uncontrollable dispersion within the inner of electrospun fibers can be avoided. Besides, it can evade the harsh electrospinning process since the surface modification is done after electrospinning [4]. Since the fibers with surface modification enable a rapid tissue-scaffold interaction after implantation and consequent a relatively fast drug release, such fibers are more suitable for treatment of acute diseases. For the chronic diseases with longer-term recovery period, the surface modification may not suffice.

Direct blending is another commonly adopted technique to encapsulate drugs by directly dissolving drugs into the precursor electrospun solution [4]. The loading efficiency, spatial distribution, release pattern of drugs mainly depend on the polymers in use and polymer-drug interactions [4]. To illustrate, drugs with low solubility in the precursor solution could lead to non-uniform distribution of drugs within fibers (mainly located on the fiber surface), which may cause undesired burst release. To render the drugs with better distribution within the fibers, NPs could be introduced to load the drugs first before electrospinning. This will form a physical barrier for drugs against the polymer, thus increasing the drug dispersibility and also providing a protection for drugs. Due to their controllable drug release profiles, fibers prepared by blending electrospinning can be used in various tissue engineering fields.

Coaxial electrospinning is often used to generate fibers with core-shell structure, where

drugs are often incorporated in the inner part (i.e., core) and the bulk polymer constitutes the outer part (i.e., shell) of the synthetic electrospun fibers [11]. As a result, the loaded drugs can be well protected by the outer shell from harsh environment and further extend its release time length. In addition to biomolecules, the pharmaceutics such as antibiotics and antioxidants can also be loaded inside the polymeric fibers.

With regards to emulsion electrospinning, the drugs are dispersed uniformly within the electrospun solution assisted by surfactant. A core-shell fibrous structure could be obtained with drug aqueous phase constituting the core layer and polymer moulding the shell layer [12]. This technique is quite suitable for drugs that are poorly dissolved in the polymer solution. Owing to the less contact between drugs and the organic solvent, the emulsion electrospinning can be applied to a variety of drugs with different hydrophilic–hydrophobic properties. At the same time, the bioactivity of drugs can be maximumly reserved. Since these fibers fabricated using coaxial and emulsion electrospinning possess a prolonged drug release pattern, they can be used extensively for chronic diseases with a long-term therapy window. However, both the coaxial and emulsion electrospinning require introduction of new component into the fiber system, which would complicate the whole drug delivery platform to some degree. Besides, the preparation and process for coaxial and emulsion electrospinning are time-consuming with higher cost effectiveness [13]. Therefore, it is necessary to weigh various parameters comprehensively when designing an electrospun membrane scaffold.

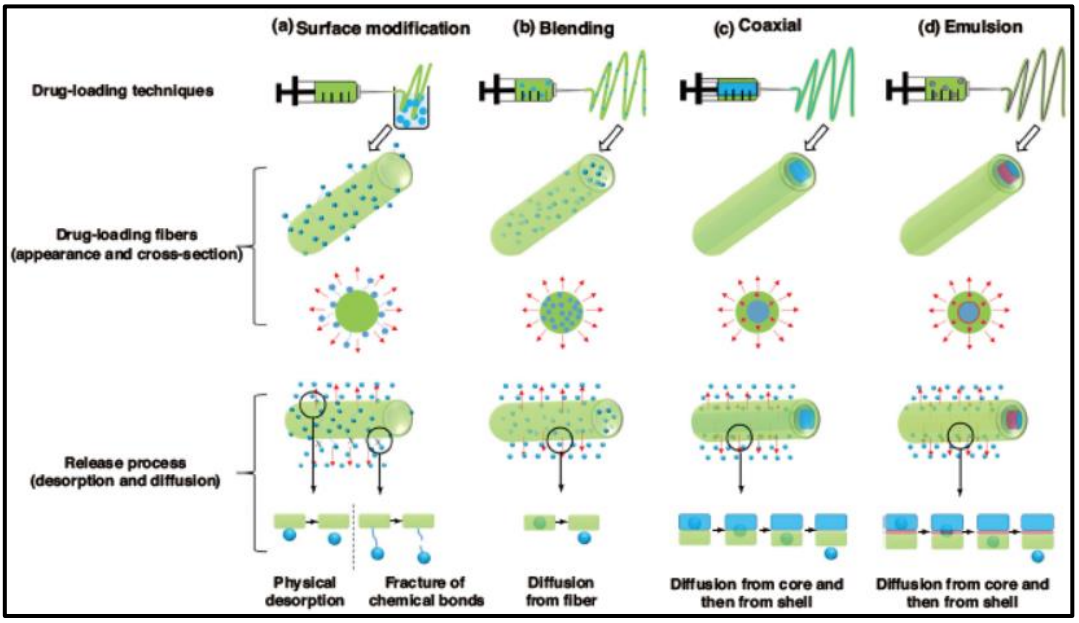

Figure 1-3. Schematic illustration of drug release loading and release processes from electrospun membranes fabricated by different drug-incorporating strategies with surface modification, blending, coaxial, and emulsion electrospinning included. Reproduced with permission from [4]. Copyright 2017, Elsevier.

1.3 Release mechanisms of drugs from electrospun scaffolds

The main drug release mechanisms from electrospun scaffolds include direct desorption from the fiber surface, diffusion in the fibers, and degradation of fibers [4, 14]. Those three mechanisms can co-exist simultaneously during drug release period. To illustrate, when the electrospun fibers are immersed into the aqueous solution, the drugs modified onto the fiber surface are released through desorption. Besides, the drugs close to the surface of nanofibers can also be released by desorption. As compared to other mechanisms, the whole desorption is a relatively rapid process, which results in a burst release pattern; such pattern is generally uncontrollable and therefore inappropriate for sustained release. As described above, blending, coaxial and emulsion electrospinning have been designed as alternatives to limit drug attachment onto the fiber surface and avoid undesired burst release. The drug release in direct blending electrospinning is dependent on the diffusion concentration gradients, therefore leaving a possibility of burst release profile. To cope with that, the incorporation of drug-loaded NPs into the electrospun fiber can set up a physical barrier for the drug against aqueous phase, which

could extend the diffusion route attenuating the burst release and prolonging the release period.

Compared with the other two mechanisms, polymer degradation could vastly influence the drug release profiles. For the nonbiodegradable polymeric electrospun fibers, drug release process only relies on the diffusion process through the polymer. However, for the biodegradable electrospun fibers, drugs can be released by diffusion as well as by the space caused by fiber degradation. Through degradation, the drugs entrapped within the fibers enter the surrounding aqueous solution. Thus, it is challenging to control the drug release from rapidly degrading polymers like chitosan or poly(vinyl alcohol). For these reasons, selection of an appropriate polymeric material and drug-incorporation strategy is vitally important to construction of a drug-carrier scaffold with satisfactory release patterns [15]. Fiber morphology plays a critical role in drug release pattern, in terms of these release mechanisms. In general, the order of drug release rate of electrospun fibers with different morphology or structure is surface modification > Blending > Coaxial ≈ Emulsion [4]. In addition, the fiber diameter also affects the drug release profile [16]. The fine fibers exhibited more obvious burst release and faster release rate in second stage, compared with coarse fibers. The fibers with large diameter would be more beneficial for their applications in long-term and smooth drug delivery.

Taken together, via controlled release of various chemicals or biologicals from electrospun fibrous membrane scaffolds, the topical TME can be modulated finely. Besides, the architecture parameters, mechanical properties, and degradation rates of electrospun scaffolds are also highly regulable to meet the practical application requirements. Currently, various electrospinning-based drug delivery systems have been widely employed in different tissue engineering fields such as bone, skin, and cardiovascular tissues [17, 18]. In this dissertation, I focused on the tendon and cancer tissues and exploited the electrospinning technique to prepare different scaffolds for intervention of disease progressions.

Chapter 2 Development of MMP-responsive siRNA-laden fibrous membranes for prevention of tendon adhesion

2.1 Introduction

2.1.1 Tendon tissue healing microenvironment

2.1.1.1 Tendon structure and composition

Tendon, as a complex connective tissue conveying the muscle-to-bone forces, plays a vital role in coordinating the joint movement [19]. With moderate mechanical strength compared to that of muscle and bone, tendon could alleviate the physical stress concentration figuring as a subtle buffer. Furthermore, tendon can store and release elastic energy during the joint locomotion and withstand the tensile stretching by outside forces, thus protecting the body joint from damage and ensuring efficient physical activity [20]. In view of its critical role, tendon injuries would not only cause substantial impact on the mobility and life quality of patients, but also pose heavy healthcare as well as economic burden due to the high prevalence.

Mature tendon is characterized by hierarchical structure with collagen as the backbone ECM interspersed with various cells and biomolecules (**Figure 2-1**) [21, 22]. In the outmost layer of the tendon, there is a thin sheet encapsulating the whole tendon which is known as 'epitenon'. The inner layer extended along the long axis of tendon is a group of fascicles which show a tube-like architecture and are enveloped by a thin membrane, also referred to as 'endotenon'. The composition of endotenon is similar to that of epitenon. The blood vessels, nerve fibers and lymphatics mainly thread through those two layers. The collagen fibril exists as the minimum structural unit in the tendon and appears to be periodically crumpled. These fibrils consist of water-soluble tropocollagen molecules with diameter of 1.5 nm which can then crosslink to form insoluble collagen molecules and aggregate into microfibril.

A normal tendon tissue is comprised of cellular and non-cellular (extracellular) composition [23]. For the cellular population, approximately 90-95% of tendon-specific cell types are tenocytes, of which the precursor cells are known as tenoblasts. These immature tendon cells are highly proliferative and responsible for synthesizing the tendon ECM; however, their activity gradually decrease during growth and aging. Besides, other cell types including synovial cells, chondrocyte cells, adipose-derived stem cells (ADSCs), mesenchymal stem cells (MSCs), vascular cells, and smooth muscle cells scatter in the different sites of tendon. In 2007, a new type of resident stem/progenitor cell population was identified for tendon (frequently termed TSPCs) [24]. TSPCs not only exhibit the innate properties of stem cells such as renewal, clonogenicity and multi-direction differentiation (e.g., bone, cartilage, and fat), but also express tendon-related markers like scleraxis (Scx) and tenomodulin (Tnmd), thereby possessing great potential to guide tenogenic regeneration and promote tendon healing.

In addition to collagen and elastin, glycosaminoglycans (GAGs) as well as proteoglycans (PGs) are rich constituents in the ECM of tendon tissue [23]. These components vary in the concentration between tendon tissues in different sites of the body. As the most plentiful protein component in the tendon ECM, collagen type I (Col-1) accounts for almost 60 of the dry mass of tendon tissue. The second major constituent of tendon ECM is the collagen type III (Col-3), which is secreted massively during tendon healing [25]. There also exist many other collagens in the tendon tissue like collagen types V, VI and XII. In general, as the main structural components of tendon, collagen fibers contribute to maintaining tissue structure, protecting tendon from mechanical failure, transmitting force load and withstanding tension during muscular exercises. The elastic fibers account for 1 to 2 percent of tendon dry weight and are crucial to promoting tendon flexibility and extensibility as well as ensuring the complete recovery after long-range deformation. The remaining contents like hyaluronan, GAGs, and PGs, despite a tiny amount in tendon (1-2%), are involved in many important physiological processes like cell behavior regulation, lubrication, support of collagen fibers and prevention of tendon breakage.

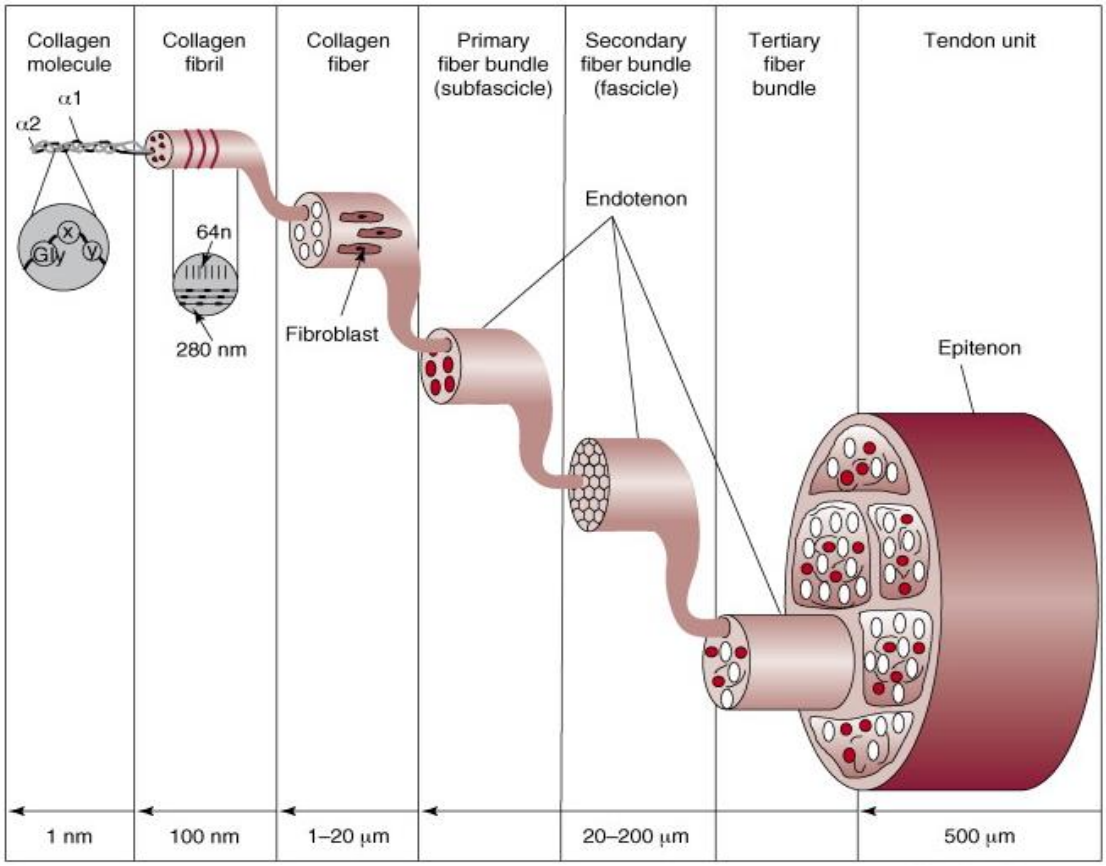

Figure 2-1. The schematic showing the hierarchical structure of tendon tissue. Reproduced with permission from [22]. Copyright 2017, Elsevier.

2.1.1.2 Biology and pathology of tendon healing

The healing after injuries to tendon progresses in three intersecting phases: 1) a relatively short inflammatory phase (lasting for a few days); 2) a proliferative and/or repairing phase (lasting for a few weeks); and 3) a prolonged remodeling and/or maturation phase (lasting for several months or even years) (**Figure 2-2 A**) [23, 26, 27]. The whole healing process is affected by many external factors (such as physical condition, treatment regimen, injury type, injury location, and etc.) and involves the contribution of multiple cell populations producing various cytokines and growth factors (**Figure 2-2 B**) [21, 26]. Specifically, during the inflammatory phase, an influx of circulating inflammatory cells (i.e., phagocytic neutrophils, monocytes) migrate to the injury site immediately after acute tendon damage and produce a cascade of

cytokines resulting in recruitment and propagation of macrophages and resident tendon fibroblasts. Moreover, secretion of angiogenic factors promotes formation of new blood vessels, which can support the survival of fibrous tissue formed at sites of injury. In the next stage of proliferative phase, the fibroblasts are recruited to the wound area, proliferate and produce a large amount of ECM components (granulation tissue) that are mainly composed of Col-3. A niche is then formed by those provisional matrixes for the growth and proliferation of various cell populations migrated to the injury site. The following extended remodeling phrase of tendon healing can be further separated into two ordinalstages: consolidation and then maturation. During the consolidation, the cellularity and vascularity dramatically decrease with the granulation tissue maturing into a scar tissue. Besides, the matrix production also reduces as Col-1 gradually substitutes the Col-3. Then, the collagen fiber assembly aligns along the long axis of tendon, remodels its microstructure and restores its mechanical performance. In the long maturation stage, the collagen fibril crosslinking further accumulates, and more mature tendon tissue will be formed.

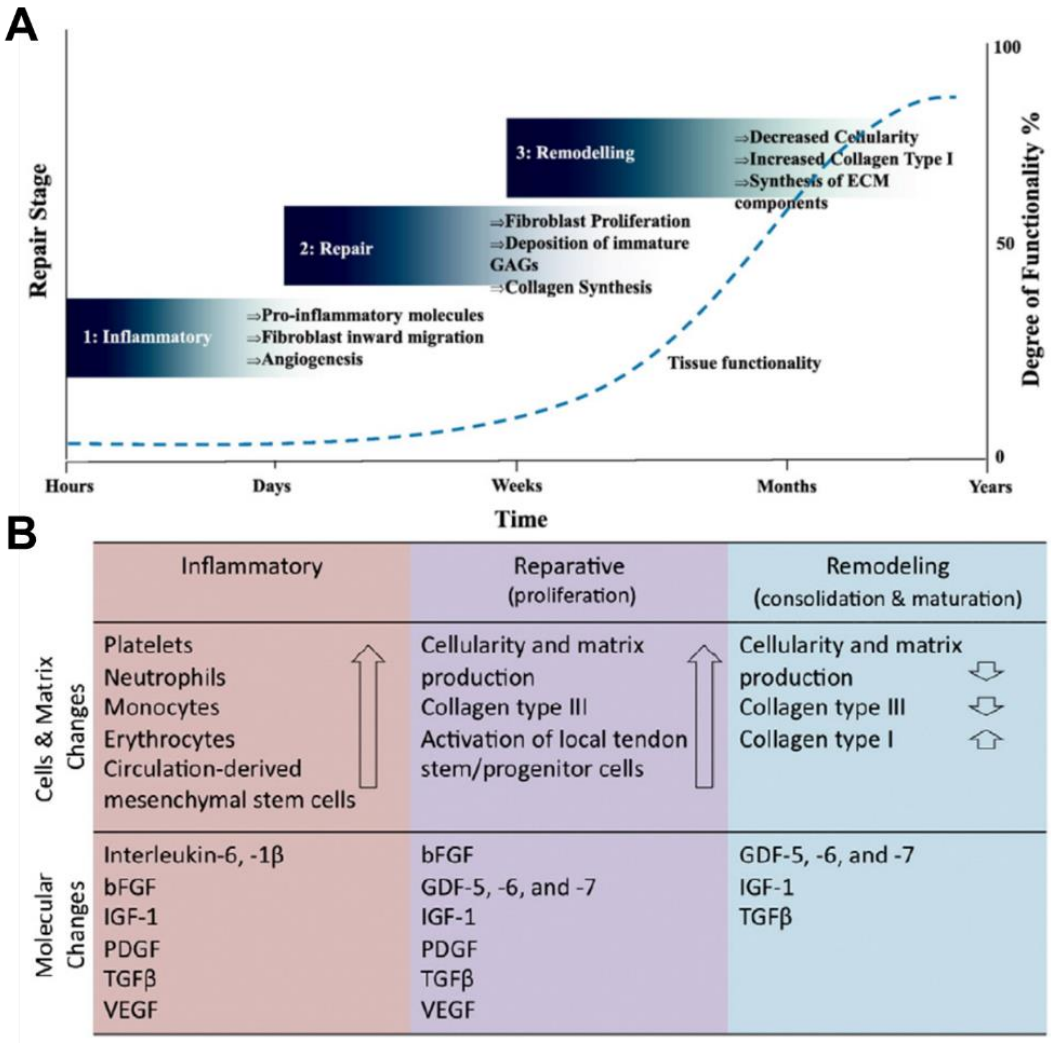

Figure 2-2. (A) The tendon healing process involves three phases including inflammation, repair, and remodelling. Reproduced with permission from [23]. Copyright 2015, Elsevier. (B) The key molecular, cellular and extracellular matrix changes in the three phrases of tendon healing. Reproduced with permission from [21. Copyright 2015, Elsevier.

Tendon healing is thought to be regulated by two cellular mechanisms: intrinsic and extrinsic healing [28]. Intrinsic healing is predominantly lead by cells from the topical tendon tissues to reorganize ECM and provide a support for new blood vessels, while the extrinsic healing is modulated by cells recruited from exogenous neighbouring tissues such as blood vessel, sheath and paratenon which facilitate cell infiltration and tendon reconstruction [29]. Since the intrinsic cells possess the characteristics of low activity and reparative capacity, extrinsic healing mechanism is the overriding one

during tendon healing process. However, excessive extrinsic healing will give rise to the emergence of scar tissue and tendon adhesion, thus reducing the tendon mechanical performance and increasing the risk of re-rupture (**Figure 2-3**) [28]. Therefore, although this dual-mechanism healing system can synergistically promote tendon repair, its repair quality is highly dependent on their subtle balance.

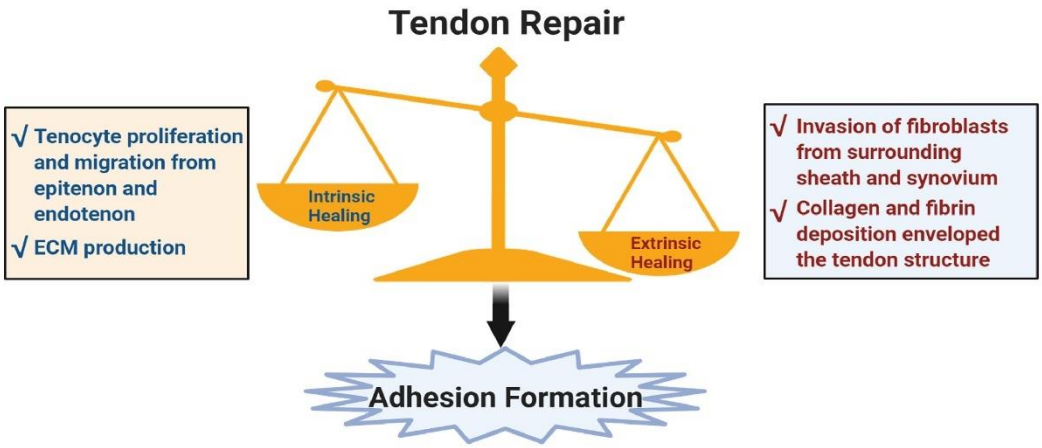

Figure 2-3. Adhesion formation caused by the excessive extrinsic healing. Reproduced with permission from [28]. Copyright 2021, Elsevier.

As discussed above, the tendon repair is finely orchestrated by various biomolecules [28]. For example, the circulating inflammatory cells can produce a variety of cytokines such as interleukin (IL)-6 and IL-1β in response to injuries. Moreover, growth factors of all sorts including basic fibroblast growth factor (bFGF), bone morphogenetic proteins (BMP), transforming growth factor beta (TGFβ), platelet-derived growth factor (PDGF) and vascular endothelial growth factor (VEGF) are generated and dynamically involved in the whole process of tendon healing, exerting diverse physiological functions [30, 31]. Altogether, the healing process after tendon injuries is intricate and long-term, where a wide range of cellular and non-cellular factors play a role. By subtly modifying these factors to modulate the healing process (e.g., enhancing the intrinsic while suppressing the extrinsic healing pathway), it is possible to restore the tendon function satisfactorily after injuries.

2.1.2 Current strategies to prevent tendon adhesion

The tendon adhesion formation remains the most severe clinical complication following the tendon surgery [28]. The core mechanism to prevent such complication is the inhibition of extrinsic healing process [28]. Since the inflammation response in the early healing stage is highly associated with later tendon adhesion formation, anti-inflammatory pharmaceuticals like NSAIDs and corticosteroids are commonly used to reduce inflammation-induced excessive secretion of collagen and so promote tendon healing. In addition, chemotherapeutic 5-fluorouracil [32] and mitomycin [33] have also been adopted to inhibit the fibroblast proliferation by suppressing the DNA replication. And indubitably, growth factors such as TGFβ and their corresponding nucleic acids have been extensively explored to prevent tendon adhesion formation [34]. Of note, TGFβ could induce the upregulation of the extracellular signal-regulated kinase 1/2 (ERK1/2) and Smads protein 2/3 (SMAD2/3) pathways to modulate exogenous fibroblast proliferation and collagen synthesis. Thus, inhibition of TGFβ, ERK and SMAD has demonstrated to successfully prevent the adhesion formation [34-36]. Yet, the effective delivery of these drugs or biologics to desired injury sites remains a challenge; various tissue engineering delivery platforms have been therefore put forwarded.

Hitherto, the delivery platforms designed for prevention of tendon adhesion formation can be broadly classified as follows: 1) nanoparticles (NPs); 2) hydrogel; 3) membranes and 4) combinations thereof [28]. Among them, NPs are the most commonly used delivery platform for treatment of various diseases [28]. They can protect vulnerable drugs and/or biologics from inactivation caused by TME. Besides, since NPs can be directly internalized by cells, the delivery efficiency and bioavailability of loaded pharmaceuticals will be significantly improved [37]. Moreover, NPs can act as a shield for loaded drugs and remarkably extend their release, which is highly advantageous for preventing tendon adhesion formation as it may take several weeks to months for adhesion to develop [37]. Zhou et al. leveraged the emulsion technique to prepare PLGA NPs loaded with TGF-β1 miRNA plasmid to restrain tendon adhesion [34]. Such

system can continuously release gene for 4 weeks, and thus inhibit the adhesion formation for a long time (over 6 weeks). However, NPs cannot serve as a physical obstacle to hinder extrinsic fibroblast migration to the defect sites, thus achieving a limited success. To address such concern, different barrier platforms have been developed including silica gel, gold foil, hydrogels, and fibrous membranes. By now, the silica gel and gold foil have already been weeded out because they are non-degradable and non-permeable. Compared with the non-degradable materials, the biodegradable materials, especially the slowly degradable polymers such as PLGA, PLLA, and polyethylene glycol, have many advantages including more suitable biocompatibility and good permeability to promote the nutrition/oxygen transportation, thus accelerating the wound healing [4]. Through different fabrication strategies, these materials have been constructed into various structures like hydrogels or membranes, which will be discussed in what follows.

Owing to its high-water content and porosity, the hydrogel can provide a favorable cell microenvironment and show excellent biocompatibility [38-40]. It can not only promote tendon repair by regulating the cell behaviors, but also suppress the tendon adhesion formation by serving as a physical barrier. Besides, we can readily control the degradability or mechanical properties of hydrogel by changing its concentration or crosslinking density to meet the needs of practical application. Currently, various injectable hydrogels have been developed to prevent the tendon adhesion formation, as it can gel at the defect site after injection and warp around the injury site to prevent scar tissue in-growth [41, 42]. Moreover, hydrogel can fit different shape of injury site without the need of special intervention. More importantly, such hydrogel delivery system is rather suitable for minor tendon injuries, since it can evade the surgical operation and promote healing in a minimal invasive manner. As a representative example, Chou et al. designed a thermo-responsive hydrogel via modifying poly(N-isopropylacrylamide) using chitosan and HA to impede peritendinous adhesion post operation [43]. *In vitro* experiment has demonstrated that the suppression effect of such hydrogel on fibroblast growth could be attributed to the cytostatic action of chitosan.

In addition to the direct role as a physical barrier to deter adhesion formation, hydrogel could load kinds of functional drugs and biologicals to enhance their anti-fibrotic ability. For example, cyclooxygenase-engineered miRNA plasmid was firstly loaded into PLGA NPs by emulsification technique and then embedded into the HA hydrogel by blending electrospinning (**Figure 2-4**) [44]. This novel gene delivery system could elude the undesired leakage during injection and prolong the release pattern covering the early inflammatory process, thereby significantly reducing adhesion while increasing the mechanical strength of healed tendon. In another study by Chen et al., an asymmetric hydrogel was developed using a self-deposition technique to imitate the outer fibrotic layer and the inner synovial layer of native tendon sheath [45]. Such biomimetic dual layer hydrogel scaffold could provide a mechanical support and inhibit the extrinsic healing, and also create a suitable cell niche for intrinsic tendon healing. Despite the above-discussed advantages, hydrogel-based scaffolds have shown inferior mechanical performances when compared with synthetic polymer grafts, thus being unable to induce the tenogenic differentiation of stem cells through mechanically sensitive pathways. Hence, a hydrogel scaffold with improved mechanical properties is highly warranted for its practice clinical application for prevention of fibrosis formation.

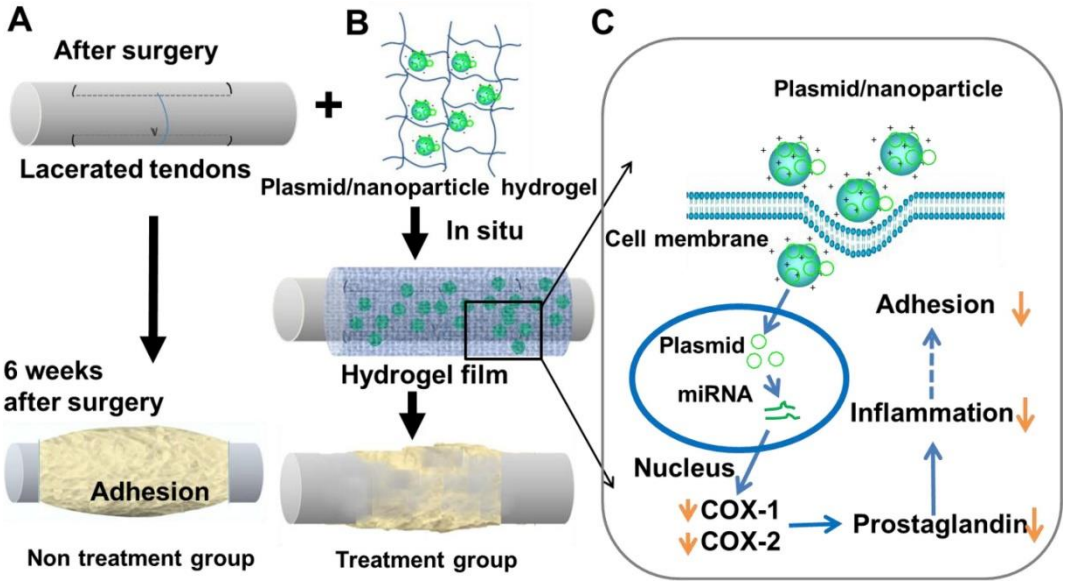

Figure 2-4. Schematic illustrating the suppression of tendon fibrosis formation by local injection of hydrogel containing miRNA-loaded NPs. Reproduced with permission

from [44]. Copyright 2018, Elsevier.

Due to the similar 3D framework to native tendon ECM, the fibrous membranes have been most utilized as a therapeutic platform for tendon repair [46, 47]. In the preparation of fibrous membranes, various technologies such as electrospinning, wet/jet spinning, melt electrowriting, and textile approaches have been adopted [28]. Among them, electrospinning is the most popular technique that can readily prepare the fibrous membrane with diameter from nano- to micron- scale [4, 48]. The detailed parameters including impressed voltage, solution viscosity, collecting distance, and flux rate that can influence the resultant fiber structure will be discussed in the later section. In general, current fibrous membrane-based therapeutic platforms can be categorized into four major types: 1) pure fibrous membranes; 2) fibrous membranes loaded with drugs; 3) fibrous membranes loaded with growth factors or genes; 4) fibrous membranes combined with other delivery systems (e.g, NPs, hydrogel, etc) and/or multi-techniques (e.g., weaving, braiding, etc). Firstly, previous studies have shown that the architecture such as topography and porosity would be of significant importance in the healing of impaired tendon by activating the mechanotransduction pathway [49]. For instance, aligned nanofibers that mimic the intrinsic *in vivo* collagen configuration have been demonstrated to improve cell orientation and elongation by influencing the cell cytoskeletal organization [50, 51]. Besides, unlike randomly oriented nanofibers, aligned ones can promote tendon-related genes expression, stimulate tenogenic differentiation, and prompt the commitment of stem cells. Apart from the fiber alignment type, the pore diameter and fiber thickness may also influence the performance of fibrous membranes to impede tendon adhesion [52]. Simply put, large pores may enable fibroblasts to infiltrate through the membranes and facilitate the extrinsic healing. Accordingly, when designing the membranes, pore size should be carefully considered to inhibit exogenous cell invasion while allowing for appropriate nutrient and waste exchange. Additionally, Erisken et al. has demonstrated the importance of fiber diameter in modulating cell behaviors [53]. They found that fibrous membranes of smaller diameters (< 500 nm) could provoke fibroblast proliferation and

collagen production, which will increase tendon adhesion formation. Otherwise, fibrous membranes of larger diameter (> 500 nm) could induce gene expression of tendon transcription factors (e.g., decorin, Scx, and Tnmd), which could prevent adhesion formation. Altogether, the physical cues of fibrous membranes can mould the balance between intrinsic and extrinsic healing processes. It is important to carefully modulate those physical parameters so as to achieve novel membrane scaffolds with optimized efficacy, thereby stimulating intrinsic healing to promote tendon repair while suppressing extrinsic healing to inhibit tendon adhesion.

As discussed above, the early-stage inflammatory reaction has a vital role in later adhesion formation. It is far from enough to prevent the tendon adhesion only by regulating the physical properties of membrane scaffolds. Similarly, different anti-inflammatory drugs and chemotherapeutics have been incorporated into membrane scaffolds to regulate cell fate for tendon adhesion inhibition [28]. For example, Liu et al. loaded ibuprofen into electrospun nanofibrous membrane and designed a long-term release system for over 3 weeks [54]. By downregulating the expression of cyclooxygenase-1 and cyclooxygenase-2, inflammatory cell invasion was significantly reduced, and fibroblast proliferation was also suppressed. In another representative study conducted by Zhao et al., chemotherapeutic mitomycin was loaded into the nanofibrous membranes with a core-shell structure (**Figure 2-5**) [55]. Such therapeutical platform manifested a rapid burst release of mitomycin at the early stage to induce fibroblast apoptosis, and a subsequent sustained release for over 40 days to prevent the late tendon adhesion formation. The modulation of fibroblast fate and inflammatory response after tendon injury by loading drugs to intervene the relevant signalling pathways have achieved great success in suppressing tendon adhesion formation. Nevertheless, these therapeutic agents have deficient ability to promote intrinsic healing. To overcome such drawback, growth factors or genes have been encapsulated into the membrane scaffolds to promote tendon regeneration without stimulating scar tissue formation. PDGF is an important growth factor that can promote cell proliferation as well as collagen deposition and accelerate ECM production during

the intrinsic healing process. To realize the targeted delivery and long-term release, PDGF was loaded into the core layer of electrospun nanofibrous membranes using emulsion electrospinning [56]. The shell structure acted as a barrier and prolonged the PDGF release from the membranes (for over 30 days). *In vivo* experiment further showed that such scaffold can enhance mechanical performance of the restored tendon and reduce the tendon adhesion formation. In addition to growth factors, genes (e.g., miRNA or siRNA) were also loaded into membrane scaffolds to genetically regulate the expression of some key signalling pathways. As compared with growth factors, gene modification can control cell behaviors in a longer-term perspective, thus being a more effective way to intervene disease progress. For example, an ERK2-siRNA was loaded into the electrospun PLLA/HA membrane via emulsion electrospinning (**Figure 2-6**) [36]. Such delivery system could release siRNA for over 30 days, and significantly downregulate the expression of ERK2 and its downstream factor SMAD3, showing a potent therapeutic efficacy on tendon adhesion prevention. Despite being promising in preclinical experiments, growth factor or gene-based delivery systems face many challenges. Firstly, the precise delivery of these cargos in a spatiotemporal pattern to further enhance their therapeutic efficacy is still technically challenging. Moreover, uncontrollable release and inferior targeted delivery could cause severe side-effects. Also, the tumorigenicity of growth factors and genes is worthy of concern before such experimental products could be transferred into clinical application. It is envisaged that future delivery vehicles should be smart enough to target the interested site without eliciting adverse effects.

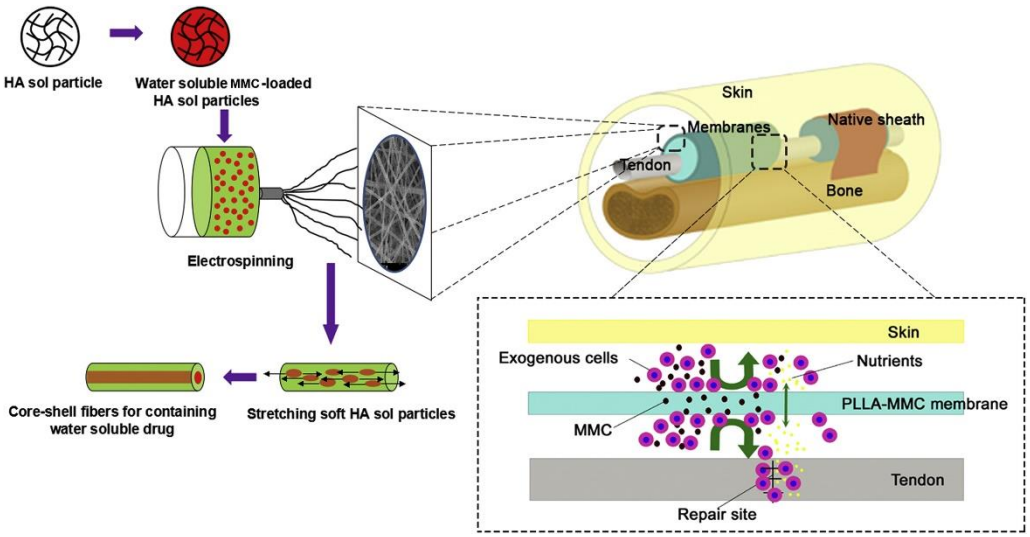

Figure 2-5. Schematic showing the process to fabricate mitomycin-loaded PLLA fibrous membrane for prevention of adhesion formation. Reproduced with permission from [55]. Copyright 2015, Elsevier.

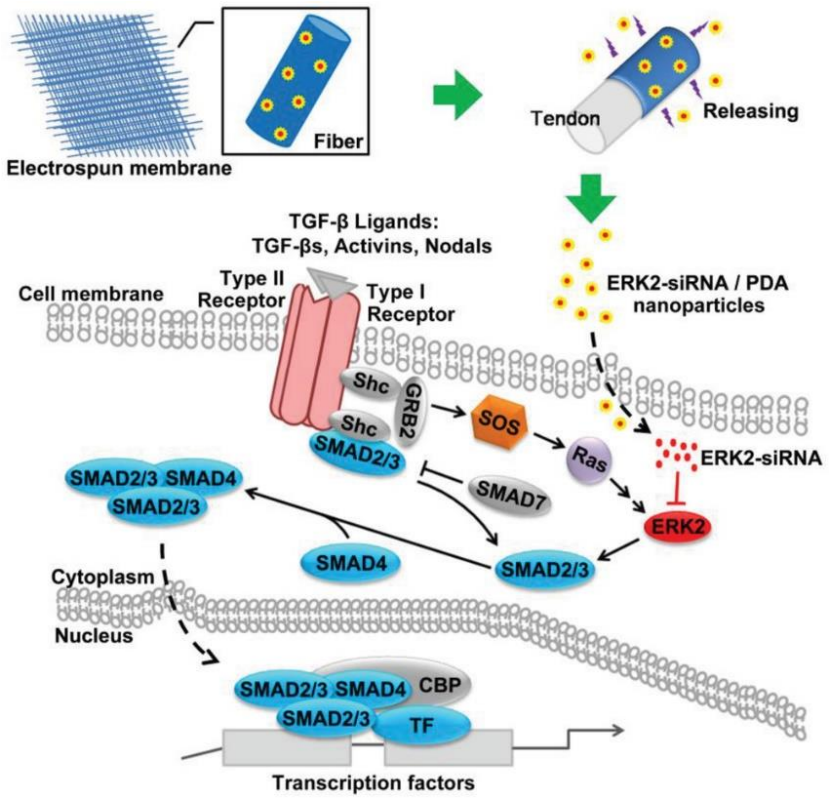

Figure 2-6. Schematic illustration of ERK2-siRNA loaded PLLA electrospun membrane as a physical barrier to suppress adhesion formation. Reproduced with permission from [36]. Copyright 2019, Wiley-VCH.

Fibrous membranes can also be combined with other therapeutic structures like NPs or hydrogels. For example, NPs could be grafted on the surface of fibrous membrane or encapsulated into its inner layer. Liu et al. firstly prepared the bFGF-loaded dextran glassy NPs which were then loaded into the PLLA electrospun membrane scaffold [57]. Such hierarchical delivery system could release bFGF in a spatiotemporal manner for over 30 days without damaging its bioactivity. Both *in vitro* and *in vivo* verified that this innovative platform could promote intrinsic healing by inducing the angiogenesis and supporting cellular growth, thus reducing the adhesion formation. Another exemplary study conducted by Jayasree et al. proposed a multiscale fibrous braided scaffold that was comprised of PCL microfibrous sheets and collagen-FGF- β nanofibrous sheets [58]. Such scaffold mimicked the structure and chemical composition of native tendon, hence purporting to offer a biomimetic microenvironment to improve tendon repair. Besides, the results of mechanical test showed that the prepared scaffolds encompassed a comparable tensile strength to human Achilles tendon. To endow this scaffold with ani-adhesion performance, alginate layer was then uniformly coated onto the surface to reduce protein absorption and fibroblast attachment.

Altogether, drug-loaded electrospun membranes have become a common strategy to prevent peritendinous adhesion. However, the drug release patterns are often uncontrollable, which cannot comply with the inherent dynamic tendon biology, causing low drug accumulation and even severe adverse effects in the tendon injury site. Therefore, novel therapeutical platforms should be designed based on the changing TME during tendon healing, to improve the treatment efficiency and safety.

2.1.3 Motivation and objective

A controllable therapeutic delivery system that can be triggered to release the cargoes in response to changing tendon TME for tendon adhesion prevention is highly sought after. Previous studies have reported that matrix metalloproteinase (MMP), especially the MMP-2, was significantly upregulated after tendon rupture in the peritendinous area,

which indicated that MMP-2 can be used as a trigger for constructing stimuli-responsive delivery system [59]. We hypothesized such MMP-2 responsive delivery system could realize on-demand release of the drugs when exposure to high MMP-2 microenvironment. Besides, such system could avoid the excessive drug release in the local tissue and prevent the side effects, thus promoting he therapeutic effects.

Targeting the key cellular signal that is critical to the pathological process of adhesion formation has demonstrated a delicate alternative solution to tendon adhesion prevention. It was well-established that fibroblasts play a vital role in adhesion formation by massive deposition of collagen. Besides, previous studies have showed that ERK2 expression is highly associated with tendon adhesion formation, and inhibition of ERK2 expression could inhibit the fibroblast proliferation and decrease the deposition of Col-3 by downregulating the SMAD2/3 [60, 61]. Thus, blocking the expression of the ERK2 may be a charming alternative for suppressing peritendinous fibrosis. Small interfering RNA (siRNA) has been a common way to downregulate the target gene expression. Therefore, ERK2-siRNA may be a promising therapeutic to block the adhesion formation.

Considering the limitations of current electrospun membranes-based scaffolds such as complex fabrication process, untargeted/uncontrolled drug delivery and consequently low therapeutical effect, we proposed, in this chapter, an MMP-2 responsive ERK2-siRNA-loaded electrospun fibrous membranes for prevention of adhesion formation. Such scaffold can release the ERK2-siRNA in response to the MMP-2, which can continuously downregulate the expression of ERK2 and its downstream signalling molecules to simultaneously serve as an obstacle to spatially separate the injured tendon site from peritendinous tissues, while as a smart gene delivery system for long-term adhesion prevention.

Objectives of this chapter include:

1. To prepare ERK2 siRNA-laden gelatin methacryloyl (GelMA) NPs by nano-

emulsification technique, characterize their morphology and siRNA release behaviour, and assess the performance of cellular uptake of siRNA released from GelMA NPs.

2. To fabricate the GelMA NPs-embedded electrospun fibrous membranes, and systematically characterize their physiochemical properties including morphology, mechanical performance, swelling and degradation property, as well as the siRNA release profile from the electrospun membranes.

3. To evaluate the *in vitro* biological functions of such hierarchically structured electrospun fibrous membranes including the bioactivity assessment of released siRNA (i.e., the ability to specifically downregulate the expression of targeted ERK2 and its downstream signalling molecules), cell growth and proliferation, as well as the cellular uptake of siRNA.

4. To explore the *in vivo* biological effects of the siRNA-containing electrospun fibrous membranes including gross observation/evaluation, H&E staining, Masson staining of the repaired tendon, immunochemical stanning and Western blot analysis of peritendinous adhesion tissue, as well as biomechanical evaluation of the healed tendon tissue.

Specifically, to achieve this goal, ERK2-siRNA was used as the therapeutic molecule. First, cationic polymer (jetPRIME®) was used to interact with ERK2-siRNA to form a hydrophilic ERK2-siRNA/jetPRIME complex. This complex will then be encapsulated into GelMA nanogels by nano-emulsification technique (**Figure 2-7**). This nanogel system has the following advantages: (1) This system is crosslinked by light and avoids the use of chemical oxidants and crosslinking agents, thereby preserving the bioactivity of the encapsulated biomacromolecules. (2) This system will provide good mechanical support and a topical aqueous microenvironment to protect the encapsulated ERK2-siRNA transfection complexes from shear stress and harsh external environments like organic solvents or electrospinning process. (3) In damaged tendons, the increased expression of MMPs will degrade the GelMA NPs to slowly release the encapsulated siRNA complexes from the nanogels. The released complexes would transfect the fibroblasts in the surrounding tissue and down-regulate the expression of ERK2 and its

downstream signaling molecules like Col-1 and Col-3, reducing cell adhesion and proliferation as well as fibrosis tissue formation, thereby minimizing tendon adhesions. This would form a positive chain reaction ("disease trigger-drug release-disease treatment"), providing temporal and spatial control of treatment according to the disease state while reducing off-target effects of the drugs. (4) When these nanogels are encapsulated in a fiber system, as the structure from outside to inside is fiber-nanogels-siRNA complexes, the initial burst release of the siRNA complexes will be minimized due to the presence of particle and fiber layers, achieving a delayed, late-stage bio-responsive drug release. More importantly, due to the low metabolization rate of PLLA inside the body, such membrane can provide a long-term barrier effect to physically prevent the in-growth of surrounding tissue, satisfying the requirement of tendon repair phase (over 1 year). The resultant membrane system will provide long-term microenvironmentally responsive anti-adhesion by release of siRNA complexes.

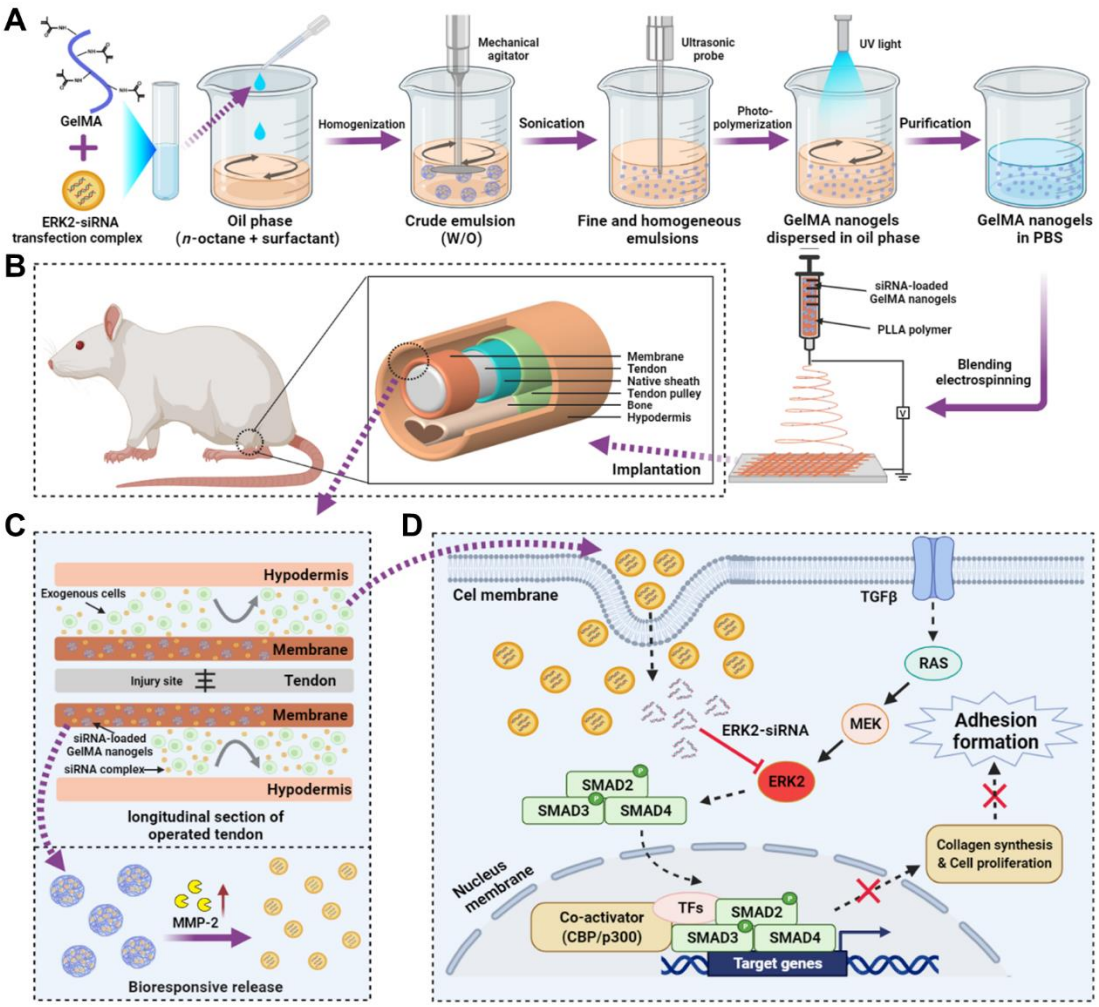

Figure 2-7. Schematic illustration of the project design of development of MMP-responsive siRNA-laden electrospun fibrous membranes for peritendinous adhesion suppression. (A) The preparation process of siRNA-loaded GelMA nanogels via nano-emulsification technique and subsequent siRNA-laden fibrous membranes via blending electrospinning. (B) The resultant siRNA-laden electrospun membranes could be implanted in the tendon injury site, serving (C) as a physical barrier to prevent exogenous cell invasion while as a drug depot to release therapeutical ERK2-siRNA molecules triggered by the elevated MMP-2 in the tendon healing microenvironment. (D) The released ERK2-siRNA complexes silenced the expression of ERK2 and its downstream signaling molecules and suppressed collagen deposition and fibroblast adhesion/proliferation, ultimately reducing the scar tissue formation and thus preventing tendon adhesions. Figure created with BioRender.com.

After preparation of the designed scaffolds, a series of characterizations were performed. Firstly, the morphology, MMP-responsive siRNA release behaviors, as well as the intracellular uptake of siRNA-containing GelMA NPs was analyzed. Then, the physiochemical properties of siRNA-laden PLLA electrospun fibrous membranes like morphology, mechanical performances, degradation, swelling properties and siRNA release profiles were systematically evaluated. Finally, their biofunctions such as biocompatibility, downregulation of targeted gene expression, inhibition of fibroblast proliferation and adhesion and *in vivo* anti-adhesion ability were thoroughly assessed.

2.2 Methodology

2.2.1 Materials

PLLA with Mw=10 kDa was acquired from the Jinan Daigang Co., Jinan, China. jetPRIME® siRNA transfection reagent was purchased from Polyplus-transfection® company, Hong Kong. MMP-2 was purchased from GIBCO-Invitrogen, Hong Kong. A series of siRNAs were prepared by GenePharma Co., Ltd., Shanghai, China with their sequences showing as follows: ERK2-siRNA: 5′-CACCAGACCUACUGUCAAATT-3′ (sense), 5′-UUUGACAGUAGGUCUGGUGTT-3′ (antisense); negative control (control-siRNA): 5′-UUCUCCGAACGUGUCACGUTTACGUGACACGUUCGGAGAATT-3′. Cy3 dye was introduced to the 5-end of the antisense strand. Quant-iT™ RNA Assay Kit was acquired from Invitrogen (Thermo Fisher Scientific, Inc. Hong Kong).

2.2.2 Preparation of siRNA-laden GelMA nanogels

To synthesize GelMA, 15.0 g gelatin (Type A, Sigma-Aldrich, Hong Kong)from Porcine Skin was firstly added into 200 mL PBS (not necessarily sterile) in Erlenmeyer flask with magnet fish, and then placed undissolved mixture on hot plate, and let it rotate at 60°C until completely dissolved [62]. Then, 16 mL of methacrylic anhydride (MAA, Sigma-Aldrich, Hong Kong) was added very slowly and dropwise (using a 1000 μl pipette) and the emulsion was allowed to rotate at 60°C for 3 hours. One hour before final 3 hours was around, preheat 800 mL of PBS in water bath 40-50°C. GelMA

solution was diluted using the preheated PBS. After mixing of PBS with concentrated solution, let it rotate under temperature for 15 min at 60°C. Prepare dialysis membrane (MWCO 12-14,000) by cutting them in proper sizes and dunk them into distilled water to make them more handily. Close one side by making a knot for example. Transfer diluted GelMA into the membranes and place those into distilled water in 5L plastic beaker. Perform the transfer into membrane with the help of a pipette. Let dialysis run at 40 to 50°C for about 1 week. Change water 2 to 3 times a day and each time reverse the membranes. On day 8, filter the GelMA using a sterile filter and transfer sterilized polymer into 50mL-Falcons. Store Falcons at -80°C for 1 day. Finally, the frozen GelMA were freeze-dried and characterized using ^{1}H-nuclear magnetic resonance (^{1}H NMR).

Firstly, according to the manufacturer instructions, a commercial transfection reagent, jetPRIME siRNA Transfection (cationic polymer), was used to interact with ERK2-siRNA to form ERK2-siRNA/jetPRIME transfection mixture to protect siRNA from being inactivated by the ribonuclease (RNase) in the ambient microenvironment and enhance its chemical stability and transfection efficiency. Briefly, the transfection mixture was prepared by firstly diluting siRNA in the distilled water , and then adding the jetPRIME reagent before 8-min incubation. The final concentration of siRNA was 10 nM. Afterwards, GelMA nanoparticles containing the ERK2-siRNA transfection mixture were prepared by water-in-oil (W/O) nano-emulsification technique [63, 64]. Briefly, 500 uL transfection mixture was added into the 3 mL PBS (pH 7.4) containing 1% (w/w) photoinitiator Irgacure 2959 (Aladdin, Shanghai, China) before being added with GelMA to make the final GelMA concentrations at 5%, 10%, and 20% (w/w). After complete dissolution at 60°C with stirring, the GelMA aqueous solution was dropwise added into n-octane oil phase containing surfactant mixtures (Span 80:Tween 80 at a weight ratio of 2:3) with a weight ratio of water phase : oil phase : surfactants at 1:4:1. The resultant mixture was kept stirring for 10 min using mechanical homogenizer at speed of 8000 rpm/min to get crude emulsions. Finally, the fine and homogeneous emulsions were obtained by ultrasonic processor under 400 watts for 1

min. The whole process was performed at 4°C in and sealed ice bath out of light. Crosslinking was carried out by exposure of emulsions to ultraviolet (UV) light (density: 10 W/cm^2 and light source: 250-450 nm) for 15 min under mild stirring (500 rpm/min). The resulting GelMA nanogels were added with tetrahydrofuran (THF) and centrifuged for 10 min at 12000 rpm/min to remove the organic phase and surfactant. Finally, the obtained pellets were freeze-dried for further use.

2.2.3 Characterization of siRNA-laden GelMA nanogels

Particle size was detected using dynamic light scattering (DLS) (Malvern Zetasizer Nano ZS; Malvern, UK). The morphology of ERK2-siRNA transfection mixture and GelMA nanogels was measured by transmission electron microscopy (TEM) (Tecnai G220 S-TWINScanning, FEI, OR, USA). To prepare the TEM samples, a drop of PBS containing samples was added onto a film grid before air-drying and 2% uranyl acetate staining. Since fibroblast plays a key role in adhesion formation by secreting massive collagen matrix, *in vitro* cell transfection of ERK2-siRNA mixture in fibroblasts was then evaluated according to the manufacturer's protocols. Here, we used the NIH/3T3 and C3H10, the commonly used fibroblast cell lines, as the model cells. The ERK2-siRNA conjugated with Cy3 (red colour) or 5'-FAM (green colour) was used to observe the location of ERK2-siRNA transfection mixture within cells, while immunofluorescence staining, PCR and western blotting (WB) was used to evaluate the expression of targeted ERK2. Special acknowledgement and gratitude are given to Mr. Yu Liu for assisting to complete this cell experiment.

To assess the siRNA release profile from the GelMA nanogels, freeze-dried siRNA containing GelMA nanogels (5 mg, n=4) were suspended in 1 ml PBS with different concentrations of MMP-2 (0, 0.2, 2 U/mL) and incubated in a water bath with 50 rpm/min spinning for 72 h [65, 66]. At given time interval, the tubes were centrifuged (13000gx for 30 min), and the supernatants (0.1 mL) were harvested for measurement followed by supplement with same amount of fresh buffer (0.1 mL). The concentration of released siRNA was analyzed using a Ribogreen RNA quantitative kit and quantified

by microplate reader (Thermo-Fisher Scientific, Hong Kong) at excitation/emission wavelength of 485/520 nm. Special acknowledgement and gratitude are given to Mr. Hanbai Wu for assisting to complete this siRNA release study. Standard curve for siRNA detection was prepared as following **Table 2-1**:

Table 2-1. The parameters to prepare the solution for drawing siRNA standard curve

Volume (ul) of TE	Volume (µL) of 2 ug/mL RNA Stock	Volume (µL) of 200-fold Diluted QuantiT™ RiboGreen® Reagent	Final RNA Concentration in Quant-iT™ RiboGreen® Assay
0	1000	1000	1 ug/ml
500	500	1000	500 ng/ml
900	100	1000	100 ng/ml
980	20	1000	20 ng/ml
1000	0	1000	blank

The siRNA loading efficiency by GelMA nanogels was evaluated following a previously reported method [66, 67]. Briefly, siRNA-containing GelMA nanogels (2 mg, n=4) were completely dispersed in 1 mL of PBS with 40 U/mL MMP-2, and rotated for 10 min. To facilitate extraction of siRNA from GelMA nanogels, the dispersion solution was kept for 2 days. Subsequently, the supernatant was harvested after centrifugation at 12,000 g for 30 min to remove residual GelMA debris. The siRNA concentration in the extracted aqueous solution was finally assessed by Ribogreen RNA quantitative kit according to the manufacturer's protocol and quantified by microplate reader (Thermo-Fisher Scientific, Hong Kong) at excitation/emission wavelength of 485/520 nm. Each sample was measured in triplicate. The siRNA loading efficiency of GelMA nanogels was calculated following the below equation:

$$\text{Loading efficiency} = \frac{\text{Total siRNA released+Total siRNA extracted}}{\text{Theoretical total siRNA loading}} \text{ X } 100\%$$

The extracts of Cy3-labelled siRNA or control-siRNA-containing GelMA nanogels were prepared by mixing GelMA nanogels with culture medium containing MMP-2 (2 U/mL) for 24 h at 37 °C. Then, intracellular uptake of Cy3-labelled siRNA or control-

siRNA released from GelMA nanogels was determined by co-culture of NIH/3T3 with the extracts. After incubation for 1 day, phalloidin staining (Thermo Fisher, Hong Kong) and 4′,6-diamidino-2-phenylindole (DAPI) staining (Thermo Fisher, Hong Kong) were performed to stain the cytoskeleton and cell nucleus, respectively [68]. Finally, the samples were observed using fluorescence microscopes (Nikon, Japan). GelMA nanogels without loading siRNA was used as negative control, while normal culture medium as blank control. The average cell area was evaluated based on 4 representative pictures via Image J software following a reported protocol [68].

2.2.4 Preparation of GelMA nanogel-embedded fibrous membranes

GelMA nanogels-embedded PLLA electrospun fibrous membranes were fabricated by dissolving PLLA into HFIP (20%, w/v) before being stirred for 30 min for complete dissolution. Then, siRNA-containing GelMA nanogels were dispersed into PLLA electrospun solution by keeping stirring for 30 min. The mass ratios of GelMA nanogels to PLLA was set at 0, 5%, 10%, and 20 % (w:w). The mixed solution was loaded into a 10mL syringe. +ve terminal is connected the syringe needle and -ve terminal is connected a collector wrapped with aluminum foil. The detailed parameter for the electrospinning is: +ve voltage: +15kv, -ve voltage: -2kv, pump rate: 1 mL/hr, distance between syringe and collector: 10 cm. The PLLA electrospun fibrous membranes without addition of siRNA-containing GelMA nanogels were used as the control group.

2.2.5 Characterization of GelMA nanogel-embedded fibrous membranes

2.2.5.1 Physical characterization of the fibrous membranes

Firstly, fluorescence microscope (Nikon, Japan) was used to observe fiber morphology and the distribution of Cy3-labelled siRNA-containing GelMA nanogels within the fibers. Special acknowledgement and gratitude are given to Mr. Chun Hei Lam for completing the fluorescence characterization. Later, the swelling properties of GelMA nanogel-embedded fibrous membranes were characterized [62]. Briefly, samples were firstly disinfected and lyophilized. Their initial (dry) weight was measured (S0). The specimen membranes (1cm diameter) of different groups were then put into a 5ml tube

containing 2 mL of PBS (pH=7.4) at 37°C. The specimen membranes were carefully taken out at specific intervals (0, 2, 4, 6, 12, 24, 48, 96 h). The residual water on the membranes' surface was drained by fresh filter papers and weighed (S1). The procedure was repeated till the sample reached a constant weight. Then, put back the sample to the solution. The swelling percentage (SP) of sample was calculated following the equation: SP = S1/S0 * 100%. The morphology changes of membranes before and after swelling in PBS for 3 days were investigated by scanning electron microscopy (SEM) (Tescan VEGA3, Czech Republic). Before SEM observation, the fibers were coated with gold in a sputter coater.

The degradation profile of GelMA nanogel-embedded fibrous membranes with time was evaluated by measuring *in vitro* mass loss in phosphate buffered saline (PBS, pH 7.4, 0.067M) [69]. Briefly, initial weight (W_0) of membrane samples (circular specimens with 1cm diameter and 1 mm thick) was recorded accurately. Then, samples were immersed in 2 mL of PBS containing different concentrations of MMP-2 (0, 0.2, 2, 10 U/mL), and incubated for 14 days with shaking at 100 rpm. The PBS solution containing MMP-2 was refreshed every 2-3 days to ensure the sustaining enzymatic activity. At a pre-determined day point (0, 2, 4, 12 h, 1, 2, 4, 7 and 14 days), samples were collected and rinsed with deionized water and freeze-dried for 24 hrs, which were then weighed to determine the residual mass (W_t). The degradation percentage of membranes was determined following the equation: Degradation percentage (%) = $(W_0-W_t)/W_0 \times 100$.

The mechanical performances of GelMA nanogel-embedded PLLA membranes were assessed by a mechanical tester (Instron, US) [68]. Briefly, the fibrous membranes were cut into 50 mm×10 mm rectangular samples. Then, the thickness of each sample was measured three times using a micrometer (Syntek, China) and fixed them to the instrument by pneumatic clamps. To obtain the stress-stain curve, the samples were subsequently stretched longitudinally at 5 mm/min until failure (n=4).

Finally, the siRNA release profiles from GelMA nanogel-embedded fibrous membranes were investigated. Briefly, approximately 10 mg amount of fibrous meshes (n=5) were prepared. Then, the membranes were incubated in a 1.5 mL tube (covered with aluminium foil) containing 1 mL PBS solution with different concentrations of MMP-2 (0, 0.2, 2 and 10 U/mL). The sample-incubated tube was then placed on a shaker table rotating at 100 rpm at 37°C. At determined time points (0, 2, 4, 8, 12, 24h, 2, 4, and 7 days), 0.2 mL PBS supernatant was harvested, and same amount of fresh PBS solution was supplemented. The RNA test should be done as soon as possible to avoid denaturation activities. If not, please store at -20 °C. Then, the siRNA concentration in the supernatants was measured via RiboGreen assay according to the manufacturer's instruction. Microplate reader (Thermo-Fisher Scientific, Hong Kong) was used to detect the fluorescence intensity. The siRNA remaining inside the fibers after 7-day release study was determined by dissolving the samples in chloroform (1 mL). Then, 200 μL of TE buffer was added to extract the siRNA-containing GelMA nanogels in the chloroform, and the aqueous phase was collected. To completely extract siRNA, this process was repeated three times (200*3=600 uL). Then, to release siRNA entrapped in the GelMA nanogels, we added 400 uL collagenase IV-containing PBS (40 U/mL) in the solution to degrade GelMA. The extracted siRNA was determined using RiboGreen assay following manufacturer's protocol.

2.2.5.2 Biological characterization of the fibrous membranes

To evaluate the biofunctions of the fibrous membranes for tendon adhesion prevention, NIH/3T3 cell line was used as the model cell and cultured following previously described methods [55]. The electrospun membranes were cut into disk pieces (diameter=15 mm, thickness=200 μm), and then sterilized by incubation of samples in 75% ethanol for 2 h before washing with PBS for further studies. To explore the influences of electrospun fibrous membranes on cell viability, adhesion and proliferation, the cell density was 4×10^4 cells/cm^2. TCPs were used as the control group.

To further analyze the influences of composite membranes on cell proliferation, the extracts from different material groups were used to culture with NIH/3T3. Briefly, different groups of fibrous membranes were immersed in the complete culture medium with or without the addition of MMP-2 (2 U/mL) for 24 h at 37°C. The proliferation assessment was performed using the 24-well plates (5 parallels per group). Firstly, the cells were seeded for overnight to enable cell adhering onto the culture dish. Then, the medium was aspirated, and the 1 mL extracts of fibrous membranes were added to the wells. The group cultured using normal medium was served as control. The extracts were changed once a day and Cell Counting Kit-8 (CCK-8, Beyotime Biotechnology, Beijing, China) solution was added into well plate at volume ratio of 10% to culture medium after culture for 1 and 3 days. After 4-h treatment, the absorbance at 450 nm was detected via a microplate reader. Cell density was recognized as proportional to the value of OD.

Quantitative real-time polymerase chain reaction (qRT-PCR) was then performed to evaluate the released ERK2-siRNA bioactivity by measuring the gene expression of targeted ERK2 and its downstream signaling molecules (collagen type I (Col-1) and collagen type III (Col-3)) by NIH/3T3 cells [62, 68]. In brief, NIH/3T3 were seeded in 24-well plates and incubated for overnight. Then, the culture medium was aspirated and same amount of extracts of fibrous membranes were added into wells, like the operations described above. After culture for 3 days, the cells were collected, and Total RNA Kit (Omega, Hong Kong) was used to extract the total RNA. The $2^{-\Delta\Delta CT}$ method was adopted to quantitatively measure the gene expression, and the glyceraldehyde-3-phosphate dehydrogenase (GAPDH) was used as an internal control. The primer sequences were showed in the following **Table 2-2**.

Table 2-2. The primer sequences used for qRT-PCR

Genes	**Sequences**
ERK2	F: 5'-CAGGTGTTCGACGTAGGGC-3'
	R: 5'-TCTGGTGCTCAAAAGGACTGA-3'

Col-1	F: 5'-GCTCCTCTTAGGGGCCACT-3'
	R: 5'-ATTGGGGACCCTTAGGCCAT-3'
Col-3	F: 5'-CTGTAACATGGAAACTGGGGAAA-3'
	R: 5'-CCATAGCTGAACTGAAAACCACC-3'
GAPDH	F: 5'-AGGTCGGTGTGAACGGATTTG-3'
	R: 5'-TGTAGACCATGTAGTTGAGGTCA-3'

The cell proliferation of NIH/3T3 after treatment with extracts from different fibrous membranes for 1 and 3 days was revealed by CCK-8 analysis, following the manufacturer's protocols. The cells cultured on the TCP was used as the control group. In brief, CCK-8 solution was added at a 10% volume of culture medium. After 4-h treatment, microplate reader was used to detect the absorbance at 450 nm. Besides, the viability of NIH/3T3 cells after culture with extracts from different fibrous membranes was analyzed by live/dead staining. Briefly, after culture for 3 days, the cells from different groups were stained with calcein-AM/ EthD-1, and observed under a fluorescence microscope (Nikon, Japan). The results were expressed by the ratio of the dead cells to live cells processed using ImageJ software. Subsequently, the cell morphology was observed by stanning the cytoskeleton and cell nucleus of NIH/3T3 cells using phalloidin and DAPI staining, respectively, after incubation with extracts of different fibrous membranes for 3 days, following the similar protocol described above. Briefly, cells in the well plate were fixed by 4% paraformaldehyde before washed with PBS with 5-minute interval. Later, 0.1% Triton X-100 (Sigma-Aldrich, Hong Kong) was added and incubated for 20 min before addition of 1% Bull Serum Albumin (BSA) to block the non-specific protein. To stain the cytoskeleton, phalloidin was added and incubated for 45 min. 1 uL/mL DAPI was then added to stain the nucleus following the manufacturer's instructions. Besides, we also performed the ERK2 staining to assess its relatively expression. Finally, the samples were observed under fluorescence microscope (Nikon, Japan). The mean cell fluorescence intensity stained by ERK2 was analyzed using ImageJ software. Here, special acknowledgement and gratitude are given to Mr. Yu Liu for assisting to complete the preliminary cell experiments.

2.2.6 *In vivo* anti-tendon adhesion studies

2.2.6.1 Animal experiment

All animal experimental protocols were approved by the Ethics Committee of the Hong Kong Polytechnic University. Special acknowledgement and gratitude are given to Mr. Kui Ma for completing the animal experiments. A total of 48 male SD rats (6-8 weeks, weighting between 200 g and 300 g) were randomly divided into four groups including control, positive control (using the SurgiWrap, a commercial biodegradable adhesion barrier film, as the wounding dressing), 10%G2/PLLA, and 10%G2/S/PLLA. The rats were anesthetized and shaved and disinfected their hind foot. Then, the tendon was transected through a posterior midline skin incision 5 mm away from the talocalcaneal tuberosity, and repaired using a modified Kessler tendon suture technique. Finally, membrane samples (1×2 cm^2) from different groups were wrapped around the surgical site. The group without membrane implantation was used as the control.

2.2.6.2 Macroscopic assessment

After surgery for 21 days, the operated limbs were retrieved for gross assessment of any inflammation or ulcer. Then, the repair sites were opened for macroscopic evaluation of the severity of peritendinous adhesions using a scoring system in a semiquantitative manner [57]. Score 1 represents nearly no adhesion; Score 2 represents few fibrous tissues were attached onto the surface of surgical sites, which can be readily separated by blunt dissection; Score 3 represents $\leqslant$50% of area around the tendon was covered with the fibrous tissues, which could be separated by blunt rather than sharp dissection; Score 4 represents 51–97.5% of area around the tendon was covered with the fibrous tissues, which could only be separated by sharp dissection; Score 5 represents >97.5% of area around the tendon was covered with the fibrous tissues, which could only be separated by sharp dissection.

2.2.6.3 Histological analysis

After macroscopic evaluation, the repaired sites of tendons were retrieved and fixed in

4% paraformaldehyde. Then, specimens were decalcificated in 10% EDTA, dehydrated with a graded series of ethanol followed by cut into sections of 4 μm thickness. These samples were then stained with hematoxylin-eosin (H&E) and Masson's trichrome. The microscopy was used to observe the sections of histologic adhesion area.

2.2.6.4 Immunohistochemical assessment

Expressions of Col-1 and Col-3 in the peritendinous adhesion tissue were evaluated by immunohistochemical staining. Briefly, the sections were firstly subjected to dewaxing pretreatment and hydration by a graded series of ethanol. Then, the sections were blocked in a 5% BSA solution and subsequently treated with primary antibody against Col-1 or Col-3 for 12h at 4 °C. After incubation with second antibody solution for 1 h at 37 °C, and immersion in DAB solution for stanning development, the samples were finally observed using a microscope (Nikon, Japan).

2.2.6.5 Biomechanical evaluation

The harvested tendon specimens were fixed onto the clamps of a mechanical tester (Instron, US) following the published protocols [70]. Then, the maximal breaking force of samples was evaluated by pulling at 10 mm/min until the tendons were ruptured. The maximum tensile strength of tendons was recorded by the mechanical tester.

2.2.6.6 Western blot analysis

The protein expressions of p-ERK1/2, p-SMAD3, Col-1, Col-3, and β-actin were evaluated by western blotting following previously published protocols [71]. The primary antibodies against p-ERK1/2, p-SMAD3, Col-1, Col-3, and β-actin (diluted 1:1000; Abcam, USA) were used. The intensity of immunoreactive bands was quantified suing ImageJ software.

2.3 Results and Discussion

2.3.1 Characteristics of siRNA-laden GelMA nanogels

Firstly, the siRNA complex was prepared by self-assembling between siRNA and JetPRIME transfection reagent accoridng to the manufacturer's protocol with some minor revision. In order to reduce the size of complexes, we selected the distilled water instead of recommended buffer to prepare the siRNA solution. As displayed in **Figure 2-9(A)**, the average size of transfection mixture was about 70 nm with polydispersity index (PDI) at 0.219, indicating that such complex showed a uniform size distribution. Considering the following size of nanogels and electrospun fibers, the small diameter of this complexes might be suitable for subsequent incorporation. TEM image further confirmed the results of DLS, demonstrating the siRNA complex showed an even spherical shape (**Figure 2-9(B)**).

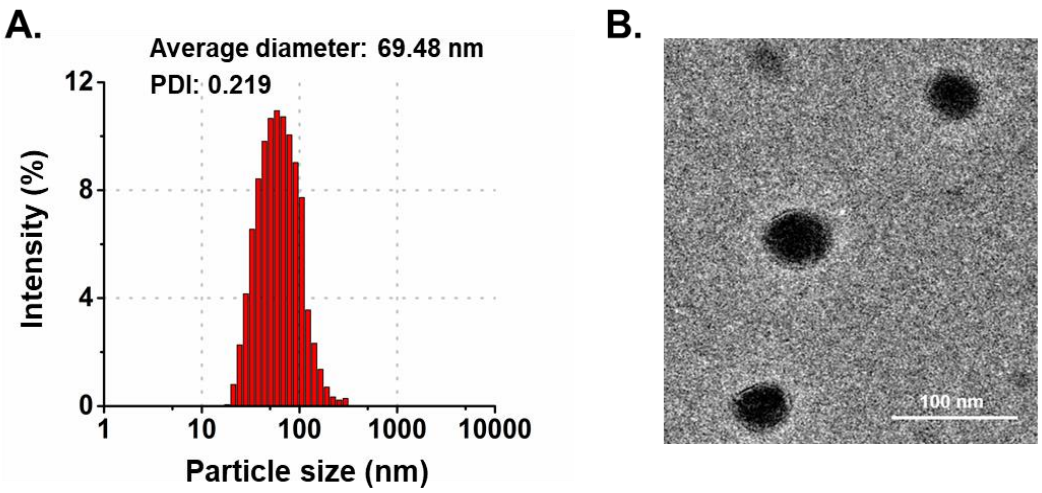

Figure 2-9. Preparation of the ERK2-siRNA/jetPRIME transfection complexes. A) The size distribution of siRNA complexes measured by DLS. B) TEM image of ERK2-siRNA complexes.

Next, we performed the *in vitro* cell transfection experiment to evaluate the biofunctions of the prepared ERK2-siRNA complex. Special acknowledgement and gratitude are given to Mr. Yu Liu for assisting to complete the cell transfection experiment. Firstly, after 30-min transfection, we observed the transfected cells using fluorescence microscope (**Figure 2-10**). It can be observed from the fluorescence images that there were many green dots within the cells, which demonstrated the

successful transfection of ERK2-siRNA in fibroblasts. The immunofluorescence staining of ERK2 was further conducted to qualitatively assess the target protein expression and observe the siRNA location within the cells. Here, to compare the transfection efficiency of ERK2-siRNA in different cells, two kinds of fibroblasts, namely NIH/3T3 and C3H10 were selected. After incubation with ERK2-siRNA complex for 24 h, we found that the ERK2-siRNA was mainly located around the cell nucleus, and the ERK2 protein expression in both NIH/3T3 and C3H10 was decreased (**Figure 2-11**). Since this phenomenon was more obvious in NIH/3T3 cells, we used the NIH/3T3 as a model cell for the following experiments. These results demonstrated the technical feasibility of the commercial transfection reagent. Besides, we have filtered the different siRNA sequences (labelled as 1, 2 and 3) designed by GenePharma Co., Ltd., Shanghai, China. From the PCR and WB results (**Figure 2-12**), we could find the sequence 1 and 3 could downregulate the ERK2 gene expressions with sequence 1 being the most significant. In addition, we also performed the ERK protein expression via western blotting (**Figure 2-13**). Similar results were obtained that sequence 1 and sequence 3 could effectively decrease the ERK expression. Thus, we selected sequence 1 to fabricate siRNA-loaded GelMA nanogels for the following study.

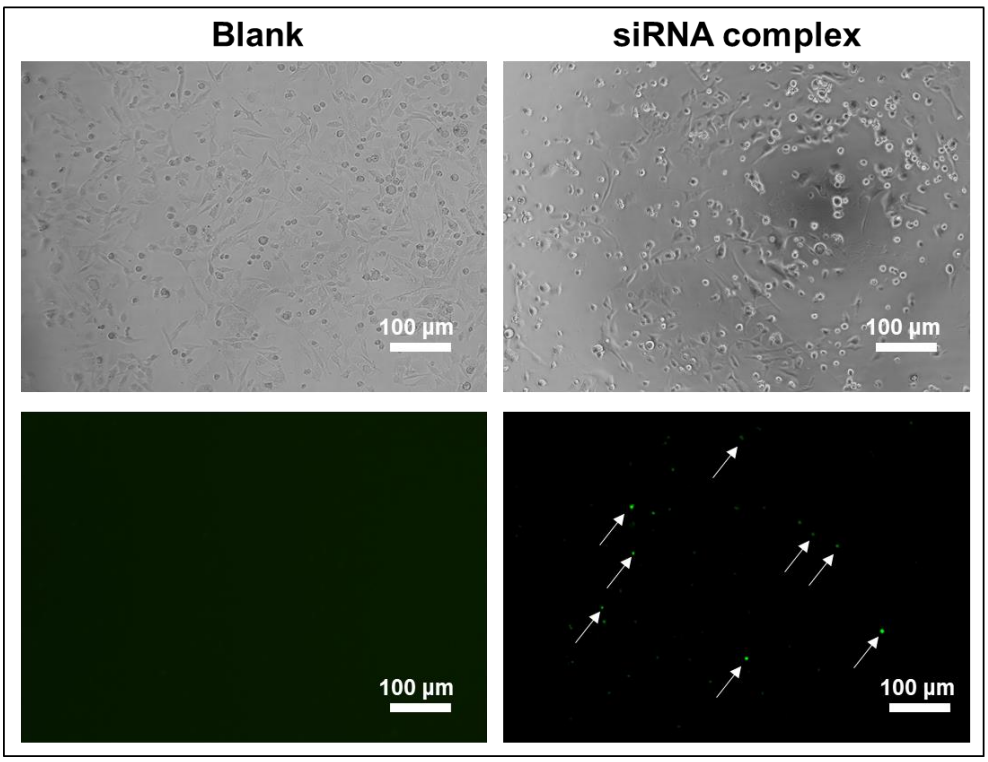

Figure 2-10. The bright field and fluorescence images of NIH/3T3 cells after transfection with 5'-FAM labelled ERK2-siRNA complexes for 30 min. The white arrows indicated the ERK2-siRNA complex (green fluorescence-labelled). Scale bar = 100 µm.

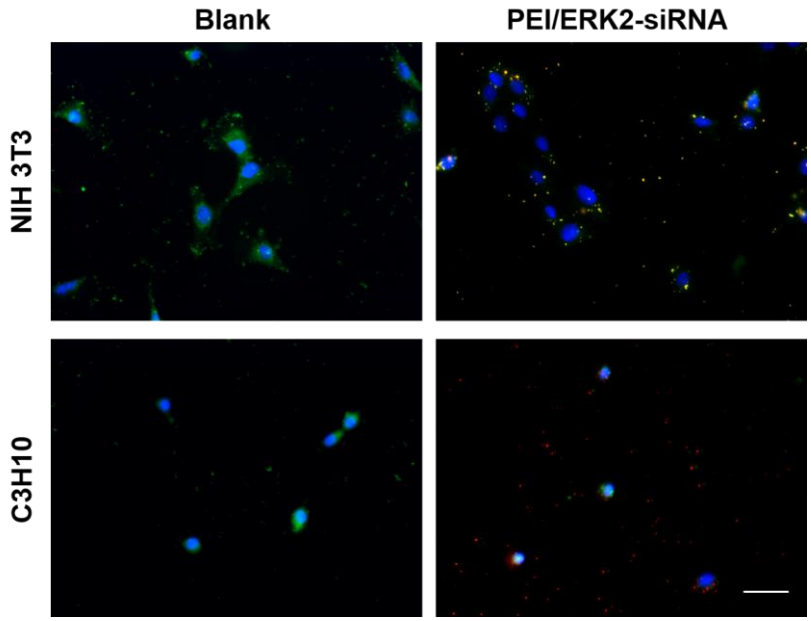

Figure 2-11. Immunofluorescence images showing the localization and reduced ERK2 expression around cell nucleus of NIH/3T3 and C3H10 fibroblasts, after 24-h

transfection. The red, green, and blue colors indicated the Cy3-labelled ERK2-siRNA, ERK2 protein, and cell nuclei, respectively. Scale bar = 20 μm.

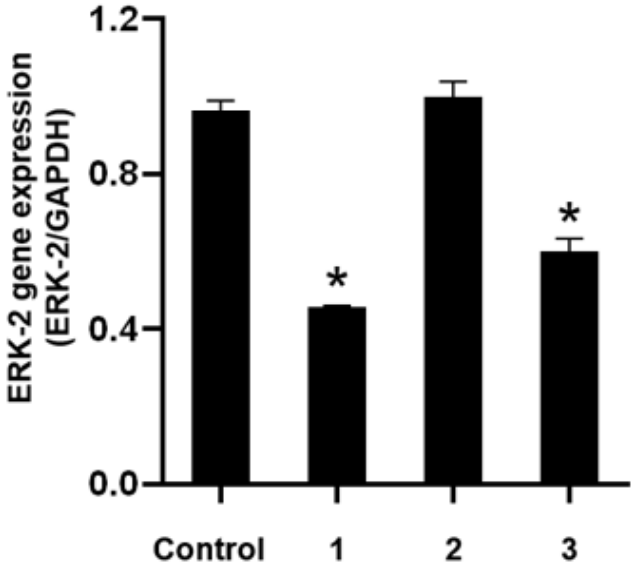

Figure 2-12. The ERK2 gene expression after transfection with different siRNA sequences (labelled as 1, 2 and 3), which were designed by GenePharma Co., Ltd., Shanghai, China.

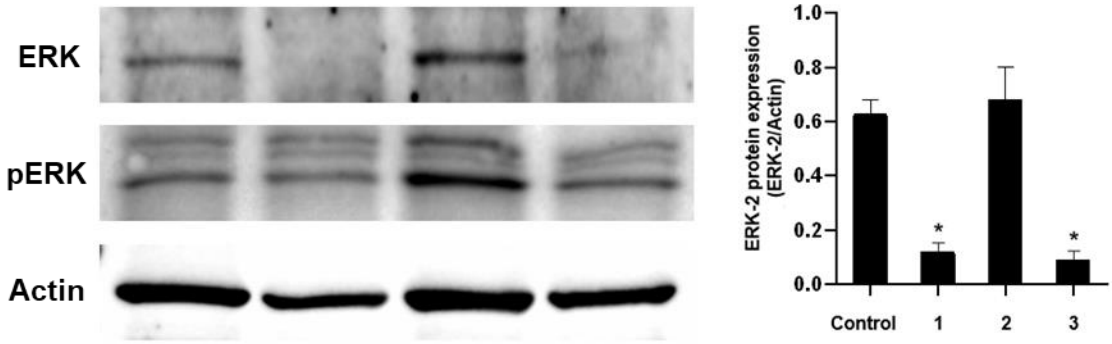

Figure 2-13. The ERK2 protein expression after transfection with different siRNA sequences (labelled as 1, 2 and 3), which were designed by GenePharma Co., Ltd., Shanghai, China.

Before preparing the GelMA nanogels, GelMA was first synthesized by chemically grafting methacrylic anhydride onto gelatin. As showed in **Figure 2-14**, the ^{1}H NMR spectrum of GelMA showed a distinctive double peak at around 5.5 ppm corresponding

to C=C double bond in the methacrylic anhydride, which demonstrated the successful synthesis of GelMA.

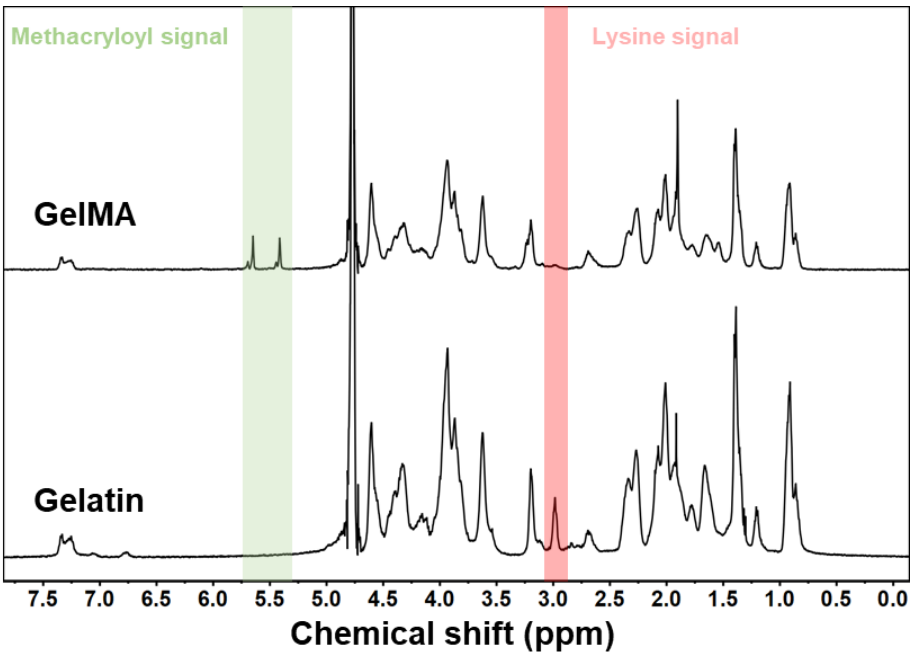

Figure 2-14. The ^{1}H NMR spectra of unmodified gelatin and synthesized GelMA .

Then, we prepared the ERK2-siRNA complexes loaded GelMA nanogels by nano-emulsification. The emulsification process was showed in **Figure 2-15**. In this part, the GelMA solution containing siRNA complexes was used as the water phase, while we tried two organic solvents as the oil phase (the dichloromethane (DCM) or *n*-octane). In the first emulsification system that DCM was used as the oil phase and span 80 as the surfactant, it is rather difficult to form stable emulsification since the emulsion was stratified after homogenization for over 10 min. In the second emulsification system that span80/tween80 mixture (at a weight ratio of 3:2) was used as the surfactant, although we have obtained the stable emulsification, it was impossible to modulate the GelMA nanogel size by changing the ultrasound time since some white foamy substance was formed in the upper layer after a long time of ultrasound. As showed in the **Figure 2-16**, the hydrodynamic size of the resultant GelMA nanogels was varied with different GelMA concentrations (5%, 10%, 20% w/w), and the PDI was relatively high (> 4), suggesting the difficulties in control over the nanogel size. In addition,

during the experimental process, we found that there was a great loss of GelMA raw materials for the 20% GelMA group, in which the GelMA materials were adhered onto the walls of the emulsifying bottle. This could reduce the diameter of the resultant GelMA nanogels, lowering the emulsification efficiency.

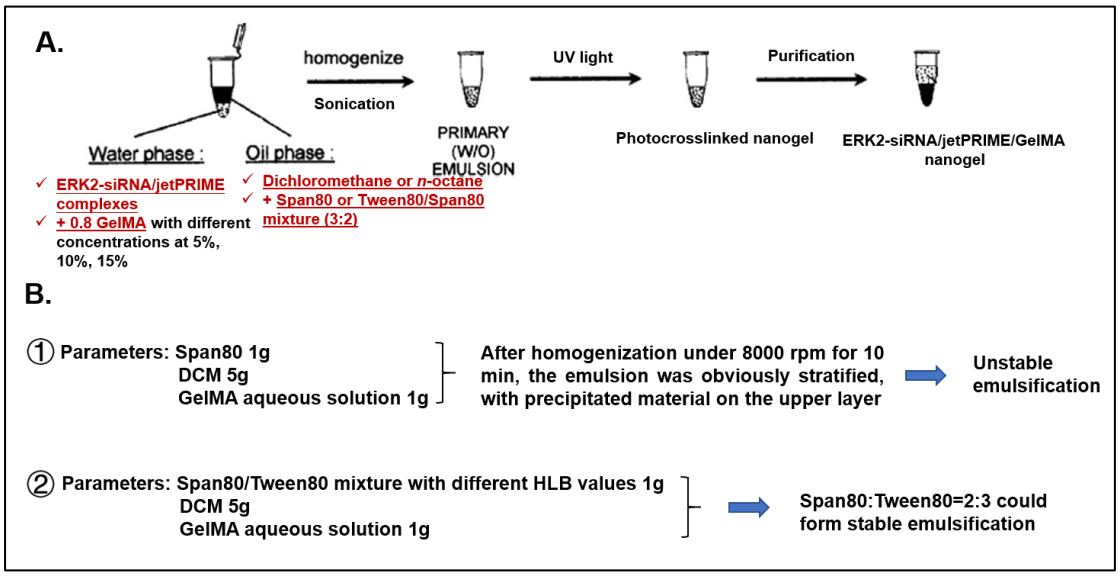

Figure 2-15. A) The emulsification process to fabricate the ERK2-siRNA/PEI complexes loaded GelMA NPs. B) The emulsification system using DCM as oil phase and Span80 as surfactant.

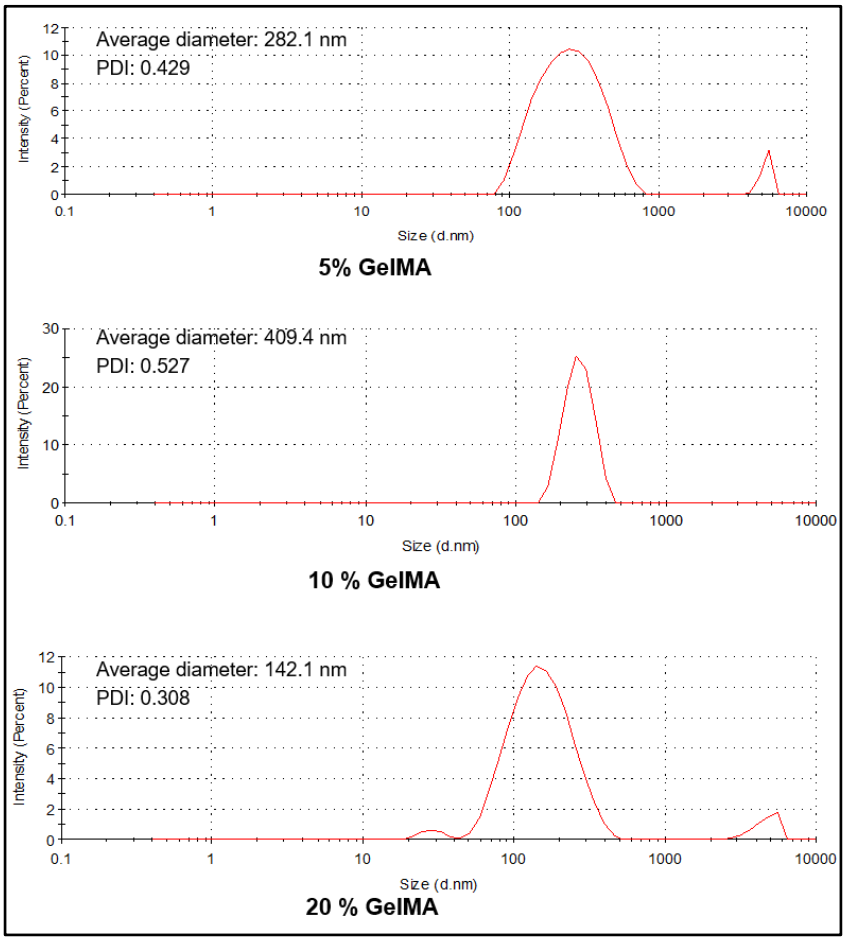

Figure 2-16. The DLS results of ERK2-siRNA complexes using DCM as oil phase and Span80/Tween80 mixture as surfactant. GelMA aqueous solutions with concentrations of 5%, 10% and 20% (w/v) were used as the water phase for emulsification.

Next, we tried to use the *n*-octane as oil phase, and the detailed emulsification parameters were showed in **Figure 2-17(A)**. After optimization of ultrasound time, mechanical shearing rate and time as well as UV irradiation time, we could obtain a fine and stable emulsions, which was transparent without phase separation occurring (**Figure 2-17(B)**). Later, we used TEM to characterize the size of prepared GelMA NPs. As showed in **Figure 2-18**, we first prepared the samples in PBS without negative staining. Frustratingly, we did not observe any GelMA nanogels in the vision field. However, we could find some shadow regions which may be attributed to the traces of water vaporizing. Further, we updated the preparation methods by dipping the GelMA nanogels (in oil phase) onto the copper grid (**Figure 2-19**). In the vision field , we could

observe some spherical samples. However, there was a large amount of oil phase residue left on the copper grid , disturbing the observation. Finally, we prepared the samples in the PBS and stained them with uranyl acetate. As showed in the **Figure 2-20(B)**, we could obtain beautiful images showing the morphology of nanogels. We found GelMA nanogels showed an even spherical shape with diameter increased with GelMA concentration. In addition, we performed DLS analysis to detect the size distribution of nanogels (**Figure 2-20(A)**). DLS results were in accordance with the TEM results, that the size of emulsified nanogels increased with their preparation concentrations. The corresponding sizes of 5%, 10% and 20% GelMA were 157.9, 208.3, and 336.9 nm, with PDI reaching 0.255, 0.342 and 0.266, respectively. From the results, we could find the NP size would be homogeneous with the increase of GelMA concentration. To sum up, by nano-emulsification, we could prepare the GelMA nanogels to load the siRNA complexes. Since NP-based delivery systems are promising in the field of biomedical engineering, we envision that the GelMA nanogels can find more practical applications in the near future as a delivery vehicle for other hydrophilic drugs, extending their research scope.

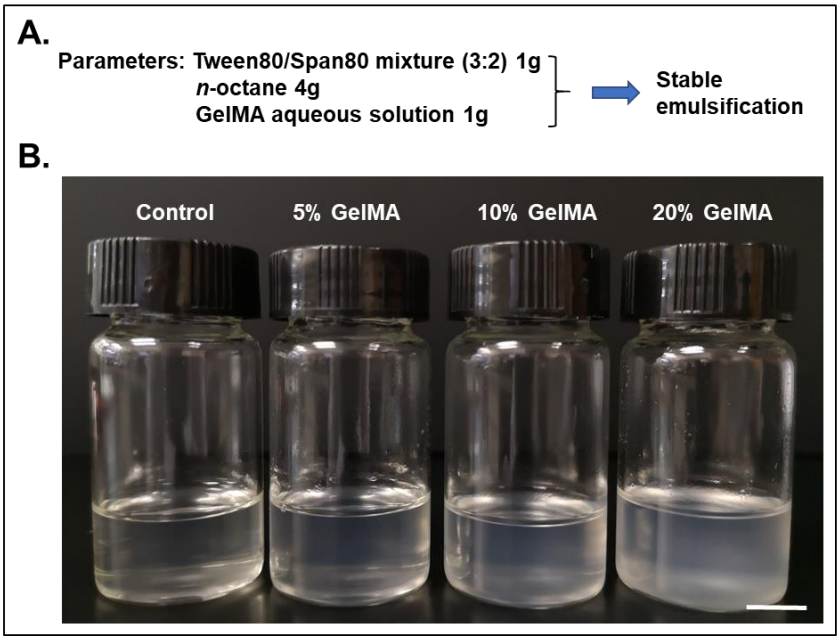

Figure 2-17. A) The emulsification parameters using n-octane as oil phase. B) The emulsification images of GelMA NPs with different concentrations (5%, 10% and 20%,

w/w). Scale bar: 1.5 cm.

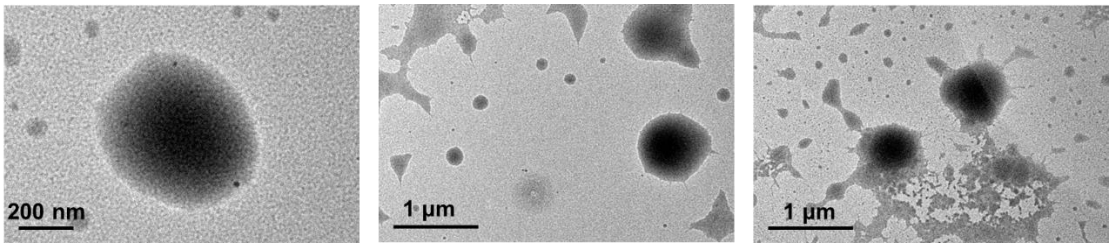

Figure 2-18. TEM images of GelMA nanogels that were prepared in PBS without negative staining.

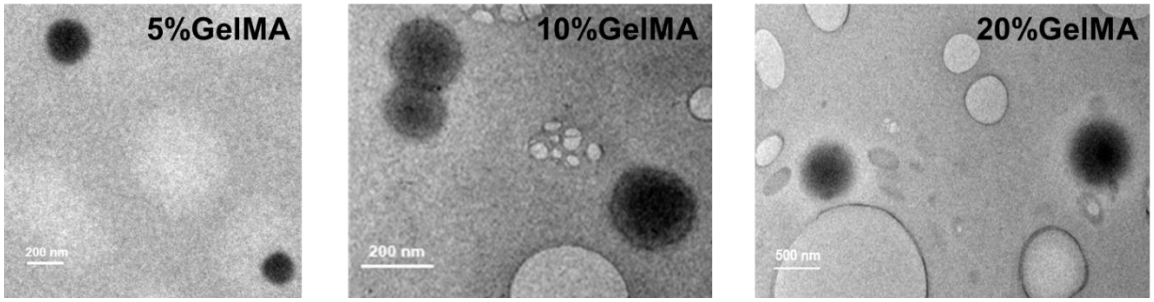

Figure 2-19. TEM images of different GelMA nanogels that were prepared in oil phase without negative staining.

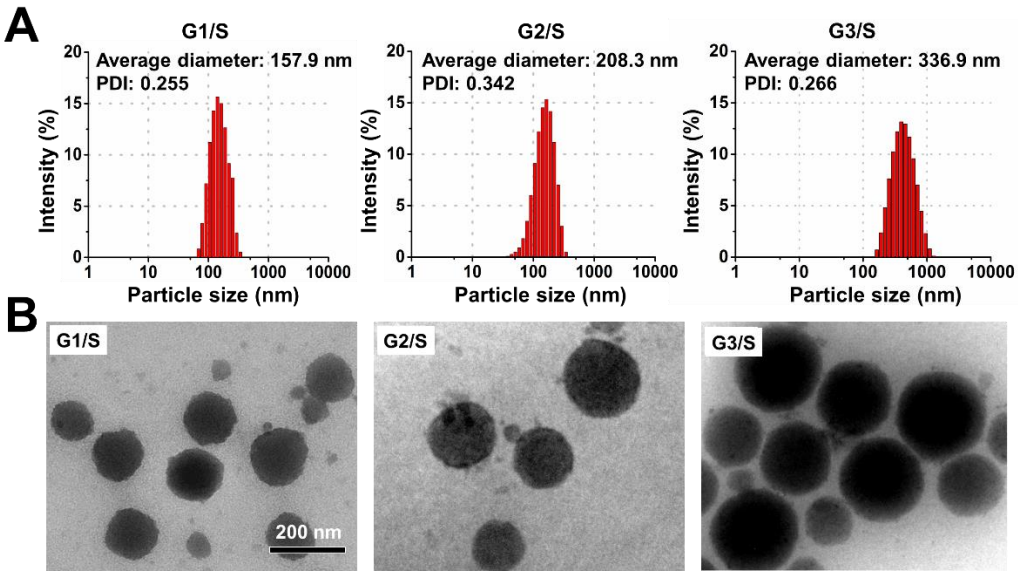

Figure 2-20. Characterizations of siRNA-loaded GelMA nanogels. (A) DLS analysis and (B) TEM images of different siRNA-laden GelMA (prepared in PBS with uranyl acetate as negative staining). G1/S, G2/S and G3/S represented the siRNA-loaded

GelMA nanoparticles prepared at GelMA concentrations of 5, 10 and 20 wt.%, respectively. Scale bar = 200 nm.

In order to demonstrate whether the GelMA nanogels encapsulated the siRNA, we further used the fluorescence microscope to observe the fluorescence signal of Cy3-labelled siRNA in the NPs. In the first trial and error, we observed the siRNA-loaded GelMA nanogels in the oil phase by fluorescence microscope. As showed in the **Figure 2-21**, we could observe a lot of spherical particles with strong red fluorescence signal; but, strong scattering and refraction occurred. To improve the results, we further tried again the experiments but similar results were obtained (**Figure 2-22(A)**). Then, we tried to disperse samples in the water before observation (**Figure 2-22(B)**). Surprisingly, the samples were distributed evenly in the vision field. In addition, we did other two tries to obtain satisfactory bright field images . Firstly, we dispersed samples into oil phase and observed them when samples were dried out (**Figure 2-22(C)**). However, we found the background was filled with greasy oil phase. Besides, although the samples could be dispersed in the ethanol, the samples were gathered together, significantly affecting the observation (**Figure 2-22(D)**). Finally, we also tried to disperse samples in the water phase and observed them when water was volatilized (**Figure 2-23**). However, despite acceptable results obtained in the fluorescence field, the bright field was still unsatisfactory. Later, we directly used fluorescence field to observe the samples in water phase without displaying the bright field images. From the fluorescent images, we could see that there were many scattered red dots in G1/S, G2/S and G3/S groups, which represented the siRNA-loaded GelMA nanogels, suggesting the homogeneous emulsification without the presence of substantial accumulation of nanoparticles (**Figure 2-24**). In addition, compared with pure GelMA, the GelMA nanogels with siRNA showed strong red fluorescence, which clearly demonstrated the successful encapsulation of siRNA into GelMA. Altogether, considering there were no toxic organic solution involved in the nano-emulsification process, such system holds great promise for preparation of GelMA nanogels to deliver a variety of biologicals or chemicals.

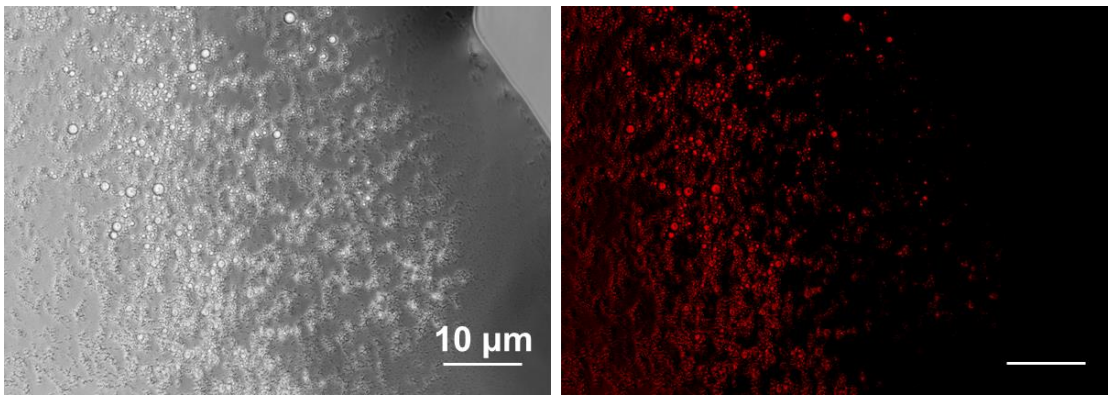

Figure 2-21. Fluorescence observation of emulsified siRNA-loaded GelMA NPs (G2/S). The nanogels was dispersed in the oil phase.

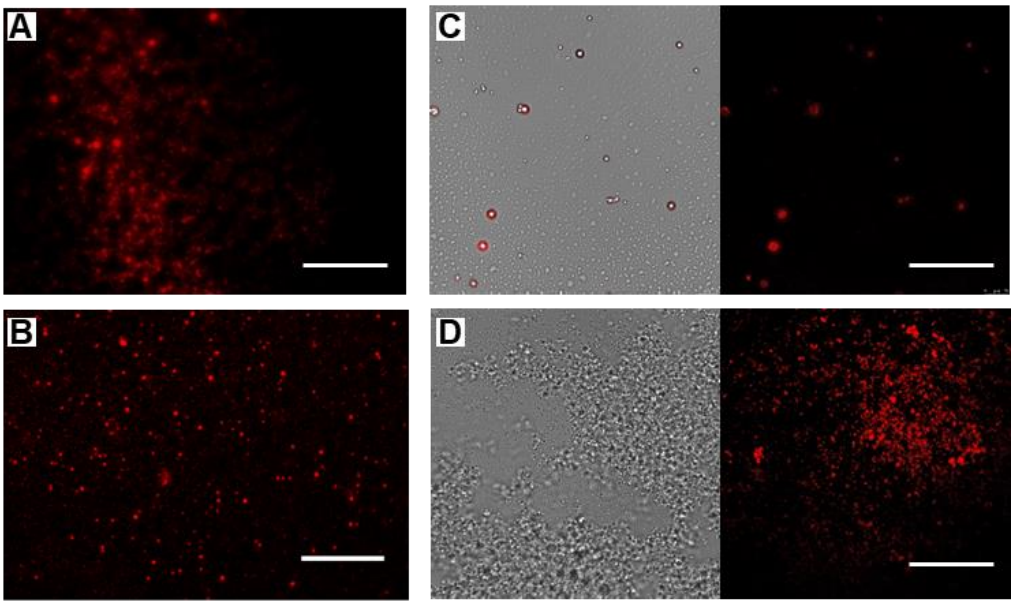

Figure 2-22. Fluorescence observation of emulsified GelMA NPs prepared by different conditions. (A) Dispersion in the oil phase; (B) Dispersion in the water; (C) Dispersion in the oil phase and observation when dry out; (D) Dispersion in ethanol and observation when dry out. Scale bar = 10 μm.

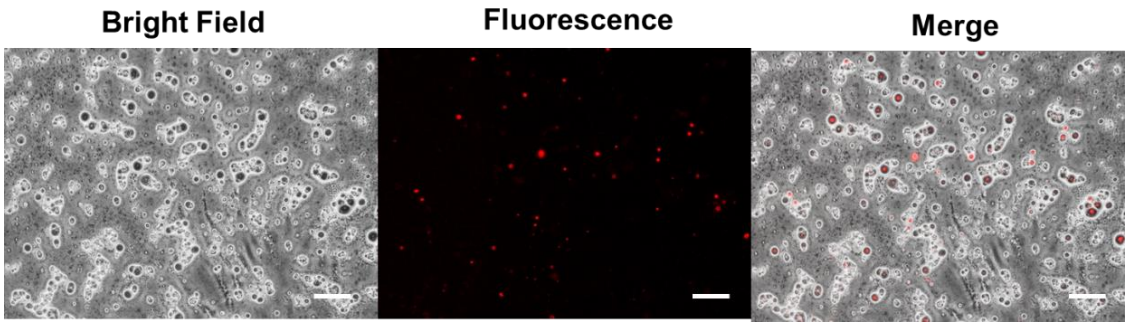

Figure 2-23. Fluorescence observation of emulsified GelMA NPs dispersed in PBS and observed when water was dried out. Scale bar = 10 μm.

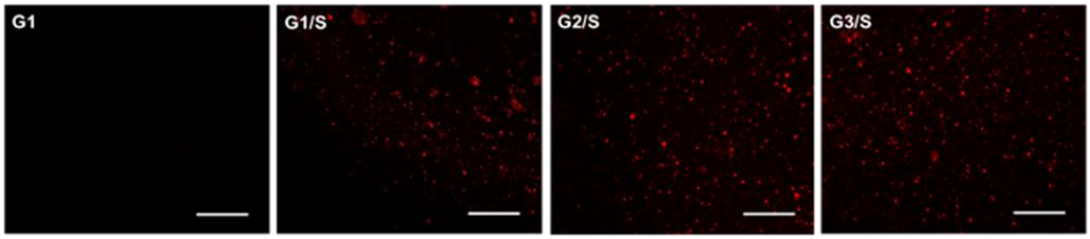

Figure 2-24. Fluorescence observation of emulsified GelMA NPs. G1 means GelMA nanoparticles prepared with 5 wt.% GelMA. the G1/S, G2/S and G3/S represent the siRNA-loaded GelMA nanoparticles prepared at GelMA concentrations of 5, 10 and 20 wt.%, respectively. Scale bar = 10 μm.

An efficient drug delivery system should have a high loading capacity, which enables the reduced quantity of both drug and excipient material for disease treatment. Thus, we subsequently examined the siRNA encapsulation efficiency (EE) and release profile of our nano-emulsification system. To calculate the siRNA EE, we first drew the siRNA standard curve (**Figure 2-25 (A)**). The R^2 was found 0.9993, indicating its good linear relationship and could be used to detect the siRNA concentration in the solution. Through calculation, we found the EE of siRNA in GelMA NPs ranging from 48.73 to 66.84% (**Figure 2-25(B)**), which was relatively higher than that of other methods to encapsulate the siRNA such as electrostatic adherence to NPs. In addition, the EE decreased with the increase of GelMA concentrations, which might be attributed to the viscosity increment that caused the loss of siRNA during nano-emulsification.

Then, we detected the siRNA release behaviors from the different GelMA nanogels. Here, special acknowledgement and gratitude are given to Mr. Hanbai Wu for assisting to complete this siRNA release study. As showed in the **Figure 2-25(C)**, the siRNA release amount was increased with the concentrations of MMP-2. In PBS (pH=7.4), a small amount of siRNA was released into solution, which might be attributed to the diffusion of siRNA complexes located onto the outer surface of GelMA nanogels. However, the release amount would rapidly reach a plateau, which might be because of the electrostatic interaction of GelMA nanogels (positive charge) and siRNA (negative charge). Notably, there was a burst release in the samples incubated in the 2 U/mL MMP-2 solution within the first 4 hours. Besides, the cumulative release amount of siRNA reached over 50%. More importantly, the siRNA release rate decreased with the increase of GelMA concentration, which might be due to the increased crosslinking density of GelMA network for higher concentration GelMA. The experimental loading efficiencies for G1/S, G2/S and G3/S were 66.84 ± 4.69 %, 64.97 ± 3.41% and 48.73 ± 5.32%, respectively. In short, such nano-emulsification system could serve as a efficiency siRNA delivery system with controllable and enzyme-responsive release. Combined with these results, we selected the 10 wt.% GelMA for the following study, since such nanogels showed relatively high encapsulation efficiency (EE) with suitable size (240 nm) for loading the siRNA complexes (70 nm).

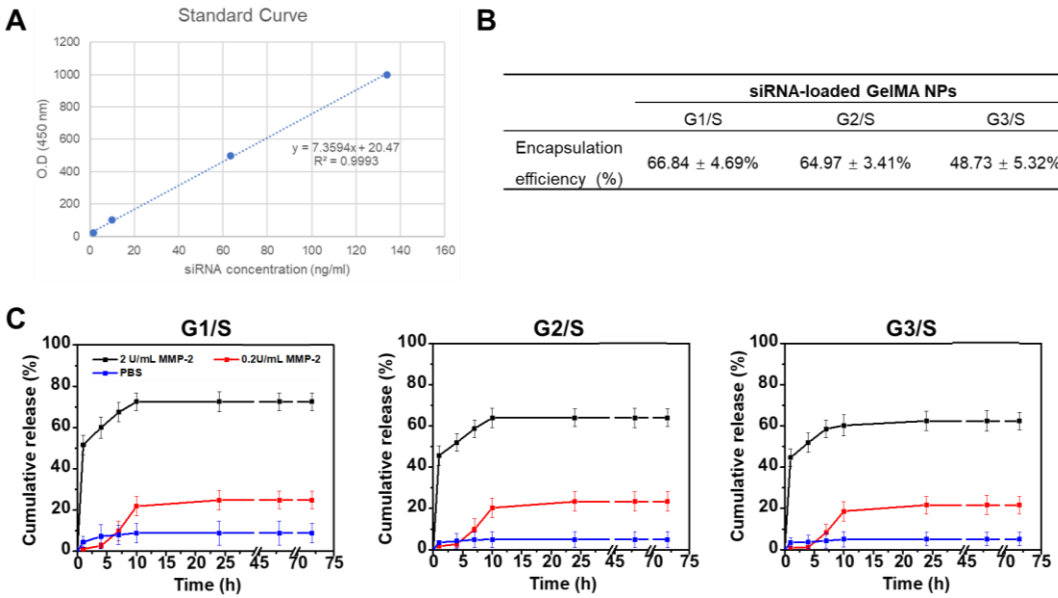

Figure 2-25. The siRNA release profile from GelMA nanogels. (A) siRNA standard curve for determining its concentration. (B) The encapsulation efficiency (EE) of ERK2-siRNA in GelMA nanogels with different concentration. (C) *In vitro* ERK2-siRNA cumulative release from different GelMA nanogels incubated in PBS with different concentrations of MMP-2. G1/S, G2/S and G3/S represent the siRNA-loaded GelMA nanogels prepared at GelMA concentration of 5, 10 and 20 wt.%, respectively.

Next, we performed the *in vitro* transfection experiment to confirm whether the siRNA in GelMA nanogels could transfect into cells. To mimic the pathological microenvironment after tendon injury, MMP-2 was added and co-cultured with cells. Since MMP-2 is an enzyme that can degrade the cell-produced collagens, it has a profound effect on the cell growth. As such, to precisely evaluate the effects of released siRNA on cell growth while excluding the possible influence of MMP-2, we firstly explore the suitable MMP-2 concentration that would not affect cell viability and proliferation when co-culture with NIH/3T3. Special acknowledgement and gratitude are given to Mr. Yu Liu for completing the MMP optimization experiments. Here, in the first experiment, we set up eight groups to detect the optimal MMP-2 concentration by culturing the NIH/3T3 with MMP-2 (ranging from 0 to 20 mg/mL) and detecting cell proliferation via CCK-8 assay. As displayed in the **Figure 2-26** (left figure), we found that higher the concentration of MMP-2 (more than 1 mg/mL), lower the cell

proliferation. Subsequently, we performed similar experiment for further evaluation by narrowing the MMP-2 concentration range (**Figure 2-26**, right figure). We found that when MMP-2 concentration was less than 0.01 mg/mL (~3 U/mL), cell proliferation was similar with control group without addition of MMP-2. Thus, we selected the 2 U/mL of MMP-2 as the high threshold value in this study for the following cell experiments.

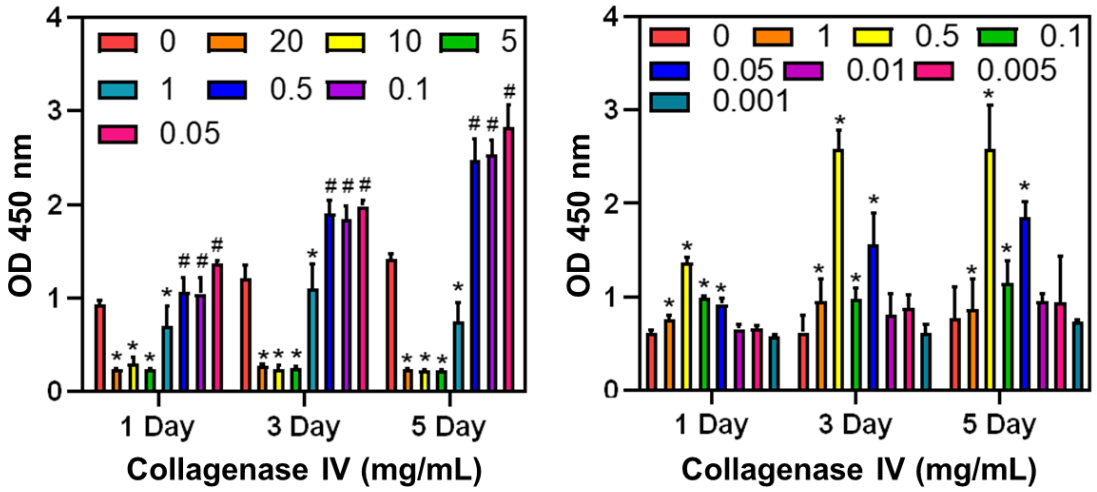

Figure 2-26. CCK-8 results of NIH/3T3 cells co-cultured with different concentration of MMP-2 (ranging from 0 to 20 mg/mL) to screen suitable concentration of MMP-2 that did not affect the cell proliferation.

Next, we cultured NIH/3T3 cells with extracts from siRNA or ERK2-siRNA-loaded GelMA nanogels to evaluate the cellular uptake of siRNA and the corresponding cell morphology change (**Figure 2-27**). Special acknowledgement and gratitude are given to Mr. Yu Liu for assisting to complete the cell uptake experiments. Compared with the control and G2 groups, we found that the Cy3-labeled siRNA could be observed in the G2/NC and G2/S groups, showing strong red fluorescence. This phenomenon suggested that the loaded siRNA could be released from GelMA nanogels and then transfected into the cells. More importantly, although no significant difference in average cell spreading area was found among control, G2 and G2/NC groups, the G2/S showed a remarkably lower cell spreading area after 1-day culture, which might be attributed to the blocking effect of ERK2-associated signaling pathway by the released siRNA

complexes that further reduce collagen expression and fibroblast adhesion [72]. Altogether, these results indicated that the activity of siRNA complexes was preserved to downregulate gene expression and regulate cellular behaviors despite being subjected to nano-emulsification process (e.g., dispersion in dichloromethane and n-octane). Also, these findings demonstrated the feasibility of our prepared GelMA nanogels as a novel carrier for MMP2-bioresponsive delivery.

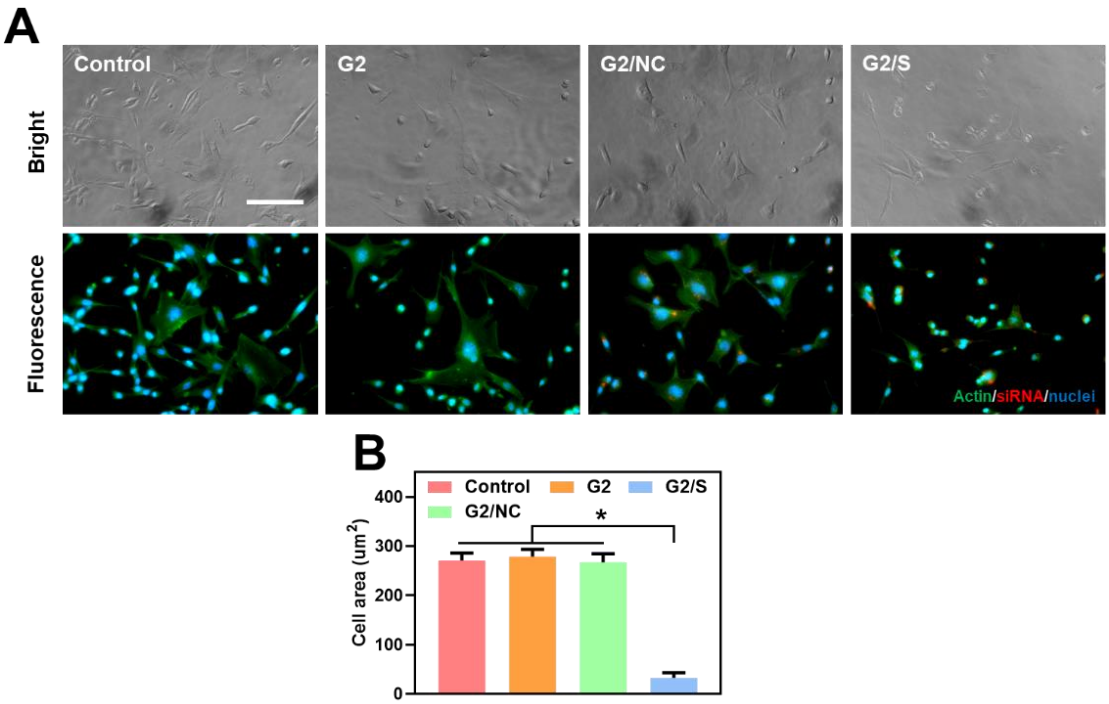

Figure 2-27. (A) Intracellular uptake of siRNA from G2, G2/NC and G2/S. The cells without any treatment were used as control. Cell actin and nuclei were stained by phalloidin (green) and DAPI (blue), respectively. ERK2-siRNA or siNC was labeled by 5'-CY3 (red). G2 means GelMA nanoparticles prepared with 10 wt.% GelMA. G2/NC and G2/S represent negative control siRNA or ERK2-siRNA-loaded GelMA nanoparticles prepared with 10 wt.% GelMA concentrations respectively. Scale bar = 50 μm. (B) Quantification of the cell area after treatment with different materials for 1 day.

2.3.2 Characterization of GelMA nanogel-embedded fibrous membranes

Then, we incorporated the siRNA-loaded GelMA nanogels into the PLLA fibers by

blending electrospinning technique to prepare the membrane scaffolds. Here, the weight ratio of siRNA-loaded GelMA NPs to PLLA was set at 1:100, 1:20, 1:10 and 1:5, namely 1%G2/S/PLLA, 5%G2/S/PLLA, 10% G2/S/PLLA and 20%G2/S/PLLA, respectively. Pure PLLA was used as the control group. Firstly, we explored which solvent were suitable for preparation of electrospun precursor solution. The DCM was used in the preliminary experiment. As showed in the **Figure 2-28**, we could obtain the electrospun membranes onto the aluminum foil. However, we harvested bead-like electrospun PLLA fibers instead of even fibers as demonstrated in the SEM images (**Figure 2-29**). Further, we tried to use HFIP as the solvent for electrospinning. By adjusting different electrospinning parameters, an even PLLA fibers could be obtained (**Figure 2-30**). For the following membrane preparation, we thus adopted HFIP as the electrospun solvent. To further demonstrate whether such PLLA fibers encapsulated GelMA nanogels, TEM was used to observe samples. As displayed in the **Figure 2-31**, the fibers exhibited even fibrous morphology; however, we could not observe the location of GelMA nanogels. Thus, we subsequently used fluorescence microscope to characterize the samples. Special acknowledgement and gratitude are given to Mr. Chun Hei Lam for completing the fluorescence characterization. In the microscopic images, the fiber diameter of 10%G/PLLA was about 1-2 μm (**Figure 2-32**). Compared with pure PLLA, there were strong even red fluorescence signal within siRNA-loaded samples in the fluorescence images, which indicated the successful encapsulation of Cy3-labelled siRNA-loaded GelMA NPs in the PLLA electrospun fibrous membranes. In addition, we found the red fluorescence intensity was enhanced with the increase of the GelMA nanogel content, indicating that we can control the siRNA loading amount by changing the incorporated GelMA nanogel contents (**Figure 2-33**). Altogether, these results demonstrated the feasibility to prepare the GelMA nanogel-embedded fibrous membranes.

Figure 2-28. Photograph of the obtained electrospun PLLA membrane collected onto the aluminum foil. Scale bar = 1 cm.

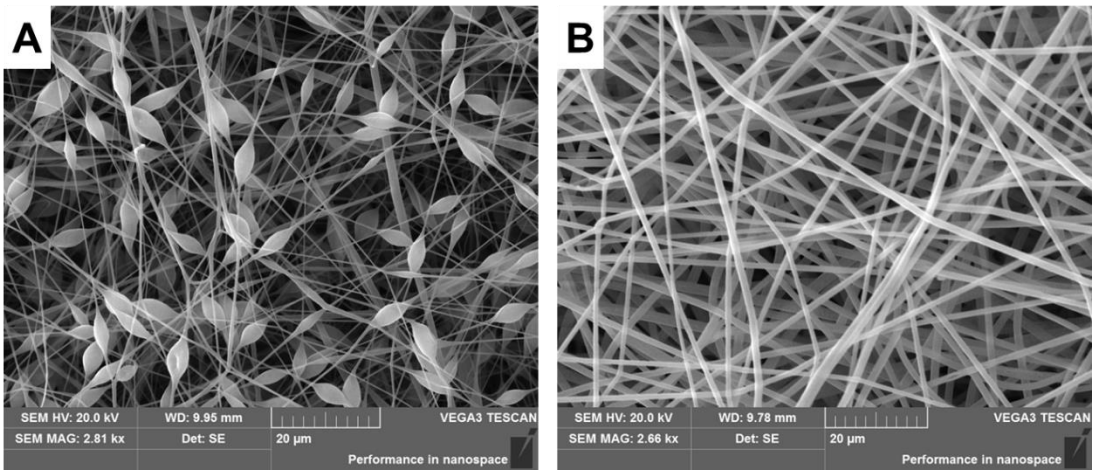

Figure 2-29. SEM images of electrospun PLLA fibers prepared at concentrations of (A) 10 wt.% and (B) 15 wt.% using DCM as the electrospun solvent.

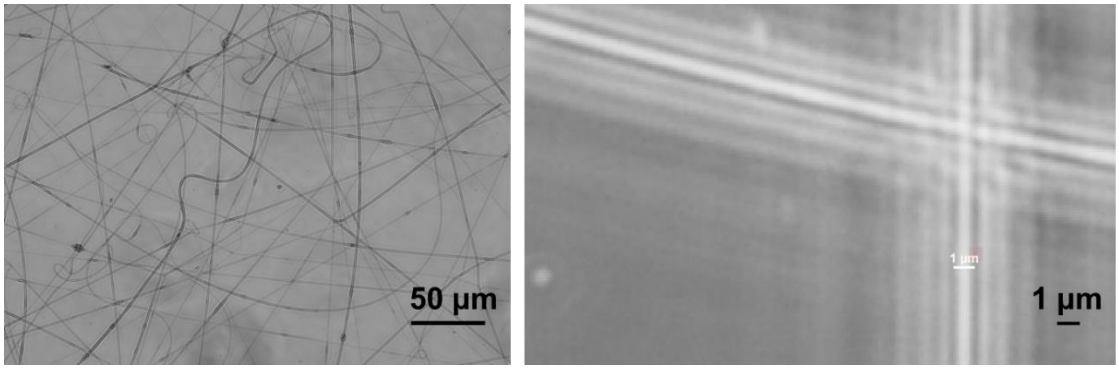

Figure 2-30. Bright field images of electrospun PLLA fibers prepared at concentrations of 20 wt.% using HFIP as the electrospun solvent.

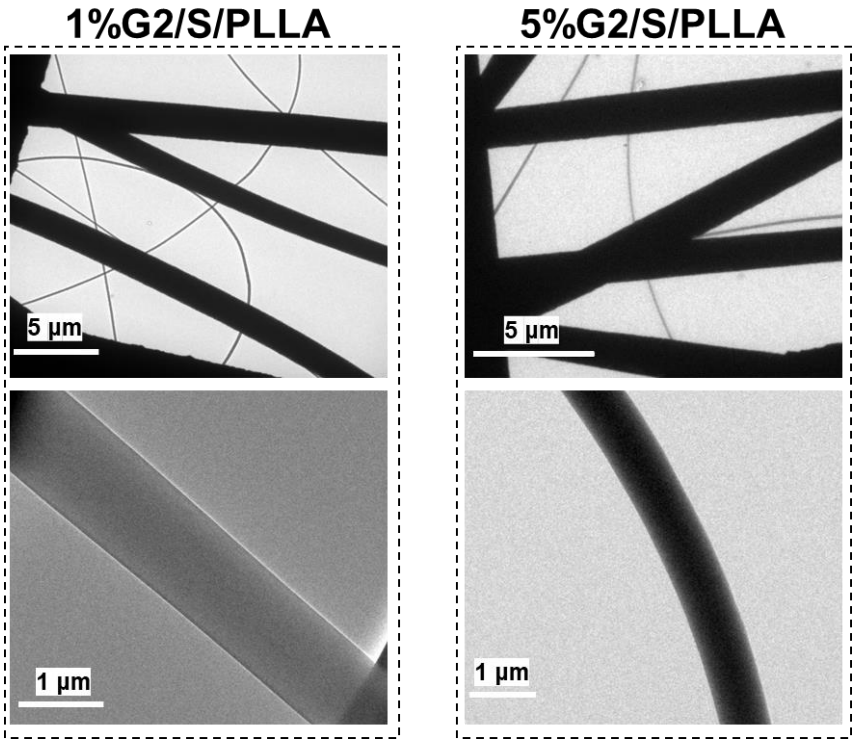

Figure 2-31. TEM images of 1%G2/S/PLLA and 5%G2/S/PLLA electrospun fibers. 1%G2/S/PLLA and 5%G2/S/PLLA indicated the PLLA membranes with different contents of G2/S at 1 and 5 wt.%, respectively.

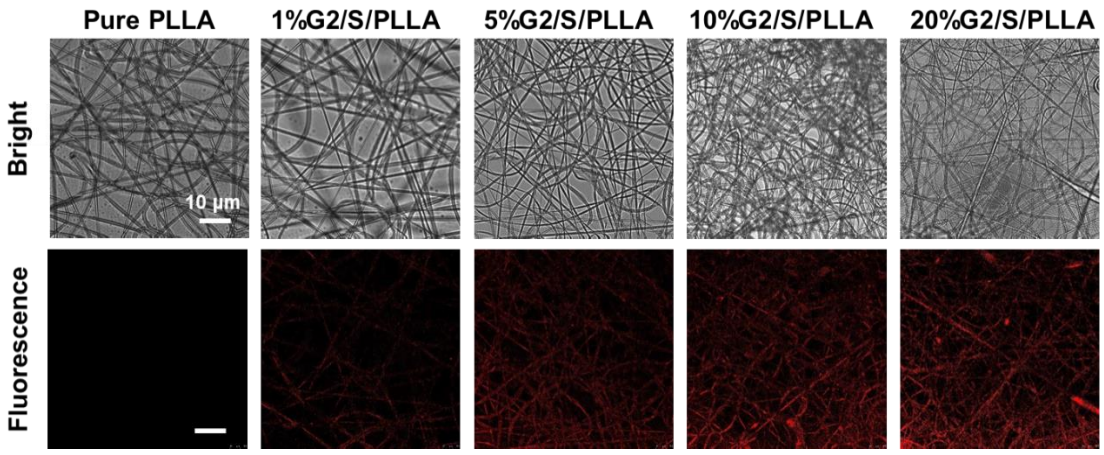

Figure 2-32. Fluorescence observation of different PLLA fibrous membranes. Red fluorescence indicated the Cy3-labelled siRNA-loaded GelMA nanogels embedded in the PLLA fibers. 1%G2/S/PLLA, 5%G2/S/PLLA, 10%G2/S/PLLA, 20%G2/S/PLLA indicated the PLLA membranes with different contents of G2/S at 1, 5, 10 and 20 wt.%, respectively. Scale bar = 10 μm.

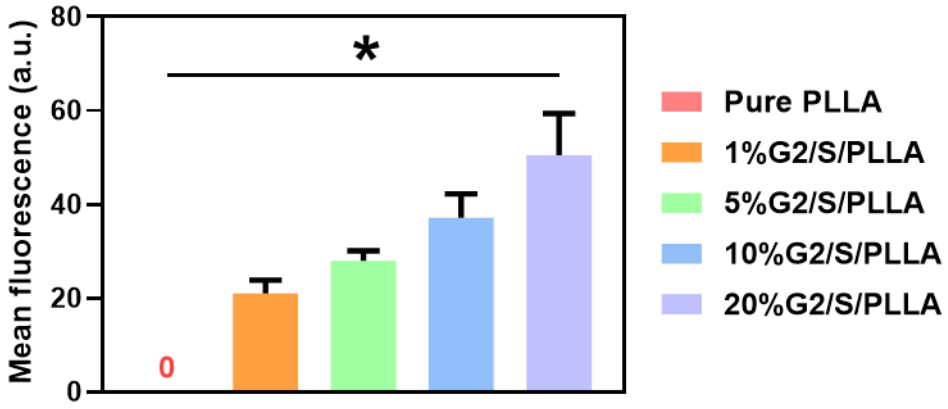

Figure 2-33. Mean fluorescence intensity of corresponding different electrospun fibers.

The morphology of the electrospun nanofibrous membranes before and after swelling in PBS was then characterized. At the beginning , we characterized the morphology of GelMA nanogel-containing PLLA fibers by SEM. Possibly due to inadequate stir, there were much more nanogels aggregated and scattered between the fibers (**Figure 2-34**). Thus, we optimized the stir time and redid the experiment. As showed in the **Figure 2-35**, all these scaffolds showed nanofibrous network. Notably, before the swelling, the scaffolds with or without addition of GelMA nanogels showed even fiber architecture, and their diameter decreased with the increase of the GelMA nanogel content. However,

after swelling in PBS for 3 days, the fibers of membranes with addition of GelMA nanogel were swollen with increased diameters compared with that of pure PLLA membranes. These results in turn demonstrated the successful incorporation of GelMA nanogel in PLLA fibers.

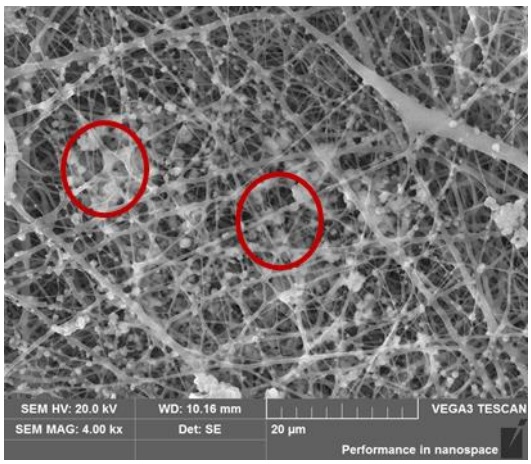

Figure 2-34. SEM image of 20%G2/S/PLLA electrospun fibrous membranes.

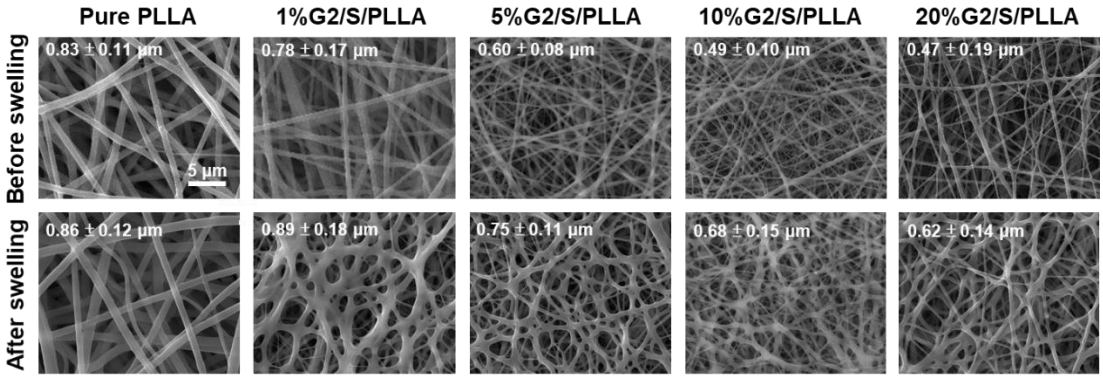

Figure 2-35. Representative SEM images of different PLLA fibrous membranes before and after swelling in PBS for 3 days. 1%G2/S/PLLA, 5%G2/S/PLLA, 10%G2/S/PLLA, 20%G2/S/PLLA indicated the PLLA membranes with different contents of G2/S at 0, 1, 5, 10 and 20 wt.%, respectively. Scale bar =5 µm.

Subsequently, the swelling properties of GelMA nanogel-embedded fibrous membranes were analyzed (**Figure 3-36**). The addition of GelMA nanogels had limited influence on swelling properties of PLLA fibrous membranes, and all these nanofibrous membranes showed low swelling ratio. Among these scaffolds, 20%G2/S/PLLA

exhibited the most distinct water sorption (absorbed water equivalent to only ~7% of its dry weight after immersion in PBS for 6 hrs). Consistent with SEM results described above, the swelling ratio of the fibrous membrane scaffolds was dependent on the incorporated GelMA nanogel content. Although no significant difference in swelling ratio was found between 5%G2/S/PLLA and 10%G2/S/PLLA, there seems an escalating trend with increasing GelMA nanogel content. To sum up, the low swelling properties bestowed upon fibrous membranes good ability as a favorable barrier to resist water sorption and prevent cell recruitment and ECM deposition during tendon healing.

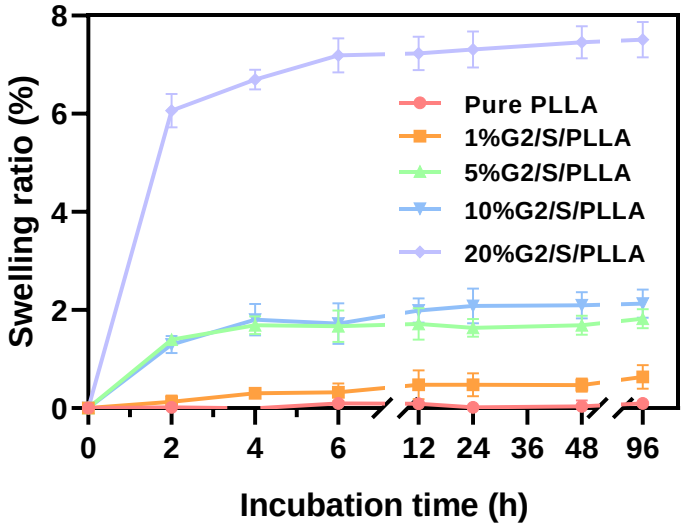

Figure 2-36. Swelling test of different PLLA fibrous membranes after incubation in PBS for 96 h. 1%G2/S/PLLA, 5%G2/S/PLLA, 10%G2/S/PLLA, 20%G2/S/PLLA indicated the PLLA membranes with different contents of G2/S at 0, 1, 5, 10 and 20 wt.%, respectively.

A good barrier scaffold should possess excellent mechanical performances to facilitate the surgical operation process and maintain structural integrity during long-term *in vivo* implantation while avoiding accident damage to surrounding tissues. Thus, the mechanical properties of GelMA nanogel-embedded fibrous membranes were evaluated by tensile stress-strain measurements. As showed in the **Figure 2-37(A)**, the mechanical properties of fibrous membranes could be reduced by increasing GelMA

nanogel incorporation content. Compared with other groups, the pure PLLA fibrous membranes showed higher tensile modulus and fracture strain; however, after incorporation of GelMA nanogels, their tensile modulus and extensibility were significantly reduced. Notably, although no significant difference in tensile modulus was found among 1%G2/S/PLLA, 5%G2/S/PLLA and 10%G2/S/PLLA groups, the 20%G2/S/PLLA group exhibited remarkably decreasing mechanical properties with a tensile modulus of 20.49 ± 5.55 MPa and an extensibility of 33.91 ± 3.90 % (**Figure 2-37(B) and (C)**). The obviously reduced mechanical properties might be probably due to the low interfacial interactions between PLLA and GelMA nanogels, as well as the nanogel aggregation upon increase of their contents in the PLLA fibers. However, even for the 20%G2/S/PLLA group, its mechanical properties could still resist external forces without graft failure, meeting the requirement of practical application. Considering the results of swelling and mechanical experiments, we selected the 10%G2/S/PLLA for the following experiments due to its relatively low swelling properties and high mechanical performances, which is more advantageous for the *in vivo* applications.

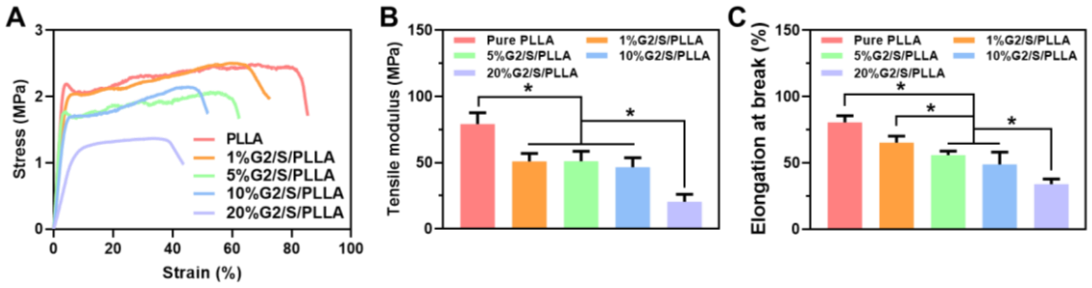

Figure 2-37. The mechanical performances of different PLLA fibrous membranes. (A) The stress-strain curve of tensile test of different PLLA membranes. (B) The tensile modulus and (C) elongation at break. 1%G2/S/PLLA, 5%G2/S/PLLA, 10%G2/S/PLLA, 20%G2/S/PLLA indicated the PLLA membranes with different content of G2/S at 0, 1, 5, 10 and 20 wt.%, respectively.

2.3.3 *In vitro* MMP2-responsive siRNA release from the fibrous membranes

To investigate whether the loaded siRNA could be released from GelMA nanogel-

embedded fibrous membranes in response to the MMP-2 within the microenvironment, fibrous membranes (10%G2/S/PLLA) were incubated in the PBS solution containing different concentration of MMP-2 to assess the siRNA release profiles. As showed in the **Figure 2-38**, the siRNA could be slowly released from the fibrous membranes in PBS with cumulative release reaching plateau (16.83 ± 3.76 %) after 24-h incubation. Such phenomenon might be attributed to the swelling process of GelMA nanogels which could slowly release siRNA when water infiltrated into the GelMA network. However, similar to the siRNA release results from GelMA nanogel, probably due to the electrostatic interaction between GelMA nanogel and siRNA, the siRNA release rate from the fibrous membrane could be significantly reduced. Furthermore, the addition of MMP-2 significantly promoted siRNA release from the fibrous membranes due to the MMP-2-mediated GelMA specific degradation. Notably, the higher concentration of MMP-2, the faster release rate and cumulative release percentage of siRNA. More importantly, when MMP-2 concentration reached 10 U/mL, the siRNA cumulative release percentage could reach 73.01 ± 5.72 %, which could release the loaded cargoes within a short time (12 h) to achieve the therapeutic purpose. In a word, these results suggested that MMP-2 could stimulate siRNA release from the GelMA nanogel-embedded fibrous membranes.

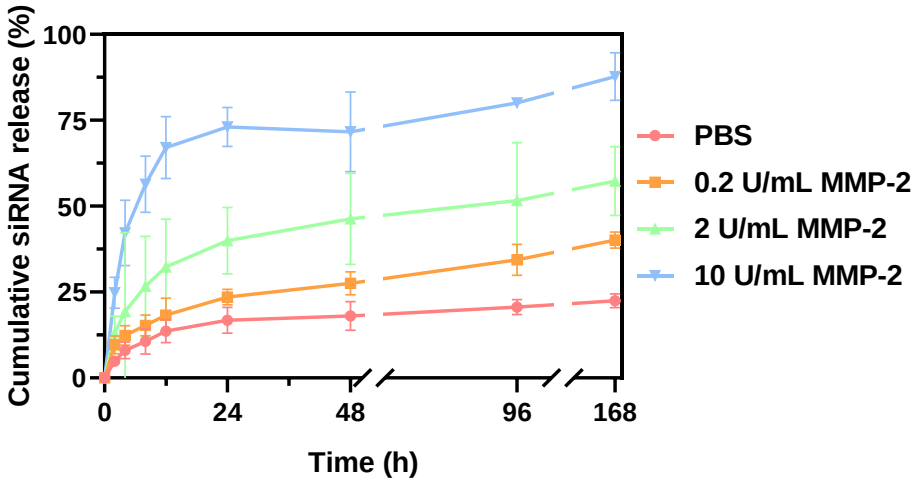

Figure 2-38. The siRNA release profiles from 10%G2/S/PLLA electrospun membranes incubated in PBS with different concentration of collagenase (0, 0.2, 2 and 10 U/mL).

As discussed in the 1.2 section, the drug release from the electrospun membranes might be through desorption from the fiber surface, diffusion in the fibers, and the fiber degradation. Since the blending electrospinning technique was used to fabricate the GelMA nanogel-embedded fibrous membranes, the GelMA nanogels might be aggregated onto the fiber surface. Thus, surface desorption and drug diffusion were involved in the siRNA release process. In addition, GelMA has been demonstrated to be specifically degraded by MMP enzyme due to the presence of MMP degradation sites [73, 74]. To investigate the MMP-2 responsive degradation of fibrous membranes, GelMA nanogel-embedded fibrous membranes were incubated in the PBS containing different concentrations of MMP-2. After incubation for different time period, the weight loss of pure PLLA or 1%G2/S/PLLA was not obvious regardless of incubation in PBS with or without addition of MMP-2 (**Figure 2-39**). However, for the 5%G2/S/PLLA, 10%G2/S/PLLA and 20%G2/S/PLLA groups, despite slight degradation in PBS solution, signification weight loss was found in MMP-2 containing PBS solution. Besides, the higher concentration of MMP-2, the more degradation percentage of electrospun membranes. These results demonstrated the MMP-2 responsive degradation of GelMA nanogel-embedded fibrous membranes could also contribute to the siRNA release from the scaffolds.

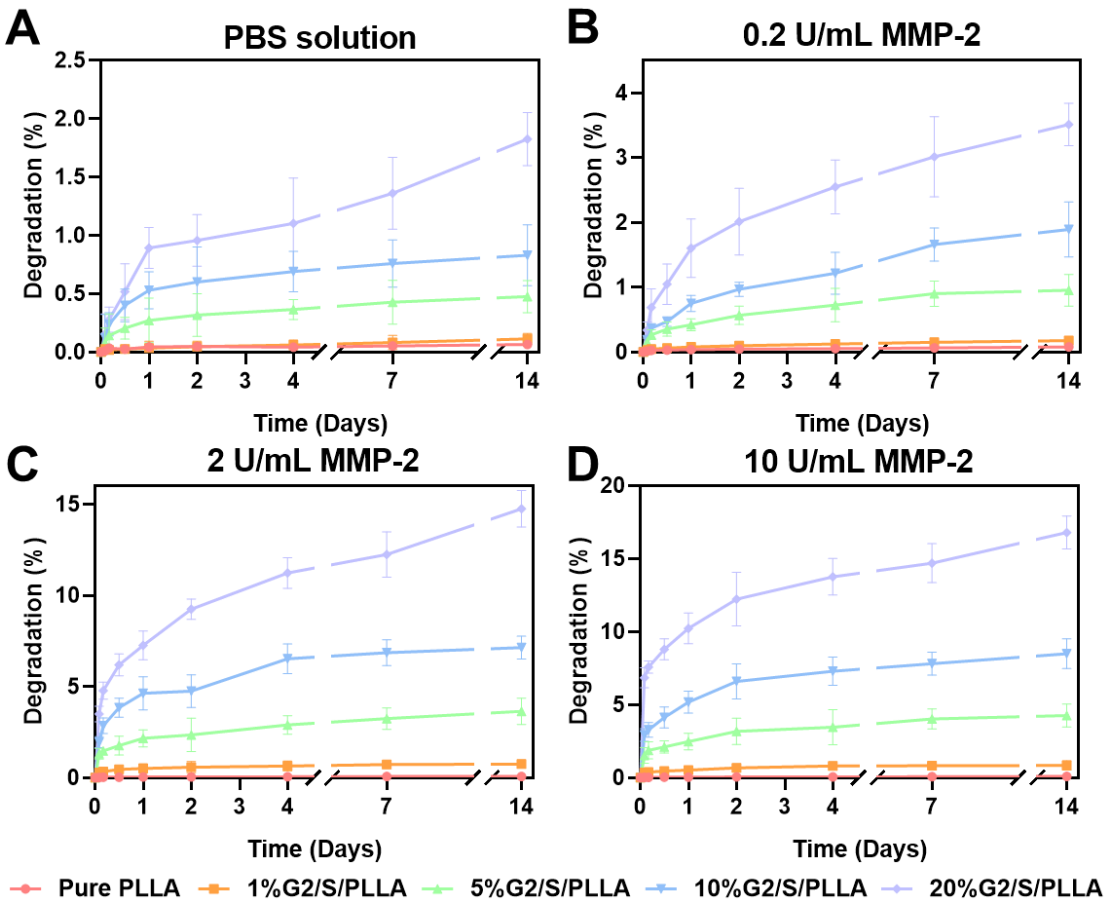

Figure 2-39. The degradation profile of different PLLA electrospun membranes with different contents of GelMA nanogels (0, 1, 5, 10 and 20 w/w %) incubated in PBS with different concentrations of collagenase (A) 0, (B) 0.2, (C) 2 and (D)10 U/mL, respectively.

2.3.4 *In vitro* biological effects of fibrous membranes

To evaluate whether the siRNA released from the GelMA nanogel-embedded fibrous membranes could regulate cell behaviors to prevent adhesion tissue formation, we assessed the ERK2 gene silencing, cell proliferation, morphology and viability of NIH/3T3 after co-culture with extracts from different material formulations. Here, special acknowledgement and gratitude are given to Mr. Yu Liu for assisting to optimize cell experimental plan and teach the key technique. First, the expressions of targeted ERK2 and associated downstream signaling molecules (Col-1 and Col-3) after treatment with siRNA-loaded membrane scaffolds were analyzed using the qRT-PCR. As illustrated in **Figure 2-40(A)**, ERK2 has been demonstrated to be critical in

regulation of collagen secretion and fibroblast proliferation [60]. Thus, blocking of ERK2 expression may hinder the associated signaling pathway transduction, reducing the risk of tendon adhesion. As expected, the expression level of ERK2 was significantly downregulated in the 10%G2/S/PLLA and 10%G2/S/PLLA+MMP2 (**Figure 2-40(B)**). Notably, the addition of MMP-2 into the GelMA nanogel-embedded fibrous membranes further decreased the expression level of ERK2. These results indicated the stability of the incorporated siRNA complex that could be triggered to release from scaffolds by elevated MMP-2, and then cause the silencing effects of ERK2.

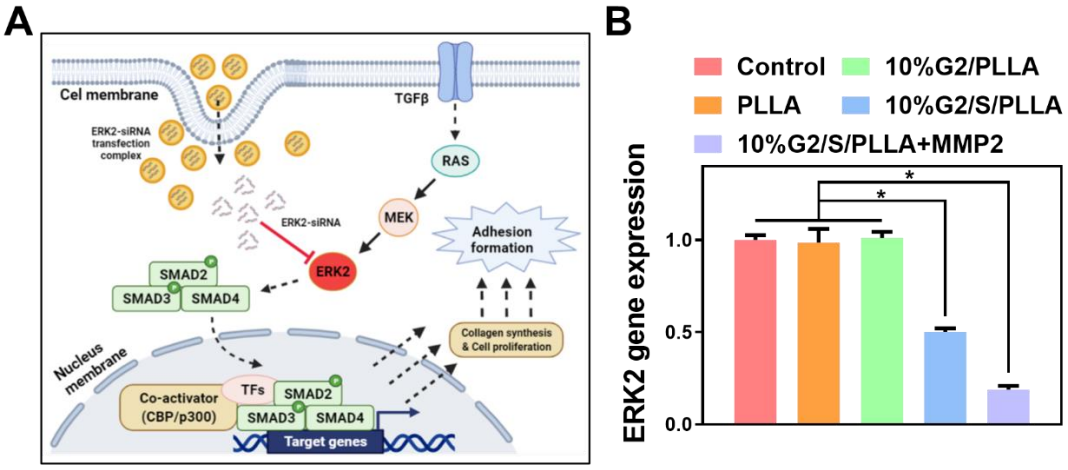

Figure 2-40. Effect of prepared electrospun membrane scaffolds on blocking of ERK2 and the associated downstream signaling moleculars. (A) Schematic showing the released ERK2-siRNA blocks ERK2 and downregulates associated downstream signaling molecules to control collagen secretion and cell proliferation, ultimately preventing adhesion formation. (B) qRT-PCR analysis of ERK2 gene expressions by NIH/3T3 cells after 3-day culture with leaching solution from different material formulations incubated with or without MMP-2. Figure created with BioRender.com.

In addition, we evaluated the downstream Col-1 and Col-3 gene expressions (**Figure 2-41**). Similarly, Col-1 gene was significantly downregulated in the MMP-2-treated siRNA-containing groups, while Col-3 gene expression was remarkably decreased in both siRNA-loaded groups. These results further confirmed that the released siRNA from electrospun membranes triggered by MMP-2 could preserve its bioactivity to

block the targeted ERK2 gene and reduce the associated downstream gene expressions.

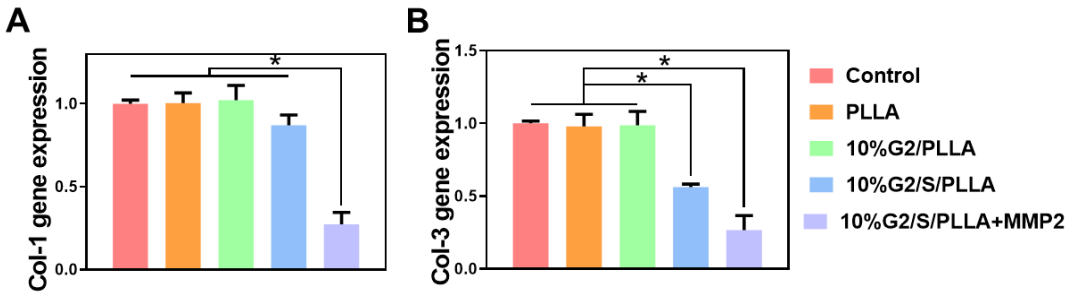

Figure 2-41. qRT-PCR analysis of ERK2-associated downstream gene expression including (A) Col-1 and (B) Col-3 in NIH/3T3 after 3-day co-culture with extracts from different material formulations incubated with or without MMP-2.

The cell proliferation of NIH/3T3 cells after treatment with different material formulations was assessed by CCK-8 analysis. As showed in the **Figure 2-42**, cell viability was significantly reduced in the MMP2-treated siRNA group after 1-day incubation. No significant difference was observed among other four groups. After incubation for 3 days, the proliferation rate of NIH/3T3 cells treated with siRNA-containing material formulations was reduced as compared to control, PLLA and 10%G2/PLLA groups. The PLLA groups showed reduced cell proliferation, possibly due to the released toxic metabolite (like lactic acid) by degradation. Of note, the MMP-2 treated siRNA group showed extremely lower proliferation compared to that of other groups, suggesting that MMP-2 induced siRNA release from membrane scaffolds to prevent fibroblast proliferation. These results were in accordance with the PCR results described above.

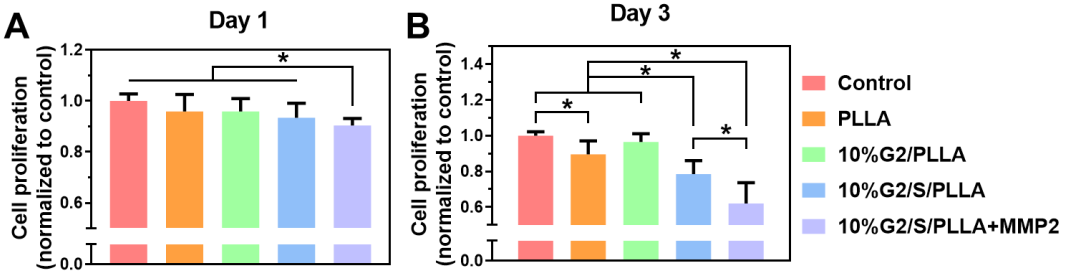

Figure 2-42. Proliferation of NIH/3T3 cells after co-culture for (A) 1 and (B) 3 days

with extracts from different material formulations incubated with or without MMP-2. The test was evaluated using CCK-8 assay, and cell proliferation was expressed by normalizing the average absorbance value to that of control group.

Next, the viability of NIH/3T3 cells was further evaluated via live/dead staining assays. As showed in the **Figure 2-43**, there were a large number of live cells in all groups after 1-day culture, and almost no dead cells were found in these groups, apart from few dead cells observed in siRNA + MMP group. Quantitative analysis further verified our observation (**Figure 2-44**) that siRNA + MMP group showed lower live/dead cell ratio. After culture for 3 days, we found much more live cells in control, PLLA, and 10%G2/PLLA groups, indicating the excellent biocompatibility of the delivery system (**Figure 2-45**). However, siRNA-containing groups exhibited obviously more cell death, and markedly higher dead/live cell rate was observed in the MMP-2 treated groups (**Figure 2-46**). These results also corresponded with those of proliferation rate evaluation and PCR tests.

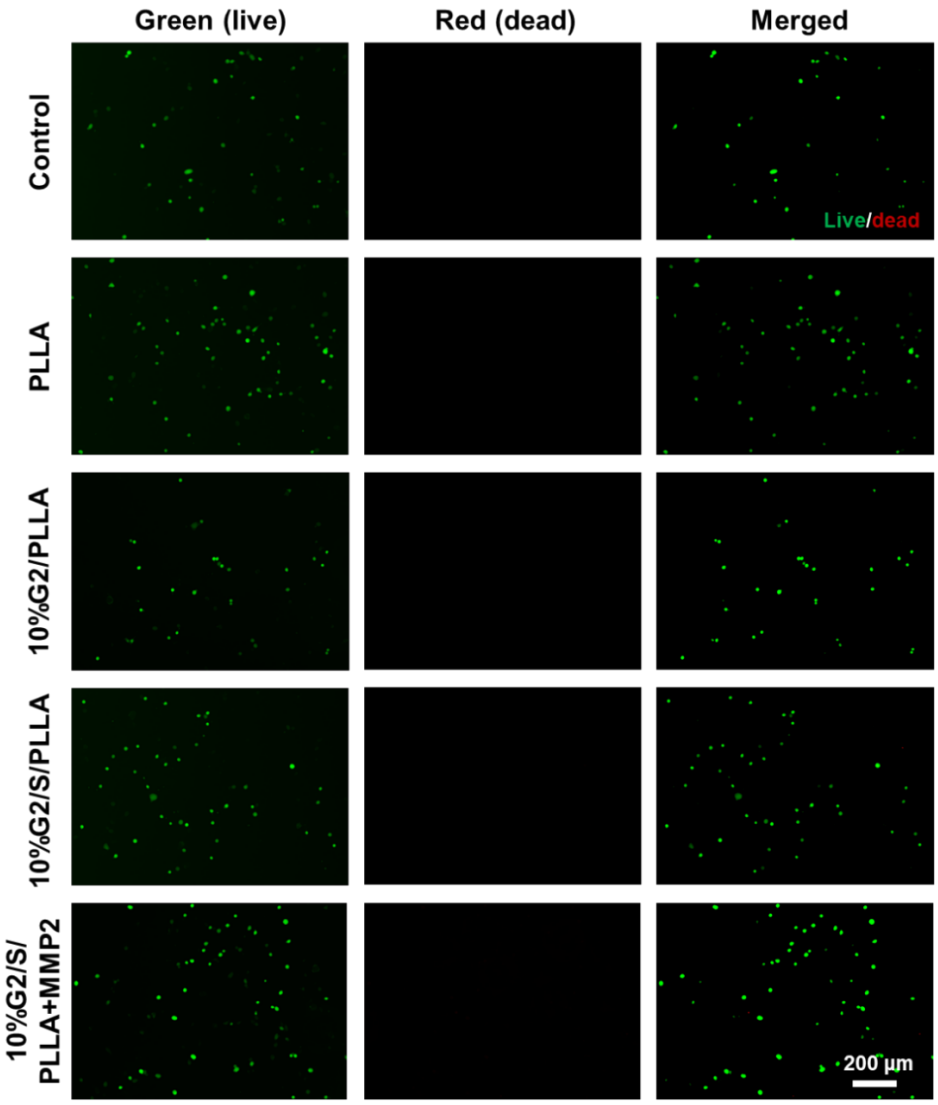

Figure 2-43. Live/dead staining of NIH/3T3 cells after co-culture with extracts from different PLLA electrospun membrane formulations for 1 days. Green and red fluorescence indicate the viable and dead cells, respectively. Scale bar = 200 μm.

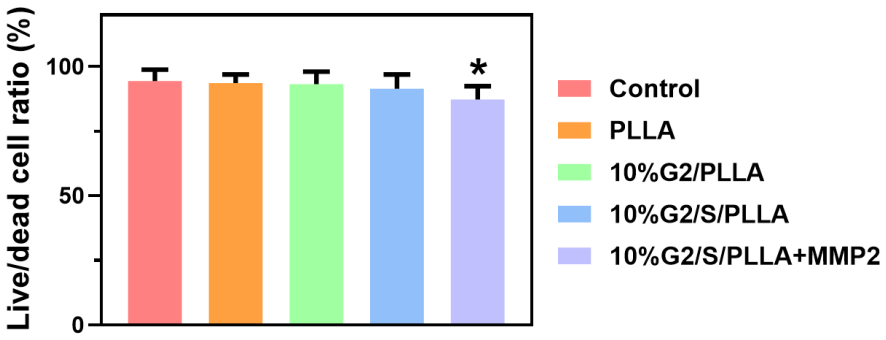

Figure 2-44. Quantitative analysis of live/dead cell ratio at day 1 based on the live/dead staining assay.

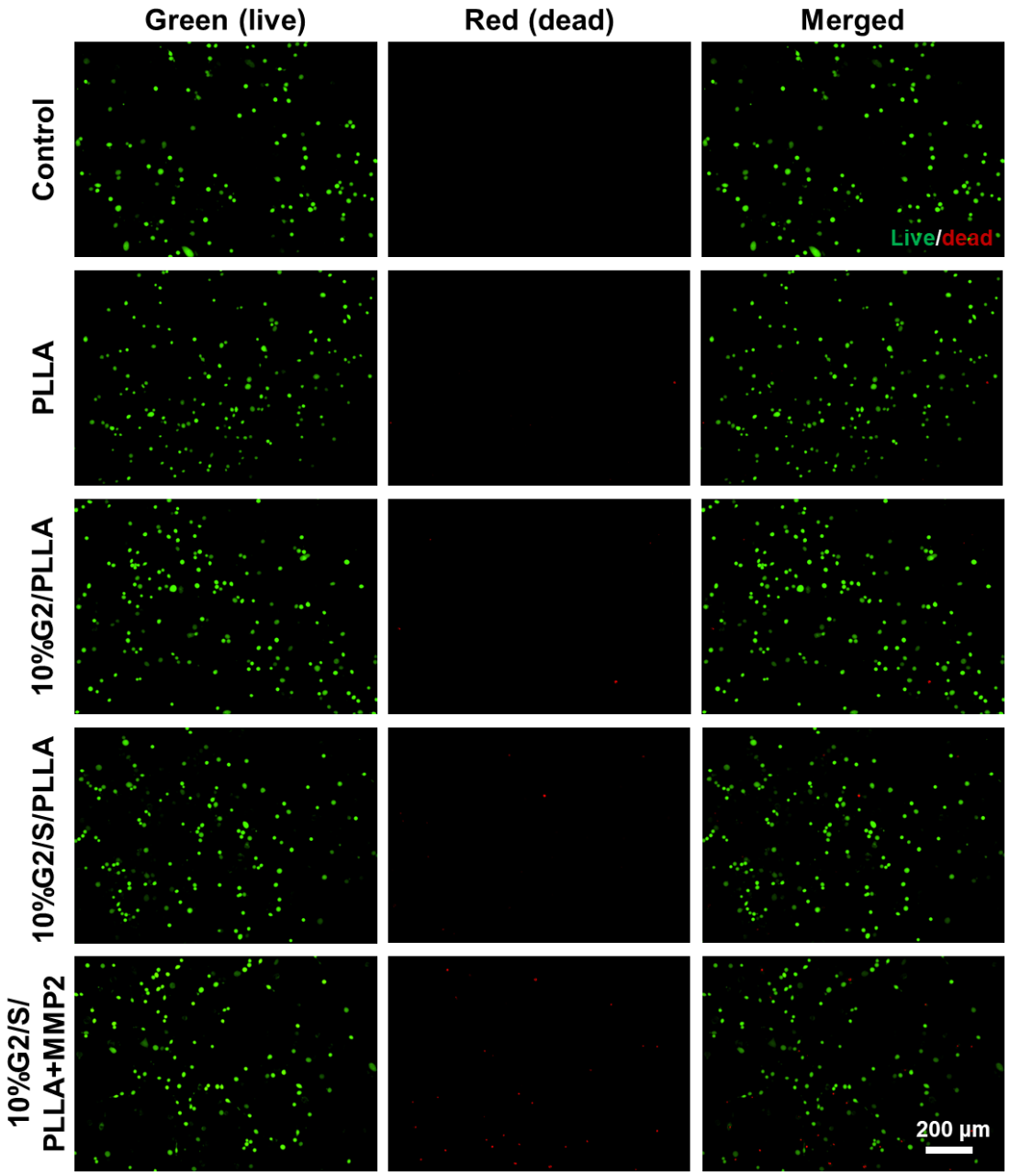

Figure 2-45. Live/dead staining of NIH/3T3 cells after co-culture with extracts from different PLLA electrospun membrane formulations for 3 days. Green and red fluorescence indicate the viable and dead cells, respectively. Scale bar = 200 μm.

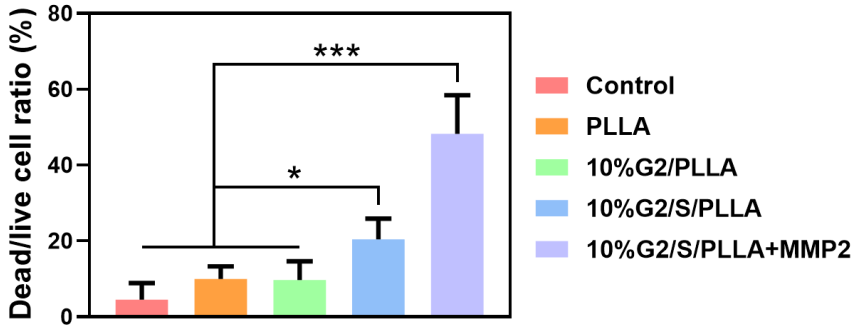

Figure 2-46. Quantitative analysis of dead/live cell ratio at day 3 based on the live/dead staining assay.

Subsequently, we performed the actin and ERK2 staining to see the cell morphology and ERK2 protein expression. As showed in the **Figure 2-47**, there were many adhered NIH/3T3 cells in the control, PLLA, and 10%G2/PLLA groups with cell spreading in a fibroblast-like shape. However, the 10%G2/S/PLLA and 10%G2/S/PLLA+MMP-2 groups showed significantly reduced cell adhesion, and cells appeared to be a long and narrow fibrous morphology with decreased spreading area. Such phenomenon was more obvious in the MMP-2 treated group. These results were in line with the fluorescence images of NIH/3T3 cells treated with the siRNA-loaded GelMA nanogels. Similarly, the ERK2 protein expression as indicated by ERK2 fluorescence intensity was significantly reduced in 10%G2/S/PLLA+MMP-2 groups, as compared with control, PLLA, 10%G2/PLLA, and 10%G2/S/PLLA groups (**Figure 2-48**). Altogether, these results demonstrated the released siRNA specifically triggered by MMP-2 could exert its biological effects on blocking ERK2 and downstream gene expressions, reducing fibroblast adhesion and proliferation, which demonstrated the feasibility of such novel nanofibrous membrane barrier to prevent tendon adhesion formation by silencing the associated fibrosis signal pathway.

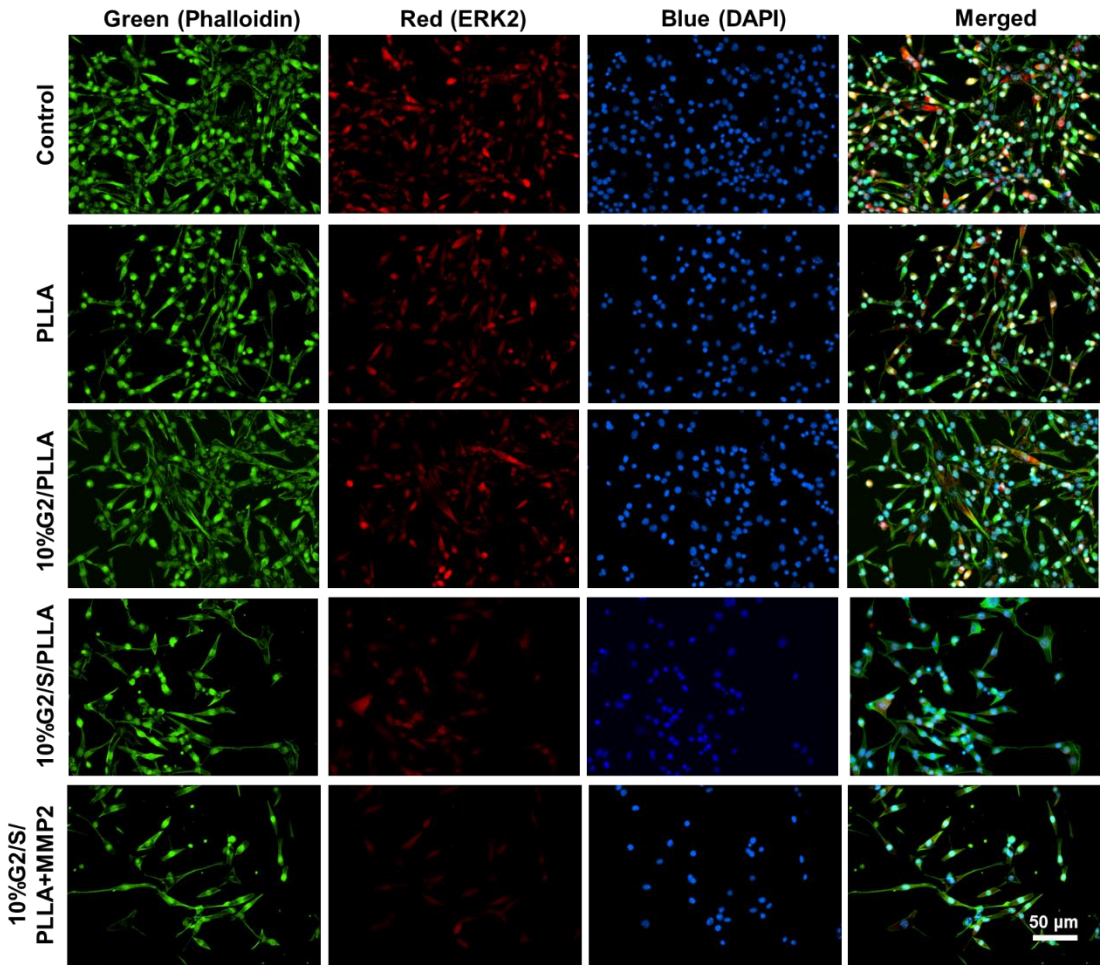

Figure 2-47. Fluorescence images of NIH/3T3 cells treated with extracts from different material formulations for 3 days and stained with phalloidin (green) and anti-ERK2 antibody (red). Cell nucleus is stained with DAPI (blue).

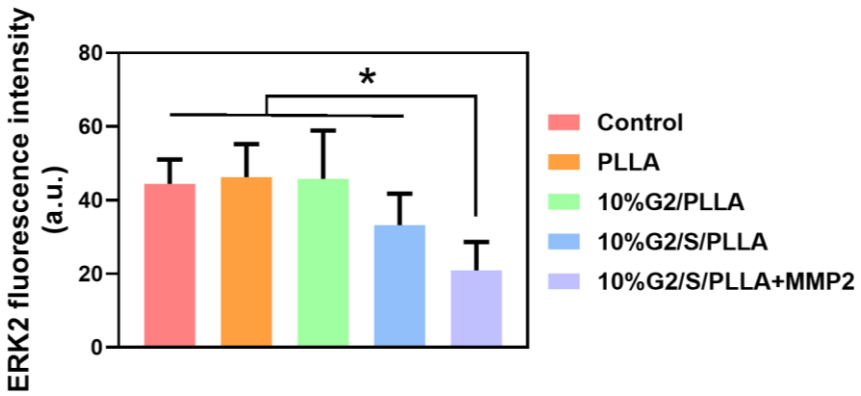

Figure 2-48. Quantification of mean fluorescence intensity of NIH/3T3 cells stained with ERK2 based on the immunochemical staining assay.

2.3.5 *In vivo* biological effects of fibrous membranes

Next, we evaluated the *in vivo* therapeutical efficacy of GelMA nanogel-embedded fibrous membranes by creating the rat tendon injury model (**Figure 2-49**). Such rat tendon injury model was established by first creating a midline skin incision to expose the surgical sites of tendon, followed by transecting the tendon and repairing it using a modified Kessler technique with a 6/0 prolene suture. Then, membrane samples were used to wrap around the operated sites of the tendon, and wound was closed with sutures. Here, special acknowledgement and gratitude are given to Mr. Kui Ma for completing animal experiments. After surgery for 21 days, the surgical sites of the repaired tendons were directly observed. There was no significant inflammation or ulcer found around the incision area. Subsequently, we macroscopically assessed the tendon adhesion using a scoring system based on the surgical observation. As showed in the **Figure 2-50**, there were massive adhesion tissues in the control group intertwining the operated tendon and surrounding tissue that was difficult to separate using blunt instrument. In contrast, in the SurgiWrap and 10%G2/PLLA groups, only small bundles of fibrous tissues were found at operated site of tendon tissue, and it was feasible to separate them by blunt dissection. Interesting, the 10%G2/S/PLLA group showed almost no dense adhesion tissue formation in the peritendinous area compared with other groups. The tendon adhesion was further semi-quantitatively evaluated by adhesion grading scale (**Figure 2-50(B)**). The 10%G2/S/PLLA group had the lowest score among the four groups, suggesting its outstanding anti-adhesion performance.

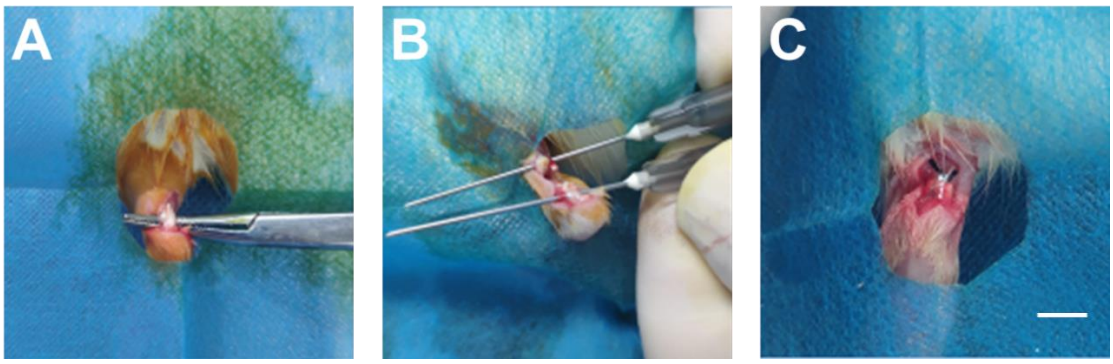

Figure 2-49. The surgical operation process including (A) exposing the surgical sites of tendon by creating a midline skin incision; (B) transecting the tendon and (C)

wrapping tendon injury site with membrane samples after repairing the tendon via a modified Kessler tendon suture technique. Scale bar=1 cm.

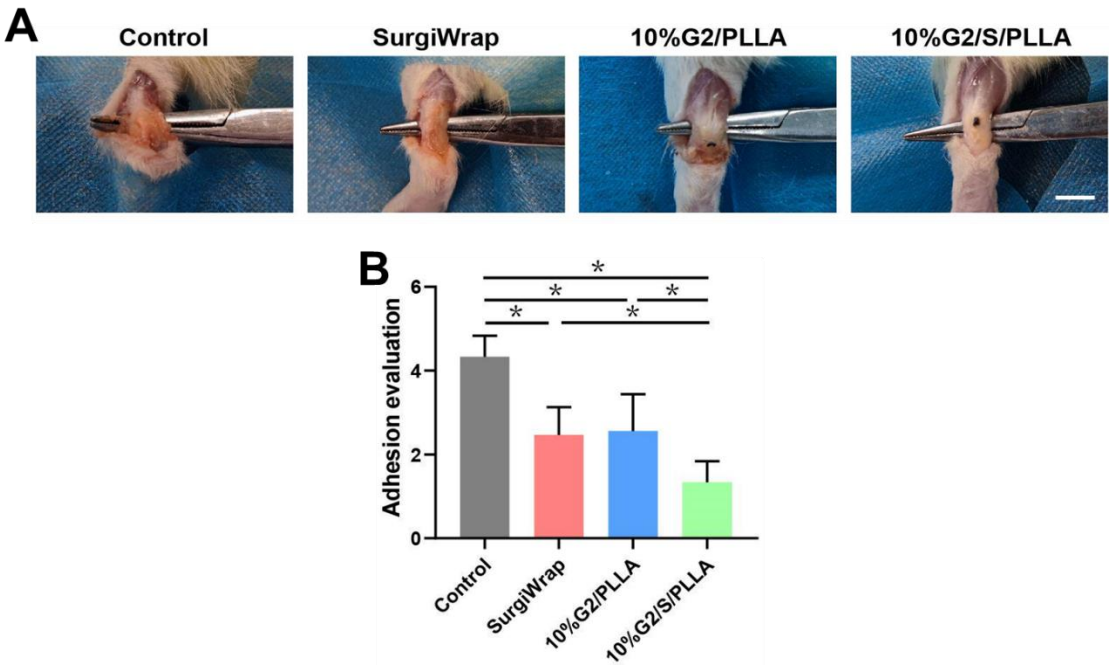

Figure 2-50. (A) Macroscopic observation and (B) evaluation of the tendon adhesion of surgical sites after different treatments for 21 days. Scale bar=1 cm.

Then, we assessed the peritendinous adhesion of repaired tendon sites by histochemical analysis including H&E staining and Masson's trichrome staining. As revealed in the **Figure 2-51(A)** and **(B)**, massive fibrous tissues were located between the repaired tendon and the peripheral tissue in the control group. These dense adhesion tissues grew into and merged with the intimal tendon, significantly reducing the tendon repair outcomes. However, there were loose fibrous bundles formed around the peritendinous area in the SurgiWrap and 10%G2/PLLA groups. Notably, only little sporadic adhesion tissues were found in the 10%G2/S/PLLA group, in which epitenon surface was relatively smoother as compared with other groups. Besides, the operated tendon was well bridged at the broken ends showing good continuity. Most importantly, the collagen fibrils in the repaired tendon site in the 10%G2/S/PLLA group were well aligned mimicking the organization of native fibrous bundles, which indicated the superior tendon regeneration [75]. Altogether, the histochemical assessment

demonstrated the intriguing ability of 10%G2/S/PLLA group to prevent adhesion formation and facilitate tendon healing.

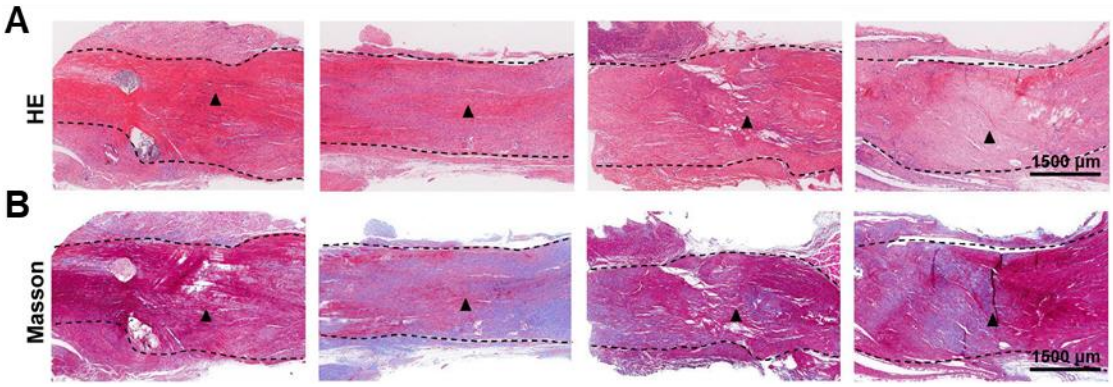

Figure 2-51. Histological evaluation of tendon adhesion of surgical sites by (A) H&E staining and (B) Masson staining. The black triangle indicated the repaired tendon tissue, while the dotted lines represented the boundary between the tendon and the peripheral granulation tissue.

Col-1 and Col-3 were the main components in the tendon adhesion tissue [76, 77]. Thereafter, we further evaluated the expressions of Col-1 and Col-3 in the peritendinous adhesion tissue by immunohistochemical staining. As showed in the **Figure 2- 52**, yellow brown, that represents the Col-1 or Col-3, appeared in all groups. Compared with control, SurgiWrap and 10%G2/PLLA groups, there was weaker staining intensity in the peritendinous adhesion tissue in the 10%G2/S/PLLA group, suggesting the ERK2-siRNA could decrease the expressions of Col-1 or Col-3 and reinforce the ability to suppress adhesion tissue formation. To further explore the underlying anti-adhesion mechanism, we detected the protein expressions of p-ERK1/2, Col-1, Col-3 and p-SMAD3 in the peritendinous adhesion tissues by Western blot method, while using β-actin as the internal control. As displayed in the **Figure 2-53**, there was no obvious difference in the expressions of p-ERK1/2 protein among the control, SurgiWrap and 10%G2/PLLA groups. However, the 10%G2/S/PLLA group showed lowest p-ERK1/2 protein expression, indicating the targeted silencing of ERK2 gene by loaded ERK2-siRNA. Similar protein expression trends of the downstream signaling molecules

including Col-1, Col-3 and p-SMAD3 were observed among these groups. Since the MMP-2 was overexpressed in the peripheral area of tendon repaired sites after injury [59], we believed such upregulated MMP-2 could cause the specifical degradation of embedded gelatin nanogels and subsequently trigger ERK2-siRNA release, specifically decreasing ERK2 and its downstream marker expressions, ultimately reducing collagen synthesis and enhancing the anti-adhesion property of electrospun membrane scaffolds.

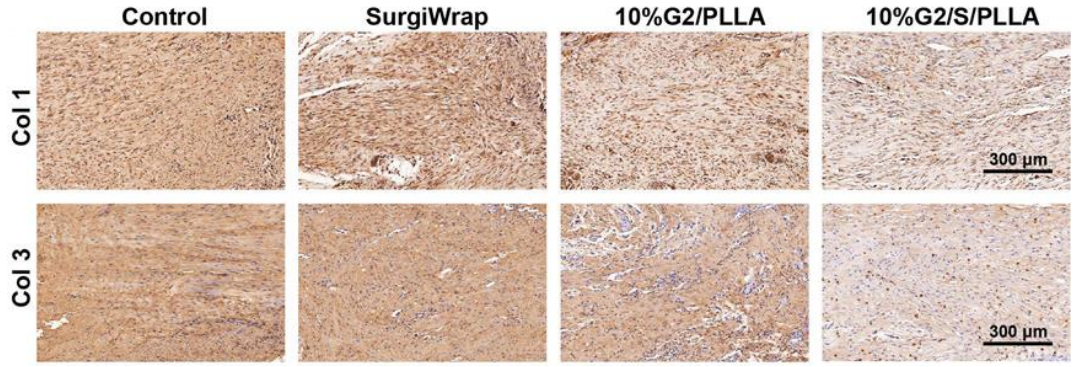

Figure 2-52. Representative images of immunohistochemical stanning of peritendinous adhesion tissues with Col-1 and Col-3.

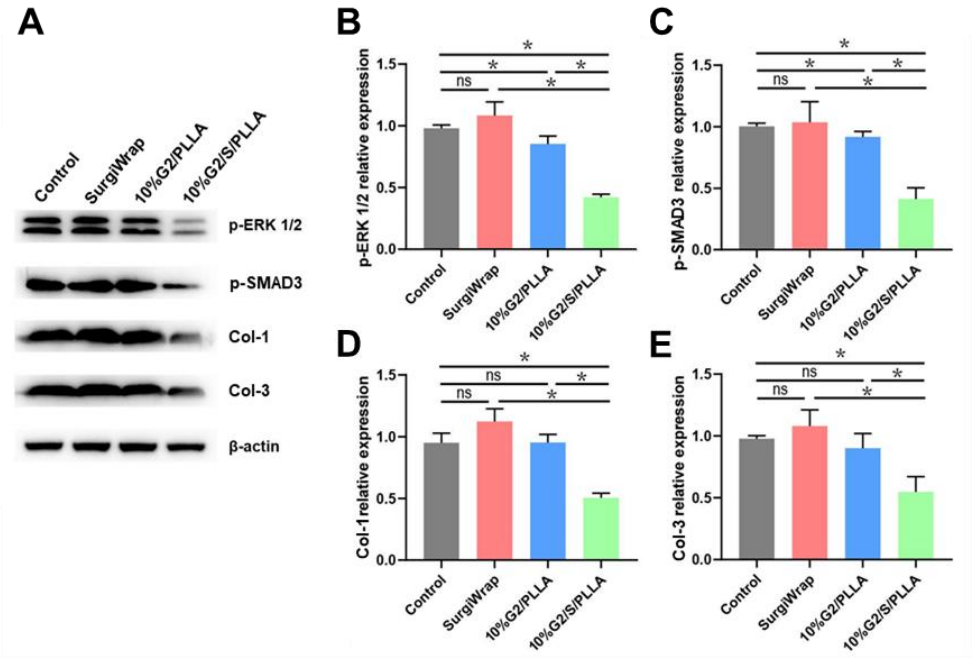

Figure 2-53. Western blot analysis of p-ERK1/2, Col-1, Col-3 and p-SMAD3 expressions. (A) The representative bands and the corresponding quantitative analysis of band intensity of (B) p-ERK1/2, (C) Col-1, (D) Col-3, and (E) p-SMAD3.

Next, we examined whether such siRNA-containing membrane scaffolds could reduce the tendon repair quality by determining the maximum breaking force of the repaired tendon tissue. The **Figure 2-54(A)** exhibited the process of measuring the breaking force via a mechanical tester. The quantitative results revealed no significant difference in breaking force observed in these four groups (**Figure 2-54(B)**), suggesting that the prepared siRNA-containing electrospun membrane scaffolds exserted no effect on mechanical performance of the healed tendon. Altogether, these data collectively demonstrated our 10%G2/S/PLLA electrospun membranes could serve as a promising platform for on-demand delivery of ERK2-siRNA and exhibit optimum anti-adhesion performance *in vivo*.

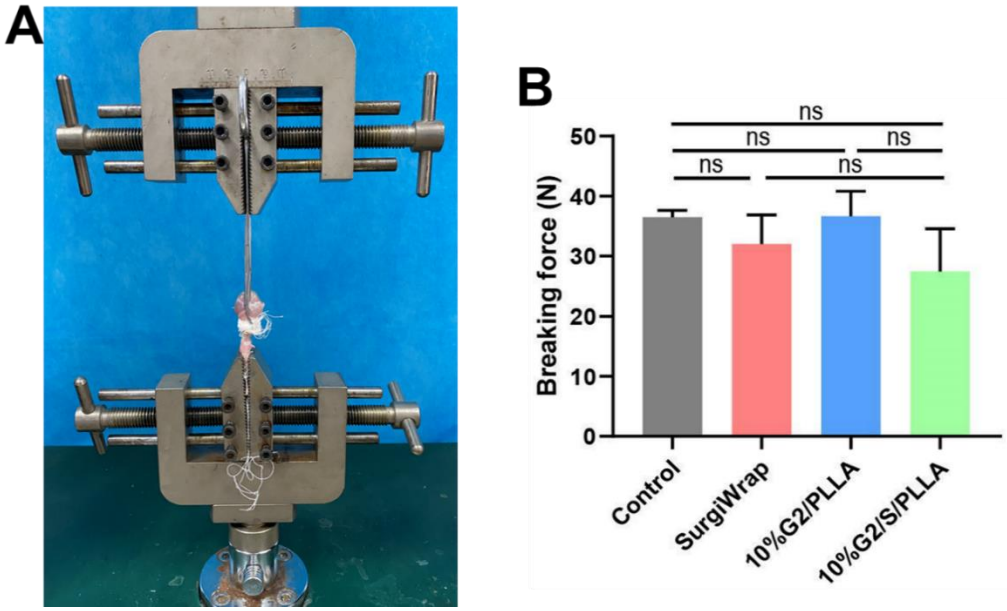

Figure 2-54. Biomechanical assessment of the repaired tendon. (A) a representative image of test process. (B) Maximal breaking forces of the repaired tendon.

2.4 Summary

In summary, we have successfully prepared MMP-2-triggered siRNA laden fibrous membranes by incorporation of siRNA-loaded GelMA nanogels into PLLA membranes using blending electrospinning technique. It could be found that siRNA-loaded GelMA

nanogels exhibited uniform spherical particle morphology and MMP-2 triggered siRNA release pattern. In addition, the whole nano-emulsification process that was used to fabricate GelMA nanogels did not detrimentally influence the bioactivity of ERK2-siRNA, as confirmed by successful siRNA transfection into cells and then reduced cell spreading area. These results indicated that our prepared GelMA nanogels could serve as a novel and all-purpose delivery system for different applications.

Next, the characterization of the physiochemical properties of GelMA nanogel-embedded fibrous membranes further confirmed their favorable performances such as controllable morphology/architecture (e.g., fiber diameter), swelling and degradation properties by changing the incorporated GelMA nanogel content. Besides, such composite fibrous membranes exhibited excellent mechanical performances even after incorporation of GelMA nanogels. More importantly, on-demand siRNA release in response to the MMP-2 could be achieved to reduce the adverse effects of ERK2-siRNA for tendon repair. Since ERK2 is key regulator of collagen production and fibroblast proliferation during the peritendinous fibrotic tissue formation, the efficient knockdown of target ERK2 gene may reduce collagen secretion by fibroblasts and inhibit the fibroblast proliferation. As expected, we demonstrated that the released siRNA was indeed able to block targeted ERK2 expression and suppress fibroblast adhesion and proliferation. *In vivo* experiments further revealed the great potential of such siRNA-containing electrospun membrane as a barrier material to attenuate peritendinous adhesion formation.

Chapter 3 Development of bio-inspired adhesive and robust Janus patch with multi-biofunctions for tendon repair

3.1 Introduction

Although the proposed MMP-2 responsive siRNA laden fibrous membranes in the chapter 2 have exhibited great potential in adhesion prevention, some limitations remain to be addressed. Firstly, the inflammatory reactions at the early stage of tendon repair have demonstrated to substantially disturb the tendon healing outcome. Besides, it was reported that excessive accumulation of reactive oxygen species is involved in the TME of impaired tendon, which may aggravate inflammatory responses and cause fibrous tissue formation, thus promoting peritendinous adhesion formation [78, 79]. In addition to adhesion, postoperative infection is another common complication after various open surgeries, which may influence the therapeutic outcomes [80]. Although systematic administration of antibiotics after surgery is an effective approach to preventing postoperative infection, it has many disadvantages such as increased antibiotic resistance, low effective drug concentration in the injury site, and other potential adverse effects. Furthermore, most of the traditional scaffolds used for tendon repair possessed low tissue adhesion properties that require suture fixation to integrate with tissue, which make the surgery operation complex and postpone the tendon healing process. For these reasons, an ideal physical barrier for tendon repair should be a drug-free robust fibrous membranes with anti-bacterial, anti-oxidative and anti-inflammatory activities. Most importantly, these membranes should possess anisotropic tissue adhesiveness to comply with the anatomy of tendon and facilitate tendon repair process, that is, the side facing the tendon should be bioadhesive and bioactive that can adhere tightly to the injured site to provide the mechanical support and favorable microenvironment for tendon regeneration, while another side facing the surrounding tissue should be non-adhesive and can protect tendon by physically inhibiting fibrotic scar invasion.

Here, we developed a Janus dual-layer membrane patch for treatment of tendon injuries, in which the inner layer was the multi-functional electrospun hydrogel patch (MEHP), while the outer layer was the poly-L-lactic acid (PLLA) fibrous membrane. MEHP was fabricated by blending electrospinning of GelMA and zinc oxide (ZnO) NP followed by tannic acid (TA) treatment (**Figure 3-1**). In this scaffold system, GelMA was used as the main matrix due to its similar chemical component to tendon fibers that is consisted of collagen, which can provide a favorable microenvironment for cell growth. Besides, our previous study demonstrated that GelMA exhibited good tissue adhesiveness because of the presence of multiple domains which could interact with the cell surface receptors and ECM protein [62]. ZnO was incorporated to improve scaffold mechanical properties as a nanofiller. In addition, ZnO NPs have been known to exhibit significant antibacterial activity against most pathogenic and non-pathogenic bacteria [81]. Most importantly, ZnO have been demonstrated to promote tendon healing by augmentation of re-epithelialization process and tendon cell proliferation [82]. The released Zn^{2+} is the important component of enzymes that are participated in various physiological processes. It was reported that Zn^{2+} could promote collagen synthesis, cellular growth and replication, and tendon differentiation, that indicated its ability to aid tendon healing process [83-85]. Finally, the simple TA treatment aimed to further increase the mechanical performances of the hydrogel membrane by strong hydrogen-bond interaction with GelMA and ZnO to increase the organic-inorganic interfacial compatibility. The introduction of secondary hydrogen-bonded network in the hydrogel matrix was also believed to reinforce the scaffold. Of course, like other mussel-inspired biomaterials, the content of catechol and pyrogallol moieties in TA molecular structure is relatively high, which would endow the composite hydrogel membrane with improved adhesive strength to tissue surfaces. What is more, numerous studies have demonstrated that TA showed intriguing biological functions like anti-oxidation, anti-inflammation, and anti-microbial properties. Altogether, in view of their respective merits, we believed that MEHP could work as a novel patch to promote tendon repair. The effects of ZnO concentrations on the morphology, structure, swelling

properties, mechanical and adhesive performances as well as the biocompatibility of the MEHP were systematically investigated. The critical properties for tendon healing like anti-oxidative, anti-inflammatory, anti-bacterial and pro-healing activity of as-prepared membrane scaffold were also assessed. Then, by virtue of the diverse adhesion ability of MEHP, we fabricated a Janus dual-layer membrane by attaching MEHP to the PLLA electrospun membrane. In this system, the inner MEHP layer was designed to accelerate the intrinsic healing process and promote tendon injury repair, while outer PLLA layer was designed to serve as a physical barrier to prevent adhesion formation. Subsequently, the morphology and mechanical properties of Janus patch was explored to demonstrate the feasibility of such dual layer membrane scaffold for tendon repair. Finally, *in vivo* therapeutical efficacies including anti-adhesion, anti-inflammation and pro-tendon healing were investigated by implantation of the Janus patch to tendon injury site.

Objectives of this chapter include:

1. To prepare the MEHP and characterize its morphology, chemical composition, swelling, adhesive and mechanical performances
2. To systematically assess the *in vitro* biological functions of prepared MEHP including biocompatibility, anti-oxidation, anti-inflammation and anti-bacterial performances.
3. To construct the Janus patch and characterize its mechanical properties and stability in PBS.
4. To examine the *in vivo* therapeutical effects of Janus patch for tendon regeneration including gross observation/evaluation, H&E staining, Masson staining of the repaired tendon, immunochemical stanning and qRT-PCR analysis of the regenerated tendon tissue.

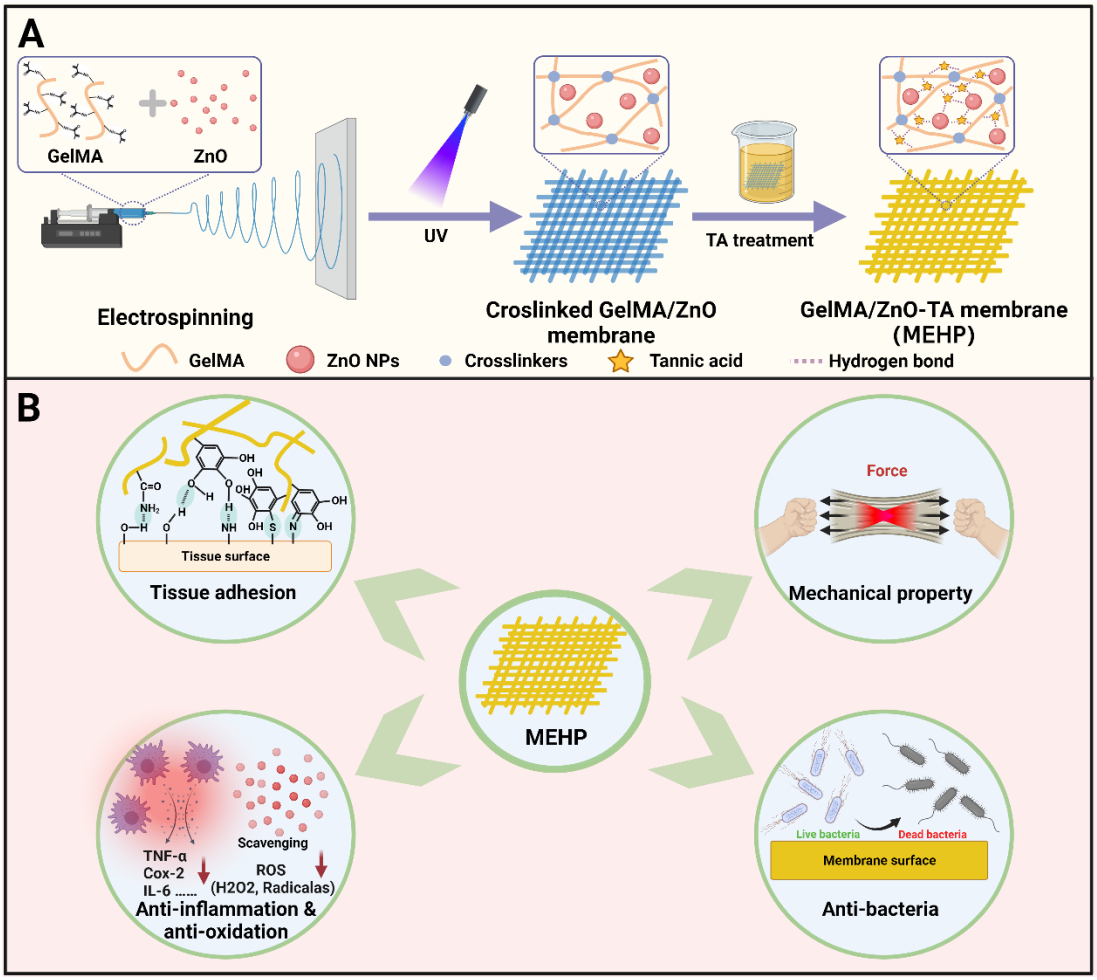

Figure 3-1. Schematic demonstrating the (A) preparation process of MEHP (i.e., GelMA/ZnO-TA electrospun membrane) with (B) multi-functions including superior tissue adhesion, mechanical properties, anti-inflammation, anti-oxidation and anti-bacteria for tendon repair. Figure created with BioRender.com.

3.2 Methodology

3.2.1 Materials

Gelatin type A, TA, ZnO NPs (<100 nm particle size), and methacrylic anhydride were purchased from Sigma Aldrich, Hong Kong.

3.2.2 Preparation of the MEHP

Firstly, GelMA was synthesized following the protocol described in 2.2.2 section. To prepare the TA-reinforced ZnO NP-loaded GelMA electrospun hydrogel membrane, we firstly fabricate the ZnO-loaded GelMA nanofibrous membrane by blending

electrospinning. Briefly, ZnO nanoparticles were accurately weighed (0, 0.005, 0.01, 0.025, 0.05 g) and completely dispersed in the 5 mL HFIP solution through ultrasonication for 45 min (avoid light). A known quantity of GelMA was then added to the above dispersions and stirred magnetically under 60 °C until the GelMA was completely dissolved (avoid light). The final concentration of GelMA was fixed at 10% w/v. For example, a 5 mL electrospun precursor solution was prepared with 0.5 g GelMA and 0.00025g, 0.005 g, 0.010g, 0.025g and 0.05 g ZnO, with weight ratio of ZnO to GelMA at 0.5% (G/0.5Z), 1%(G/1Z), 2%(G/2Z), 5%(G/5Z), and 10%(G/10Z) w/w, respectively. The detailed electrospinning parameters: The voltage was fixed at 15 kV, the distance between injector and collector was 20 cm, and the flow rate of injector was 1 mL/h. Subsequently, we prepared the photo-crosslinking solution by dissolving 5% (w/v) photoinitiator Irgacure 2959 (Sigma-Aldrich) in ethanol. Uncrosslinked GelMA/ZnO membranes were immersed in the photo-crosslinking solution for 2 h and exposed to UV light at 10 cm working distance for 40 min. Then, the crosslinked membranes were then subject to deionized water or absolute ethanol to remove excess photo-initiator followed by drying the membranes under vacuum oven. Next, we prepared 30% w/w TA aqueous solution and immersed the GelMA/ZnO membranes in the TA solution for 24 h. Finally, the TA-reinforced ZnO NP-loaded GelMA electrospun membranes (i.e., MEHP) were washed repeatedly to remove the free TA molecules followed by drying under vacuum oven for 24 h for subsequent *in vitro* experiment.

3.2.3 Characterization of the MEHP

3.2.3.1 Physical characterization of the MEHP

We firstly characterized the morphology of ZnO nanoparticle, and ZnO-loaded GelMA fibers by TEM (Tecnai G220 S-TWINScanning, FEI, OR, USA). Besides, the diameter distribution of ZnO was analyzed by DLS (Malvern Zetasizer Nano ZS; Malvern, UK). The morphology changes before and after TA treatment were assessed using SEM (Tescan VEGA3, Czech Republic). In addition, the energy dispersive X-ray spectroscopy (EDS) were used to analyze the elementary components of the scaffolds.

The specific chemical bonding before and after TA treatment was assessed using the Fourier transform infrared (FTIR). X-ray photoelectron spectroscopy (XPS) was carried out to evaluate the surface composition of prepared scaffolds. Next, swelling ratio of the scaffolds was measured. In brief, the specimen membranes (1 cm diameter) of different groups were incubated in a tube containing 2 mL of PBS (pH=7.4) at 37 °C for 24 h. Then, the samples were taken out and wiped with paper to eliminate remaining water. The weight of wet samples was recorded as the W_w. Then, the samples were freeze-dried, and the weight was recorded as W_d. The swelling ratio were measured following the Equation: swelling ratio = W_w / W_d × 100%.

3.2.3.2 Tissue adhesion performance assessment

We then evaluated the adhesion strength of MEHP by burst pressure test based on the ASTM F2392-04 standard protocol [62]. Briefly, porcine sausage skin membranes were cut into square pieces (4 × 4 cm), and rinse thoroughly to remove the excess fat onto the surface. Then, the skin membrane was fixed to a self-made measuring device, which was connected to a syringe pump filled with PBS solution. after making a 2 mm incision onto the skin membrane surface, the samples were placed onto the surface of incision for about few minutes to enable the complete attachment between materials and porcine sausage. Burst pressure was recorded as the peak pressure before loss. Next, we further measured the shear strength of the adhesive MEHP by lap shear test based on the ASTM F2255-05 standard. Firstly, the fresh porcine skins were cut to rectangular pieces (30 mm long, 5 mm wide), and cleaned thoroughly to remove the subcutaneous fats and hairs. Then, the hydrogel samples were cut into rectangular shape (20mm in length, 5mm in width) and then placed uniformly between two porcine skin tissues. After applying a 200 g external load for 2 h to enhance the bonding, the adhesion strength could be measured through a mechanical tester (Instron, US). Samples were stretched = at a constant 1 mm/min at room temperature until separated. Adhesion strength = the maximum load (force) / the overlapping contact area of porcine skins.

3.2.3.3 Mechanical performance evaluation

Uniaxial tensile tests were performed to analyze the mechanical performances of the MEHP using a mechanical tester (Instron, US) [62]. Briefly, as-prepared MEHP were soaked in sterile de-ionized water for 24 h and then cut into 50 mm×10 mm rectangular samples. Then, we measured the thickness of each sample 3 times using a micrometer (Syntek, China) and fixed them to the instrument by pneumatic clamps. To obtain the stress-stain curve, the samples were subsequently stretched longitudinally at 5 mm/min until failure (n=4).

3.2.4 Biocompatibility assessment

BMSCs are the most studied and characterized cell types for tendon repair. In this study, BMSC was used as the model cell to evaluate the biocompatibility of MEHP [62]. Firstly, we assessed the viability of BMSCs by live/dead staining. Briefly, samples were cut into disk pieces (diameter=10 mm) and pre-soaked in the medium for at least 24 h prior to cell seeding. Then, BMSCs were seeded at cell density of 1×10^4 cells/cm^2 and incubated with samples for 24, 48 and 72 h. At each time point, the cell was stained with calcein-AM/ EthD-1 for 20 min and observed under a fluorescence microscope. The results were expressed by the ratio of the live cells to total cells processed via ImageJ software. The cell proliferation of BMSCs after different treatments for 1 and 3 days was revealed by CCK-8 analysis, following the manufacturer's protocols. The cells cultured with the pure GelMA was used as the control group. In brief, CCK-8 solution was added at a 10% volume of culture medium. After 4-h treatment, the absorbance at 450 nm was measured via a microplate reader.

3.2.5 Anti-oxidation assessment

To evaluate the anti-oxidative ability of the as prepared MEHP, we firstly assessed the *in vitro* H_2O_2 scavenging capacity measured by Hydrogen Peroxide Assay Kit (Beyotime Biotechnology, Beijing, China) [86, 87]. Briefly, 75 mg of sample was added to 1 mL H_2O_2 solution (100 uM). After incubation for 20, 60, 100, and 120 min, 50 μL of each sample was added together with another 50 μL of master mix containing horseradish peroxidase and red peroxidase substrate. After 30-min incubation sheltered

from light, the fluorescence intensity at excitation/emission wavelength of 540/590 nm was measured, which was proportionate to the H_2O_2 concentration. Besides, we investigated the extracellular ROS scavenging effect of MEHP. Briefly, after seeding the BMSCs in a 24-well plate at cell density of 1×10^5 cells/cm^2 for overnight, the culture medium was replaced with 1 mL of fresh MEM-α (control group), MEM-α containing 100 uM H_2O_2 (positive group), and MEM-α containing 100 uM H_2O_2 added with different material samples. After continuous culture for 24 h, the culture medium was collected and centrifuged at 3000 rpm for 20 min. Amplex® Red ROS assay was then performed to quantify the whole ROS level in the medium. Furthermore, we explored the cellular ROS scavenging activity of the scaffolds by 2'-7'dichlorofluorescin diacetate (DCFH-DA) assay. After seeding the BMSCs in a 24-well plate at cell density of 1×10^5 cells/cm^2 and culturing for overnight, different samples were added into each well and continuously incubated for another 6 h. Next, after treated with 100 uM H_2O_2 at 37 °C for 45 min, cells were rinsed and the culture medium was replaced using fresh medium containing 25 mM of DCF-DA. After 45-min incubation under dark conditions at 37°C, cells were washed with PBS, and fixed by 2.5% paraformaldehyde. The samples were then observed using a fluorescence microscope (Nikon, Japan). The mean cell fluorescence intensity was determined by using ImageJ software. At last, we also examined the ability of scaffolds to maintain cell viabilities against the ROS environment. In brief, after seeding the BMSCs in a 24-well plate at cell density of 1×10^5 cells/cm^2 and culturing for overnight, different samples was added and continuously cultured for another 12 h. Then, cells were treated with 100 uM H_2O_2 for 45 min at 37 °C followed by washing with PBS and replacement of medium with fresh culture medium. After incubation for 6 and 24h, CCK-8 solution was added to each well at a 10% volume of culture medium. After 4 h, the sample absorbance at 450 nm was measured by a microplate reader (Thermo-Fisher Scientific, Hong Kong).

3.2.6 Anti-inflammation and anti-bacterial assessment

RAW 264.7 cells have been commonly used for anti-inflammation test in bone and

tendon research. Here, we selected RAW 264.7 cells as model cells and evaluated the *in vitro* anti-inflammatory effects of different scaffold formulations by measuring the expression of pro-inflammatory factors including tumor necrosis factor alpha (TNF-α), cyclooxygenase-2 (Cox-2) and Interleukin 6 (IL-6) by RAW 264.7 cells treated with lipopolysaccharide (LPS, Sigma-Aldrich, Hong Kong) [87]. RAW 264.7 cells were the gift from group of Dr. Chunyi Wen. In brief, RAW 264.7 cells (1×10^5 cells/cm^2) were seeded in 24-well plates and treated with different scaffolds for 24 h. Subsequently, LPS (1 μg/mL) was added to induce inflammation. After culture for 3 days, the cells were collected, and Total RNA Kit (Omega, Hong Kong) was used to extract the total RNA. The $2^{-\Delta\Delta CT}$ method was used to quantitatively evaluate the gene expression, and the GAPDH was used as an internal control. The primer sequences were showed in the following **Table 3-1**.

Table 3-1. The primer ssequences used for qRT-PCR

Genes	Sequences
TNF-α	F: GAGCATCGTAGTTGTTGGAAAT
	R: CAGGTCTACTTTGGAGTCATTG
Cox-2	F: GAAGTTGATAACCGAGTCGTTC
	R: CCATAGAATAACCCTGGTCG
IL-6	F: GAAATGATGGATGCTACCAAACTG
	R: GACTCTGGCTTTGTCTTTCTTGTT
GAPDH	F: AGGAGCGAGACCCCACTAACA
	R: AGGGGGGCTAAGCAGTTGGT

Subsequently, we assessed the anti-bacterial activity of different scaffolds against *Escherichia coli* (*E. coli*, ATCC 25922) by an agar disc diffusion test. Special acknowledgement and gratitude are given to Miss. Di Suo for completing the anti-bacterial experiment. Firstly, samples were cut into round pieces (Φ=10 mm) and sterilized under UV light for 4 h. Then, 100 μL bacteria suspension (about 1×10^6 CFU/mL) was evenly coated on the surface of LB agar plates followed by

placement of samples in the plate middle. After 24-h culture, the average diameter of inhibition zones was recorded using digital Vernier caliper.

3.2.7 Promoting effects on tendon healing

Since the early-stage cell localization play a critical role in tendon repair, we then evaluated the promoting effects of as-prepared scaffolds on tendon healing by measuring *in vitro* cell attachment on the scaffolds. In brief, samples were cut into disk pieces with diameter of 10 mm and pre-soaked in the medium for at least 24 h. Then, BMSCs (1×10^4 cells/cm^2) were seeded on the surface of different scaffolds. After culture for 3 days, samples were fixed using 4% paraformaldehyde for 20 min and stained with intracellular filament F-actin (phalloidin, Alexa Fluor 488, Thermo Fisher, Hong Kong) and cell nuclei (DAPI, Thermo Fisher, Hong Kong).

3.2.8 Construction and characterization of Janus patch

To prepare the Janus patch, we first fabricated the PLLA fibrous membranes via electrospinning. Briefly, PLLA precursor solution of 20% w/v was prepared by dissolving PLLA (Mw=10 kDa, Jinan Daigang Co., Jinan, China) in HFIP by magnetically stirring overnight at room temperature. Subsequently, electrospinning was performed using below parameters: 1 mL/h flow rate, 15 kV applied voltage, and 10 cm working distance. Then, Janus patch was prepared by attaching MEHP (i.e., G/2Z-TA) onto PLLA membranes. The mechanical properties of Janus patch were characterized following the protocols described in section 2.4. The interfacial stability between MEHP layer and PLLA layer was assessed by incubating Janus patch in PBS solution for 3 days and then observing using SEM.

3.2.9 Animal study design

Animal experimental procedures were approved by the Ethics Committee of PolyU and performed based on the protocols of the Institutional Animal Care and Use Committees guidelines. The animal experiments were conducted by Hualianke Biotechnology Co. LTD, Wuhan, China. A total of 48 male Sprague Dawley (SD) rats weighting 200-300g

were randomly divided into four groups: Control, PLLA, MEHP (i.e., G/2Z-TA), Janus (PLLA+G/2Z-TA). Firstly, 3% pentobarbital sodium (30 mg/kg) was intravenously injected to anesthetize the rates. After the local skin of hind foot was shaved and disinfected, a 2-cm midline incision was created at the site of Achilles tendon. Then, tendon was transected approximately 5 mm from the talocalcaneal tuberosity and sutured using a modified Kessler technique with 6-0 silk suture. Different membrane samples (0.8×1.5 cm^2), after disinfection with 75% (v/v) alcohol and ultraviolet light irradiation, were adopted to wrap around the operated tendon site. The skin wounds were then closed with a 4-0 silk suture.

3.2.10 Gross evaluation

At 3 weeks post-surgery, the inflammation, ulcer, and infection at the surgical sites were examined and documented. Then, rats were euthanized using an overdose of anesthetics, and the tendon repair sites were opened. The severity of tendon adhesion at the operated sites was macroscopically assessed using a grade 1–5 adhesion scoring system based on the surgical observations [57]. Grade 1, nearly no adhesion; Grade 2, few adhesion tissues are formed around the surgical sites, which can be separated by blunt dissection alone; Grade 3, adhesion tissues cover ≤50% of the area around the tendon, which can be separated by sharp dissection; Grade 4, adhesion tissues cover 51–97.5% of the area around the tendon, which can be separated by sharp dissection; Grade 5, adhesion tissues cover >97.5% of the area around the tendon, which can be separated only by sharp dissection. All specimens were assessed in parallel by two independent observers without knowing the experimental groups.

3.2.11 Histological analysis

The repaired tendons were harvested and fixed with 10% formalin for 24 h. After wash with PBS and dehydration with graded series of ethanol, the tendons were embedded in paraffin wax and horizontally cut into sections with 5-mm thickness using a rotary microtome. Then, sliced tissues were stained by hematoxylin and eosin (H&E) and Masson’s trichrome and observed using a microscopy (Nikon, Japan) under white light.

3.2.12 Immunohistochemical examination

The expressions of Col-1, Col-3, F4/80, and TNF-α were detected by immunohistochemical staining. Briefly, paraffin-embedded sections were dewaxed using xylene and hydrated in gradient alcohol. Then, antigen retrieval was carried out by incubating sections in a citrate buffer solution (10 mM, pH=6.0) at 37°C for 20 min. Next, 3% hydrogen peroxide was used to eliminate the activity of endogenous peroxidase, while 10% goat serum (1:100 diluted, Maixin, Fuzhou, China) was used to block unspecific antigen cross-reaction. Afterwards, sections were incubated with primary antibody against Col-1 (1:100 diluted, Bioswamp, Wuhan, China), Col-3 (1:100 diluted, Bioswamp, Wuhan, China), F4/80 (1:50 diluted, Bioswamp, Wuhan, China), and TNF-α (1:50 diluted, Bioswamp, Wuhan, China) overnight at 4°C. Subsequently, samples were incubated with anti-sheep IgG secondary antibodies (Maixin, Fuzhou, China) for 45 min at 37°C, developed in DAB solution (Dako, Germany) and counterstained with hematoxylin. Finally, the sections were observed under a microscope (Nikon, Japan) and semi-quantitatively analyzed using Image J software.

3.2.13 Gene expression of inflammatory markers

To assess the *in vivo* anti-inflammatory efficacy of our prepared patches, gene expressions of inflammatory markers including Cox-2, TNF-α, IL-6, Interleukin 1 beta (IL-1β), matrix metalloproteinase-3 (MMP-3), receptor activator of nuclear factor kappa-B ligand (RANKL) were evaluated by qRT-PCR. First, harvested tendon tissues were homogenized using TRIzol reagent (Ambion, Life Technologies). The purity and concentration of total RNA were then determined with a spectrophotometer (Nano300, Allsheng, Zhejiang, China). cDNA synthesis was conducted using PrimeScriptTM RT reagent kit (TaKaRa, Dalian, China) following the manufacturer's instructions. The corresponding primer sequences were showed in **Table 3-2**. The relative mRNA expression levels were calculated based on the $2^{-\Delta\Delta CT}$ method and GAPDH was used as an internal control.

Table 3-2. The primer ssequences used for qRT-PCR

Genes	Sequences
TNF-α	F: CCACGCTCTTCTGTCTACTG
	R: GCTACGGGCTTGTCACTC
Cox-2	F: CTTCGGGAGCACAACAGAG
	R: GCGGATGCCAGTGATAGAG
IL-6	F: TGGAGTTCCGTTTCTACCTGG
	R: GGATGGTCTTGGTCCTTAGCC
IL-1β	F: GGGATGATGACGACCTGCT
	R: CCACTTGTTGGCTTATGTTCTG
MMP-3	F: CTCATCCTACCCATTGCAT
	R: GTCCAGCTTCCCTGTCATC
RANKL	F: TCGGGTTCCCATAAAGTC
	R: GAAGCAAATGTTGGCGTA
GAPDH	F: CAAGTTCAACGGCACAG
	R: CCAGTAGACTCCACGACAT

3.3 Results and discussion

3.3.1 Characterization of the MEHP

Firstly, we characterized the ZnO nanoparticles used for fabricating the electrospun nanofibrous membranes via TEM. As showed in the **Figure 3-2**, we tried two methods to prepare the samples by dispersing them in ethanol or in water. The samples in both groups were dispersed evenly and showed a uniformly spherical shape. Besides, the DLS results were in accordance with the TEM images that the diameter of ZnO nanoparticles was about 78 nm with even diameter distribution (PDI = 0.227) (**Figure 3-3**).

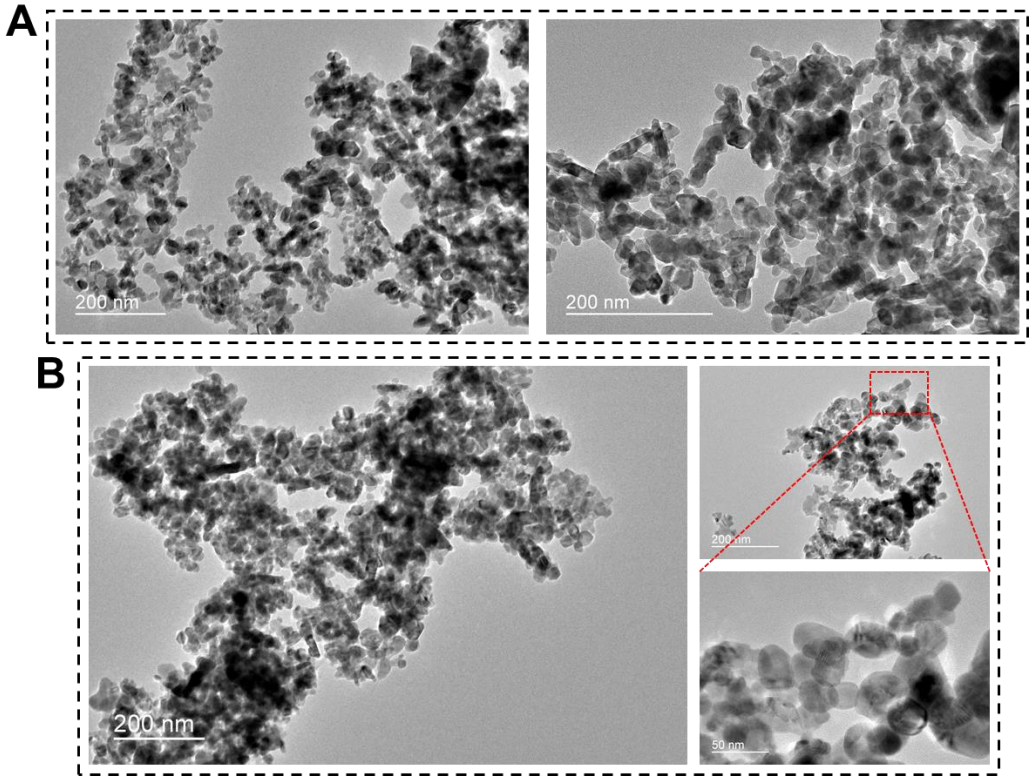

Figure 3-2. TEM images of ZnO NPs dispersed in (A) ethanol and (B) DI water.

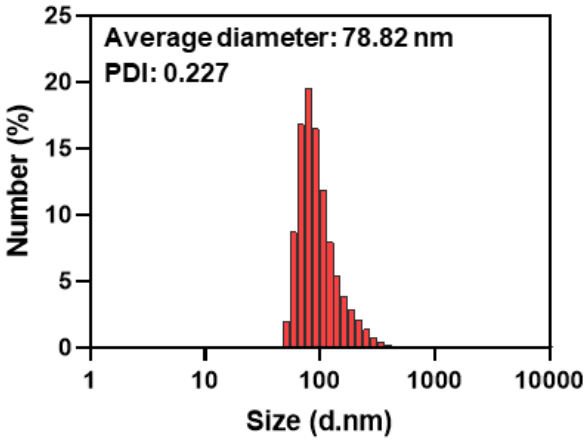

Figure 3-3. DLS analysis of ZnO NPs.

Nest, we prepared ZnO-loaded GelMA (G/Z) nanofibrous membranes fabricated by blending electrospinning of ZnO and GelMA. We characterized their morphology by TEM and aimed to observe the ZnO distribution in the GelMA fibers. On the first try, although we could find the ZnO NPs were evenly distributed in the fibers, the quality of TEM images was relatively low (**Figure 3-4**). Thus, we reperformed the experiments. In the second try, all groups showed a fibrous architecture and possessed a uniform

diameter. In addition, the ZnO was distributed in the fibers evenly without significant aggregation, which suggested the feasibility of blending electrospinning to prepare the nanofibrous membranes.

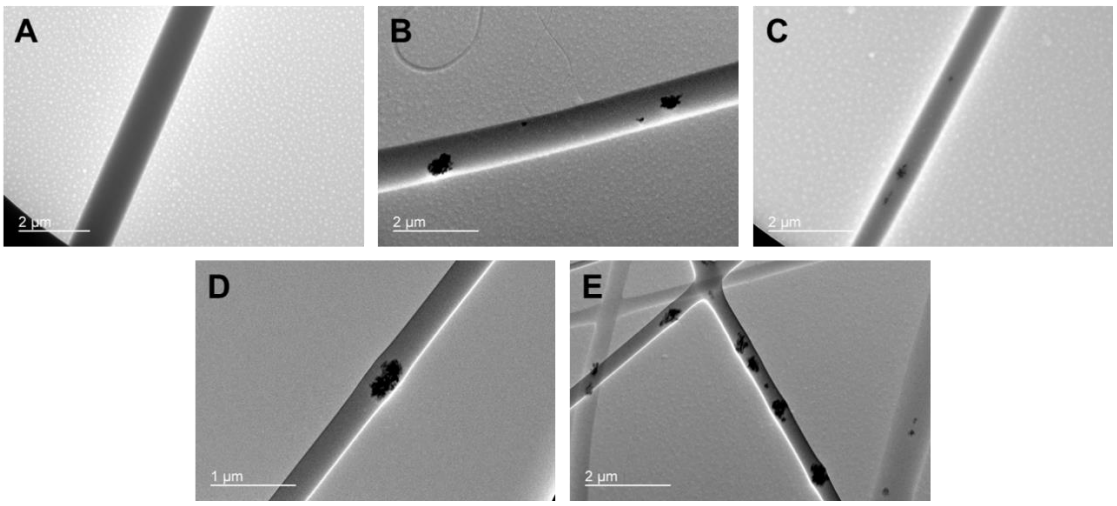

Figure 3-4. TEM images of GelMA electrospun membranes containing (A) 0 wt. %, (B) 1 wt. %, (C) 2 wt. %, (D) 5 wt. %, and (E) 10 wt. % of ZnO nanoparticles.

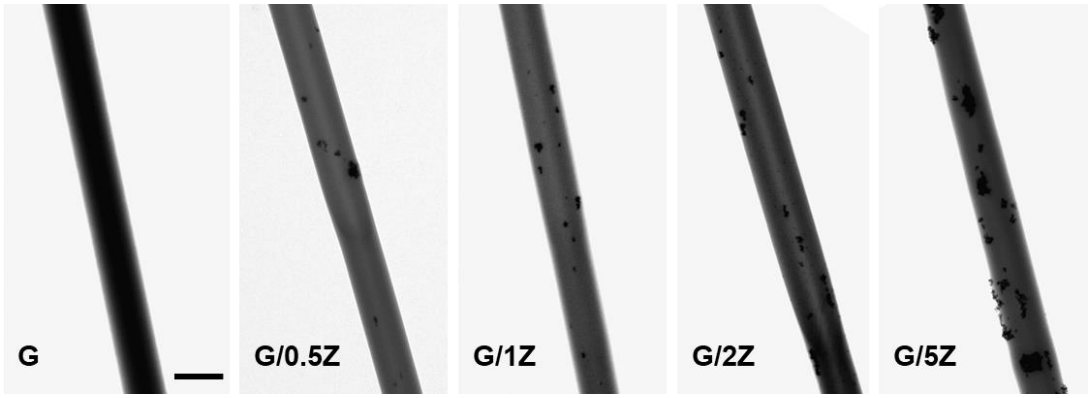

Figure 3-5. Representative TEM images of GelMA electrospun membranes containing different contents of ZnO nanoparticles. Scale bar = 1 μm.

Subsequently, to further enhance the mechanical and adhesive performances of the G/Z electrospun membrane, and endow them with multifunctionality, we incubated the G/Z electrospun membrane in the TA solution for 24 h. To this end, we first crosslinked G/2Z by incubation in PI2959-containing ethanol and irradiation under UV light for 20

min (**Figure 3-6(A) and (B)**). After wash with water and incubation in TA solution for 1 day, we could finally obtain the MEHP (**Figure 3-6(C)**). However, the samples showed the gum-like materials instead of membrane-like scaffolds. After analysis, we thought the significant swelling for G/Z during water wash process may affect the final shape (**Figure 3-7**).

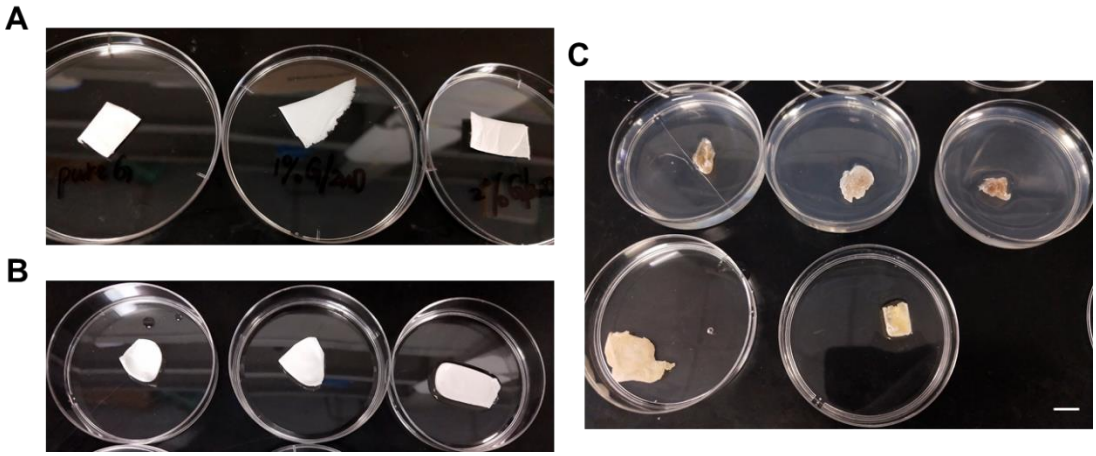

Figure 3-6. The preparation process of MEHP. (A) The resultant electrospun membranes were firstly (B) crosslinked under UV for 20 min, and then washed with DI water before (C) incubation in TA solution for 1 days. Scale bar = 1 cm.

Figure 3-7. The swollen membranes by washing the membranes with DI water after photocrosslinking. Scale bar = 1 cm.

In the following preparation process of MEHP, we tried to use ethanol to wash the samples without involving any water. After incubation in TA solution for 24 h, we did

get the membrane hydrogel scaffolds despite obvious volume shrinkage (**Figure 3-8**). Surprisingly, TA could directly crosslink the membranes and maintain their shape by strong hydrogen bond interaction even incubated in DI water for 1 day. By observing the solution changes after incubation of membranes for 1 days, we found the TA solution became darker brown with increase of ZnO concentration, indicating that the oxidation of TA by ZnO particles (catechol groups to quinone).

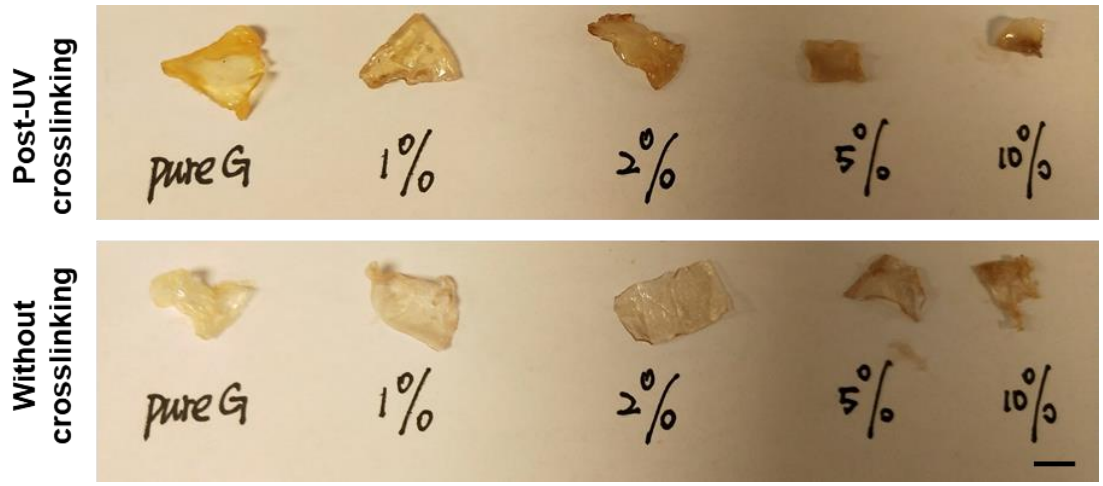

Figure 3-8. The membranes with or without UV crosslinking after TA treatment for 24 h. Scale bar = 1 cm.

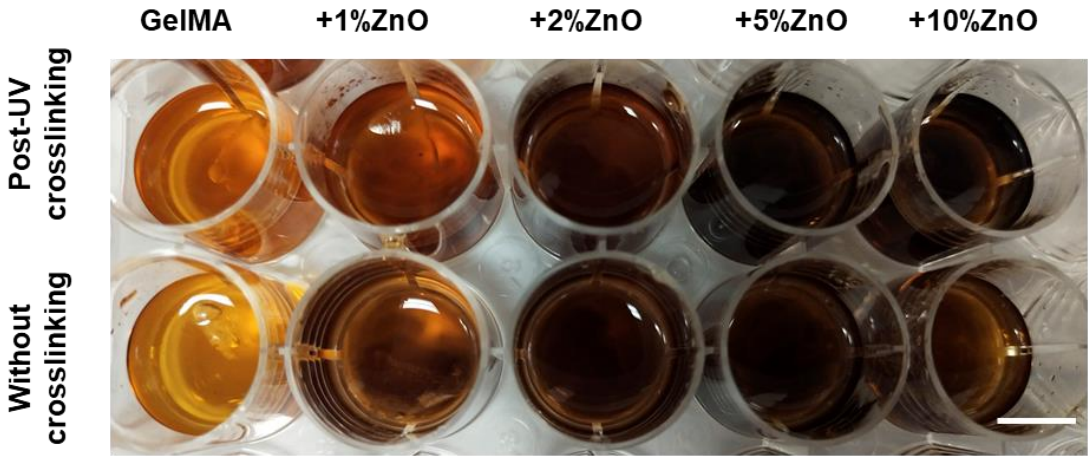

Figure 3-9. The solution changes after incubation of membranes in TA solution for 2 days. Scale bar = 1 cm.

Next, we performed a series of experiments to characterize the membrane scaffolds.

First, we observed the morphology of G/Z electrospun membrane before TA treatment using SEM. As displayed in the **Figure 3-10**, all groups showed a fibrous morphology before and after crosslinked in ethanol under UV light, and their diameters were similar. Then, we characterized the fiber diameters of samples after TA treatment. It could be found that ZnO-containing samples exhibited no fiber morphology and there was a dense layer formed onto the sample surface after TA treatment (**Figure 3-11**). We guessed such phenomenon might be attributed to problem of operation, fabrication process, freeze drying that lead to the sample failure. Thus, we performed this experiment again.

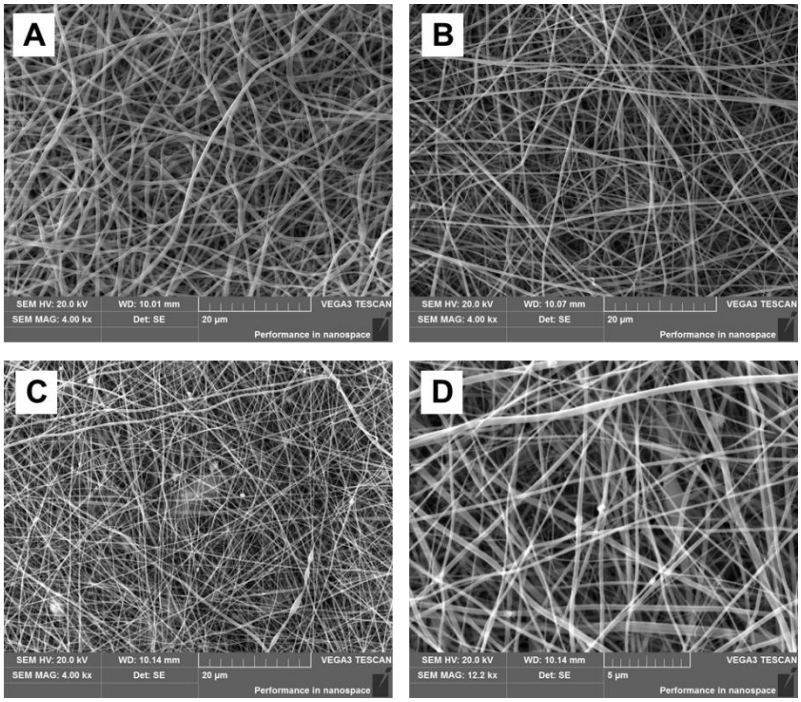

Figure 3-10. SEM images of (A) crosslinked and (B) uncrosslinked GelMA membranes and (C) crosslinked and (D) uncrosslinked G/2Z.

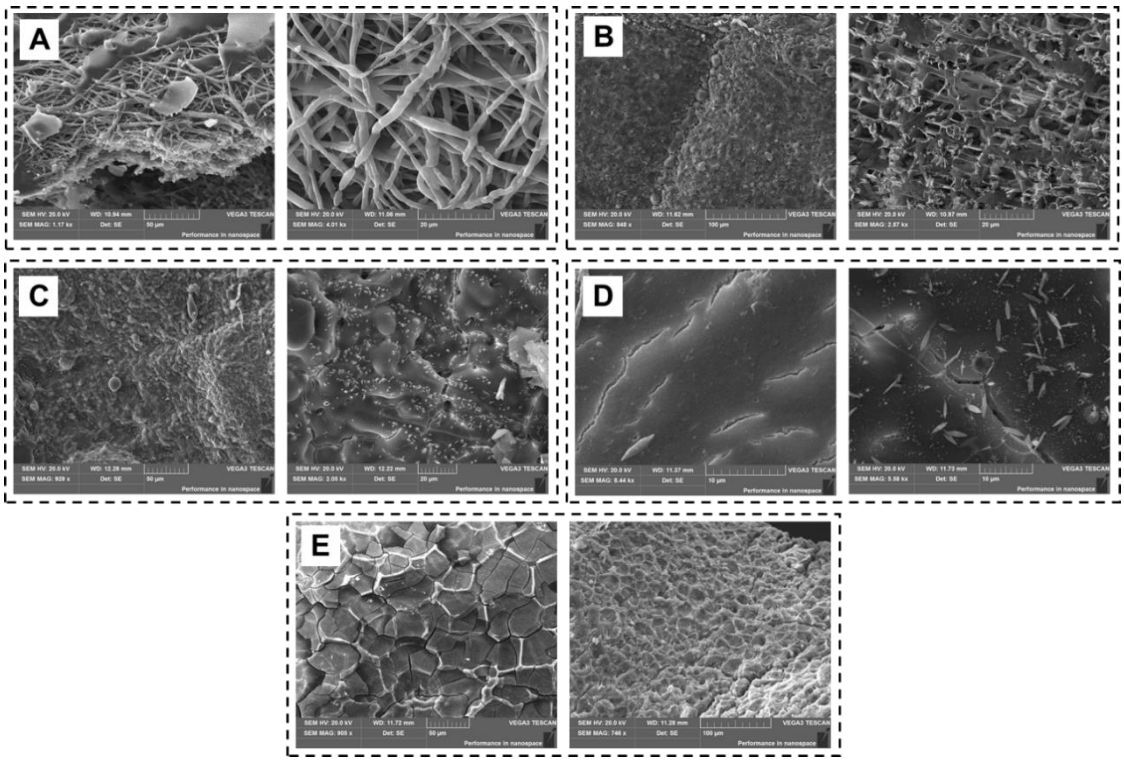

Figure 3-11. SEM images of (A) G-TA, (B) G/1Z-TA, (C) G/2Z-TA, (D) G/5Z-TA, and (E) G/10Z-TA.

To maintain fibrous shape stability after TA treatment, we further enhance the crosslinking strength by increasing photo-initiator concentrations and prolonging the UV irradiation time. As illustrated in the **Figure 3-12**, the resultant membranes exhibited a high mechanical strength as compared with our previously prepared membranes. Then, we explored the effects of ZnO contents and TA concentrations on the shape of resultant membranes (**Figure 3-13**). We found membranes was secondly crosslinked by TA, and there were some color changes in the TA solutions containing ZnO, and the color became darker with the increase of ZnO concentration in GelMA (like report before). However, the membrane (G/10Z) may be destroyed after TA (60 and 100 w/v %) treatment. This may be attributed to the partial dissolution of ZnO, which may cause structural collapse of fiber. Next, we used SEM to characterize the fiber morphology of the obtained membranes. As demonstrated in **Figure 3-14**, the fiber diameter of GelMA membranes is significantly increased after TA treatment. Besides, there seem to be a TA membrane formed between the different fibers that

integrate the fibers together. In addition, there are some particles adhered on the fiber surface that may be the PI 2959. For the ZnO-containing samples, a thin layer (i.e., film) will be formed between fibers and the membrane surface. The thickness and morphology of the membrane will be significantly changed with the increase of ZnO concentrations and TA concentrations. The possible reasons we speculated were: Firstly, the TA was oxidated by ZnO (we can see the color change in the TA solution after incubation) and formed a thin layer by self-polymerization; Then, oxidated TA can crosslink with GelMA via chemical interaction (Schiff base reaction between NH2- of gelatin backbone and carbonyl groups of oxidated TA) and physical interaction (hydrogen bonds); The thickness and morphology of layer can be controlled by ZnO and TA concentrations. In terms of these results, we selected the 30 wt. % TA solution to prepare the multi-functional membranes due to the favorable fibrous morphology after TA treatment.

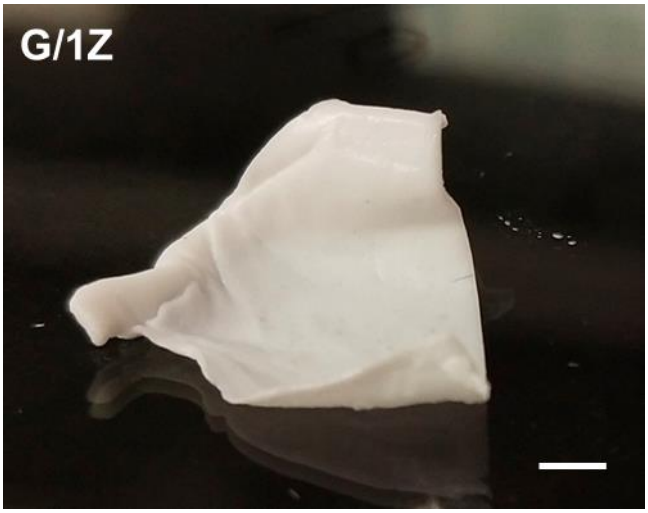

Figure 3-12. Crosslinked G/1Z after incubated in PI-2959-containing ethanol (10 w/v %) for overnight and crosslinked under UV light for 1 h and then washed with ethanol for three times. Scale bar = 1 cm.

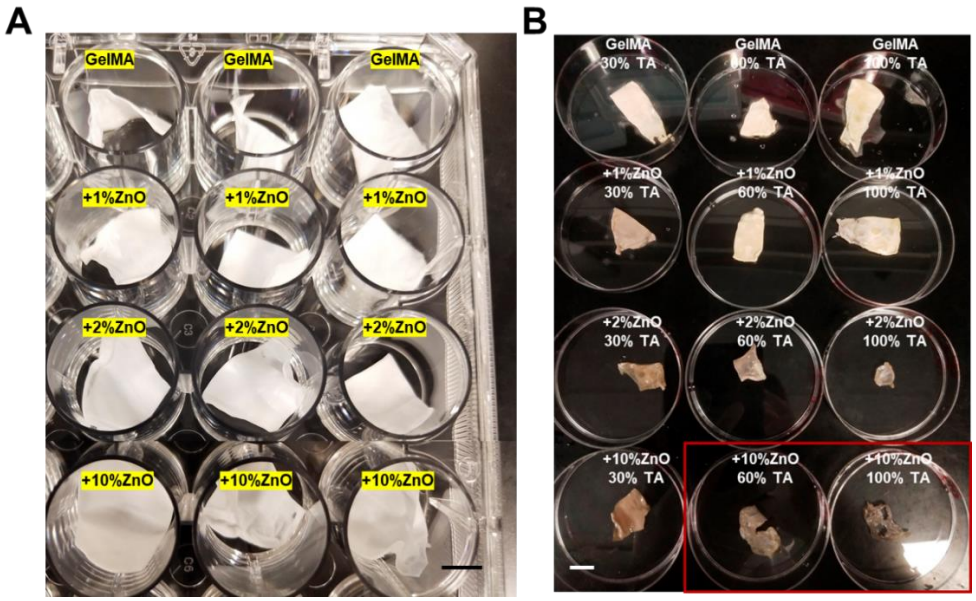

Figure 3-13. The parameter optimization of multi-functional membranes by changing the ZnO contents and TA concentrations (A) before and (B) after TA treatment for 24 h. Scale bar = 1 cm.

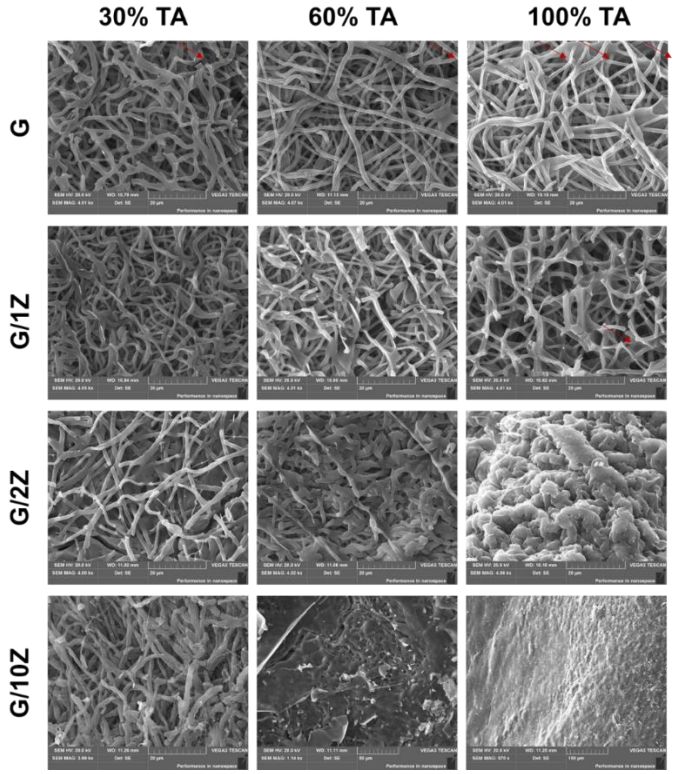

Figure 3-14. SEM images of different samples (G, G/1Z, G/2Z, G/10Z) after treatment with different concentrations of TA solutions (30, 60, and 100 wt. %).

After optimization of preparation process, we reperformed SEM to characterize the morphology of the MEHP. As showed in **Figure 3-15**, there was no significant difference in fiber diameters of different samples without TA treatment. However, the fiber diameter was significantly increased after TA treatment. In addition, the fiber diameter was higher in the sample with higher ZnO content (possible due to different swelling ability, which was demonstrated in the following part). Notably, the fiber morphology almost disappeared in the G/5Z group, indicating its structure destruction after incubation in TA. Altogether, TA-reinforced ZnO-loaded GelMA electrospun membrane (i.e., G/Z-TA or MEHP) showed a fibrous architecture, which resembled the native ECM structure facilitating nutrition/waste transportation, while could serve as a suitable 3D niche for the cell growth and proliferation.

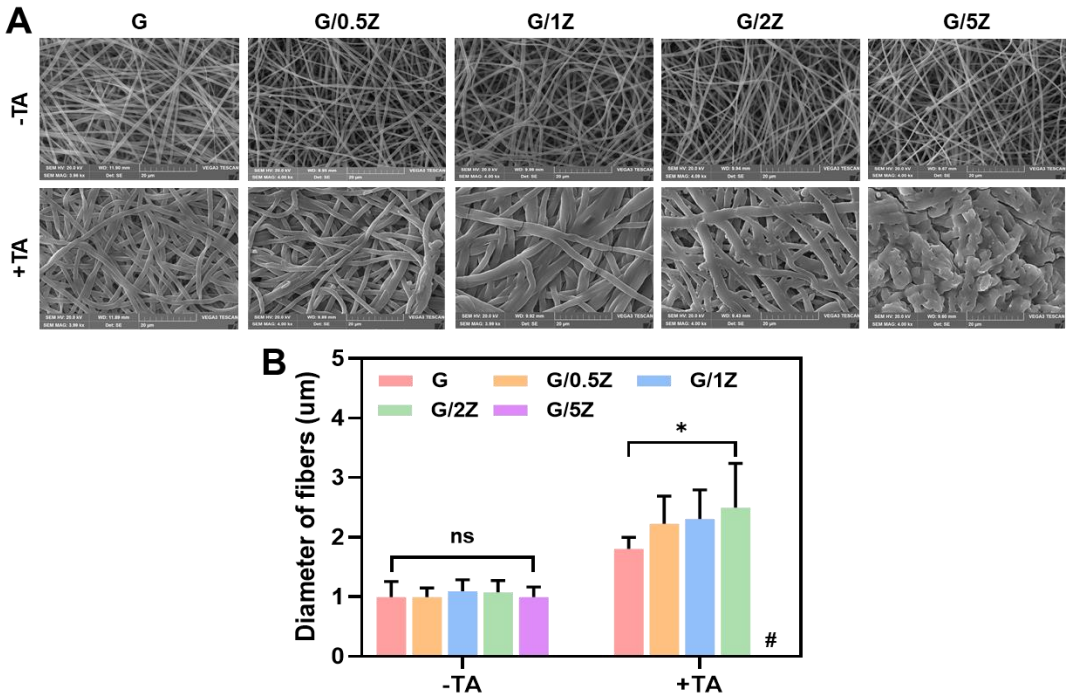

Figure 3-15. Morphology of MEHP before and after TA treatment for 24 h. (A) Representative SEM images of different electrospun membranes. (B) Fiber diameter calculated based on SEM images. G means GelMA, G/0.5Z, G/1Z, G/2Z and G/5Z indicate GelMA added with 0.5%, 1%, 2% and 5% ZnO nanoparticles, respectively. # indicated the failure to measure the fiber diameter of G/5Z-TA group.

We further used the EDS to analyze the elementary components of the prepared MEHP. Firstly, we used EDS mapping to analyze element composition of the resultant membranes. As showed in the **Figure 3-16**, we can see Zn was distributed onto the membrane, indicating the successful incorporation of ZnO. However, it was difficult to observe Zn distributed along the fibers. Later, we also performed EDS spectrum analysis to evaluate element content. The results showed that the MEHP was mainly composed of the elements carbon, nitrogen, oxygen and zinc (**Figure 3-17**). Besides, compared with EDS spectrums of G and G+TA, there was a significant Zn signal peak in the G/2Z and G/2Z+TA, indicating the successful ZnO incorporation. At the same time, compared with the G and G/2Z groups, the C and O contents were significantly increased in G/TA and G/2Z+TA, suggesting the successful TA modification. Additionally, we performed the FTIR test to evaluate the chemical structure of MEHP (**Figure 3-18**). A typical wave appeared at around 3100-3600 cm^{-1} in the spectra of TA-containing groups. This may be due to the formation of hydrogen bonds that caused the peak wavenumber shift of amine N-H and galloyl O-H. In addition, the characteristic peak of TA at around 1716 cm^{-1} was observed in the GelMA-TA and G/2Z-TA, indicating the successful modification of scaffolds with TA. Besides, we also analyzed the membranes with different ZnO contents and TA concentrations by FTIR (**Figure 3-19**). We found that there was no significance difference among the FTIR spectrums of GelMA containing different ZnO contents. In addition, there also no significance difference among the FTIR spectrums of GelMA/ZnO after TA treatment at different concentrations. Since the incorporation of ZnO did not cause a remarkable shift of the characteristic bands, we additionally performed XPS to evaluate the presence of ZnO in the fibers. As displayed in the **Figure 3-20**, a significant Zn 2p peak at 1020-1043 eV appeared in the XPS spectra of G/2Z-TA electrospun membranes, suggesting that ZnO was successfully incorporated into the nanofibrous system. In a word, these results demonstrated that MEHP could be successfully prepared by blending electrospinning and subsequent TA immersion.

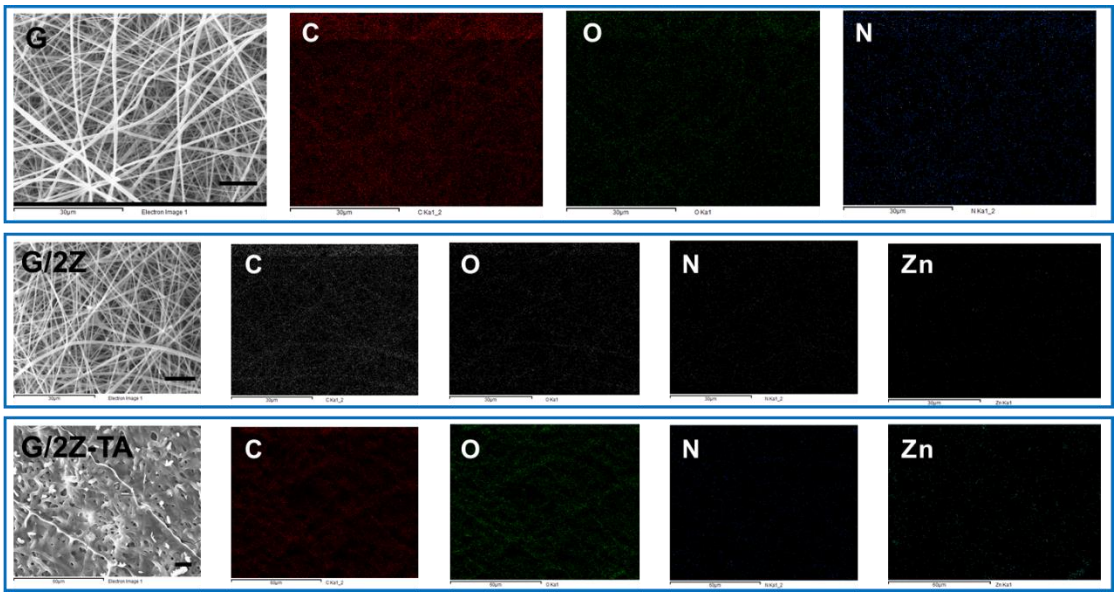

Figure 3-16. EDS mapping of the elementary components of the G and G/2Z before and after TA treatment. Scale bar = 10 μm.

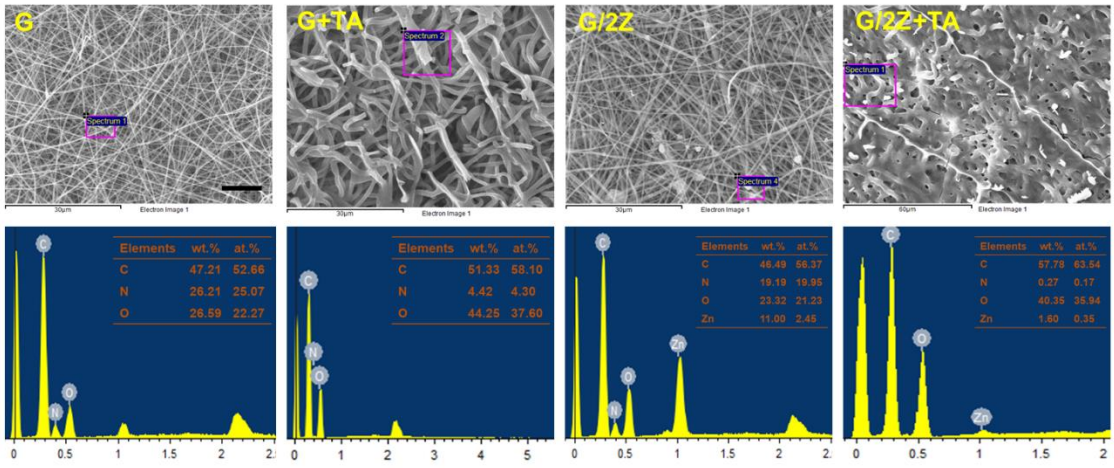

Figure 3-17. EDS analysis of the elementary components of the G and G/2Z before and after TA treatment. G means GelMA and G/2Z indicate GelMA added with 2% ZnO nanoparticles.

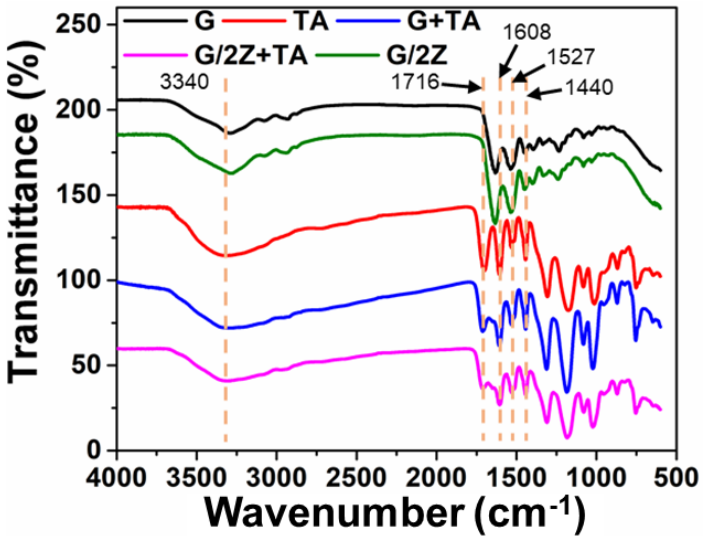

Figure 3-18. The chemical component analysis of different material formulations by FTIR. G means GelMA and G/2Z indicates GelMA added with 2% ZnO nanoparticles.

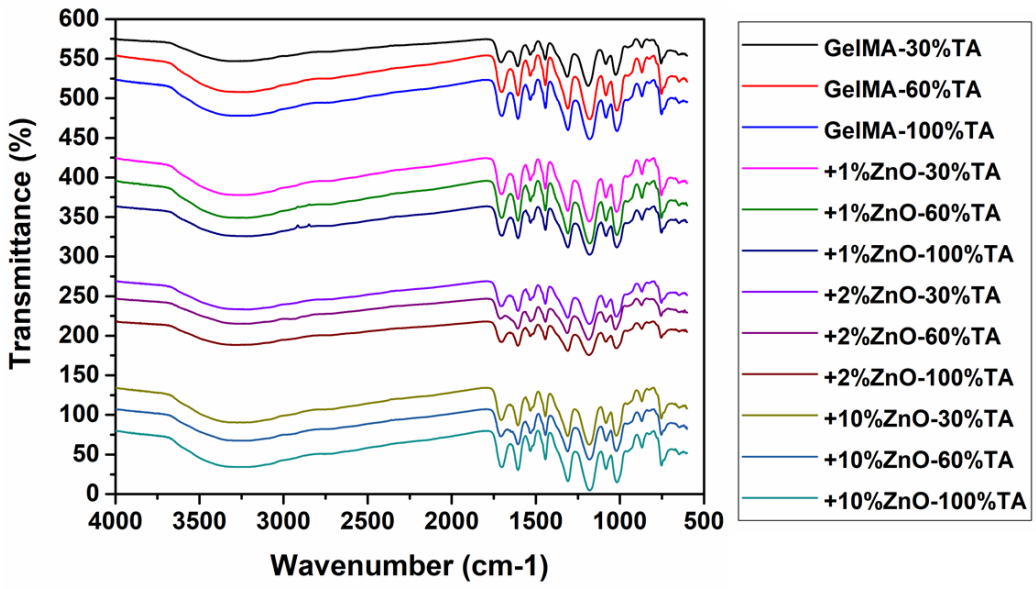

Figure 3-19. FTIR of GelMA containing different concentrations of ZnO (0, 1, 2, 10 w/w %) after TA treatment (30, 60 and 100 w/v %)

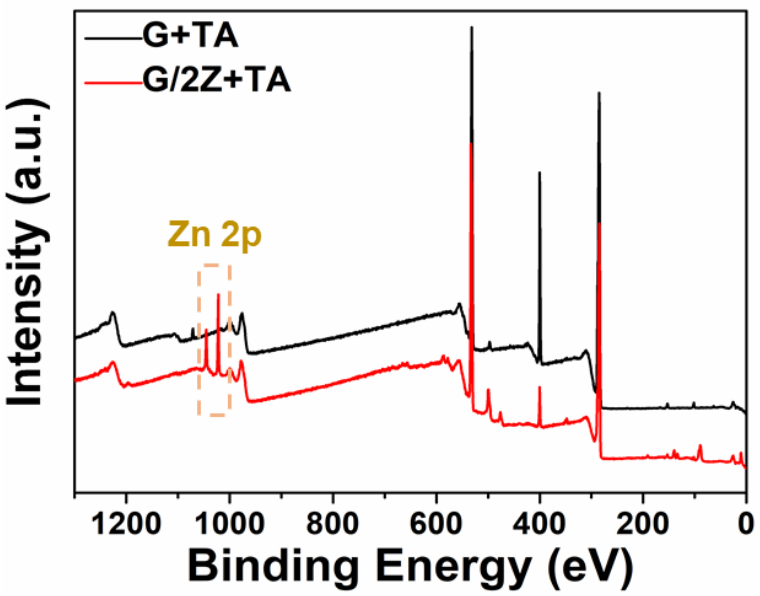

Figure 3-20. The chemical component analysis of different material formulations by XPS. G means GelMA and G/2Z indicates GelMA added with 2% ZnO nanoparticles.

Next, we evaluated the stability of MEHP in different pH or urea condition. In the **Figure 3-21** and **Figure 3-22**, when incubated in basic environment and urea condition, the membranes were destroyed. The membranes were relatively stable under acid and neutral environment. Besides, the membranes became gelatinous hydrogels under alkaline condition, and its mechanical properties were decreased with ZnO concentration, indicating the breakdown of hydrogen bond and following oxidation of TA. Furthermore, we found the color of incubation media became darker in the basic environment. The higher content of ZnO in PLLA fibers, the darker color the incubation media, which might be due to the easier oxidation in basic environment for TA. Besides, we also observed the change of incubation media by taking out the samples (**Figure 3-23**). Many ZnO nanoparticles were leaked from fibrous membranes after incubation in the urea solution, which may be caused by the destroy of hydrogen bond. This result further confirmed the hydrogen bond formation in MEHP.

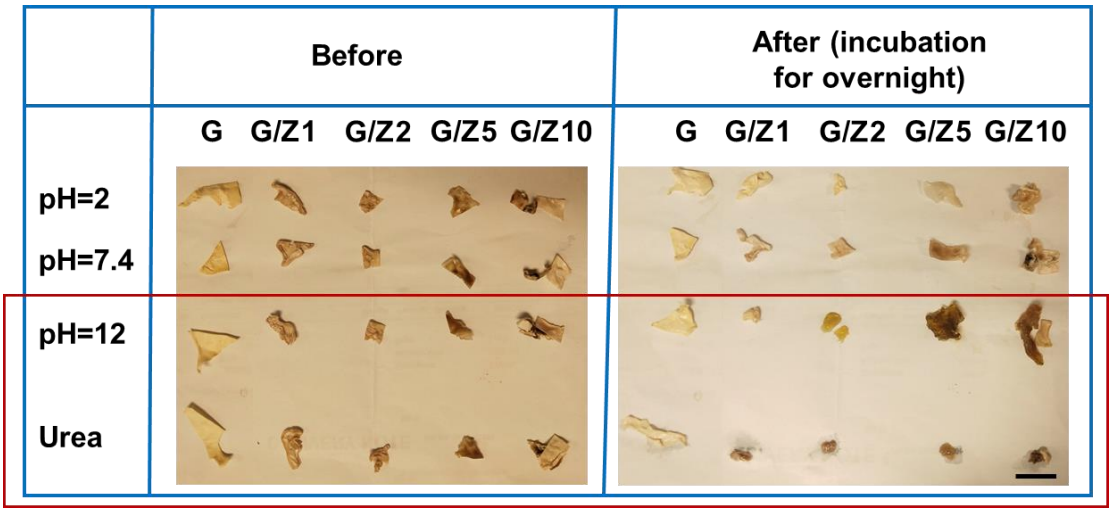

Figure 3-21. The stability of electrospun GelMA/ZnO membranes in different pH environment. Scale bar = 1 cm.

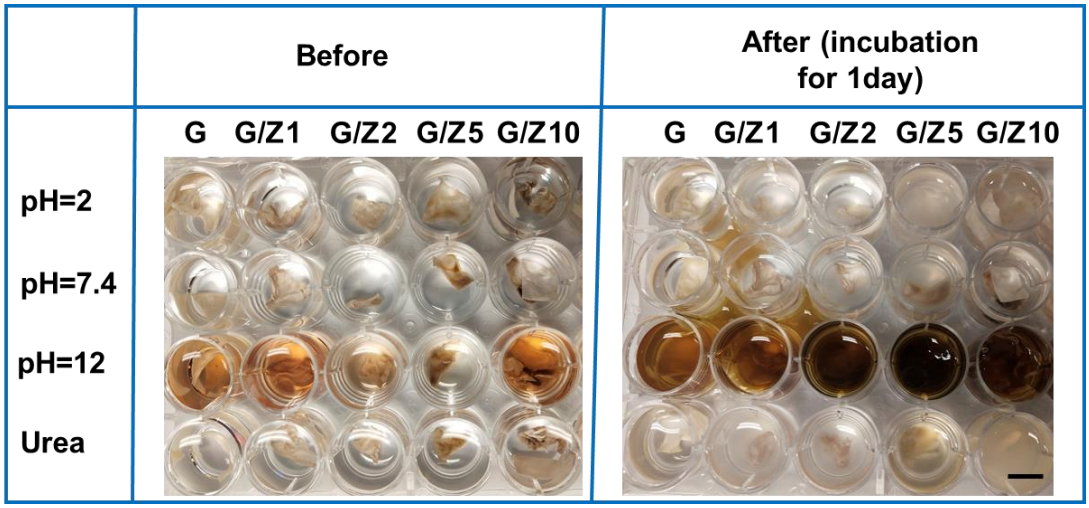

Figure 3-22. The stability of electrospun GelMA/ZnO membranes in urea condition. Scale bar = 1 cm.

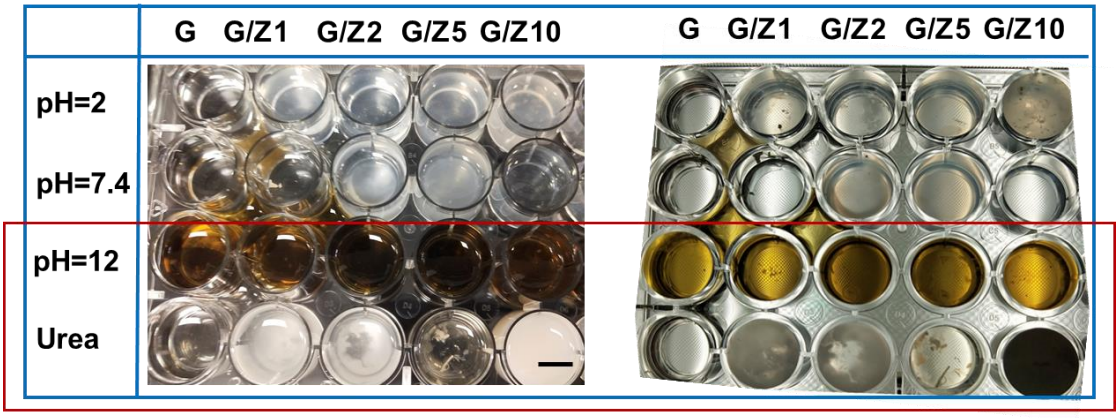

Figure 3-23. The incubation media change after removal of samples. Scale bar = 1 cm.

The swelling properties significantly influence the outcomes of biological functions and *in vivo* applications. As a *in vivo* implant for tendon injury healing, it should possess low swelling index, since high swelling ratio may produce compression to surrounding tissues, which may aggravate ischemia and impact healing process. Thus, the swelling properties of different electrospun membranes were assessed. As showed in the **Figure 3-24**, membranes without TA treatment displayed high swelling ability, and such swelling behavior was enhanced with increase of ZnO content in GelMA. Besides, we found with TA concentration increased, the swelling ratio was significantly decreased, indicating formation of stronger and much more hydrogen bonding in higher TA concentration microenvironment. By optimization, we reperformed the swelling test. We found G and G/Z possessed high swelling ratio (**Figure 3-25**). Among them, the G/5Z showed a maximum swelling ratio reaching 3400 %. Besides, we found that the swelling properties were enhanced with increase of the ZnO contents in the membranes, which may be attributed to the hydrophilic nature of ZnO NPs. However, after TA treatment, the swelling property was markedly decreased. Even for the G/5Z-TA group, its swelling ratio was only 600%. The possible reasons for such phenomenon may be the formation of strong hydrogen bonds by TA molecules in the G/ZnO composite network. In addition, since the G/Z membrane had a high swelling ratio, when we incubated the dry G/Z membrane into the TA solution, TA molecule could enter the network of G/Z membrane rapidly, and reinforce the membrane by introduction of a secondary network. We also observed the changes of incubation media after swelling test (**Figure 3-26**). It could be found that the solution after incubation of ZnO-containing samples for 24 h became turbid. The solution became more turbid with increase of ZnO content in samples. However, solution became clearer after treatment with higher concentrations of TA, indicating TA could act as a barrier to prolong the ZnO release. Taken together, these results verified that TA could serve as a cross-linkage to network of G/Z membrane to prevent polymer network from further swelling.

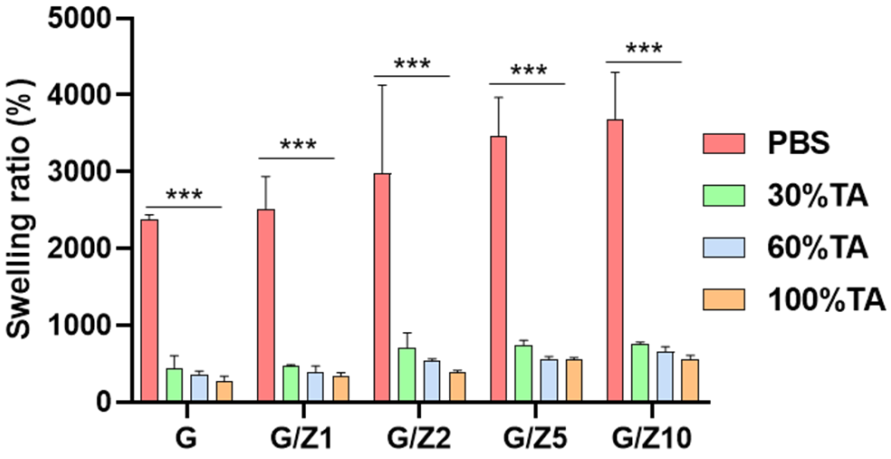

Figure 3-24. Swelling properties of the electrospun GelMA/ZnO membranes with different TA treatment.

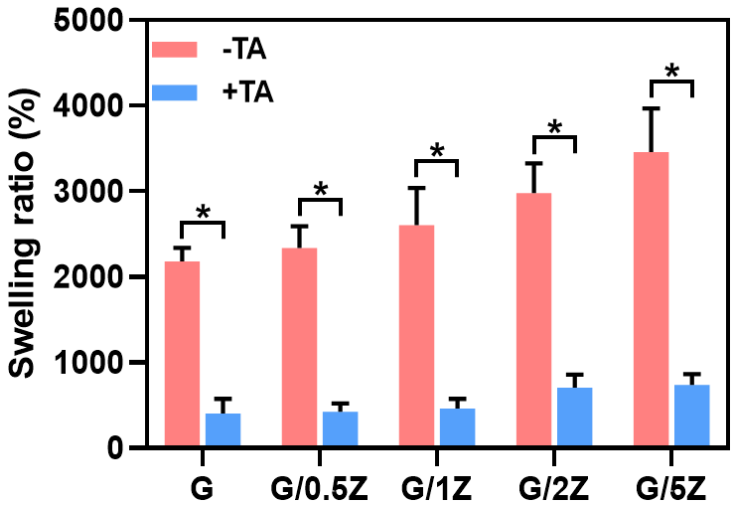

Figure 3-25. Swelling properties of the electrospun GelMA/ZnO membranes with or without TA treatment. G means GelMA, G/0.5Z, G/1Z, G/2Z and G/5Z indicate GelMA added with 0.5%, 1%, 2% and 5% ZnO nanoparticles, respectively.

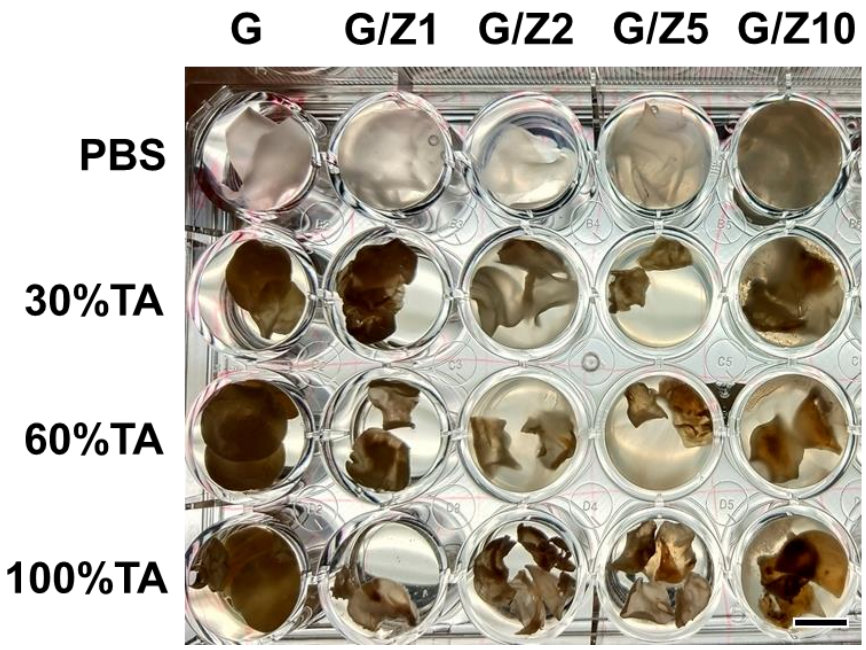

Figure 3-26. The membranes after swelling in PBS for 24 h. Scale bar = 1 cm.

3.3.2 Mechanical and adhesive strength of the MEHP

To retain structure integrity without any deformation during implantation and evade the accidental damage to surrounding tissue, the tendon-repairing patch should possess suitable mechanical properties. For this reason, tensile stress-strain measurements were performed to evaluate the mechanical performances of MEHP. As showed in the **Figure 3-27**, such membrane could adhere to finger surface tightly. When finger was bended, the membrane was still attached to its surface without significantly change or detachment, suggesting the excellent flexibility of the membranes. Subsequently, we evaluated the mechanical performances of membranes via a Instron machine. The detailed process was showed in **Figure 3-28**. On the first try, we found that sample after TA treatment showed significantly improved mechanical properties (**Figure 3-29(A)**). However, modulus was decreased after treatment with higher concentrations of TA. Due to the failure samples for G/5Z and G/10Z, we could not measure the mechanical properties for these two samples (**Figure 3-29(B)**). Thus, we tried again to detect the mechanical properties of all these samples. It was found that pure GelMA possessed low mechanical properties, while the addition of ZnO in the GelMA could further increase the mechanical performance (**Figure 3-30**). In detail, the tensile strength,

elongation at break and tensile modulus of pure GelMA were 12.89 ± 2.85 kPa, 70.53 ± 8.56 %, and 29.19 ± 3.56 kPa, respectively, while 51.26 ± 7.22 kPa, 114.39 ± 14.32 %, and 55.87 ± 5.49 kPa for G/2Z group. After TA treatment, the mechanical properties for corresponding hydrogel patches were significantly improved. For instance, the tensile strength, elongation at break and tensile modulus of G+TA were 141.98 ± 10.25 kPa, 55.47 ± 6.95 % and 620.92 ± 46.78 kPa, respectively. Compared with the pure G, the strength and modulus of sample reinforced by TA were increased by 11 and 21 times, respectively. Although such improvement in G/2Z group was not as significant as in the G group, the tensile strength, elongation at break and tensile modulus for G/2Z were still increased by 9, 1.7 and 4.3 times, respectively, as compared to the samples before TA treatment. Altogether, these results showed that the TA reinforcement could remarkably enhance the mechanical performances of samples, and the mechanical performances of our prepared MEHP could be readily regulated by changing the incorporated ZnO content to resist external forces during implantation without scaffold damage.

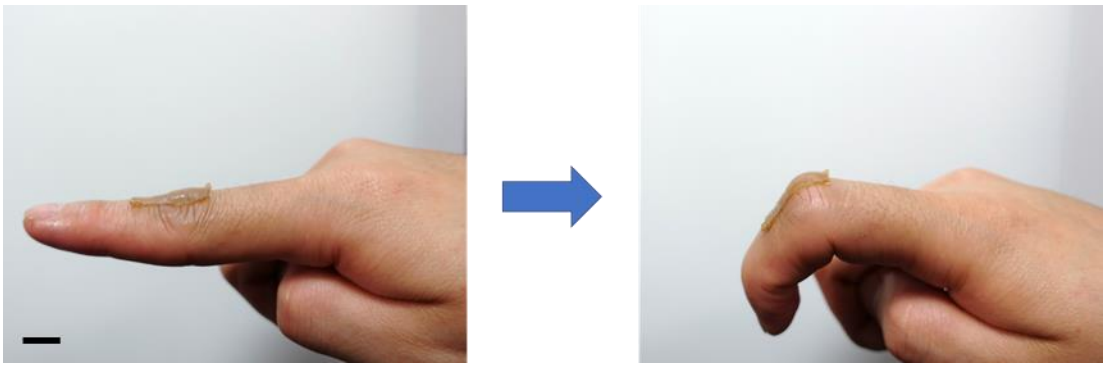

Figure 3-27. Macroscopic observation of the flexibility of electrospun scaffolds adhered on finger. Scale bar = 1 cm.

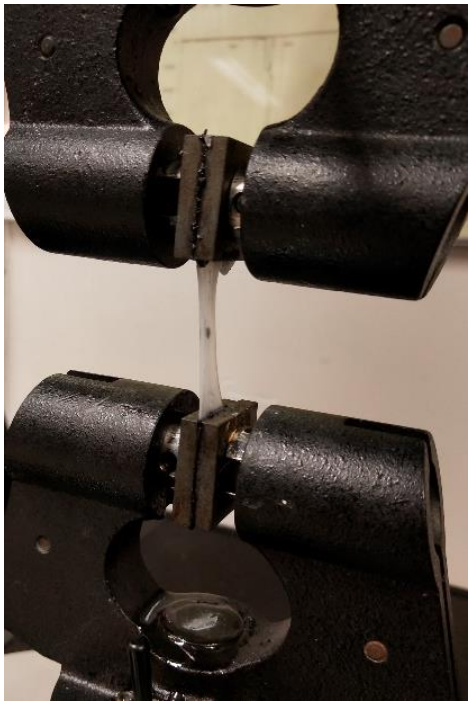

Figure 3-28. The test process of mechanical properties by an Instron machine.

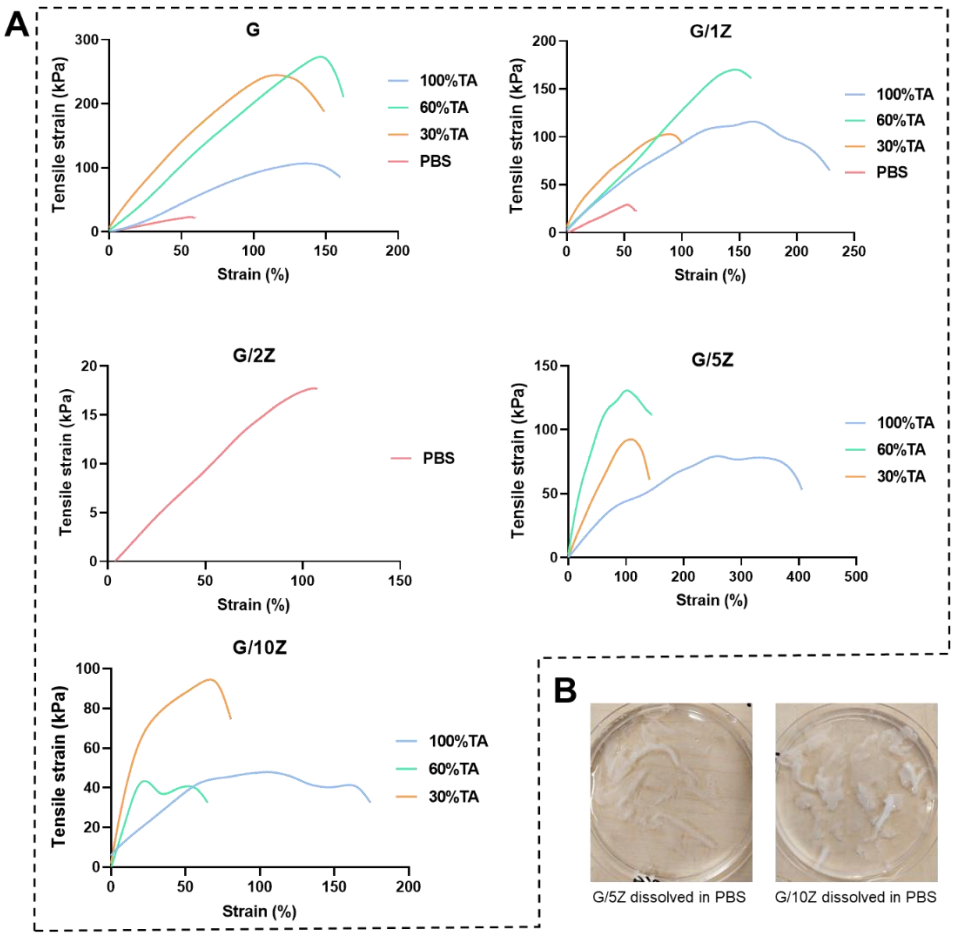

Figure 3-29. The mechanical tests of different membranes in the preliminary

experiment. (A) The tensile stress-strain curve of different membranes. (B) The failed reasons for G/5Z and G/10Z samples due to unstable crosslinking.

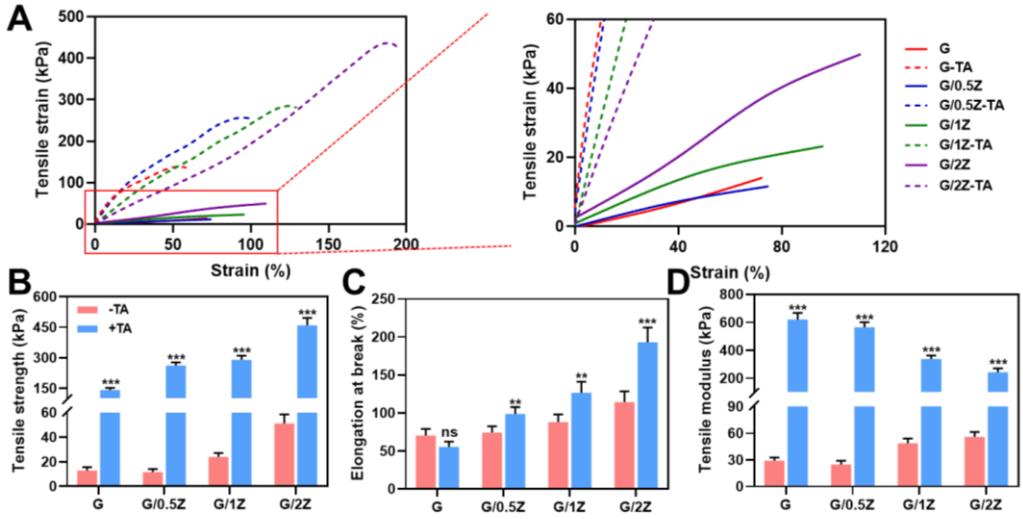

Figure 3-30. Mechanical properties of different electrospun membrane in the second experiment. (A) Tensile stress-strain curves, and corresponding (B) strength, (C) elongation at break, and (D) modules of different material formulations in the tensile test.

An ideal tendon-repairing path should adhere to injury site fast and stably, serving as a physical barrier to suppress the surrounding tissue ingrowth and withstand the external compression, while serving as a niche to offer a suitable microenvironment for cell survival and proliferation to enhance tendon repair. Here, we firstly investigated the anti-detachment properties of MEHP by lap shear test. As showed in the **Figure 3-31(A)**, the hydrogel patch was placed between the two layers of porcine skin, and tested using Instron machine. The results confirmed its robust adhesion performance. As compared with pure G, the TA treatment significantly increase the adhesion stress (2.12 ± 0.59 v.s. 35.46 ± 6.52 kPa for G and G/2Z+TA groups, respectively) (**Figure 3-31(B)**). However, adhesion stress was markedly compromised upon excessive incorporation of ZnO (> 5%), which may be attributed to the cohesion failure (reduced toughness) caused by ZnO nanoparticle aggregation in the matrix network. Altogether, the adhesion stress of MEHP outperformed the clinical used tissue patches like Fibrin Glue (15.4 ± 2.8 kPa),

showing great potential in clinical application for tendon repair [88]. Next, we further measured the resistance of MEHP to blood or tissue pressure by burst pressure test. As illustrated in the **Figure 3-32**, similar to the results of lap shear test, the burst pressure was significantly enhanced after TA treatment, with the burst pressure of 120.75 ± 10.05 mmHg for G/2Z+TA group. Due to higher burst pressure than the normal systolic pressure (<120 mmHg), the MEHP could evade accidental detachment caused by surgical operation or blood flow pressure. Next, we analyzed the possible mechanisms of such high adhesive strength for the MEHP (**Figure 3-33**). It could be ascribed to the formation of (1) hydrogen bonding between amide, hydroxyl and carbonyl groups in hydrogel patch and -CONH and -OH groups on the tissue surface; (2) In addition, after oxidation of TA into reactive quinones by O_2, hydrogel patch could readily react with -NH_2 and -SH groups on the tissue surface to form covalent -C=N and -S-C bonds by Schiff-base and Michael addition reactions. In short, such MEHP showed excellent mechanical and adhesive performances, which would be beneficial for clinical practical operations.

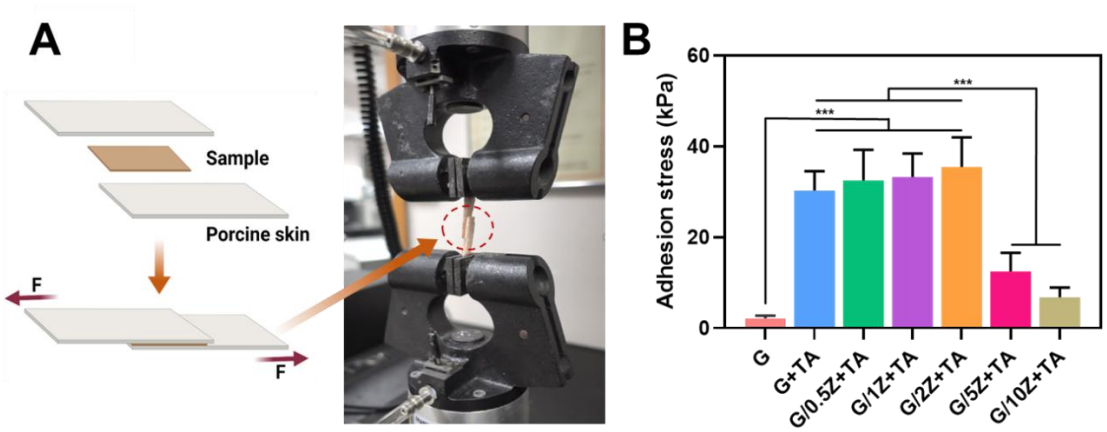

Figure 3-31. (A) Schematic illustration and representative photograph of lap shear test process to determine the shear strength of prepared samples. (B) Quantitative analysis of average shear strength of different samples. G means GelMA, G/0.5Z, G/1Z, G/2Z, G/5Z and G/10Z indicate GelMA added with 0.5%, 1%, 2%, 5% and 10% ZnO nanoparticles, respectively. Figure created with BioRender.com.

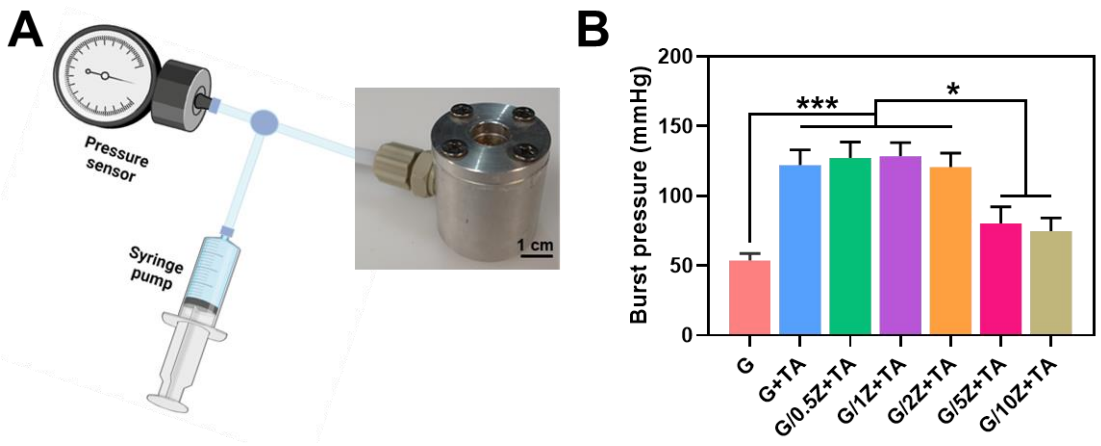

Figure 3-32. (A) Schematic illustration and representative photograph of burst pressure test process to determine the burst pressure of prepared samples. (B) Quantitative analysis of average burst pressure of different samples. G means GelMA, G/0.5Z, G/1Z, G/2Z, G/5Z and G/10Z indicate GelMA added with 0.5%, 1%, 2%, 5% and 10% ZnO nanoparticles, respectively. Figure created with BioRender.com.

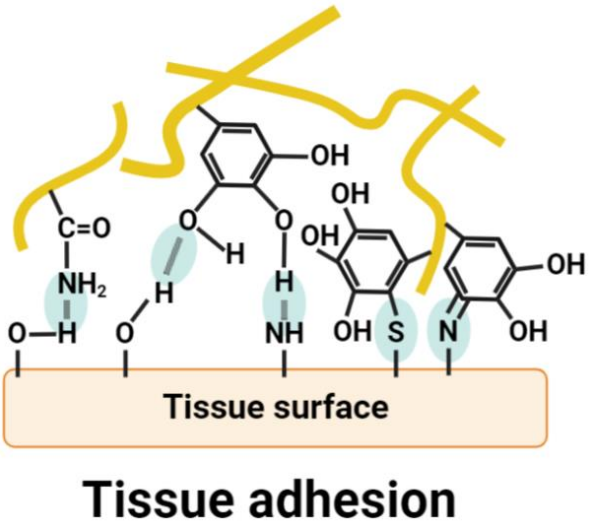

Figure 3-33. Proposed adhesion mechanisms of MEHP to tissue surface. Figure created with BioRender.com.

3.3.3 Cell viability and proliferation

As a bio-scaffold for tissue repair, it must possess excellent biocompatibility without influencing the normal tissue growth and induce target tissue regeneration by promoting cell proliferation. We firstly evaluated cell viability of BMSCs by live/dead staining. As showed in the **Figure 3-34**, all scaffolds could support cell survival with a larger

number of green fluorescence-labelled live cells onto the scaffolds. Quantitative analysis based on the live/dead staining images further confirmed the excellent biocompatibility of our prepared MEHP with >90% cell viability at all measure time points (24, 48 and 72 h) (**Figure 3-35**). In addition, we performed CCK-8 assay to evaluate the cell proliferation. As showed in the **Figure 3-36**, the cells in all groups proliferated with time. Notably, with more addition of ZnO (2%) into the hydrogel patches, the proliferation rate was better. In addition, the G/2Z+TA showed the best proliferation rate compared with other groups, indicating its superior biocompatibility for biomedical application.

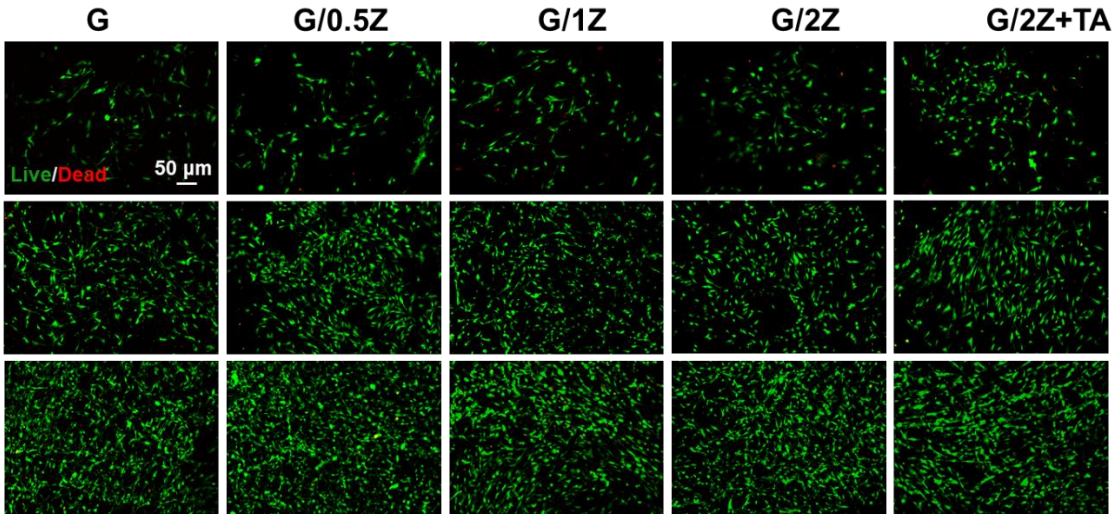

Figure 3-34. Live/dead staining of BMSCs after treatment with the different electrospun membrane formulations for 24, 48 and 72 h. Green fluorescence and red fluorescence represent the viable and dead cells, respectively.

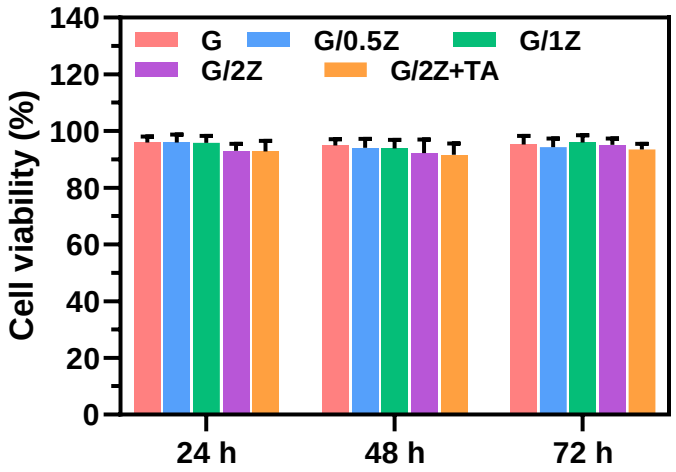

Figure 3-35. Corresponding cell viability calculated based on the live/dead staining.

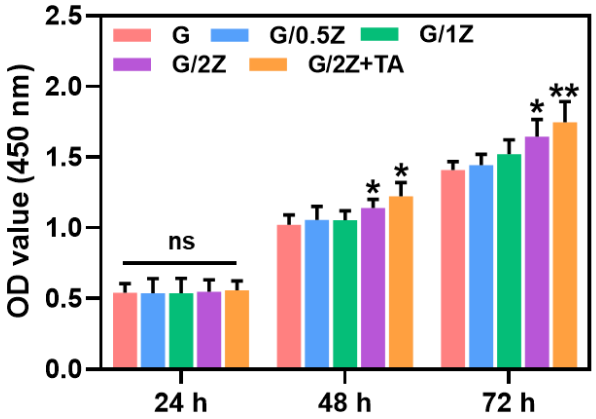

Figure 3-36. The cell proliferation of BMSCs after treatment with different electrospun membrane formulations for 24, 48, and 72 h measured by CCK-8 assays.

3.3.4 Anti-oxidation effects

It was reported that oxidative stress would be getting intense after tendon surgical operation within first 24 h, which could stimulate fibrosis and inflammation, promoting peritendinous adhesion formation and deteriorating tendon repair quality [78]. To turn the scale, we introduced TA into the scaffold system to endow the resultant scaffold with anti-oxidative and anti-inflammatory effects. Here, to demonstrate our hypothesis, we performed a series of experiments to confirm the anti-oxidative and anti-inflammatory ability of prepared MEHP. Firstly, we evaluated the *in vitro* H_2O_2 scavenging capacity of different electrospun membrane formulations using Hydrogen

Peroxide Assay Kit. As displayed in the **Figure 3-37(A)**, as expected, after TA (a well-known antioxidant) modification, the G/2Z-TA could significantly reduce H_2O_2 level as compared with control, G and G/2Z groups. In addition, the H_2O_2 scavenging percentage was increased with incubation time for G/2Z-TA group with elimination of near 50% H_2O_2 within 20 min, and 72 % H_2O_2 after 120-min incubation (**Figure 3-37(B)**). This verified the potential of the MEHP as a strong ROS scavenger to decrease the ROS *in vitro*.

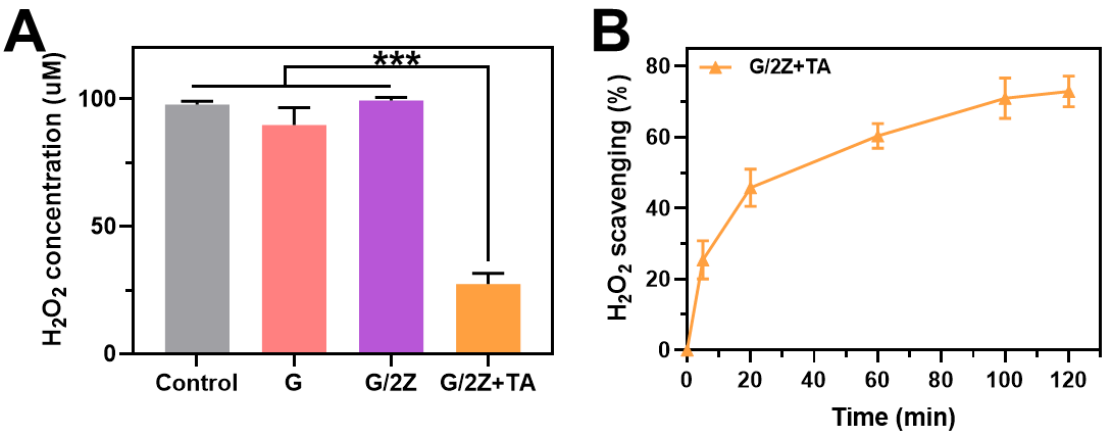

Figure 3-37. (A) *In vitro* H_2O_2 scavenging capacity of different electrospun membrane formulations measured by Hydrogen Peroxide Assay Kit. (B) The H_2O_2 scavenging capacity of G/2Z+TA at different time points (5, 20, 60, 100, and 120 min).

Besides, we assessed the extracellular ROS and intracellular ROS scavenging activity of different electrospun membrane formulations after stimulation of cells with H_2O_2. First, we quantitatively evaluated the extracellular ROS levels using Amplex® Red ROS assay. As illustrated in the **Figure 3-38**, the extracellular H_2O_2 levels for H_2O_2 treatment group was significantly elevated, as compared to the control group. The G + H_2O_2 and G/2Z + H_2O_2 groups exhibited no significant difference in the extracellular H_2O_2 levels, indicating they did not possess ROS scavenging ability. However, for the G/2Z+TA group, it could markedly decrease the extracellular H_2O_2 levels compared with H_2O_2 treatment group. Next, the intracellular ROS levels after different treatments were examined by DCFH-DA assay, and the green fluorescence indicated the cellular

ROS level (**Figure 3-39**). On the first try, although we found significantly reduced green fluorescence signal in G/2Z-TA+H_2O_2 group, the cell density was quite lower. Thus, in the second try, we increased cell seeding density and reperformed the experiments. Similarly, green fluorescence became strong after H_2O_2 treatment compared with the control group (**Figure 3-40**). The G + H_2O_2 and G/2Z + H_2O_2 groups exhibited similar green fluorescence signals compared with pure H_2O_2 treatment group. The quantification of fluorescence intensity further confirmed the results that TA modified scaffolds could reduce the intracellular ROS level (**Figure 3-41**). These results collectively demonstrated the ability of MEHP to decrease the ROS levels both in extracellular microenvironment and inside cells.

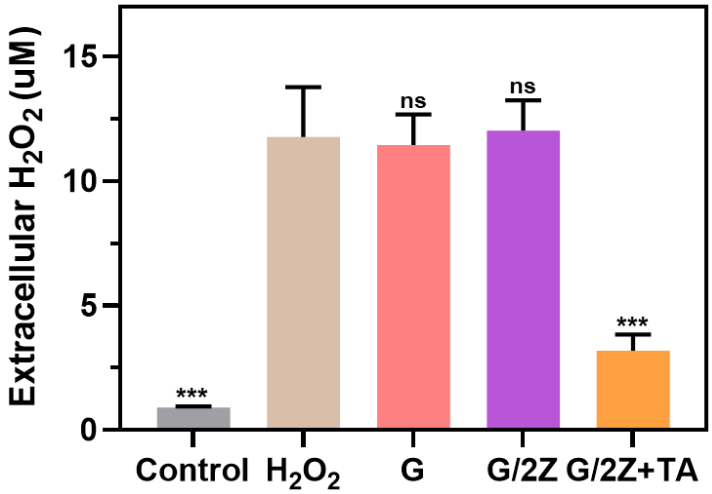

Figure 3-38. Extracellular ROS levels of BMSCs treated with fresh medium (control), fresh medium containing 100 μM H_2O_2 or fresh medium containing 100 μM H_2O_2 added with different electrospun membrane formulations.

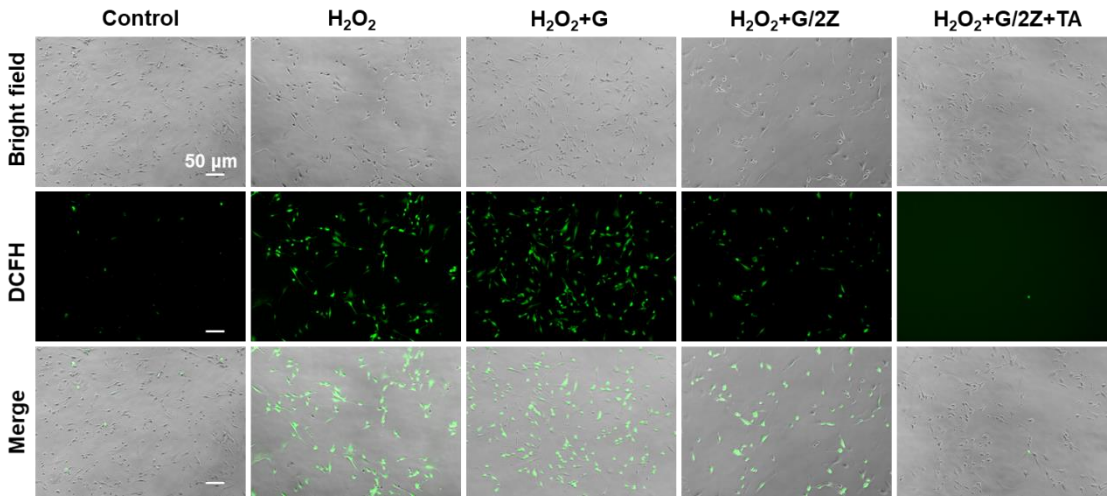

Figure 3-39. Cellular ROS scavenging activity of different electrospun membrane formulations determined by DCFH-DA assay (cell density: 1×10^4 cells/cm^2). Green fluorescence indicated the cellular ROS level.

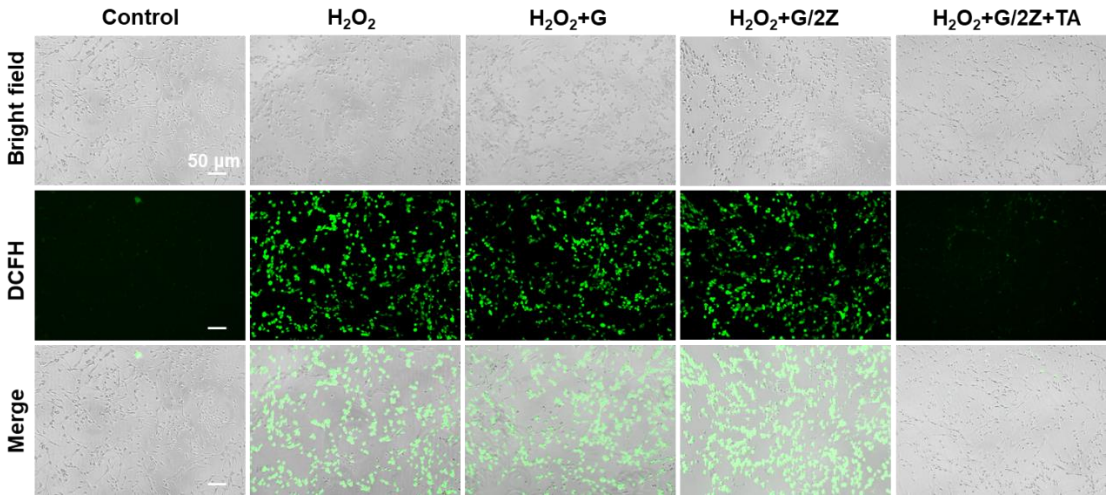

Figure 3-40. Cellular ROS scavenging activity of different electrospun membrane formulations determined by DCFH-DA assay (cell density: 1×10^5 cells/cm^2). Green fluorescence indicated the cellular ROS level.

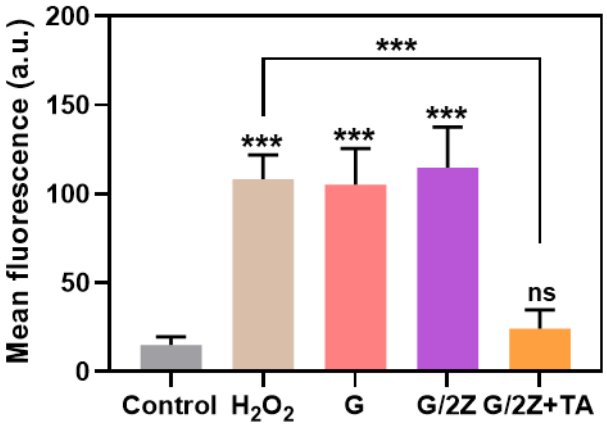

Figure 3-41. Mean fluorescence of cells after different treatments (cell density: 1×10^5 cells/cm^2).

To explore whether the scaffolds could protect cells against the ROS environment, the cell proliferation after H_2O_2 treatment for 12 and 24 h was measured by CCK-8 assay. As showed in the **Figure 3-42**, after 100 uM H_2O_2 treatment, compared with control group, G and G/2Z exhibited similar cell viability at 12 h, while cell viability in the G/2Z-TA group were much higher than other groups. Interestingly, the cell proliferation in the G and G/2Z groups were reduced at 24 h compared to that at 12 h; however, G/2Z-TA group showed a significantly increased cell proliferation at 24 h. These results demonstrated MEHP could protect cells from the toxic ROS microenvironment, causing increased cell proliferation.

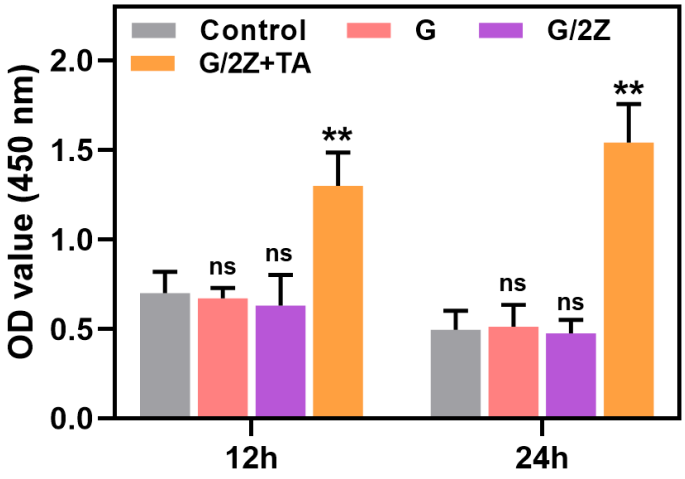

Figure 3-42. Protective effects on cell viabilities in toxic ROS environment detected

using CCK-8 assay.

3.3.5 Anti-inflammation effects

It is widely recognized that the increase of ROS in the microenvironment can accelerate the inflammation process since ROS can act as a signal molecule to induce inflammation response [86]. Thus, we subsequently assessed the *in vitro* anti-inflammatory effects of MEHP on LPS-treated RAW 264.7 cells by measuring the mRNA levels of pro-inflammatory cytokines including TNF-α, Cox-2 and IL-6 using qRT-PCR. As showed in the **Figure 3-43**, cells in the LPS-treated group showed the increased expressions of TNF-α, Cox-2 and IL-6, as compared to the control group. Moreover, a similar trend was found in both G and G/2Z groups that mRNA levels of pro-inflammatory cytokines were significantly increased. Besides, the expression levels of pro-inflammatory cytokines in G and G/2Z groups were comparable to those of LPS-treated group, indicating their lack of ability to suppress inflammatory process. Notably, although G/2Z+TA group showed higher mRNA levels of pro-inflammatory cytokines than control group, the expressions of these pro-inflammatory cytokines were significantly reduced as compared to the LPS-treated group, G and G/2Z. These results confirmed that the released TA from hydrogel patch maintained its bioactivity to alleviate inflammatory reaction. The potential mechanisms for anti-oxidative and anti-inflammatory effects may be attributed to the released TA from the MEHP, which can (1) directly eliminate oxygen free radicals like ROS, 1,1-diphenyl-2-picrylhydrazyl (DPPH) and 2,2′-azino-bis (3-ethylbenzothiazoline -6-sulfonic acid) (ABTS)-free radicals to block activation of NLRP3/caspase-1 pathway; (2) increase the activity of anti-oxidative enzymes like glutathione peroxidase (GSH-Px), catalase (CAT) and superoxide dismutase to reduce the oxygen free radicals; (3) protect IκB from degradation to enhance anti-inflammatory ability by inhibiting NF-κB signaling pathway (**Figure 3-44**) [89, 90]. Taken together, these results collectively confirmed the superior anti-oxidative and anti-inflammatory effects of our MEHP, demonstrating its great potential in reduce inflammatory reaction after tendon injury.

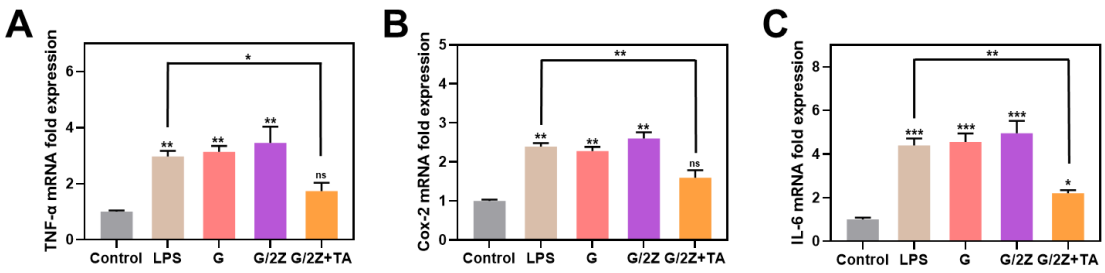

Figure 3-43. *In vitro* anti-inflammatory effects evaluated by measuring the mRNA levels of (A) TNF-a, (B) Cox-2, (C) IL-6 by RAW 264.7 cells after 3-day culture.

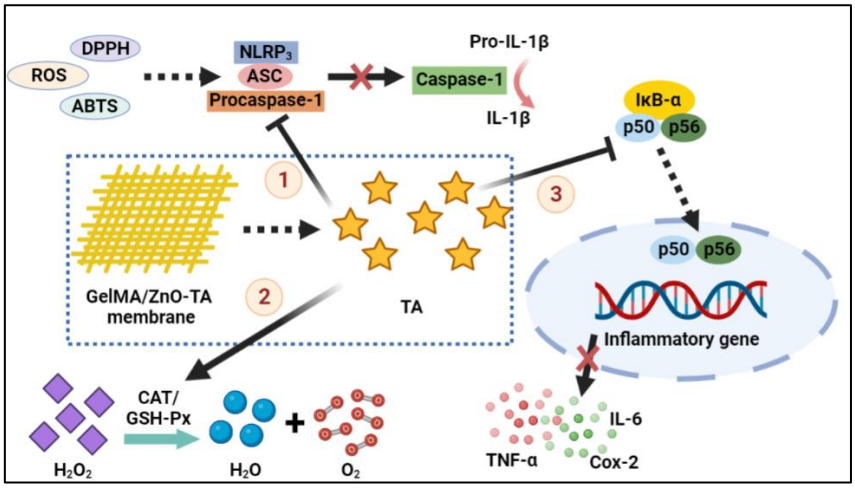

Figure 3-44. The possible mechanism of the anti-oxidative and anti-inflammatory effects of G/2Z+TA electrospun membranes. Figure created with BioRender.com.

3.3.6 Anti-bacterial and pro-healing effects

The postoperative infection affects the progression of wound healing. For tendon injury, the local infection is a devastating complication after surgical operations, since it may be difficult to treat due to the low blood supply of tendon that limits the local concentrations of systematically administrated antibiotics [91]. Besides, it was reported that the postoperative infection was highly associated the poor therapeutical outcomes, which will increase the rates of rupture [92]. A tendon-repairing graft that owns good anti-bacterial efficacy is getting more attentions for practical application. Herein, we next evaluated the anti-bacterial effects of MEHP by agar disc diffusion test. Here, special acknowledgement and gratitude are given to Miss. Di Suo for completing the anti-bacterial experiment. The *E.coli*, a typical infection-causing bacteria strain, was

used as model bacteria. As displayed in the **Figure 3-45**, after incubation with samples for 24 h, there was a transparent band (i.e., bacteria inhibiting loop) around the G/2Z and G/2Z+TA membranes, while the bacteria inhibiting loop was not significant in the G group. Quantitative analysis further demonstrated the higher bacteria inhibiting loop for G/2Z group compared to the G. Besides, G/2Z+TA exhibited excellent anti-bacterial effects with diameter of bacteria inhibiting loop remarkably higher than both G/2Z and G groups. These results demonstrated the superior anti-microbial property of MEHP. Such excellent anti-bacterial ability may be attributed to combined anti-bacterial efficacy from ZnO and TA. In our system, the ZnO may be released from hydrogel patch and direct contact with cell membrane to increase membrane permeability. In addition, the released Zn^{2+} may be another possible mechanism since Zn^{2+} can damage the cell membrane and penetrate the intracellular contents [93]. For the TA, it can make cytoplasmic membrane unstable, and increase membrane permeability and inhibit enzyme activity by interacting with protein within bacteria [94].

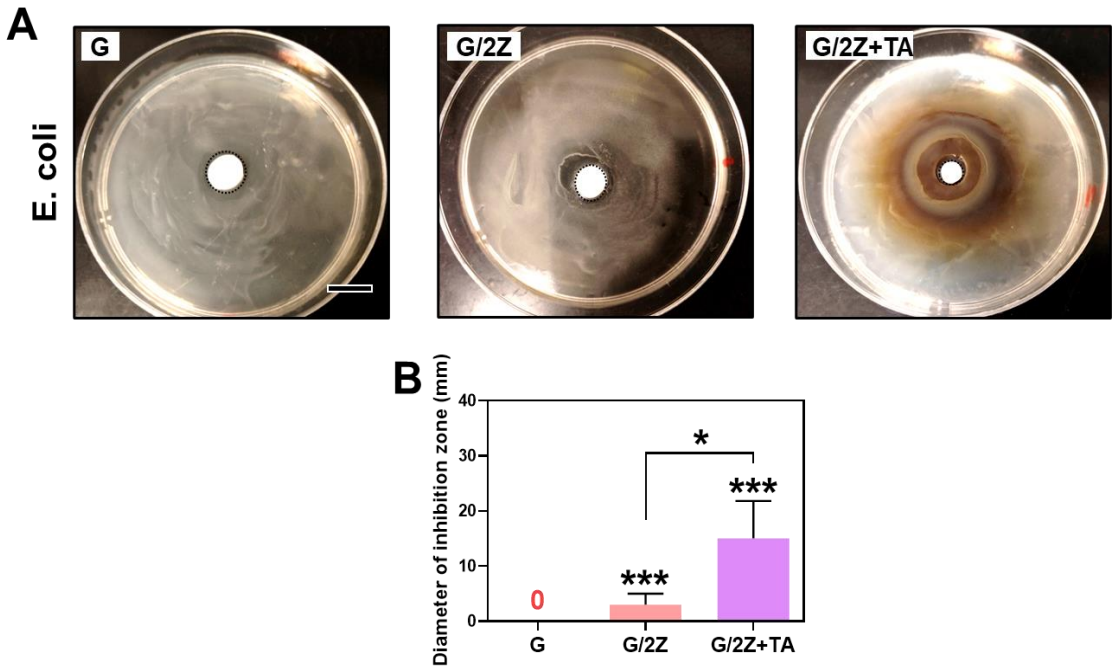

Figure 3-45. (A) Photographs of agar diffusion test result for G, G/2Z and G/2Z+TA against *E. coli*. The dotted circles indicate the original size of samples. (B) The diameter of inhibition zone. Scale bar = 1 cm.

A graft for tissue repairing should support cell adhesion after implanted into the body to accelerate healing process. To evaluate cell adhesion onto the different electrospun hydrogel patch, we performed actin and nucleus staining. As showed in the **Figure 3-46**, after 3-day incubation, the BMSCs on the G, G/2Z and G/2Z-TA showed similar spread morphology with elongated shape. Interestingly, the cell numbers on the G/2Z-TA and G/2Z seems to be much more than the G groups, which was consisted with the cell proliferation results. This suggested that G/2Z-TA and G/2Z could provide a suitable microenvironment to enhance cell adhesion. It has been widely demonstrated that ZnO NPs could promote wound healing by enhancing cell proliferation and adhesion by released Zn^{2+} [95-97]. The further increased cell attachment after TA treatment may be due to the increased protein adsorption mediated by TA as well as the direct interaction between protein onto cell membrane and TA molecule onto the hydrogel patch surface [98].

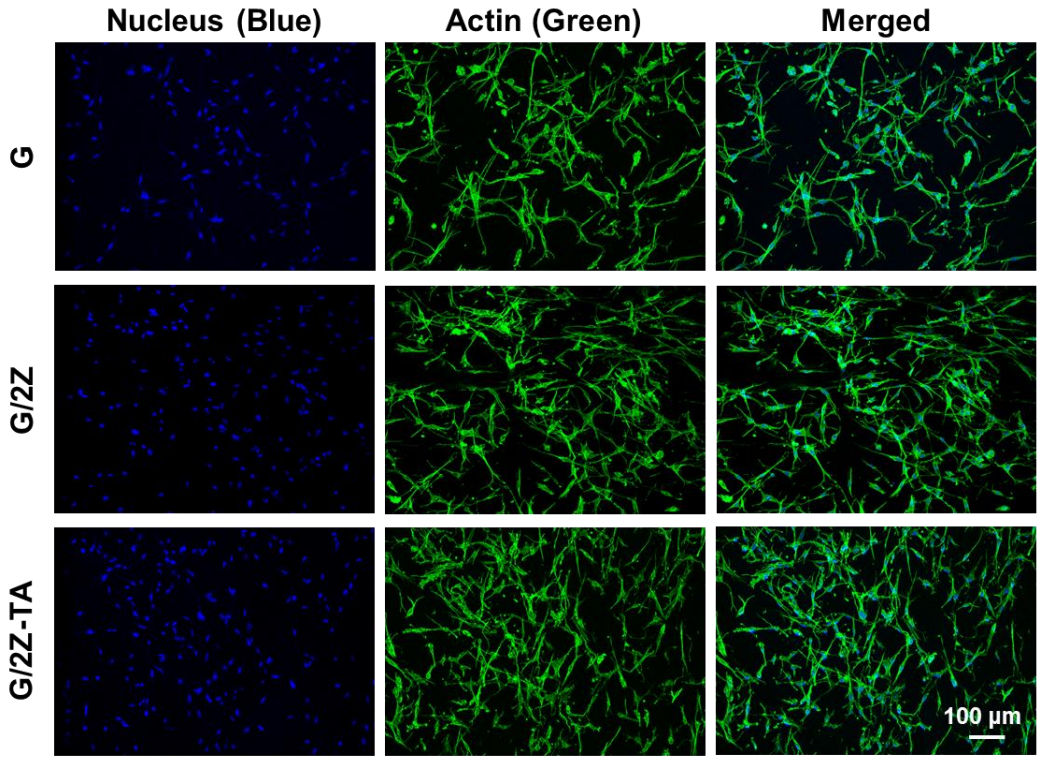

Figure 3-46. Representative Actin/DAPI images of BMSCs adhered on surface of different electrospun membranes after 3-day culture. Green fluorescence and blue

fluorescence indicate cell actin and nuclei, respectively.

3.3.7 Construction of the dual-layer membrane scaffold

Considering the multi-functions of MEHP like high mechanical and adhesive performance, anti-oxidative, anti-inflammatory, and anti-bacterial properties as well as the tendon pro-healing efficacy, we believed that such hydrogel patch would serve as an ideal graft for tendon repair. However, although our MEHP could serve as a physical barrier to prevent surrounding tissue ingrowth, their ability to prevent tendon adhesion was limited as extrinsic cells could also migrate and proliferate onto the patch surface. To further enhance the anti-fibrosis capacity of the graft, we proposed to construct a Janus dual-layer membrane scaffold, in which the inner layer was MEHP (i.e., G/2Z-TA) while the outer layer was the PLLA electrospun fibrous membrane (**Figure 3-47**). The PLLA membrane has been demonstrated the superior ability as physical barrier to prevent tendon adhesion formation [47]. Taking advantage of the adhesive ability of MEHP to diverse surfaces, such dual layer can be prepared readily by attaching the MEHP patch to PLLA membrane. As showed in the **Figure 3-48**, the MEHP was adhered tightly to the PLLA layer, while maintained the excellent adhesive properties to figure surface. In addition, such Janus patch exhibited good flexibility, showing great application potential to accommodate different deformations of tissue and wrap the tendon injury site for tendon repair. In addition, we also evaluated the interface stability between MEHP and PLLA layers after incubation in PBS for 3 days by SEM. It was demonstrated that such two layers were attached closely after incubation in PBS for 3 days (**Figure 3-49**). This may be possibly attributed to the excellent wet adhesive properties of TA [99]. In addition, we further assessed the mechanical properties of such two-layer scaffolds via Instron machine (**Figure 3-50**). We observed a similar mechanical performance for both pure PLLA and the Janus patch, which indicated that introduction of adhesive MEHP layer did not compromise the mechanical properties of PLLA scaffold (**Figure 3-51**). In terms of their own unique characteristics, we believed inner MEHP layer would serve as a repairing path to promote tendon healing, while outer PLLA layer would serve as a physical barrier to prevent tendon adhesion

formation. Taken together, such Janus patch could be fabricated feasibly and exert their specific effects synergistically for tendon repair.

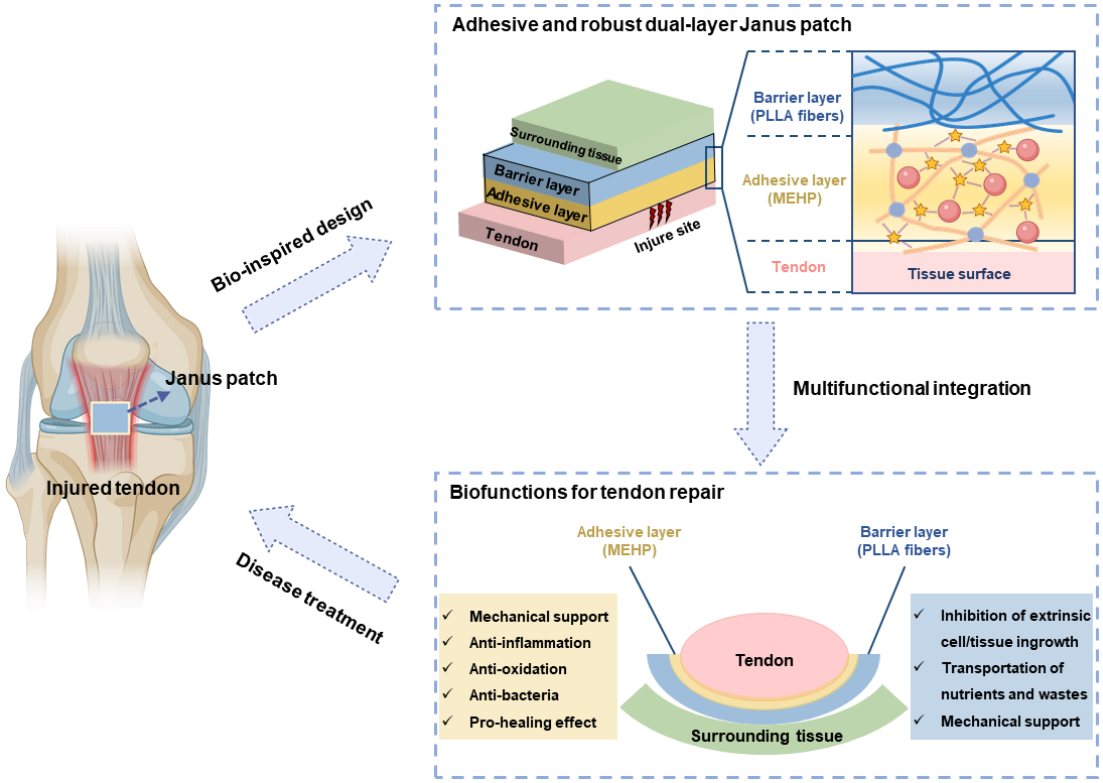

Figure 3-47. Schematic showing the design of a Janus patch for tendon repair, which was consisted of an outer barrier layer (i.e., PLLA electrospun membrane) and an inner adhesive layer (i.e., MEHP). Figure created with BioRender.com.

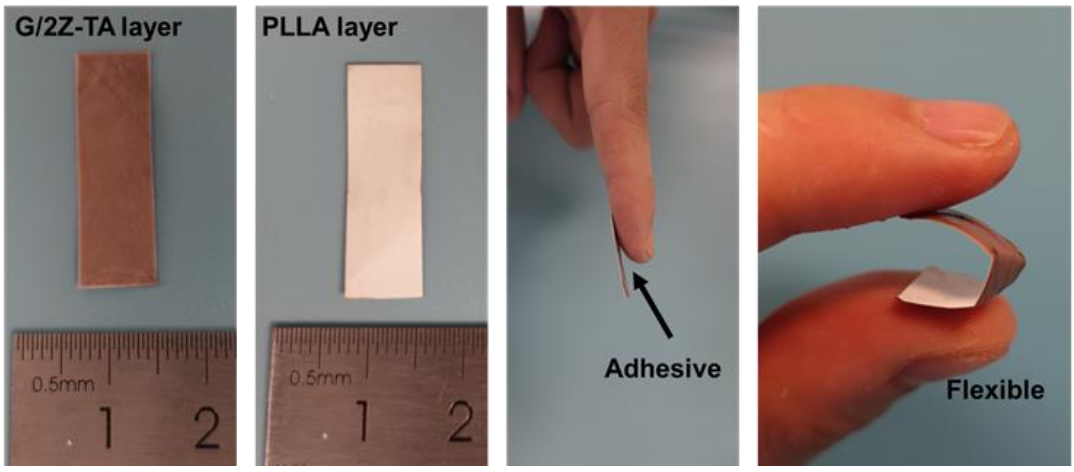

Figure 3-48. Digital images of Janus patch, which was comprised of a MEHP (i.e.,

G/2Z-TA) inner layer and a PLLA outer layer. Such Janus patch exhibited good tissue adhesion and suitable flexibility.

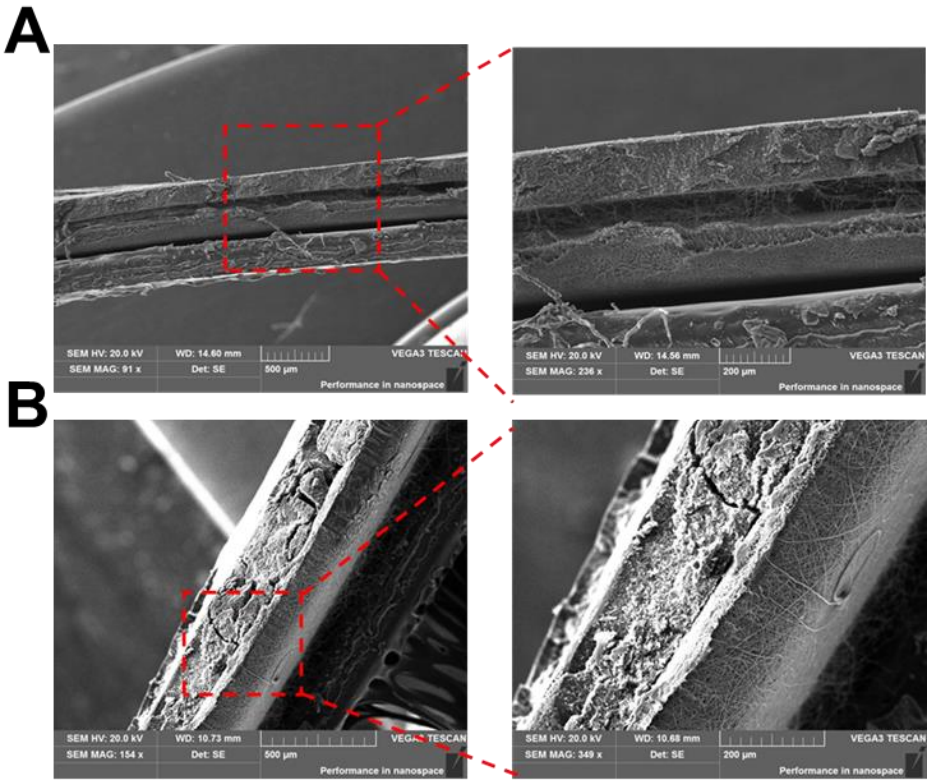

Figure 3-49. Cross-sectional SEM images of Janus patch (A) before and (B) after incubation in the PBS for 3 days.

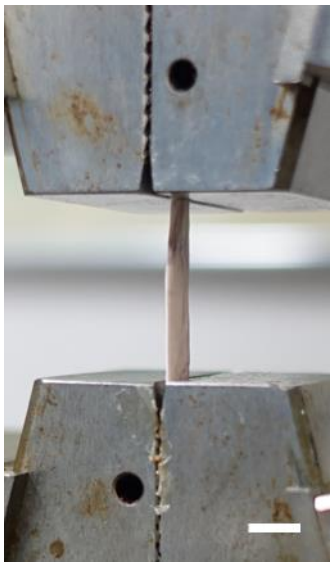

Figure 3-50. The process of mechanical evaluation of Janus patch via Instron machine. Scale bar = 1 cm.

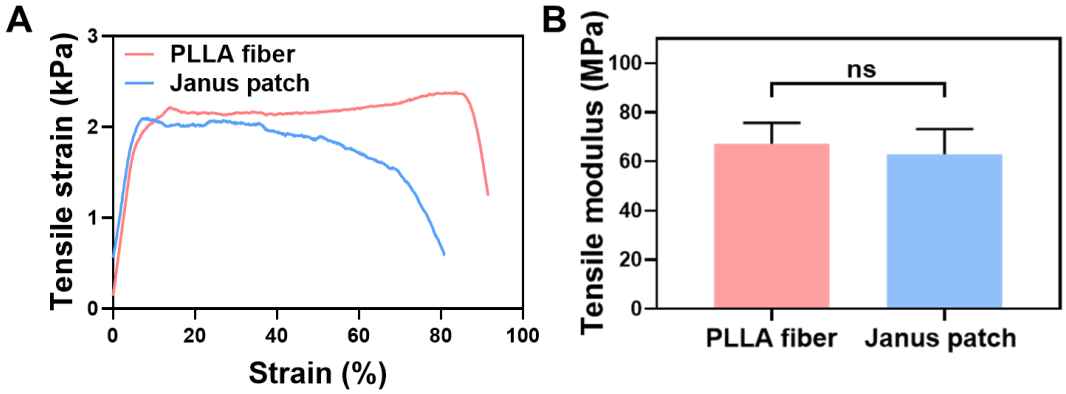

Figure 3-51. Mechanical properties of Janus patch evaluated by tensile test.

3.3.8 *In vivo* tendon regeneration potential

The therapeutical efficacy of Janus patch was further assessed by first establishing a tendon injury model, and then implanting the scaffolds into the surgical site. Here, special acknowledgement and gratitude are given to Hualianke Biotechnology Co. LTD for completing animal experiments. As showed in **Figure 3-52**, after suturing the rupture site, Janus patch could be readily used to warp around the tendon injury site. Then, after surgery for 21 days, the surgical sites of the repaired tendons were directly observed. There was no significant inflammation or ulcer found around the incision area. Then, the tendon adhesion was assessed using a well-established scoring system based on the gross observation. As displayed in **Figure 3-53**, massive fibrous tissues were deposited in the peritendinous area that connected the tendon to surrounding tissue. However, PLLA and Janus groups showed few adhesion tissues around the surgical sites which was easy to be separated using blunt instrument. Quantitative analysis further demonstrated the Janus patch group had the lowest score among these four groups, showing best anti-adhesion effects (**Figure 3-54**).

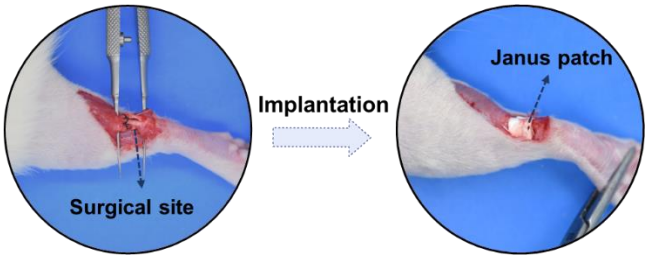

Figure 3-52. The implantation of Janus patch into tendon operated site during surgery.

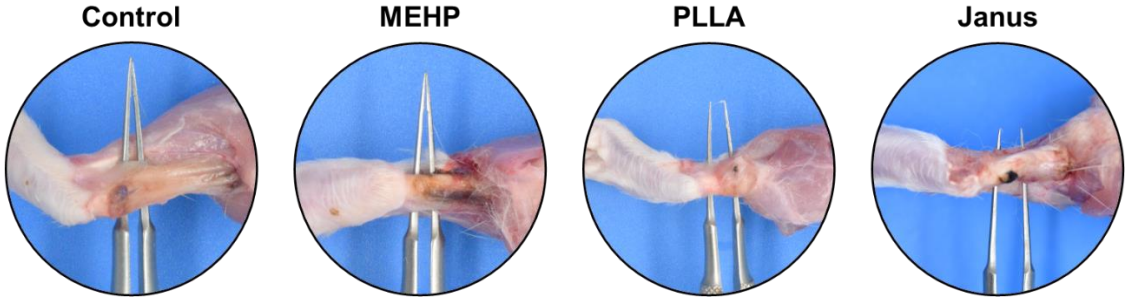

Figure 3-53. Macroscopic observation of tendon operated sites after implantation of scaffolds for 21 days.

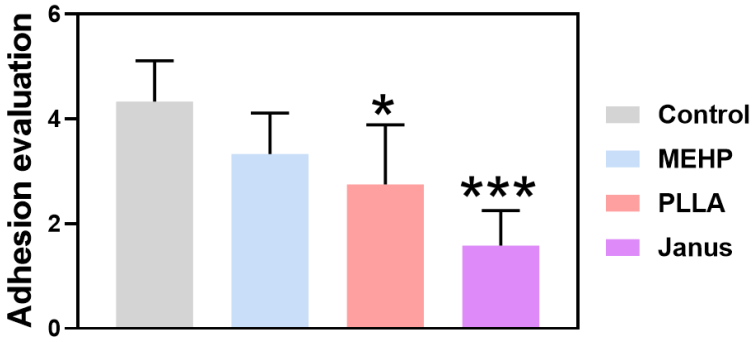

Figure 3-54. Evaluation of tendon adhesion based on the surgical observation according to the established scoring system.

Next, histological analysis using H&E staining and Masson's trichrome staining was performed to examine the outcomes of tendon repair. As revealed by H&E staining in **Figure 3-55**, severe adhesion between the regenerated tendon and surrounding tissue was found in the control group. In contrast, PLLA and Janus groups exhibited lower adhesion formation. More importantly, compared with control and PLLA group, MEHP

and Janus groups showed fewer inflammatory cells in the repair sites, indicating lower the inflammatory responses. Masson's trichrome staining was further performed to evaluate the collagen deposition (blue color) and its fiber morphology. It was found that there were much more collagen generation in the MEHP and Janus groups, compared with the control and PLLA groups. The neo-collagen in the Janus group was much denser than that in other three groups, and fibers were aligned along the long axis of tendon, suggesting better repair quality.

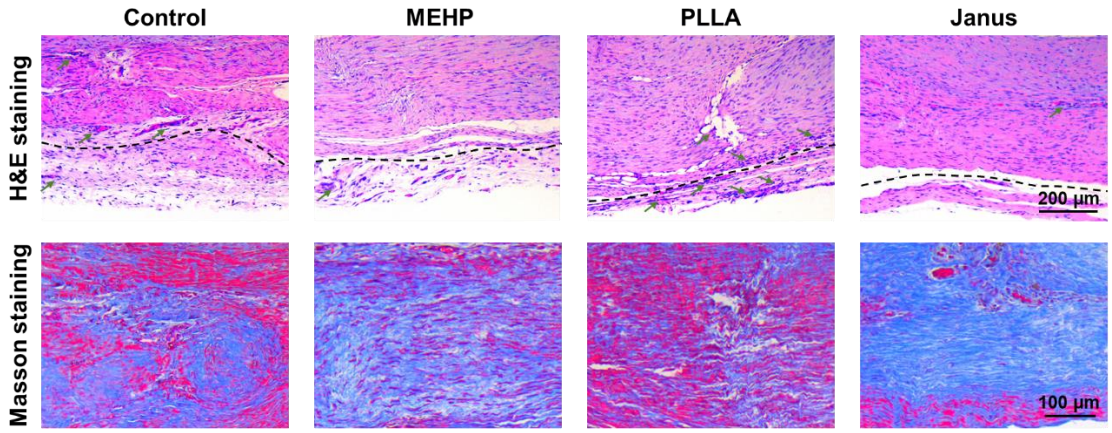

Figure 3-55. Histological evaluation of repair sites of Achilles tendon after surgery for 21 days via H&E staining and Masson's trichrome staining. The dotted lines represented the boundary between the tendon and the peripheral granulation tissue. The green arrows indicated the inflammatory cells.

Col-1 is the major component of tendon matrix (accounting for almost 60 of the dry mass of tendon tissue), which is beneficial for tensile loading. Col-3 is often secreted massively during the early inflammation and proliferation phases of tendon healing. The increased expression of Col-3 in the later reconstruction phase has been showed to lead to thinner collagen fibers with a lower mechanical strength. Thus, we performed the immunohistochemical staining to detect the amounts of Col-1 and Col-3 at the regenerated tendon sites after surgery for 21 days. As revealed in **Figure 3-56**, both control group and PLLA groups exhibited a strong expression of Col-3, with little Col-1 deposited in the tendon matrix. In contrast, Janus group displayed a substantial Col-

1 expression in the matrix, but retained a weaker Col-3 deposition in the rupture site, implying such scaffold might contribute to the tendon healing. Both F4/80 (a maker of macrophages) and TNF-α (an inflammatory cytokine) are the indicators of inflammatory reactions. Next, we used immunohistochemical staining to explore the inflammation status at the surgical site. As showed in the Figure 3-55, control and PLLA groups had the darkest F4/80 and TNF-α stained color, suggesting the most severe inflammatory response. However, weaker staining intensity was found in the MEHP and Janus groups. This phenomenon endorsed that our prepared Janus patch could alleviate the *in vivo* inflammation reaction by virtue of its inner MEHP layer.

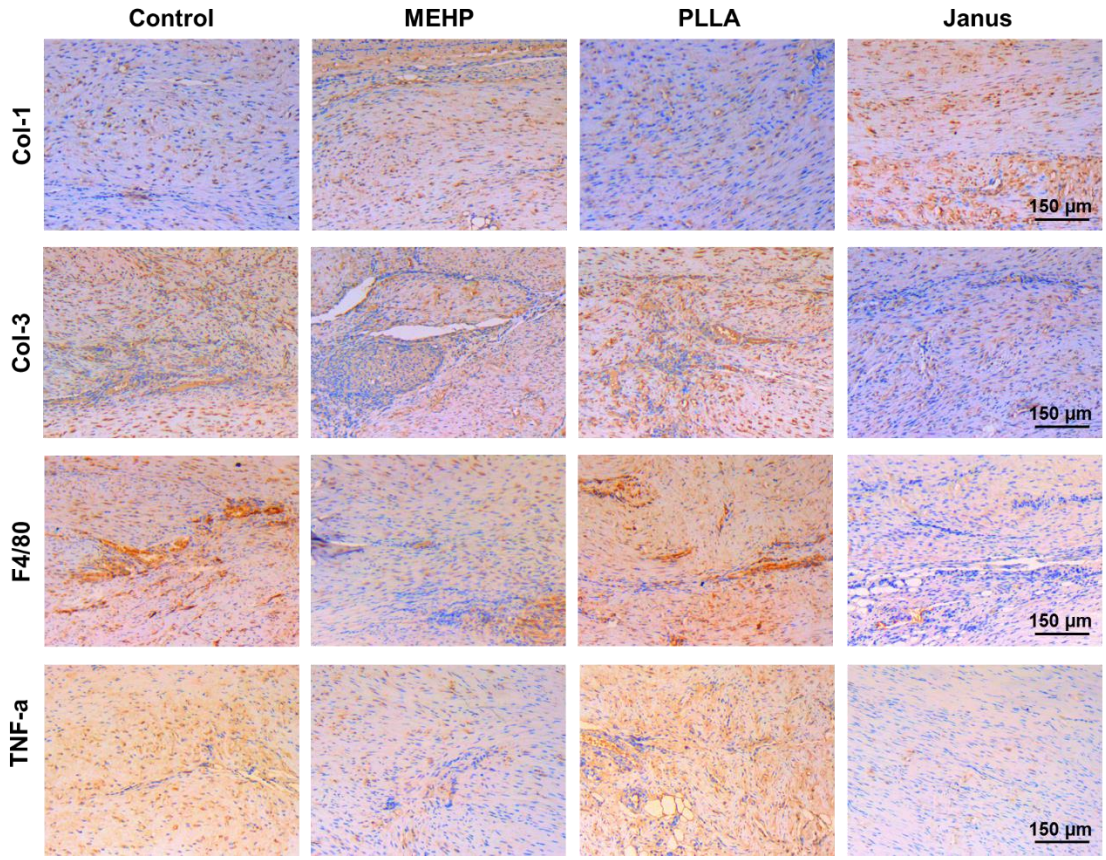

Figure 3-56. Representative images of immunohistochemical stanning of repaired tendon tissues with Col-1, Col-3, F4/80 and TNF-α.

Subsequently, we adopted the qRT-PCR test to further confirm the *in vivo* anti-inflammation effects of our Janus patch (**Figure 3-57**). As expected, Both MEHP and Janus groups could decrease the gene expressions of inflammatory makers such as Cox-

2, MMP-3, TNF-α, IL-1β, IL-6, RANKL. This result from PCR test was consistent with that from *in vitro* cell experiments and immunohistochemical staining, indicating that our MEHP could reduce *in vivo* inflammation, while endowing the Janus patch with superior *in vivo* anti-inflammatory efficacy.

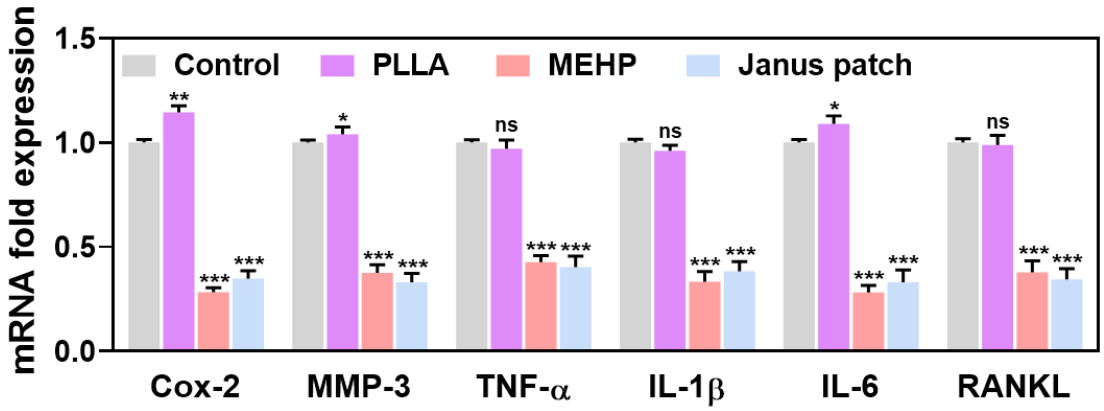

Figure 3-57. qRT-PCR analysis of the gene expressions of inflammatory makers including Cox-2, MMP-3, TNF-α, IL-1β, IL-6, RANKL.

3.4 Summary

In summary, an adhesive and robust Janus patch was successfully fabricated for tendon repair, which was consisted of a MEHP inner layer and a PLLA membrane outer layer. The MEHP could be readily prepared by co-electrospinning of GelMA and ZnO and subsequent TA treatment. The simple but delicate combination of these components bestowed upon MEHP low swellability, superior mechanical and adhesive properties, favorable biocompatibility, anti-oxidative, anti-inflammatory, and anti-bacterial performances. Owing to these advantages, after implantation of our Janus patch *in vivo*, the inner MEHP layer could be attached to the tendon defect site tightly and allow for material-tendon fixation and integration, providing an adequate mechanical support and suitable niche for tendon healing. Meanwhile, the outer PLLA layer could protect tendon from surrounding tissue or cell ingrowth, thereby suppressing peritendinous adhesion formation.

Considering the drug, cell and biologicals free nature, our MEHP can evade side effects

like ectopic tissue formation and cancerization. Besides, due to the simple fabrication process, the largescale preparation of such scaffolds was highly feasible, which represents a ready-to-use treatment mean for tissue construction. Furthermore, such hydrogel patch showed great potential in clinical translation in terms of its material components, which are all naturally derived with defined structure and bioactivity. Most importantly, apart from being grafts for tendon repair, our proposed system can also act a plaster and/or band-aid for skin or bone regeneration after injury, showing diversified application prospects. All in all, our intelligent Janus patch with integrated multiple functions will promote further advancement of high-performance bio-scaffolds and find extensive applications in biomedical engineering field.

Chapter 4 Development of anti-bacterial electrospun fibrous scaffolds for pancreatic cancer therapy

4.1 Introduction

4.1.1 Brief introduction of pancreatic cancer

Pancreatic cancer (PC) is recognized as one of the deadliest cancer types, with a 5-year survival rate less than 8% [100, 101]. Despite the advancement of modern therapeutic and diagnostic technologies, the clinical treatment outcomes of PC are still unsatisfying due to its non-specific latent symptoms and rapid metastasis. It was reported that PC would emerge as the second major cause of cancer-related mortality in USA by 2030. Currently, the well-recognized determinants for PC development include demographic (e.g., age, gender), lifestyle (e.g., cigarette smoking, alcohol drinking) and metabolic (e.g., obesity, type II diabetes) factors [102]. Among them, lifestyle habits such as alcohol abuse and smoking are the best-studied modifiable risk factors of PC. Tobacco use has been confirmed to be linked to PC incidence and mortality, which highlights the significance of relevant health education [103]. The most common histotype of PC is pancreatic ductal adenocarcinoma, comprising >90% of all pancreatic malignancies [104]. Several genetic mutations such as KRAS activation (95%), TP53 (75%), CDKN2A (90%) and SMAD4 (50%) mutation have been evidenced to raise the risk of pancreatic tumorigenesis by affecting protein synthesis and cell metabolism/proliferation. As observed histologically by pathological section, desmoplastic stroma existed in the PC microenvironment, which was believed to serve as a fence to promote cancer cell proliferation and reduce the effective dose of systematically administered anti-tumor drugs, thus causing chemoresistance [105]. Given the limited therapeutic strategies for PC patients, it is imperative to better understand various cellular and extracellular components in the TME of PC, in hope of developing novel therapy methods to increase the clinical efficacy and improve the prognosis as well as far-reaching survival quality in PC victims (**Figure 4-1**).

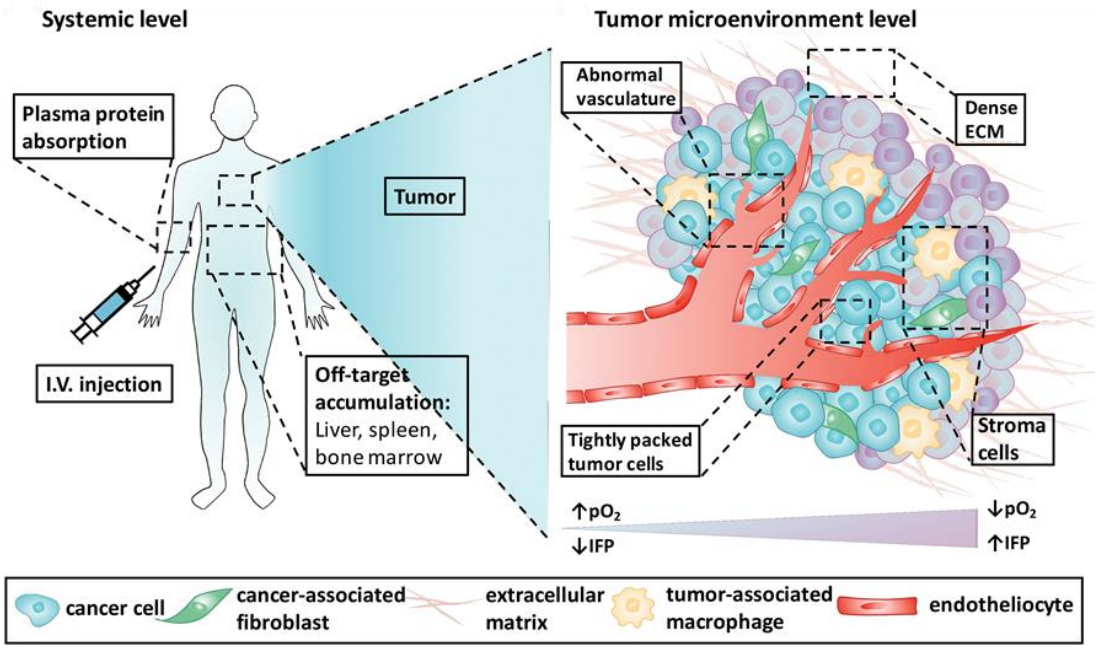

Figure 4-1. Schematic of (A) current barriers regarding to the systematically administered drug delivery for PC therapy and (B) PC microenvironment with aberrant vasculature, high interstitial fluid pressure, dense ECM, tightly packed tumor cells and stroma cells included. Reproduced with permission from [118]. Copyright 2018, Elsevier.

4.1.2 The landscape of pancreatic tumor microenvironment

Cellular components

The stromal cells in the TME of PC contains many cell types such as endothelial and immune cells, pericytes and cancer-associated fibroblasts (CAFs). During the tumorigenesis, those stromal cells gradually acquire tumor-associated phenotypes through genetic, metabolic and morphological changes, further altering the expression of signalling molecules, ECM remodelling, and neovascularization [106]. CAFs, derived from activated fibroblasts, epithelial cells, pericytes, mesenchymal progenitor cells or stem cells, are the most abundant population of stromal cells in the TME of PC [107]. They can secrete various cytokines like VEGF, IL-6, and hepatocyte growth factor to stimulate vascularization and cell proliferation in cancer tissue, thus promoting tumor progression. In addition, CAFs are also involved in the production of ECM including collagens and proteoglycans. The increased ECM deposition and matrix

stiffness further activate integrin signalling, improving cancer cell survival and proliferation. Furthermore, some specific enzymes like matrix metalloproteases (MMPs), lysyl oxidase and plasmin can be secreted by CAFs to modify ECM structure [108]. All these alterations are highly linked to cancer metastasis and oncotherapy sensitivity.

The exterior of blood vessels in the TME of PC mainly consists of endothelial cells, smooth muscle cells, and pericytes [109]. In contrast to the normal vessels where endothelial cells are interconnected and anchored to the ECM tightly via focal adhesion protein, the tumor blood vessels are aberrant with immature phenotypes featured by lower VE-cadherin expression and poor adherent junctions between endotheliocytes, due to the excessive production of various cytokines (i.e., VEGF, bFGF and tumor necrosis factor) by stromal cells. Similarly, the morphology of tumor pericytes is pathologically abnormal and connected with endothelial cells loosely. These abnormalities cause leakage of plasma protein and suppress the blood flow, thus hindering the therapeutical outcomes [110].

Adaptive immune cells (e.g., T-lymphocytes and B-lymphocytes), along with myeloid cell populations (e.g., myeloid-derived suppressive cells [MDSCs] and tumor-associated macrophages [TAMs]), collectively act a sophisticated role in the tumorigenesis and are critically involved in the immunoregulation balance of TME of PC [111-113]. T lymphocytes have multiple cell population types, exerting both pro- and anti-tumorigenic functions in the TME. To illustrate, the cytotoxic CD8+ memory T cells have exhibited strong immunosuppression effect against cancer development, while CD4+FoxP3+CD25+ T regulatory cells have proved to stimulate tumor growth and inhibit the activity of cytotoxic T cells through generation of anti-inflammatory cytokines (i.e., IL-10 and TGFβ) [114]. By now, targeted delivery of therapeutics mediated by T cells (e.g., grafting the nano-carrier on their cell surface) have achieved great preclinical success. B cells, located in the draining lymph nodes and adjacent zones of invasive carcinoma, have showed tumor-promoting effects [115]. B cells

inhibit anti-tumor immune microenvironment by producing a large number of cytokines like IL-10 and programmed cell death ligand 1 (PD-L1). MDSCs, derived from hematopoietic stem cells, are mainly driven to tumor site by chemokines. They would differentiate into various cell types like macrophages, dendritic cells, and granulocytes after exposure to specific signalling molecules. MDSCs are known to induce angiogenesis and epithelial-mesenchymal transition, and meanwhile suppress anti-tumor immune responses, thus stimulating tumor growth [116]. Similarly, TAMs have various subpopulations that play distinct roles in the tumor progression [117]. When circulating monocytes enter into the tumor TME and expose to cytokines, they can rapidly undergo differentiation and transform from proinflammatory M1 phenotype to anti-inflammatory M2 phenotype. M2 macrophages inhibit cytotoxic T-cell-mediated anti-tumor performance, stimulate tumor growth and aggravate cancer progression by secreting various anti-inflammatory factors like IL-10 and IL-13. Notably, many studies have showed the feasibility of TAMs to promote nanomedicine-mediated drug delivery because of their active infiltration into inner site of tumor [118].

Extracellular components

The stroma is the main extracellular component in the TME of PC, accounting for ~80% of tumor tissue [119, 120]. It provides suitable physical/mechanical cues to establish the relationship between the structural protein and other matrix components, ensuring the pancreatic tissue integrity [121]. In the pancreatic TME, MMPs and tissue inhibitor of matrix metalloproteinases together modulate the dynamic balance of ECM [122]. As the major component of ECM, collagen plays a complex role in the PC progression [123]. It can interact with integrins to regulate motility and protein binding of fibril and further enhance structural stability of tumor composition. Col-1 affects E-cadherin level and promotes the production of β-catenin/E-cadherin complexes, aggravating the PC progression [124]. In addition, previous studies have showed that the Col-1 was able to promote metastatic potential of PC cells by increasing the expression of N-cadherins [125]. Notably, the spatial structure of collagen is distinctive with a high alignment and increased length as well as width, which significantly impacts cancer development and

indicates a poor prognosis. Polysaccharide hyaluronan is another extensively evaluated component in the TME of PC. Previous research has demonstrated a close relationship of hyaluronan with angiogenesis as well as increased cell proliferation/migration [126]. Therefore, current treatment strategies have shifted to targeting hyaluronan in the TME of PC to enhance tumor therapeutic effect.

Besides, the complex network of different signalling pathways is involved in the TME to establish links between cancer cells and the tumor milieu. For example, increased expression of Sonic ligand in the Hedgehog signaling pathway promotes desmoplastic reaction and induces pancreatic cancer cell activation [127]. Src/FAK is another important signalling pathway that remarkably affects tumorigenesis [128]. The activation of Src kinase facilitates tumor invasiveness and metastasis formation. On the contrast, inactivation of Src using inhibitors can decrease cancer invasion and delay tumor growth.

Microbiome has been recently demonstrated to inhabit and colonize in the tumor TME [120, 129]. To illustrate the complicated relationship between microbiome and carcinogenesis has become an important research hotspot in the cancer field. In 2017, a paper published on Science journal found that Gammaproteobacteria were the most prevalent bacteria in the TME of PC [130]. This kind of bacteria could ad hoc diminish the chemotherapeutic efficacy of Gemcitabine (GEM) by secreting cytidine deaminase to convert GEM into its inactive form, that is 20,20-difluorodeoxyuridine. Thus, the chemoresistance may be highly relevant to the existence of microbiome in the tumor TME. In another study, Pushalkar et al. using an animal PC model suggested oral antibiotic administration could modify the TME promoting T-cell activation and TAMs differentiation and therefore transforming to immunoactive state [131]. Besides, the antibacterial treatment could substantially increase PD-1 expression, and further improve immunotherapy sensitivity. However, several studies argued that the influence of bacterial on PC should be indirect; rather, the bacterial would cooperate with oncogenic KRAS to tilt the balance of Th1/Th2/Th17 cell ratio, thus promoting tumor

development [132]. Some other studies have showed that microbiome colonization could contribute to the development of PC risk factors such as pancreatitis and diabetes, which may result in microbial dysbiosis and increased gut permeability, translocating the gut microbes to the pancreas [133]. Taken together, antibacterial application has a strong relation with cancer therapy, and mounting evidence further suggests that microbiome in the TME of PC is a potential therapeutic target to prolong survival of patients with PC [134].

4.1.3 Current strategies to intervene the pancreatic cancer progression

The current treatment policy for PC includes surgery, chemotherapy, radiation therapy, immunotherapy, and tissue engineering-based therapy [135]. Among them, the surgical resection is still the most effective approach to treatment of PC in clinic. It can significantly improve the survival compared with other treatment strategies [136]. The commonly adopted surgical operations include pancreaticoduodenectomy, distal pancreatectomy with splenectomy, and total pancreatectomy. Laparoscopic approach is often used in the surgery practice to achieve minimum invasion.

To maximize therapy efficacy, other treatment means also coordinate with surgery. Chemotherapy is the main choice for treatment of metastatic PC in clinic [137]. Among various chemotherapeutics, GEM is a first-line standard of chemotherapy for PC with symptoms improvement seen in 20-30% of PC patients. In a representative example, the treatment outcomes of GEM and fluorouracil were compared [138]. They found that median survival was significantly improved to 5.65 months after using GEM chemotherapy. Besides, it is reported that as compared to GEM alone, the addition of some other drugs (e.g., erlotinib) can improve the overall survival. In another clinical trial, the addition of nanoparticle albumin-bound paclitaxel in GEM could significantly improve the treatment response and increase the overall survival for the metastatic pancreatic cancer [139]. Thus, for the newly diagnosed PC patients with compromised performance only, GEM monotherapy could be adopted; but for patients with other different symptoms, GEM should be administrated together with other pharmaceuticals

or biotechniques.

Immune-based therapy remains the research hotspot for cancer treatment [140]. The basic principle is to stimulate the immune system of patients by recruiting and activating T cells, and then subsequently recognizing and killing cancer cells. At present, cancer vaccines and immune checkpoint inhibitors are the most studied field in the PC treatment [141, 142]. Cancer vaccines are used to elicit the active systemic immune responses and recognize the specific antigen on tumor cells. TLP0-001, a dendritic cell vaccine, has entered clinical trial for treatment of advanced PC which is quite challenging for standard chemotherapy [143]. Immune checkpoint is a unique molecule expressed on the surface of immune cells, which can inhibit the body immune system and reduce anti-tumor immune responses. So far, the most studied immune checkpoint molecules for PC treatment include PD1, CTLA4 and Tim3. Immune checkpoint inhibitors are a kind of monoclonal antibody that can specifically block the functions of corresponding immune checkpoints, thus alleviating their inhibitory effect on immune system. Despite success in preclinical experiments, none of the available immune checkpoint inhibitor has entered the phase III of PC clinical trials. The challenges such as non-specific delivery of inhibitor into the tumor tissue, low effectiveness and overt toxicity remain to be solved.

In such context, to enhance the anti-tumor efficiency of chemotherapy and immunotherapy, tissue engineering-based strategies have been more and more explored (**Figure 4-2**) [144]. To illustrate, to overcome the penetration limitation caused by intense desmoplastic reaction, NPs with active targeted delivery ability such as Au NP [145], mesoporous silica NP [146], and micelle NP [147] have been designed and evaluated. Besides, regarding the TME characteristics described above (i.e., acid pH, high expression of MMP, hypoxia), TME-responsive delivery systems have been constructed to specifically trigger the on-demand cargo release. The hydrogel has also been introduced for PC treatment due to its inhibiting effects on tumor metastasis and prolonged drug release. For example, naphthalene-capped tripeptide (D-Phe-D-Phe-D-

Tyr-p) was developed to constitute nanofibrous physical barrier in the topical tumor site under ALP stimuli. On account of the high expression of alkaline phosphatase placental-like 2 (ALPPL2) in the cancer TME, such hydrogel could serve as a cage in response to ALP to suppress the cancer cell metastasis [148]. Furthermore, fibrous membranes have been used for PC treatment. The drug-loaded fibrous membrane could act as a reservoir to continuously release drug in situ with slow membrane degradation, thus overcoming the limitations of intravenous administration like low efficient delivery and bioavailability. Since PC is a kind of cancer with high recurrence risk after surgery, fibrous membrane-based drug delivery platform would be a good choice to sustainedly kill cancer cells when treating PC [149].

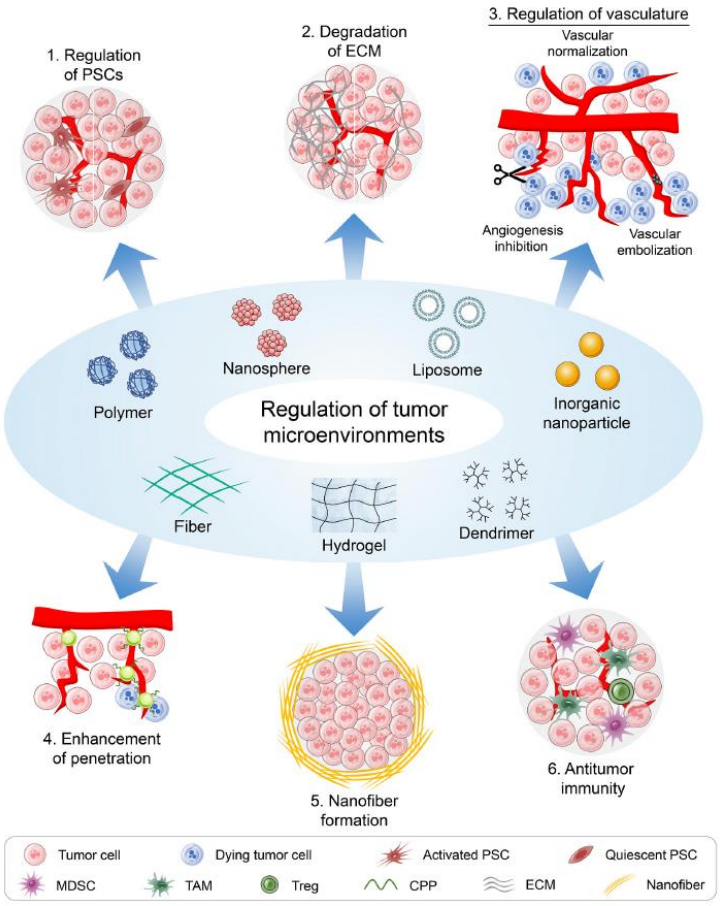

Figure 4-2. Schematic showing different tissue-engineered therapeutical platforms such as polymer/inorganic NP, nanosphere, liposome, fiber, hydrogel and dendrimer molecule for PC treatment. Reproduced with permission from [144]. Copyright 2021, Elsevier.

4.1.4 Motivation and objective

Although adjuvant chemotherapy, like use of GEM, could reduce the recurrence risk of PC and improve the prognosis after surgery, its therapeutical efficacy is highly limited since the systemic administration may cause nonspecific drug distribution, which may reduce the bioavailability and result in severe adverse effects. In addition, the dense fibrous connective tissues within PC may serve as a natural barrier to hinder the drug from enrichment in the disease site through blood circulation, thereby significantly reducing the therapeutic outcomes. Furthermore, sparse blood vessels characteristic for PC further makes the systemic drug delivery low efficient, limiting the capacity of GEM to combat tumor cells. Most importantly, recent studies demonstrated that microbiome in the microenvironment of PC like *Gammaproteobacteria* can reduce GEM chemotherapeutic efficacy and enhance drug resistance by transforming GEM into inactive form [130]. For these reasons, novel anti-PC treatment means seek to incorporate the antibacterial function, with an aim to locally combat the cancer cells and bacteria synergistically and thus better improve the drug delivery efficacy and ultimately cancer therapy outcome.

Electrospun fibrous membranes have been widely used in drug delivery for cancer therapy in terms of their high surface area, high drug loading efficiency, controllable drug release, and diversified structure [4]. Unfortunately, these conventional electrospun fibers have a single biofunction and only focus on the clearance of tumor cells, thus failing to balance curative effects and side effects during the long-term adjuvant chemotherapy. In this study, we proposed to fabricate a multifunctional electrospun membrane scaffold with anti-bacterial and anti-cancer performances for locally implanting in the tumor resection margins to enhance chemotherapeutical outcomes, preventing the recurrence of pancreatic cancer after surgery (**Figure 4-3**). To this end, we first prepared GEM-loaded PLLA electrospun membrane scaffolds by feasible blending electrospinning, followed by two-step in-situ reduction of Ag mediated by TA. Due to the superior good adhesive capacity, TA can form a

multifunctional coating onto PLLA fibers and then reduce the silver nitrate to Ag NPs tightly bound to the surface of TA coating. The resultant electrospun fibers are expected to have multiple synergistic effects after implantation *in vivo*: (1) the surface-deposited TA/AgNP complexes work as an armour onto the PLLA fibers, acting as a barrier to impede GEM diffusion and facilitate a sustained release pattern; (2) TA/AgNP complexes equip the system with excellent anti-bacterial performance, which is believed to reduce surgical site infection rate and alleviate the GEM resistance; (3) the delivery system itself (i.e., PLLA-TA-Ag) exhibits superior inhibitory effects on tumor cell growth both *in vitro* and *in vivo*, and can work together with GEM to enhance the anti-tumor efficacy. The morphology, drug release profiles, biocompatibility, anti-bacterial and anti-cancer activity was systematically evaluated. This study provided a proof-of-concept demonstration of the combined anti-cancer and anti-bacterial strategy to effectively enhance the efficacy of postoperative adjuvant chemotherapy and prevent cancer recurrence. We envision our system represents a safe and efficient scaffold to significantly improve patient's survival after surgery.

Objectives of this chapter include:

1. To fabricate a multifunctional GEM-loaded PLLA-TA-Ag electrospun membrane scaffold via blending electrospinning and two-step *in-situ* Ag NP reduction strategies.
2. To characterize the morphology, chemical composition, mechanical properties, and GEM release behavior of the prepared electrospun membrane scaffold.
3. To evaluate the *in vitro* cytotoxicity, anti-tumor, and anti-bacterial performances of the PLLA-TA-Ag electrospun scaffold.
4. To demonstrate the ability of PLLA-TA-Ag electrospun scaffold to prevent cancer recurrence *in vivo* and explore the underlying mechanisms.

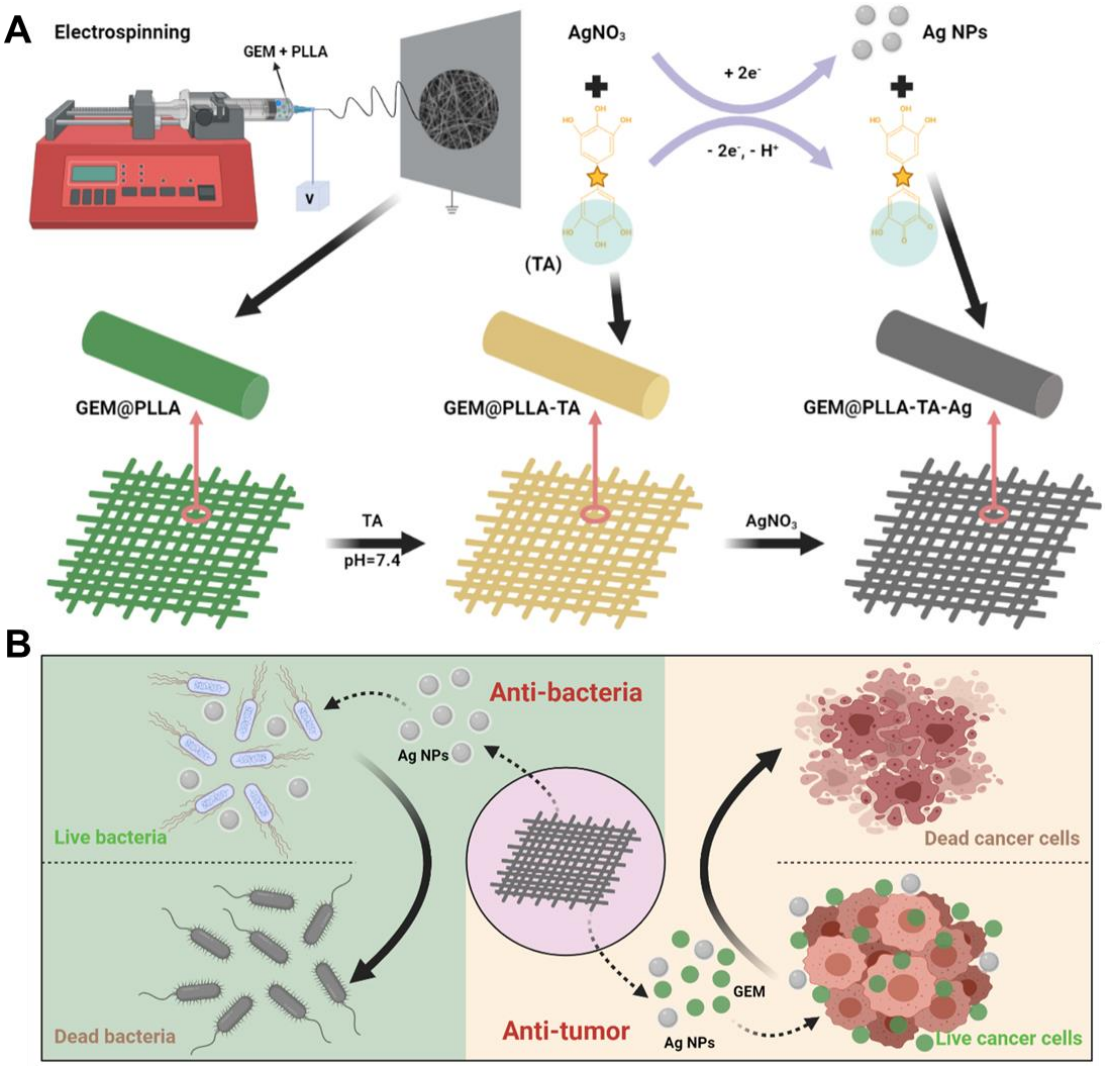

Figure 4-3. Schematic showing (A) the fabrication process of the GEM@PLLA-TA-Ag nanofibrous membrane and (B) its synergistical anti-bacterial and anti-tumor effects for prevention of pancreatic cancer recurrence. Figure created with BioRender.com.

4.2 Methodology

4.2.1 Materials

PLLA with M_w=100 kDa was acquired from Jinan Daigang Co. (Jinan, China). PI 2959, HFIP, and GEM was purchased from Aladdin, Shanghai, China.

4.2.2 Preparation of anti-bacterial and anti-cancer fibrous membrane

GEM-loaded PLLA electrospun membranes were prepared by blending GEM into the PLLA electrospun precursor solution prior to electrospinning. PLLA precursor solution

was firstly prepared at 20 w/v % (obtained by adding 0.6 g PLLA into 3 mL HFIP followed by constant stirring until completely dissolved). Then, different weights of GEM (90, 180, 360 mg) were added into the PLLA precursor solution to finally obtain the electrospun solutions (named GEM1@PLLA, GEM2@PLLA, and GEM3@PLLA, respectively). The detailed electrospinning parameters was showed as follows: the distance between collector and injector was 20 cm; voltage was fixed at 15-20 kV; electrospun solution was pumped at a speed of 1 mL/h. PLLA without addition of GEM was used as the control group.

Next, the TA-mediated in-situ Ag reduction onto the surface of GEM-loaded PLLA fibers was achieved by simple two-step dipping strategy. Firstly, the as-prepared GEM-loaded PLLA fibers were immersed in a TA aqueous solution (60 wt%) for 24 h with constant stirring to enable TA molecule infiltrate into electrospun membranes. Then, the membranes were rinsed thoroughly with deionized water to remove the free TA molecule. After drying, the TA-treated electrospun membranes were dipped into silver nitrate aqueous solution (20 mg/mL) at room temperature for overnight to enable in-situ reduction of Ag NPs onto the PLLA fiber surface mediated by TA. Then, the GEM@PLLA-TA-Ag membranes were rinsed with deionized water thoroughly to remove the excessive uncoated Ag NPs and stored at 4°C for further experiments.

4.2.3 Characterization of the fibrous membrane

The morphology of electrospun membranes was examined by SEM. The samples were sputter-coated with gold before observation. Subsequently, the EDS was used to assess the element composition of the resultant electrospun membranes. FTIR was also used to analyze the chemical structure of different electrospun membranes. Special acknowledgement and gratitude are given to Mr. Bo Liang for FTIR characterization. In addition, uniaxial tensile tests were performed to analyze the mechanical properties of as-prepared scaffolds using a mechanical tester (Instron, US) [62]. Briefly, samples were cut into 50 mm×10 mm rectangular samples. Then, we measured the thickness of each sample 3 times using a micrometer (Syntek, China) and fixed them to the

instrument by pneumatic clamps. To obtain the stress-stain curve, the samples were subsequently stretched longitudinally at a speed of 5 mm/min until failure (n=4).

4.2.4 *In vitro* GEM release

The fibrous membrane samples (25 × 25 mm, total mass ≈ 70 mg) were immersed in a 15 mL centrifugal tube containing 5 mL PBS (pH 7.4), and maintained in a thermostat shaker at 37°C with 100 cycles min^{-1}. After incubation for different time periods (0, 2, 8, 12, 24, 36, 48 h, 4, 7, 10, 14, 18, 24 and 30 days), 1.0 mL supernatant was collected from the centrifugal tube for analysis, while 1 mL fresh PBS was added into the centrifugal tube. Then, high-performance liquid chromatography (HPLC) was used to measure the quantity of released GEM in the supernatant. Special acknowledgement and gratitude are given to Mr. Shang Lv for detecting GEM concentrations via HPLC. The detailed parameters were showed as followed: a mixed solution of ammonium acetate buffer (0.05 mol/L) and methanol (90:10 v/v %) was used as the mobile phase, flow rate was fixed at 1 mL/min, the detection wavelength was 268 nm, C18 column (50 mm × 4.6 mm for length, 5 μm for filler size) was used in the test with temperature of 30 °C. To evaluate the long-term anti-cancer properties, PANC-1 cells, a human pancreatic cancer cell line, were treated with extracts from the membranes after 30-day incubation. Briefly, PANC-1 cells were seeded at a density of 1×10^4 cells/cm^2, and then different scaffolds after release test were added into each well. After co-culture for 1 and 3 days, live/dead staining was performed to evaluate cell viability. Cells were stained with calcein-AM/propidium iodide for 20 min, and observed under a fluorescence microscope. The ratio of live cells to total cells. i.e., cell viability, was calculated using ImageJ software. Furthermore, cell proliferation was revealed by CCK-8 analysis, following the manufacturer's instructions. In brief, CCK-8 solution was added at a 10% volume of culture medium. After 4-h treatment, the absorbance at 450 nm was measured by a microplate reader.

4.2.5 Biocompatibility test

The biocompatibility of prepared PLLA, PLLA-TA, PLLA-TA-Ag membranes were

evaluated by live/dead staining. Special acknowledgement and gratitude are given to Mr. Bo Liang for assisting to complete the biocompatibility experiment. Briefly, the samples were incubated in the culture medium for 24 h at 37°C. Then, the extracts of different scaffolds were added to PANC-1 cells (seeded at a cell density of 1×10^4 cells/cm^2) and co-cultured for 1, 3 and 5 days. Subsequently, the live/dead staining (Thermo Fisher, Hong Kong) was performed following above-described protocol to evaluate cell viability.

4.2.6 Cell morphology observation

To observe the morphology of cells onto the scaffolds, PANC-1 and NIH/3T3 were used as the model cells. After complete sterilization of samples by ethanol and UV irradiation, the cells were seeded onto the membrane at a cell density of 1×10^4 cells/cm^2. After culture for 1 day, samples were rinsed with PBS and fixed using 4% paraformaldehyde for 20 min, followed by staining with intracellular filament F-actin (phalloidin, Alexa Fluor 488, Thermo Fisher, Hong Kong) and cell nuclei (4',6-Diamidino-2-phenylindole dihydrochloride, DAPI, Thermo Fisher, Hong Kong) according to the manufacturer's instructions. Finally, the samples were observed using a confocal microscopy (Leica TCS SPE Confocal Microscope).

4.2.7 Cytotoxicity of GEM-loaded membrane

The tumour-killing effect of the GEM-loaded membranes was evaluated by live/dead staining. Special acknowledgement and gratitude are given to Mr. Bo Liang for assisting to complete the cytotoxicity test. Briefly, PANC-1 and NIH/3T3 were seed at a cell density of 1×10^4 cells/cm^2. After culture for 1 day, the extracts of different scaffolds prepared using the protocol described above were added to culture dish and continue to co-culture for 1, 3 and 5 days. Subsequently, the live/dead staining (Thermo Fisher, Hong Kong) was performed following above-described protocol to evaluate cell viability.

4.2.8 Anti-bacterial test

The *in vitro* anti-bacterial assessment of different samples was assessed against *Citrobacter freundii* (a representative *Gammaproteobacteria*) using the colony counting method [94]. Special acknowledgement and gratitude are given to Miss. Di Suo for completing the anti-bacterial study. Briefly, bacterial cells were cultured in Mueller-Hinton broth (MHB) for 24 h in a 37°C incubator with 100 rpm in a shaker. Then, 0.5 mL of bacterial suspension (1×10^6 CFU/mL) were spread onto the samples and incubated for another 24 h at 37°C. The bacterial suspension without treatment with samples was set as the control group. Then, 2 mL PBS was added to each group and keep shook for 20 min to re-suspend the survival bacteria. After a series of dilution, the bacterial suspension was spread onto Luria-Bertani agar plates. The number of colonies on the Luria-Bertani agar plates were finally counted after 24-h culture.

4.2.9 Residual tumor model

Tumor model was established by subcutaneously inoculated ~1×10^7 pancreatic cancer cells (PANC-1) into the left side of the nude mice's back. When the tumor volume increased to 100 mm^3, mice were randomly divided into four groups (n = 4) (control, GEM, PLLA-TA-Ag and GEM2@PLLA-TA-Ag groups). Special acknowledgement and gratitude are given to Mr. Yang Luo for helping the animal experiment. Then, we made a small incision on the mice skin and removed three-quarters of the tumor. The control group and GEM group were intraperitoneally injected with saline and GEM (100 $mg\cdot kg^{-1}$) respectively twice a week. Then, the 2×2 cm electrospun fibrous membranes were implanted into the residual tumor site of the remaining treatment groups. After that, the mice were weighed and the tumor size was calculated as follows: $V = (a \times b^2)/2$ (a and b represent the length and width of the tumor, respectively). After the mice were euthanized, residual tumors were collected for further H&E staining analysis and immunohistochemical analysis.

4.2.10 Histological examination

At day 14, all mice were euthanized, and the residual tumor tissues were collected, scaled, and photographed. Then, these tumor tissues were fixed in 4% formaldehyde, dehydrated with gradient ethanol, embedded in paraffin blocks, cut into sections with 5-μm thickness, and stained with hematoxylin and eosin (H&E) (Beyotime, China) for microscopic observation. To better understand the antitumor efficacy of our membrane, immunohistochemical analysis was then conducted by incubating tumor slices with the rabbit polyclonal antibodies such as Ki-67, B-cell lymphoma-2 (Bcl-2), and cleaved caspase-3 (Abcam, UK). After staining, an optical microscope (Olympus, Japan) was used to observe and photograph. Semi-quantitative analysis of immunohistochemical staining results was carried out according to previously published literature [149, 150].

4.3 Results and Discussion

4.3.1 Characterization of the electrospun fibrous membrane

In this project, we aim to fabricate a multifunctional membrane scaffold with anti-bacterial and anti-cancer performances to suppress the recurrence of pancreatic cancer after surgery. To this end, we first prepare the GEM-loaded PLLA membrane scaffolds by blending electrospinning. As showed in the **Figure 4-4**, the pure PLLA electrospun membrane showed even fibrous structure, and the incorporation of GEM into the PLLA membrane did not change the morphology of membrane scaffolds. Besides, fibers diameters for PLLA, GEM1@PLLA, GEM2@PLLA, and GEM3@PLLA are 3.22 ± 0.07, 1 ± 0.11, 1 ± 0.12, and 1 ± 0.13 μm respectively. The incorporation of GEM into PLLA decrease its fiber diameter; however, the fiber diameter in GEM-containing groups showed no obvious difference.

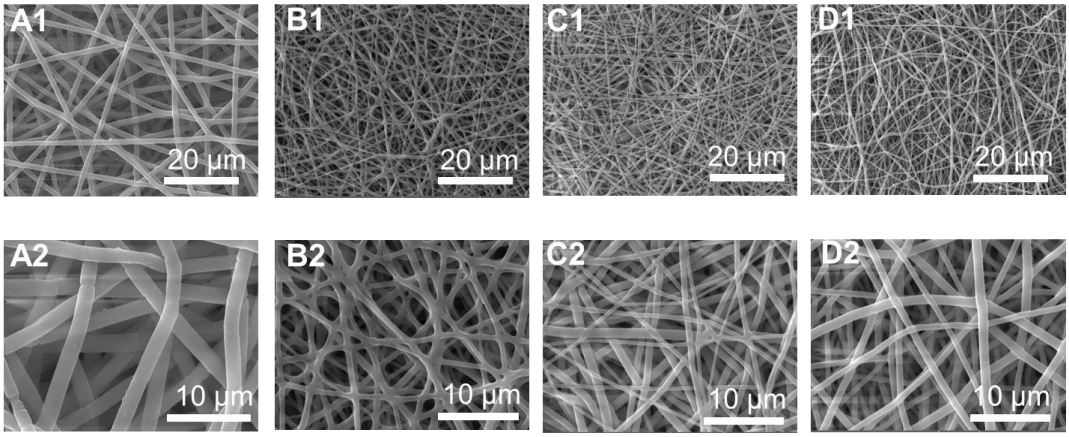

Figure 4-4. SEM images of PLLA electrospun fibrous membranes containing different GEM content: (A) 0 mg/ml; (B) 30 mg/ml (GEM1); (C) 60 mg/ml (GEM2); and (D) 120mg/ml gemcitabine (GEM3). A2, B2, C2 and D2 were the magnified figures of A1, B1, C1, and D1 images.

Next, we use the EDS to characterize the chemical components of different membrane scaffolds. As showed in the **Figure 4-5**, there was a F signal in the EDS spectra of GEM-containing groups, which indicated the successful incorporation of GEM into the membrane scaffolds. It is worth noticing that the F element weight was increased with GEM incorporation amount, which demonstrated we could adjust the GEM loading amount by easily changing the amount of GEM blended.

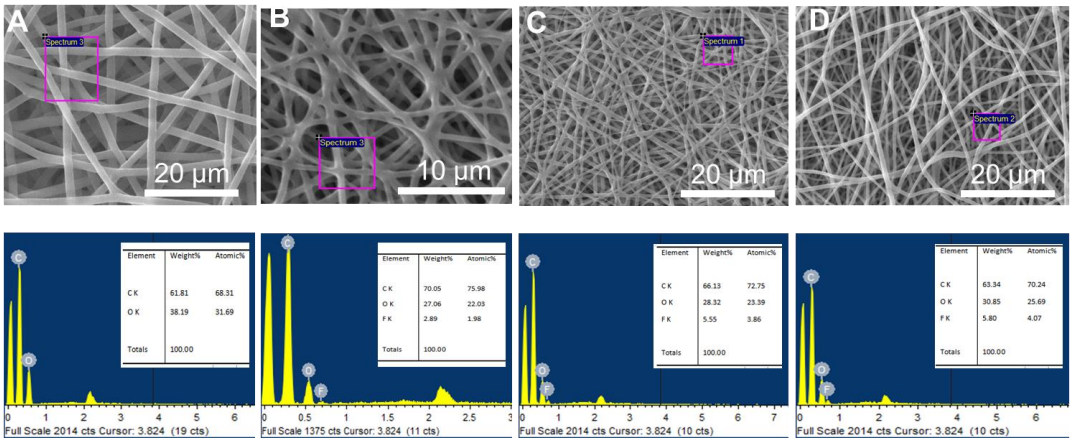

Figure 4-5. EDS results of (A) pure PLLA, (B) GEM1@PLLA, (C) GEM2@PLLA, and (D) GEM3@PLLA.

In the next stage, we used the TA as the reducing agent to modify the surface of membrane scaffolds, and then endowed the scaffolds with excellent anti-bacterial performance by *in-situ* reduction of Ag NPs onto the membrane fibers. Such facile two-step modification strategy was conducted in aqueous solution at room temperature without involvement of any organic solvent, showing great potential in the practice biomedical application. Due to the high specific surface area of electrospun fibrous scaffolds, we believe such membrane will be beneficial for *in-situ* Ag NP reduction. Here, we explored two methods to prepare the samples. On the first try, we incubated samples into TA solution without any treatment after obtaining the GEM-loaded PLLA electrospun fibers. As showed in the **Figure 4-6**, the membrane showed white color, and there were many reduced NPs located onto the PLLA membrane. In addition, the EDS results further confirmed the existence of Ag NPs. However, few Ag NPs were observed inner layer of PLLA membranes, which might be due to the less diffusion of TA solution into the hydrophobic PLLA membranes. Next, we modified some steps to expedite TA solution diffusion into fibers by kneading these membranes slightly when incubation into TA solution. As expected, the membrane showed a transparent color indicating the adequate incubation of TA into PLLA fibers. The SEM images showed there were many NPs located onto the electrospun fibers both in the surface and inner layer of membrane. Moreover, we found such two-step modification process did not change the fiber structure of membrane scaffolds (**Figure 4-7**). Since there was still the porous structure in the membrane scaffolds, we believe such microstructure would be beneficial for adequate cell attachment and exert its biological functions. In addition, the EDS further showed the obvious Ag element signal after two-step modification. Altogether, these results demonstrated we have successfully prepared GEM-loaded Ag NPs-anchored PLLA electrospun membranes by combination of blending electrospinning technique and TA-mediated two-step dipping strategy.

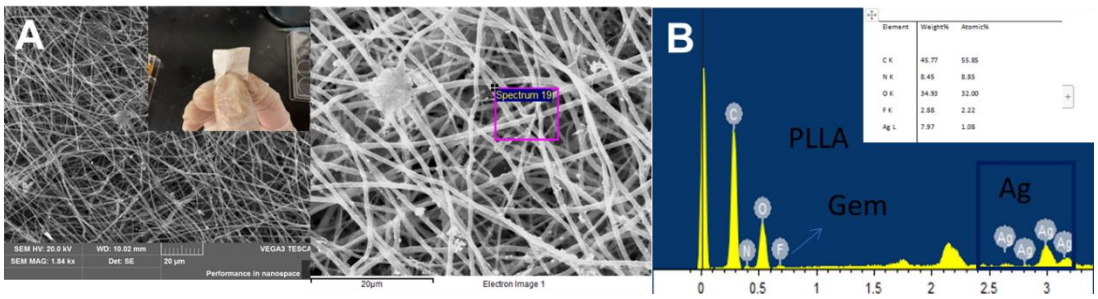

Figure 4-6. (A) SEM images and corresponding (B) EDS results of GEM2@PLLA-TA-Ag membranes prepared by immersing the scaffolds in TA solution for 24 h without adequate immersion by hand and then incubating in AgNO3 solution (20 mg/mL) for 24 h.

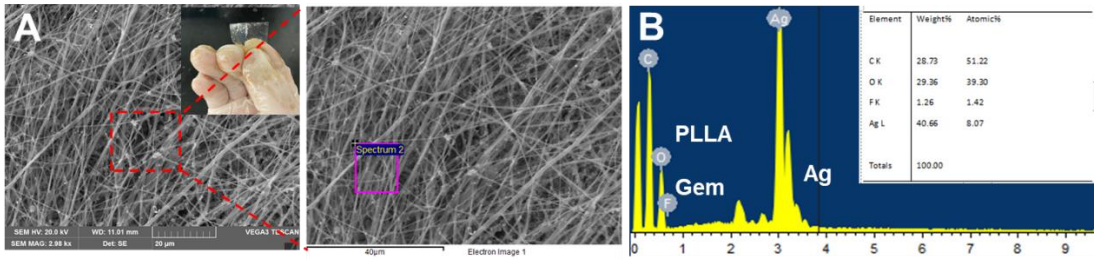

Figure 4-7. (A) SEM images and corresponding (B) EDS results of GEM2@PLLA-TA-Ag membranes prepared by immersing the scaffolds in TA solution for 24 h with adequate immersion and then incubating in AgNO3 solution (20 mg/mL) for 24 h.

Later, we use the FTIR to further characterize the chemical structure of different membrane scaffolds. Special acknowledgement and gratitude are given to Mr. Bo Liang for completing FTIR characterization. The FTIR spectrum of GEM-containing samples exhibited the peak of carbonyl group C=O at 1636 cm^{-1} and 1750 cm^{-1} (**Figure 4-8(A)**). The GEM was verified by increase in the C=O at 1636 cm^{-1} with the increase amount of GEM incorporation. This also further demonstrated the feasibility of GEM loading by blending electrospinning. In addition, compared to original PLLA fibers, neither new peak nor peak shift was found in the FTIR spectrum of PLLA-TA fibers (**Figure 4-8(B)**) [151]. However, the interactions between PLLA chain molecules and Ag NPs are associated with the peak at 3493 cm^{-1}. In addition, compared with PLLA, the carbonyl peak was shifted from 1746 to 1752 cm^{-1} in PLLA-TA-Ag, indicating that Ag

NPs interacted with carbonyl groups from PLLA or oxidized TA by electrostatic or van der Waals forces [152].

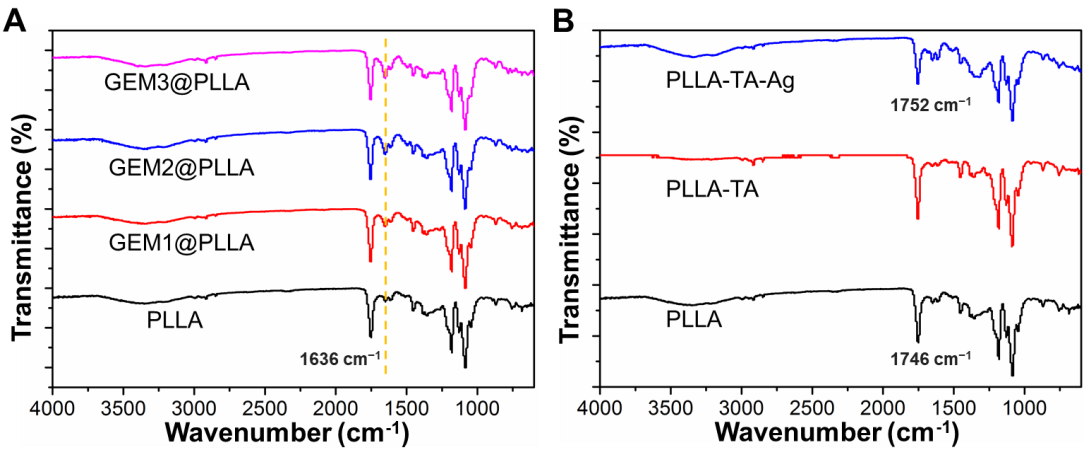

Figure 4-8. FTIR spectra of (A) GEM-loaded PLLA electrospun fibrous membranes and (B) PLLA membranes with TA or Ag treatment.

Next, we evaluated the mechanical properties of different PLLA electrospun fibrous membranes. As showed in the **Figure 4-9**, the mechanical properties were significantly decreased after incorporation of GEM into the PLLA membranes, in terms of the tensile strength, extensibility and tensile modulus. In detail, the tensile modulus for PLLA, GEM1@PLLA, GEM2@PLLA and GEM3@PLLA were 59.02 ± 4.52, 54.52 ± 2.16, 46.67 ± 4.63 and 44.73 ± 3.89 kPa, respectively. In addition, we found that the tensile modulus of GEM2@PLLA was markedly decreased after TA-mediated two-step in-situ reduction of Ag NPs (46.67 ± 4.63 vs 32.71 ± 5.15 kPa). Despite the decrease in mechanical performances of GEM2@PLLA-TA-Ag, its strength and stretchability still meet the requirements of clinical applications. Altogether, our GEM2@PLLA-TA-Ag exhibited good mechanical properties, which would facilitate the surgical operations as a tissue filler after local resection of the tumor tissue, showing great potential in field of biomedical engineering.

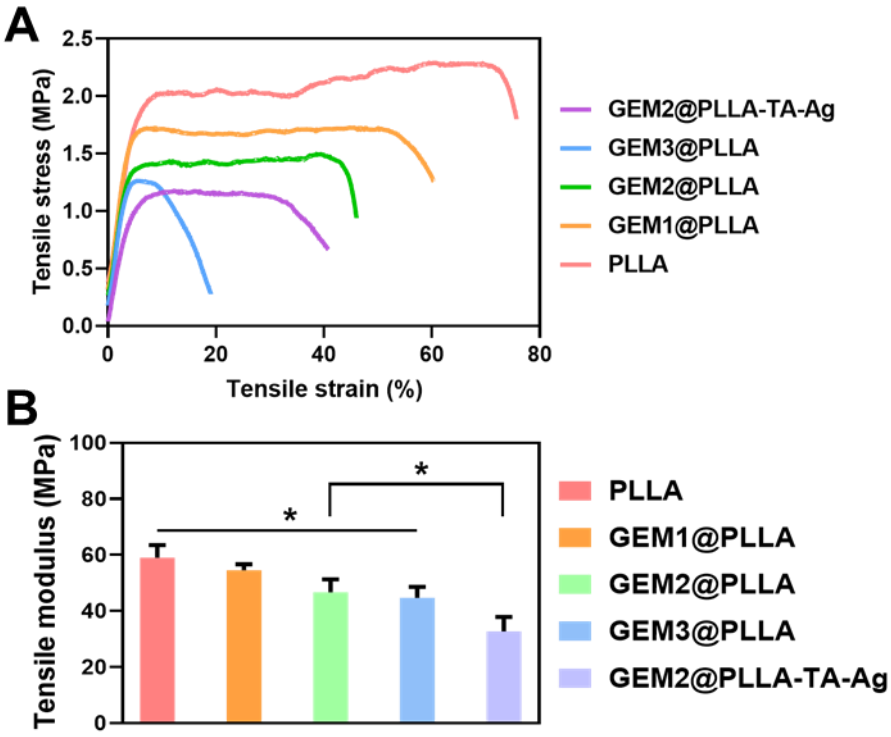

Figure 4-9. The mechanical performances of different PLLA fibrous membranes. (A) The stress-strain curve and corresponding (B) tensile modulus of different material formulations obtained by tensile test.

4.3.2 Characterization of gemcitabine release profiles

Subsequently, we investigated the GEM release profiles from the PLLA electrospun fibers containing different contents of GEM. First, we prepared a standard curve for GEM release (**Figure 4-10(A)**). The R^2 for fitted curve was 0.99996 (~1), indicating its good linear relationship and could be used to accurately detect the GEM concentration in the solution. As displayed in the **Figure 4-10(B)**, the GEM release rate was significantly increased with the increase in the amount of GEM incorporated. In addition, we observed a remarkable burst release of GEM of 37.33 ± 5.07, 47.08 ± 6.61, and 53.17 ± 6.13 % in the first 36 hours and a long-term GEM release pattern of over two weeks for GEM1@PLLA and GEM2@PLLA groups. The burst release of GEM may be beneficial for the elimination of locally residual tumor cells after surgery, while the long-term release may play a critical role in prevention of cancer recurrence. Furthermore, we found after TA-mediated two-step *in-situ* Ag reduction, the GEM

release was significantly decreased. The initial GEM release from GEM2@PLLA-TA-Ag was 21.2 ± 5.45 % within 36 h, significantly lower than that released from GEM2@PLLA group. The GEM release from the PLLA electrospun fibers was mainly through diffusion. The initial burst GEM release was possibly due to the GEM diffusion from the PLLA fibers into the solution after immersion of fibers in water. in addition, the extended GEM release for GEM2@PLLA-TA-Ag may be attributed to the formation of a barrier by TA-Ag complexes, which increase the GEM diffusion way into the surrounding solution. In a short, the GEM2@PLLA-TA-Ag exhibited a satisfactory GEM release profile, showing great potential as a drug carrier for pancreatic cancer therapy.

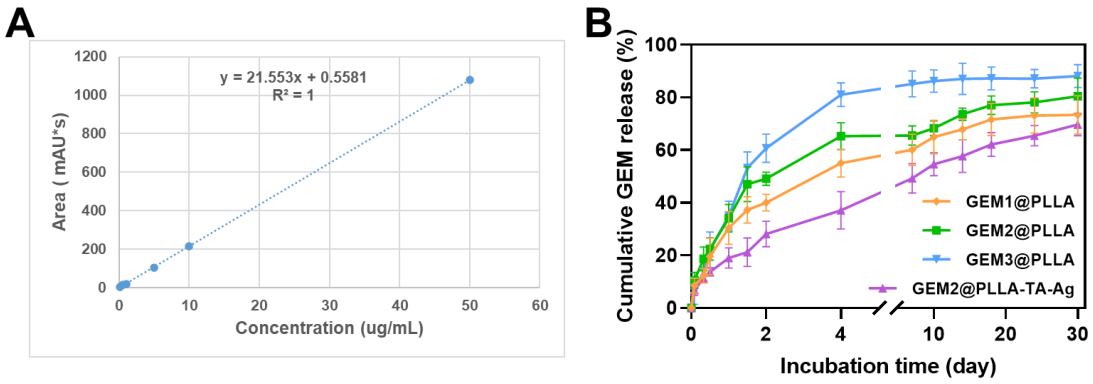

Figure 4-10. (A) Standard curve for GEM release. (B) Cumulative GEM release percentage from the different PLLA electrospun fibers (GEM1@PLLA, GEM2@PLLA, GEM3@PLLA, GEM2@PLLA-TA-Ag).

4.3.3 *In vitro* biocompatibility

Since fibroblast cells have been demonstrated being involved in the PC progression (e.g., promoting PC cell proliferation and metastasis and inducing the GEM resistance), we used NIH/3T3 (a cell line of mouse embryonic fibroblasts) and PANC-1 (a human pancreatic cancer cell line) as the model cells to explore whether the non-GEM-loaded electrospun membranes could influence the growth of fibroblasts and PC cells. We first investigated the biocompatibility of electrospun fibrous membranes by live/dead staining. Special acknowledgement and gratitude are given to Mr. Bo Liang for

assisting to complete biocompatibility evaluation. Both NIH/3T3 and PANC-1 were separately cultured in 24-well plates for one day, and then treated with the extracts of different scaffolds before co-culture for 1, 3 and 5 days. As illustrated in the **Figure 4-11**, there were many green fluorescence NIH/3T3 cells in the control, PLLA and PLLA-TA groups. Quantitation analysis further confirmed that cell viability was similar among these three groups, which suggested their excellent biocompatibility (**Figure 4-12**). However, the cells grown in the PLLA-TA-Ag groups showed a significantly reduced cell viability with almost all cells died after 3-day culture for NIH/3T3 and 5-day culture for PANC-1. Similar results could be found in the PANC-1 cells that PLLA-TA-Ag was harmful to cell growth, indicating its potential anti-cancer effect (**Figure 4-13** and **4-14**). Such phenomenon may be attributed to the oxidative stress induced by Ag NPs, which may induce cell damage by generation of ROS. In addition, the autophagy and apoptosis may also be involved in this progress [153, 154]. These results demonstrated Ag NPs in-situ reduced by TA displayed remarkable cytotoxicity to NIH/3T3 and PANC-1, which may further enhance PC treatment effect.

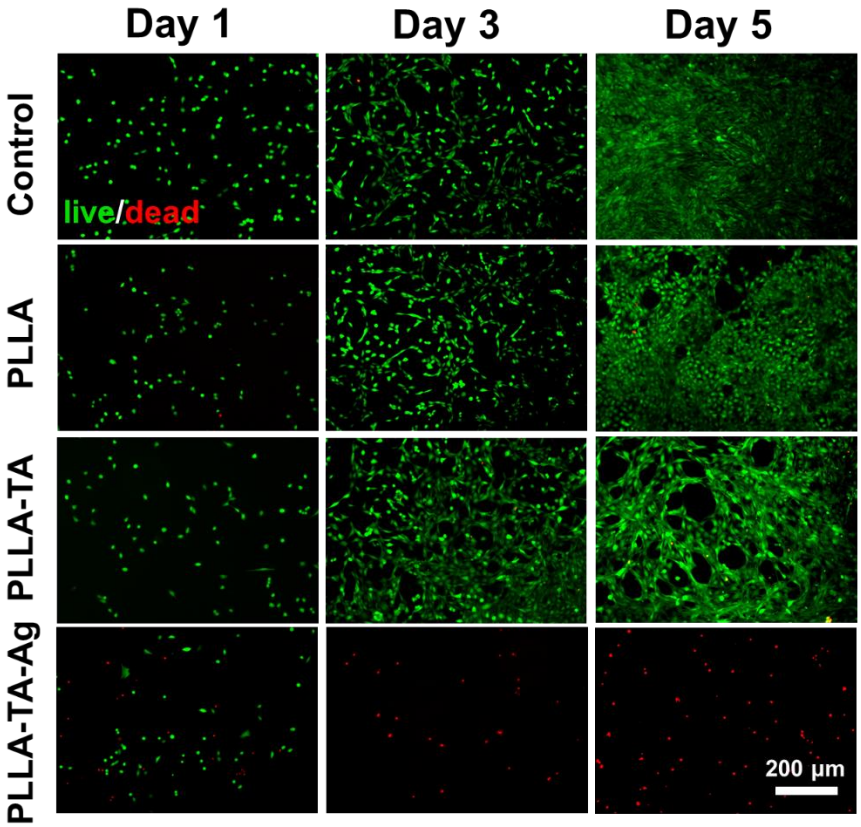

Figure 4-11. Biocompatibility of scaffolds by co-culture of NIH/3T3 with scaffold extracts for 1, 3 and 5 days evaluated by live dead staining.

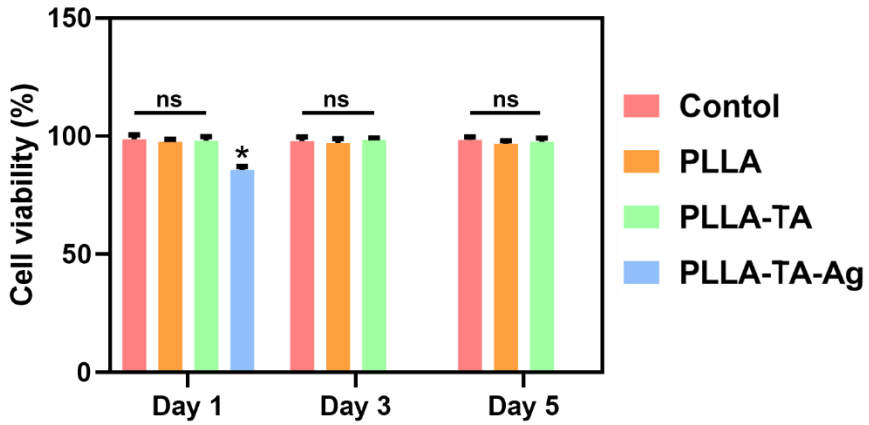

Figure 4-12. Corresponding cell viability of NIH/3T3 after different treatments calculated based on the live dead staining assay.

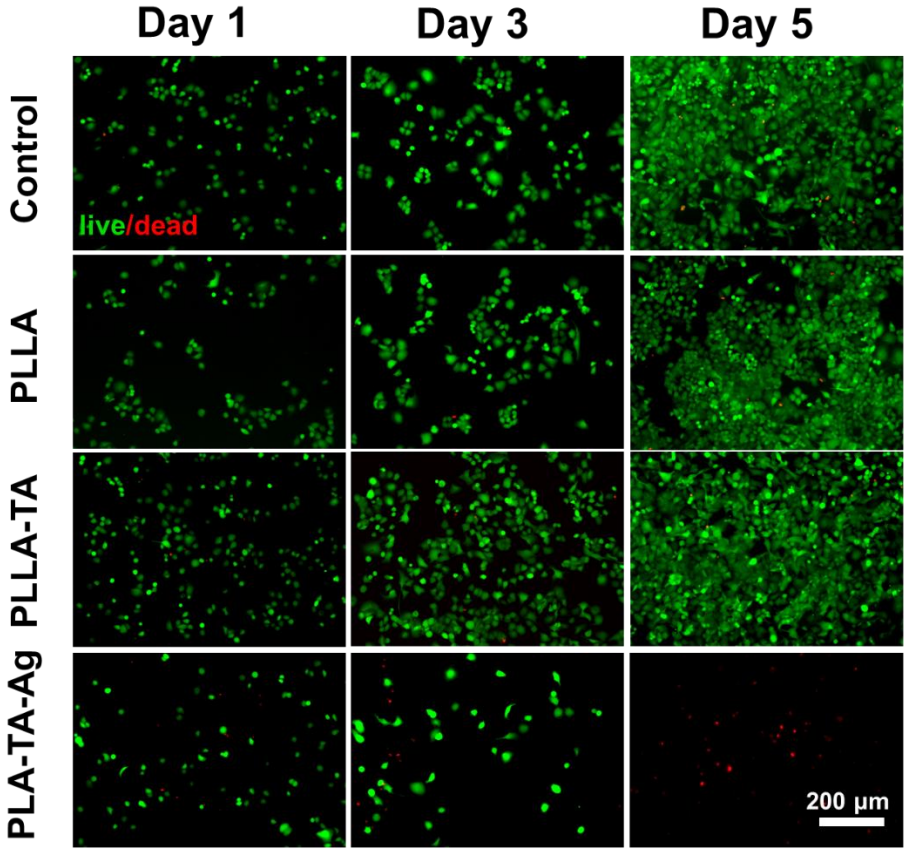

Figure 4-13. Biocompatibility of scaffolds by co-culture of PANC-1 with scaffold extracts for 1, 3 and 5 days evaluated by live dead staining

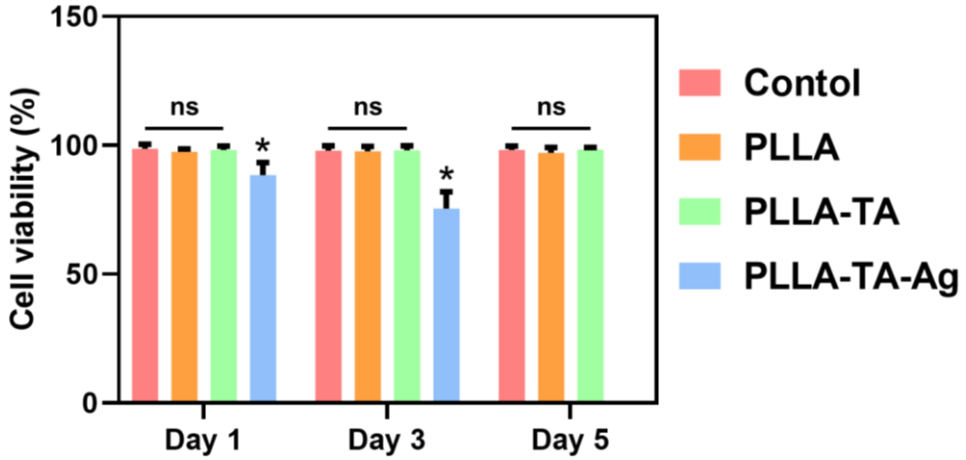

Figure 4-14. Corresponding cell viability of PANC-1 after different treatments calculated based on the live dead staining assay.

Since cell morphology change was associated with cell function, we then evaluated the cell adhesive morphologies onto the different electrospun membranes on day 1 by actin/DAPI staining. As displayed in the **Figure 4-15,** on the first try to assess the cell morphology, although we found the reduced cell number in PLLA-TA-Ag group, the cell morphology was not clear due to the staining failure. Thus, we redid the experiments. As showed in the **Figure 4-16** and **Figure 4-17**, cells on the PLLA and PLLA-TA groups showed similar morphology; the NIH/3T3 showed a shuttle shape while PC cells exhibited a polygonal shape. However, there were much more cells adhered onto the PLLA-TA groups compared with PLLA group, indicating their excellent cell adhesion ability. This could be explained by increased hydrophilicity by TA modification, that facilitated cell attachment [155]. In addition, the increased protein adsorption mediated by TA as well as the direct interaction between protein onto cell membrane and TA molecule onto the PLLA fiber surface maybe the other mechanisms for such enhanced cell adhesion properties [98]. However, the cells on the PLLA-TA-Ag showed an obviously different morphology; both NIH/3T3 and PANC-1 showed an elliptical shape, indicating the poor growth condition. This may be due to the cytotoxicity of reduced Ag NPs as demonstrated in the live/dead staining. Altogether, after implantation of the PLLA-TA-Ag scaffold into the tumor resection

site, the modified TA could rapidly recruit the surrounding residual cancer cells to the scaffold, and then reduced Ag NPs would suppress or even kill the cancer cells, which might be beneficial for *in vivo* PC prevention. The above results showed that our PLLA-TA-Ag scaffolds could work synergistically with GEM-dominated chemotherapy (cargoes) to improve the treatment outcomes of PC therapy.

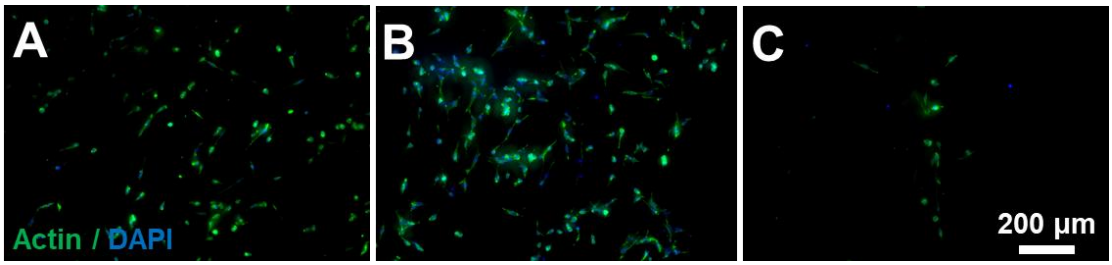

Figure 4-15. The first try to evaluate morphology of NIH 3T3 grown on (A) PLLA, (B) PLLA-TA and (C) PLLA-TA-Ag electrospun membranes for 1-day incubation detected by actin (green) and nucleus (blue) staining.

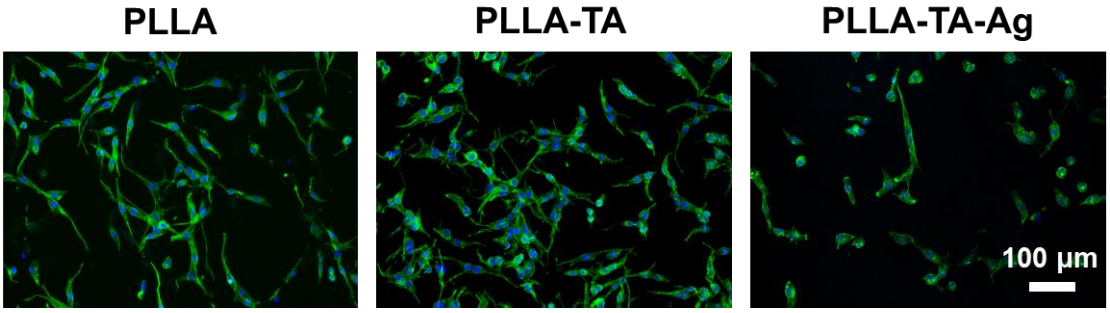

Figure 4-16. Morphology of NIH 3T3 grown on PLLA, PLLA-TA and PLLA-TA-Ag electrospun membranes for 1-day incubation detected by actin (green) and nucleus (blue) staining.

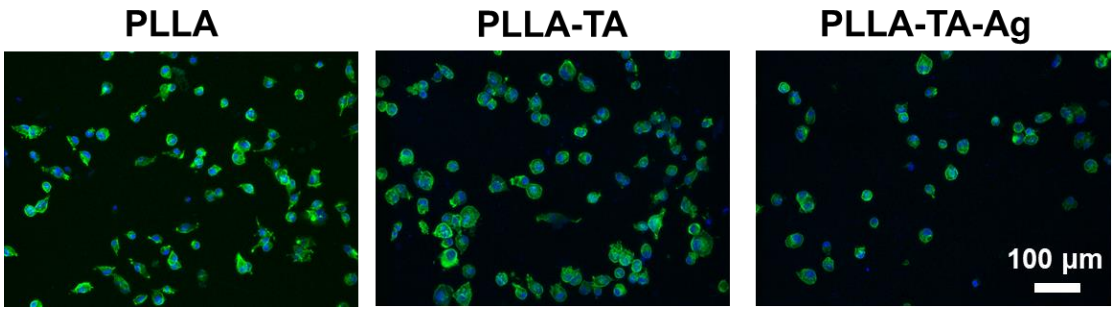

Figure 4-17. Morphology of PANC-1 grown on PLLA, PLLA-TA and PLLA-TA-Ag electrospun membranes for 1-day incubation evaluated by actin (green) and nucleus (blue) staining.

4.3.4 Anti-cancer effects

The anti-cancer effects of GEM-loaded electrospun membranes were evaluated using live/dead staining. As displayed in the **Figure 4-18** and **4-19**, there were some live cells in the GEM1@PLLA group after 1-day culture. However, almost all cells were died at day 3 and day 5. For the GEM2@PLLA, GEM3@PLLA and GEM2@PLLA-TA-Ag, there was no live cells after only 1-day culture, suggesting that GEM released from these scaffolds maintained its bioactivity to induce cell death. These results demonstrated the excellent anti-cancer effects of GEM2@PLLA-TA-Ag. Here, special acknowledgement and gratitude are given to Mr. Bo Liang for assisting to complete short-term cytotoxicity assessment. Then, we further evaluated the ability of these scaffolds to prevent cancer recurrence for a long time. After incubation of electrospun membranes in PBS for 30 days, scaffolds were rinsed and added to culture plates to co-culture with cells for 3 days prior to live/dead staining assay (**Figure 4-20**). The results demonstrated that GEM-loaded PLLA groups showed a slight cytotoxicity, while GEM2@PLLA-TA-Ag exhibited a significant cytotoxicity, as confirmed by much more dead cells (red color) in GEM2@PLLA-TA-Ag group. The results of CCK-8 assay were similar to that of live/dead staining; the GEM2@PLLA-TA-Ag group showed remarkable inhibition effects on cell proliferation. Altogether, GEM2@PLLA-TA-Ag exhibited a combination of short- and long-term anti-cancer ability.

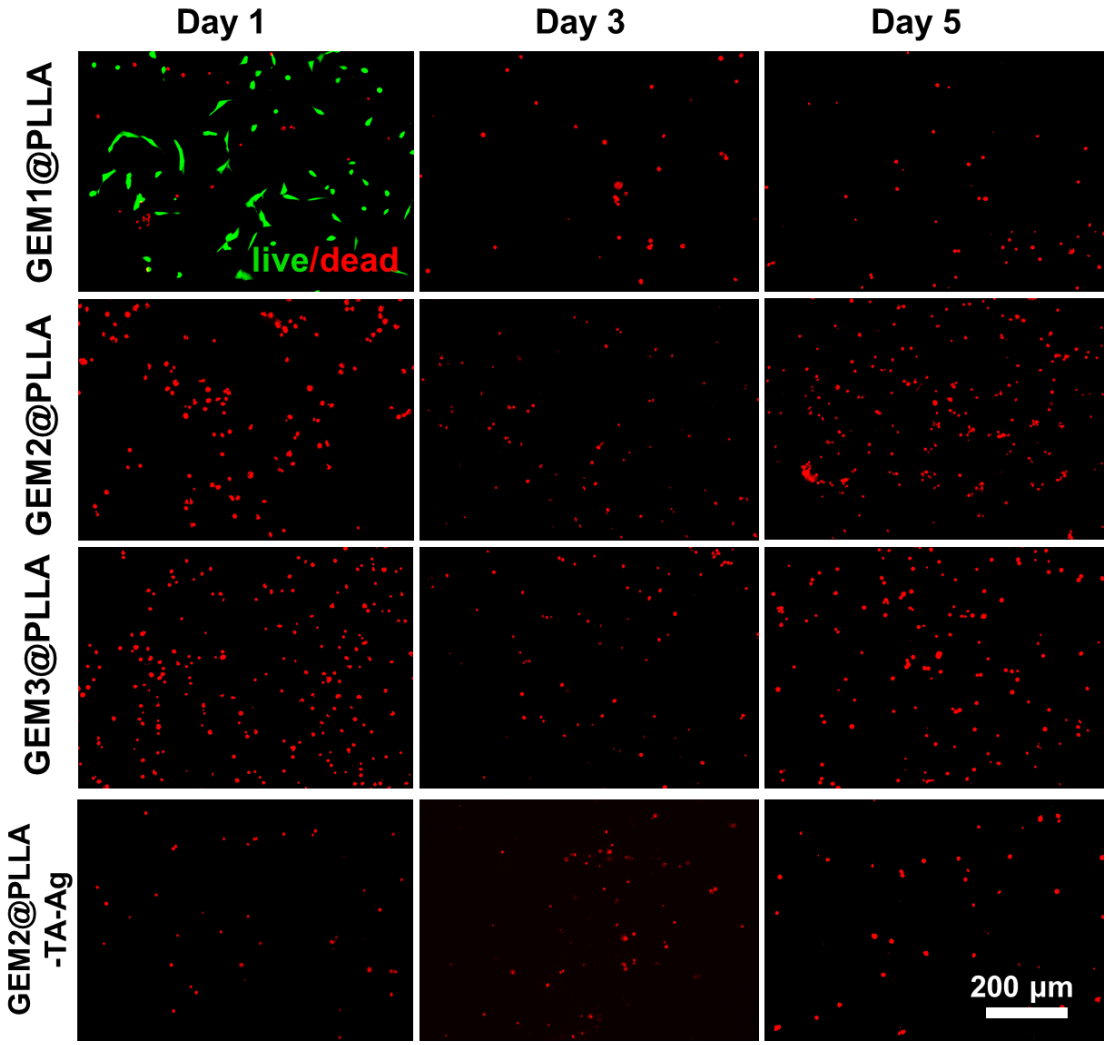

Figure 4-18. Cytotoxicity evaluation of different GEM-loaded PLLA electrospun membranes by co-culture of NIH/3T3 with the scaffold extracts from for 1, 3 and 5 days.

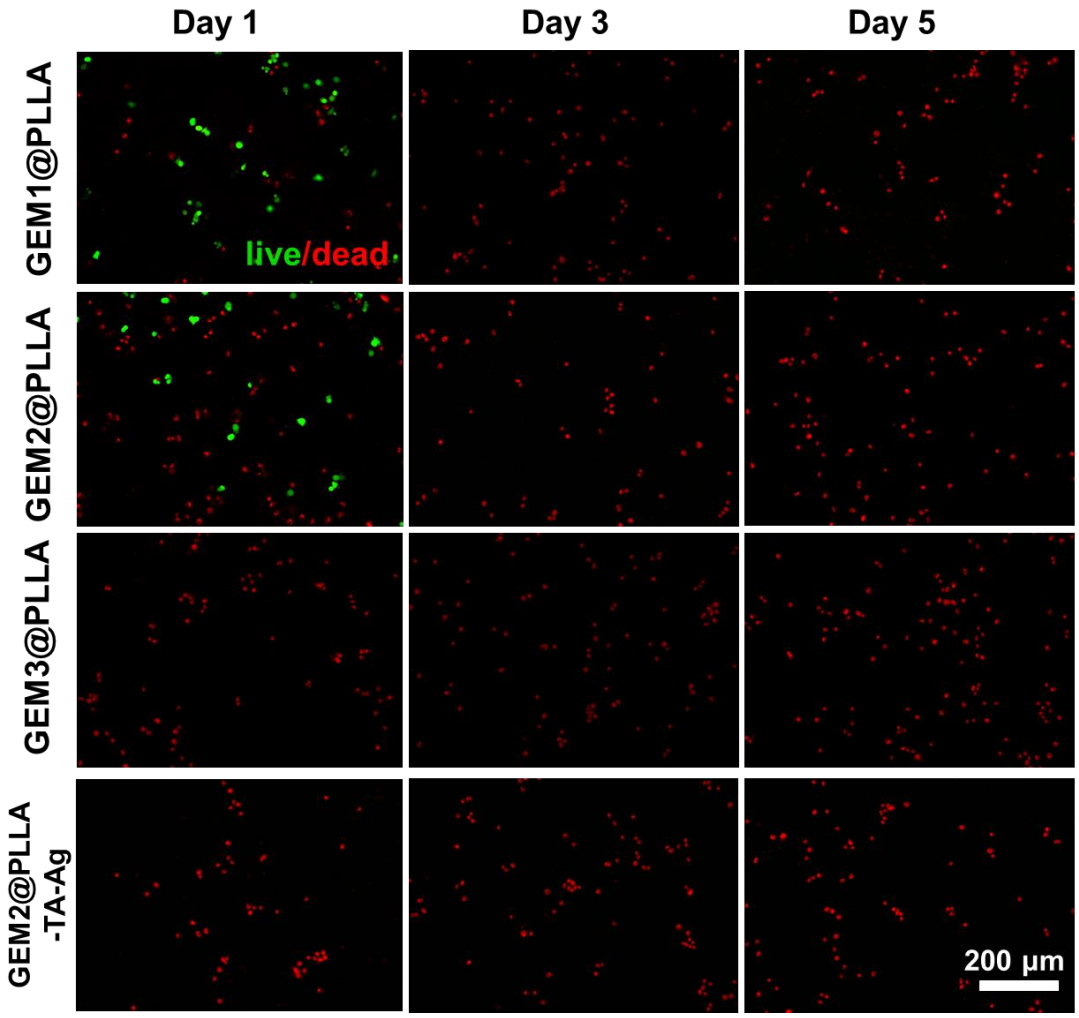

Figure 4-19. Cytotoxicity evaluation of different GEM-loaded PLLA electrospun membranes by co-culture of PANC-1 with the scaffold extracts from for 1, 3 and 5 days.

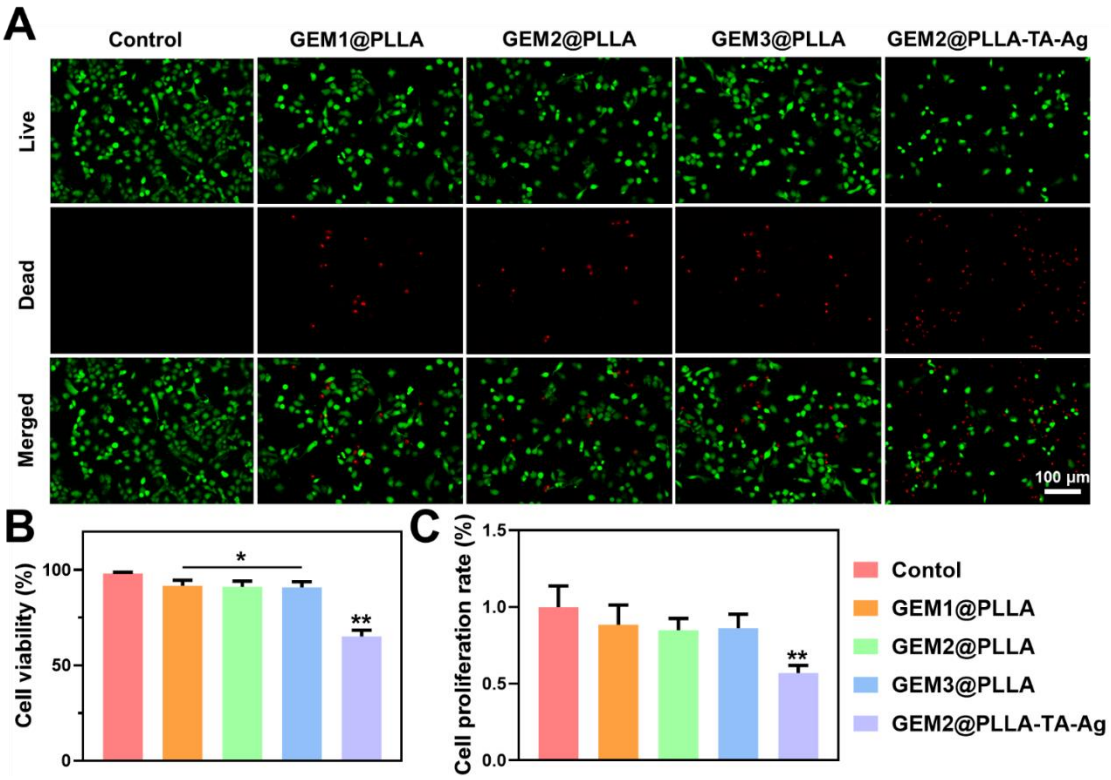

Figure 4-20. Long-term anti-cancer effects of different GEM-loaded PLLA electrospun membranes. (A) Live/dead staining and (B) corresponding cell viability of PANC-1 cells after treatment with different scaffolds for 3 days. (C) Proliferation analysis of PANC-1 cells by CCK-8 assay.

4.3.5 Anti-bacterial effects

Previous studies have demonstrated the *Gammaproteobacteria, the* most prevalent bacteria in the TME of PC, could diminish the chemotherapeutic efficacy of GEM by secreting cytidine deaminase to convert GEM into inactive form, 20,20-difluorodeoxyuridine. To eliminate the influence of *Gammaproteobacteria*-mediated on GEM chemotherapy, we design a dual-functional electrospun fibrous membranes with anti-cancer and anti-bacterial performances. Above results have verified the anti-cancer ability of as-prepared scaffolds. Here, to demonstrate the anti-bacterial effects, we selected the *Citrobacter freundii*., a common subtype of *Gammaproteobacteria* as the model bacteria to evaluate the anti-bacterial performance. Special acknowledgement and gratitude are given to Miss. Di Suo for completing the anti-bacterial experiment. The results showed that colonies of *Citrobacter freundii* on agar

plate of PLLA-TA-Ag and GEM2@PLLA-TA-Ag groups were significantly less than that of PLLA and PLLA-TA group after directly contact with different membranes for 24 h (**Figure 4-21**). Quantitation analysis further confirmed that GEM2@PLLA-TA-Ag group exhibited the most excellent anti-bacterial effects as compared with other groups. Such outstanding anti-bacterial capacity can be mainly ascribed to the inherent antibacterial activity of reduced Ag NPs, which have been demonstrated to combat bacteria by inducing denaturation of cell membranes or generating the ROS [156, 157].

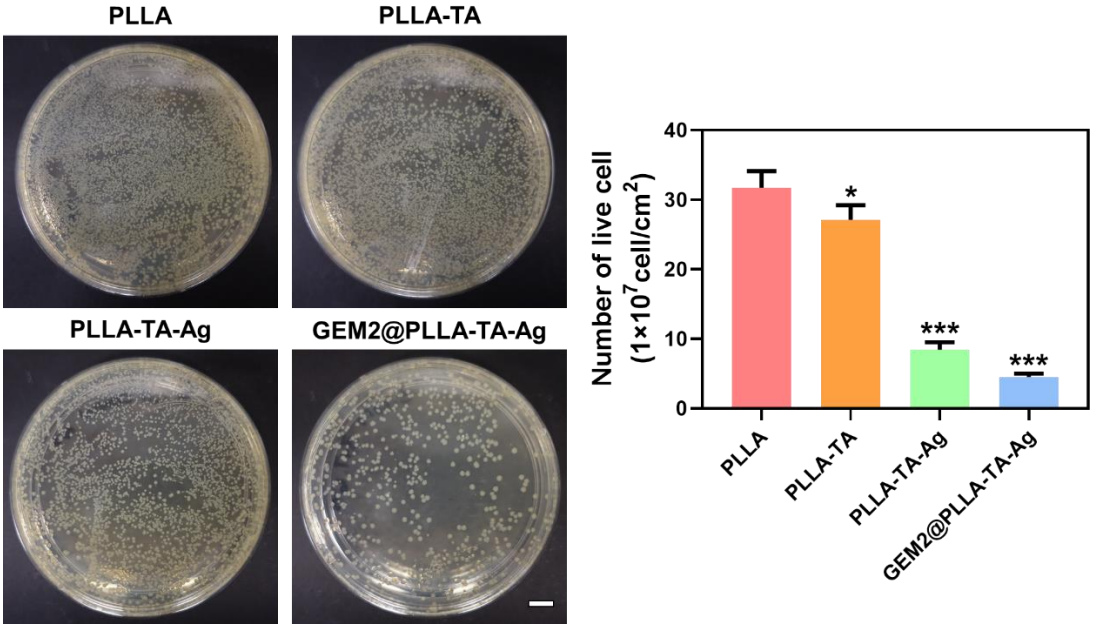

Figure 4-21. (A) Photographs of plates showing the anti-bacterial effects of different electrospun membranes against *Citrobacter freundii*. (B) Relative bacterial viability of *Citrobacter freundii* after contact with different electrospun membranes for 24 h. Scale bar = 1 cm.

4.3.6 *In vivo* anti-tumor recurrence assay

The anti-tumor recurrence ability of electrospun fibrous membranes were further studied *in vivo*. Here, special acknowledgement and gratitude are given to Mr. Yang Luo for helping the animal experiment. As shown in **Figure 4-22A**, the schematic showed the implantation of GEM2@PLLA-TA-Ag electrospun fibrous membrane into

residual tumor for local therapy. It should be mentioned that in clinical setting, such scaffold could be fixed with suture to remain in the surgical site to exert its biofunctions. In **Figure 4-22B**, corresponding residual tumor images displayed that the GEM2@PLLA-TA-Ag group showed the best antitumor effect compared with GEM group and PLLA-TA-Ag group. The variation of tumor volume (**Figure 4-22C**) suggested that the GEM2@PLLA-TA-Ag group had the smallest mean tumor volume (~52 mm^3) among all treatment groups at day 14. As can be seen from **Figure 4-22D**, the residual tumor weight in the PLLA-TA-Ag-GEM group were significantly lower than that in GEM and control group. The above results proved that GEM2@PLLA-TA-Ag group possessed the best of therapeutic effect, which may be due to the synergistic effect of Ag and GEM. In addition, there was almost no significant change in the body weight of nude mice in GEM2@PLLA-TA-Ag group, suggesting that the systemic toxicity was low (**Figure 4-22E**). In order to further confirm the therapeutic effect, histological analyses of tumor tissues were analyzed after 14 days' treatment. H&E staining demonstrated the GEM2@PLLA-TA-Ag group presented more tumor cells apoptosis and the destruction of membrane integrity (**Figure 4-22F**).

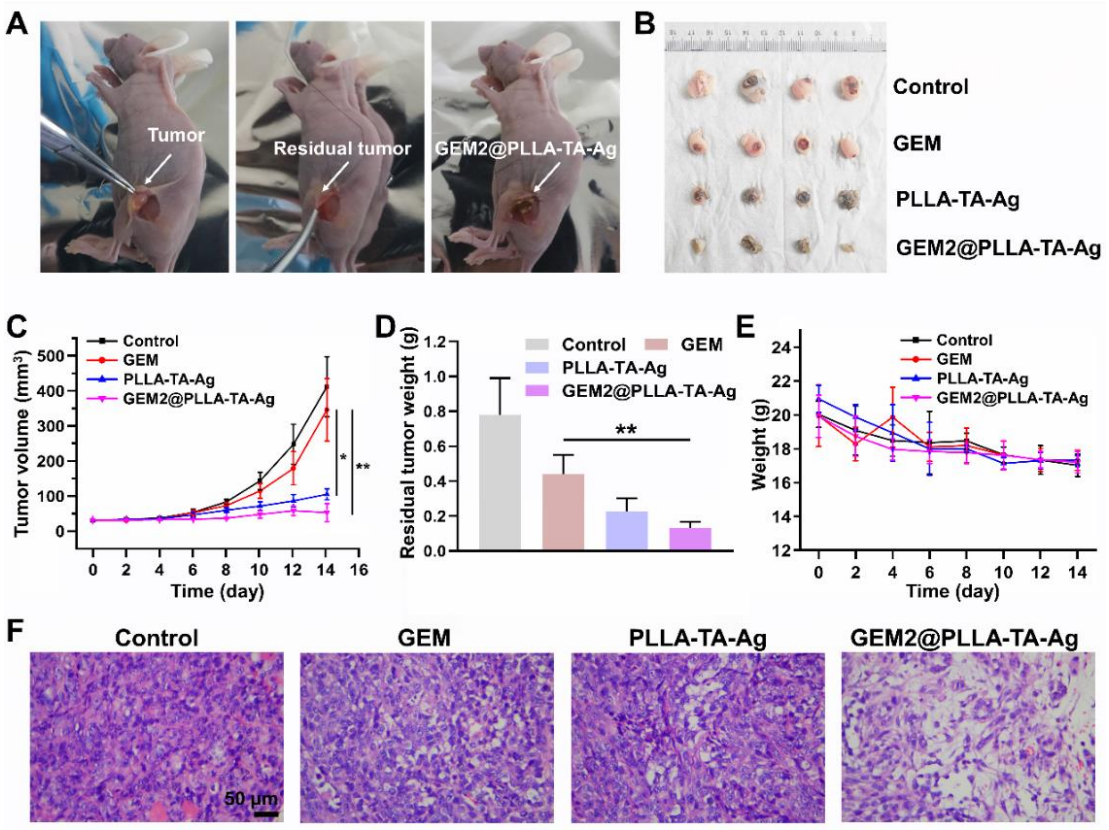

Figure 4-22. *In vivo* anti-recurrence effect in pancreatic tumor-bearing nude mice. (A) The photos of implantation of GEM2@PLLA-TA-Ag in residual tumor of nude mice for local therapy. (B) Photograph of residual tumor of pancreatic cancer (n = 4). (C) Changes of the tumor volume within 14 days. (D) Residual tumor weight of different groups. (E) Mice weight of different groups. (F) H&E staining of the residual tumor after treatment with different groups.

In addition, we investigated the expression of Bcl-2, Ki-67, and cleaved-caspase3 by immunohistochemical staining (**Figure 4-23A**). As shown in **Figure 4-23B**, the anti-apoptosis index Bcl-2 and proliferation index Ki-67 were lower in GEM2@PLLA-TA-Ag group, and the apoptosis index cleaved-caspase3 was higher in GEM2@PLLA-TA-Ag group compared with GEM group and PLLA-TA-Ag group. The results indicated that local Ag and GEM delivery with PLLA-TA-Ag had a good inhibitory effect on tumor recurrence, which was consistent with the above results. In all, these results

indicated that the GEM2@PLLA-TA-Ag has a great capacity of anti-tumor recurrence and certain clinical application potential.

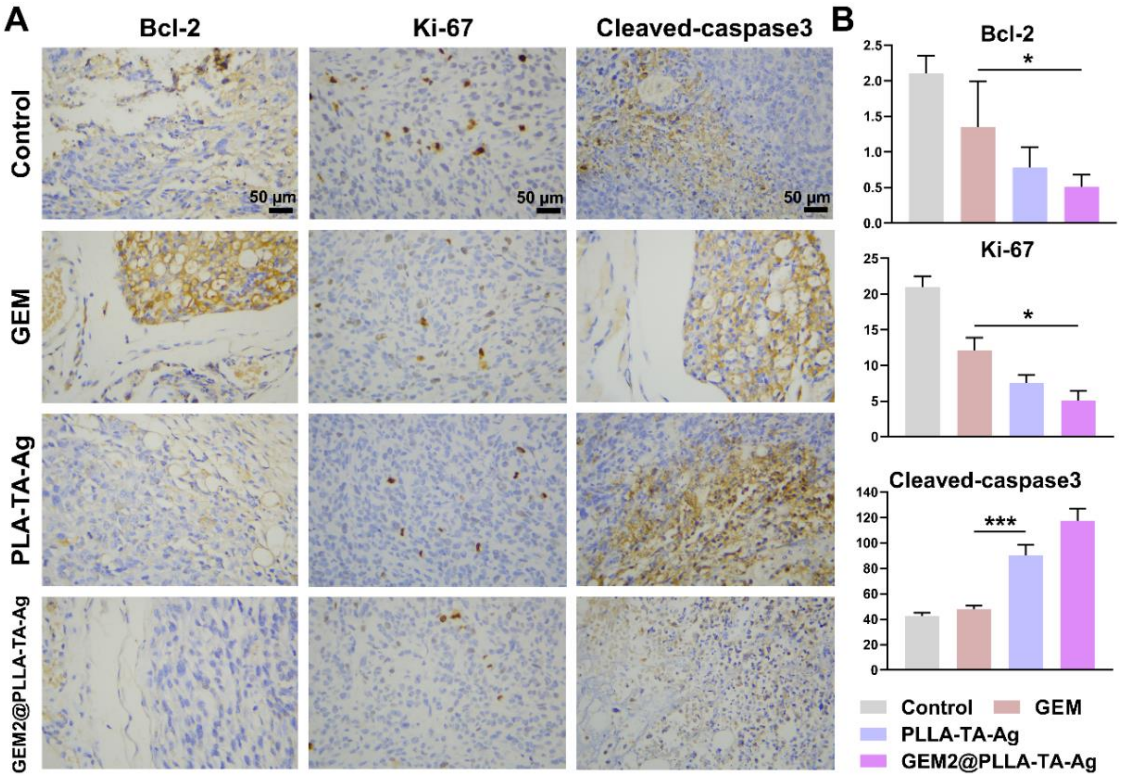

Figure 4-23. (A) Immunohistochemical staining of Bcl-2, Ki-67, and cleaved-caspase3 of tumor tissues at day 14. (B) Semi-quantitative analysis of Bcl-2, Ki-67, and cleaved-caspase3.

4.4 Summary

In summary, we have successfully fabricated a multifunctional GEM-loaded PLLA-TA-Ag membrane scaffold. This facile but delicate design endowed the scaffolds with favourable fibrous architecture and appropriate mechanical property, which could be readily implanted at the tumor resection site during the surgical operation. Besides, this kind of locally implanted GEM-loaded electrospun membrane exhibited a short- and long-term anti-cancer performance, showing its promising application prospect to reduce adverse reactions of intravenously administered GEM and improve treatment outcomes of cancer recurrence after surgery. Furthermore, the Ag NPs on the scaffolds

prepared by two-step in-situ reduction strategy exhibited synergistical anti-tumor effects and excellent anti-bacterial ability. Due to simple fabrication process, we believe such strategy could be extended to other scaffold preparation to prolong drug release and thus facilitate long-term disease treatment. All in all, in terms of the excellent anti-bacterial and anti-cancer performances, we envision the resultant GEM2@PLLA-TA-Ag will have great potential in addressing the issue of chemotherapy drug resistance caused by bacteria in the pancreatic microenvironment after direct implantation in surgical site and exerting its powerful synergistic anti-tumor recurrence effects.

Chapter 5 Conclusions and recommendations for future work

TME occupies a prominent place in the progression of disease and tissue regeneration. The principal focus of this work was to engineer novel scaffolds for tendon repair and PC therapy inspired by the microenvironment in the tendon and PC tissue. For the tendon repair, we first focus on the elevated expression of MMP enzymes to design an MMP-responsive drug release system to realize an on-demand TME-triggered drug therapy. Besides, based on the promoting effects of ERK2 activation on tendon adhesion, we chose the ERK2-siRNA as the therapeutic agent to sustainedly suppress ERK2 expression, achieving the targeted gene therapy. For the second project, we designed a Janus dual-layer patch with anti-oxidative and anti-inflammatory performances for tendon repair inspired by the ROS accumulation and inflammation response during the early healing stage that might affect the tendon repair outcomes and later adhesion formation. For the third project, we proposed to prepare an anti-bacterial and anti-cancer system for PC therapy inspired by the presence of bacteria in the PC microenvironment that might reduce the chemotherapeutic efficacy of GEM by secreting cytidine deaminase to convert GEM into inactive form, 20,20-difluorodeoxyuridine. To sum up, these scaffolds in these three projects were engineered and constructed based on the corresponding TME, aiming to reverse the adverse environmental factors and ultimately intervene in the disease progression. These concepts will inspire the design of other high-performance implants in tissue engineering field for improved tissue regeneration and disease treatment.

Due to high surface area, native ECM-like architecture and controllable physical properties, electrospinning has become a facile and multifunctional technique to prepare ultrafine and continuous fibrous membrane scaffolds for tissue regeneration and disease treatment. In this dissertation, we exploited the electrospinning technique to fabricate various membrane scaffolds. For the first project, we prepared ERK2-

siRNA-loaded GelMA nanogels using nano-emulsification technique followed by incorporation of these nanogels into PLLA fibers by blending electrospinning. For the second project, we fabricated the ZnO-loaded GelMA fibrous membranes by blending electrospinning, and then reinforced such membranes by TA treatment to form a secondary hydrogen-bond-mediated network in the polymer matrix. For the third project, we continued to use the blending electrospinning to prepare the GEM-loaded PLLA electrospun nanofibrous membranes. Then, a two-step TA-mediated Ag NP reduction strategy was adopted to *in-situ* form Ag NPs onto the PLLA fibers. Altogether, the fabrication processes were simple and feasible, and time-saving (the scaffold preparation time: 2-3 days for the first scaffold; 2-3 days for the second scaffold; 3-4 days for the third scaffold). They enabled to prepare the scaffolds in large quantities with high repeatability, which was liable to popularization. The major findings and inspirations for future research of each project were described as follows.

5.1 Major findings and conclusion

In the first study, an MMP-2-responsive ERK2-siRNA-laden PLLA electrospun membrane scaffold was successfully prepared, providing an intriguing platform for prevention of tendon adhesion formation. It showed that the as-prepared siRNA-loaded GelMA nanogels exhibited obvious MMP-2-triggered drug release profile. Besides, the siRNA released from GelMA nanogels still maintained its bioactivity to transfect into cells and reduce ERK2 expression. By incorporation of siRNA-loaded GelMA nanogels into the PLLA fibers by blending electrospinning, the resultant siRNA-laden electrospun membrane showed controllable morphology/architecture, favorable swelling and degradation properties, as well as the excellent mechanical performance. Furthermore, such delivery system exhibited an on-demand siRNA release in response to the disease state, which was believed to reduce the adverse effects of uncontrollable drug release. More importantly, the released siRNA from the membranes restrained its biofunction to block targeted ERK2 expression and suppress fibroblast adhesion, growth and proliferation, and exhibited superior ability to attenuate peritendinous adhesion formation *in vivo*. Altogether, these results collectively demonstrated that our

ERK2-siRNA-laden PLLA electrospun membrane could serve as a physical barrier to prevent extrinsic cells invasion, while acting as a smart drug delivery vehicle to realize siRNA on-demand release, cooperatively suppressing the fibrosis formation during tendon healing.

In the second study, a Janus dual-layer patch was prepared, in which its inner layer was a MEHP while outer layer was PLLA fibers. The MEHP was developed by blending electrospinning of GelMA and ZnO followed by TA reinforcement. It was found that the as-prepared MEHP showed a fibrous architecture, a controllable swelling ratio, outstanding adhesive and mechanical performances. In addition, such membrane could scavenge *in vitro* H_2O_2, decrease the extracellular and cellular ROS levels and protect cells against the ROS microenvironment, showing superior ability to reduce oxidative stress. Moreover, the expression of TNF-a, Cox-2, and IL-6 by LPS-treated cells was significantly decreased in the prepared hydrogel patch, suggesting the good anti-inflammatory effects. Combined with the anti-bacterial properties and pro-healing effects, we envision that such hydrogel patch would serve as a novel and efficient platform for tendon repair. By virtue of the diverse adhesion ability of MEHP, Janus patch could be prepared by attaching MEHP to PLLA fiber surface. Our results demonstrated the Janus patch was stable and showed good mechanical properties. *In vivo* experiments further confirmed the anti-tendon adhesion and pro-tendon healing ability of the Janus patch. Due to the drug, cell and biologicals free nature, our MEHP can avoid side effects like ectopic tissue formation and cancerization. Besides, due to the simple fabrication process, the largescale preparation of such scaffolds was highly feasible, which represents a ready-to-use treatment mean for tissue construction. Furthermore, such hydrogel patch showed great potential in clinical translation in terms of its material components, which are all naturally derived with defined structure and bioactivity. All in all, our Janus patch with integrated multiple functions will accelerate tendon healing, ultimately improving tendon repair quality.

In the third study, an anti-bacterial and anti-cancer GEM-loaded PLLA-TA-Ag

membrane scaffold was prepared by blending electrospinning of GEM and PLLA and a TA-mediated two-step in-situ Ag NPs reduction strategy. Such scaffold displayed even fibrous structure, excellent mechanical properties, and suitable GEM release profile, indicating the feasibility as a local drug delivery system to be implanted at the tumor resection site during the surgical operation for PC treatment. Besides, this kind of locally implanted GEM-loaded electrospun membrane showed a combination of short- and long-term anti-cancer performance, indicating its promising application prospect to reduce adverse reactions of intravenously administered GEM and improve treatment outcomes of cancer recurrence after surgery. Furthermore, the Ag NPs on the scaffolds prepared by two-step *in-situ* reduction strategy exhibited synergistical anti-tumor and anti-bacterial effects. All in all, we envision that the resultant GEM2@PLLA-TA-Ag electrospun membrane will provide a promising solution to the issue of chemotherapy drug resistance caused by bacteria in the pancreatic microenvironment, and synergistically enhance anti-tumor recurrence ability.

All taken together, inspired by the microenvironmental factors in different tissues, we prepared various scaffolds by electrospinning in combination with other fabrication techniques. These electrospinning strategies we adopted are straightforward, feasible, time-saving, and thus easy to be popularized. In addition, these material components like GelMA, ZnO, PLLA, TA are low cost with well-defined chemical structure and bioactivity, which may be beneficial for clinical translation and subsequent commercialization. Most importantly, these scaffolds enable large-scale preparation, representing an off-the-shelf strategy to accelerate surgical operation. We envision our proposed scaffolds can exert their functions to accelerate tissue repair and promote disease treatment, offering new avenues in biomedicine.

5.2 Recommendations for future work

For future work, there is much room to explore. For instance, regrading to the first project, considering the elevated MMP expression is also found in TME of other diseases like colorectal carcinoma, pancreatic tumor and osteoarthritis, the GelMA

nanogel-based smart drug delivery system can be further explored to be applied for other disease treatments. In addition, due to the excellent biocompatibility, the proposed membrane could be used for other adhesion-related disease prevention like peritoneal and pelvic adhesion, instead of only locally covering it on the tendon or skin surface. Furthermore, we can upgrade the function of prepared scaffold by integrating multiple stimulus-responsive drug release properties into the system, so that the resultant scaffolds can achieve a multi-drug release in a spatial and temporal difference pattern to fit the natural tendon healing phase, ultimately preventing the adhesion formation while promoting tendon healing.

For the second project, apart from being grafts for tendon repair, such MEHP can also act a skin or bone patch to induce their regeneration after injury. The diverse applications for the MEHP can be investigated in the future. Moreover, by virtue of the good adhesive properties, our proposed MEHP could be easily combined with various membrane scaffolds, e.g., PLLA electrospun membrane, to prepare graft with hierarchical architecture. Such combination of multiple scaffolds renders the resultant composite scaffolds with the diversified space structure and multifunctions to regulate cell behavior, ultimately achieving reconstruction of targeted tissue. Thus, more physical and biological characterizations can be done to evaluate the therapeutical outcomes of such composite scaffolds.

For the third project, the ability to prevent metastasis by the GEM@PLLA-TA-Ag can be explored, since PC is highly prone to metastases, especially spreading to the liver and lung tissue. Besides, due to simple fabrication process, such preparation strategy could be extended for other disease treatment, e.g., replacing GEM with other therapeutic agents like ibuprofen to realize an anti-inflammation and anti-bacterial combined treatment for skin infection. More importantly, since it is extraordinarily intricate to create a *Gammaproteobacteria*-bearing PC animal model with existing knowledge and technology, we can, in future study, leverage *in vitro* models such as microfluidic-based multi-organ chips or organoids to systematically investigate the *in*

vivo inhibitory effects of prepared multi-functional membranes on *Gammaproteobacteria* growth and consequent improved GEM-based chemotherapy.

Despite the promising prospect in clinical use, to promote commercialization of our proposed scaffolds, more experiments are suggested to evaluate their therapeutical efficacy and safety by constructing a more biomimetic *in vitro* pathological microenvironment of tendon injury and pancreatic tumor. This also might be beneficial to understanding of underlying mechanisms and later *in vivo* experiment. In addition, assessment of the treatment outcomes of these scaffolds in large animals like sheep and pig is also necessary, which is quite critical in ultimate clinical translation.

In conclusion, the TME-inspired scaffolds are more adaptable to the dynamic tissue repair process and can intervene the disease process more effectively to improve the therapeutic effects. We envision these novel treatment platforms will promote development of various high-performance bio-scaffolds and find extensive applications in tissue engineering field.

References

[1] V. Hernandez–Gea, S. Toffanin, S.L. Friedman, J.M. Llovet, Role of the microenvironment in the pathogenesis and treatment of hepatocellular carcinoma, Gastroenterology 144(3) (2013) 512-527.

[2] R. Mata, Y. Yao, W. Cao, J. Ding, T. Zhou, Z. Zhai, C. Gao, The Dynamic Inflammatory Tissue Microenvironment: Signality and Disease Therapy by Biomaterials, Research 2021 (2021) 4189516-4189516.

[3] B. Rani, Y. Cao, A. Malfettone, C. Tomuleasa, I. Fabregat, G. Giannelli, Role of the tissue microenvironment as a therapeutic target in hepatocellular carcinoma, World Journal of Gastroenterology 20(15) (2014) 4128.

[4] Q. Zhang, Y. Li, Z.Y.W. Lin, K.K. Wong, M. Lin, L. Yildirimer, X. Zhao, Electrospun polymeric micro/nanofibrous scaffolds for long-term drug release and their biomedical applications, Drug Discovery Today 22(9) (2017) 1351-1366.

[5] J. Zhao, W. Cui, Functional electrospun fibers for local therapy of cancer, Advanced Fiber Materials (2020) 1-17.

[6] G. Yang, X. Li, Y. He, J. Ma, G. Ni, S. Zhou, From nano to micro to macro: Electrospun hierarchically structured polymeric fibers for biomedical applications, Progress in Polymer Science 81 (2018) 80-113.

[7] J. Han, L. Xiong, X. Jiang, X. Yuan, Y. Zhao, D. Yang, Bio-functional electrospun nanomaterials: From topology design to biological applications, Progress in Polymer Science 91 (2019) 1-28.

[8] J. Cheng, Y. Jun, J. Qin, S.-H. Lee, Electrospinning versus microfluidic spinning of functional fibers for biomedical applications, Biomaterials 114 (2017) 121-143.

[9] R. Ashraf, H.S. Sofi, A. Malik, M.A. Beigh, R. Hamid, F.A. Sheikh, Recent trends in the fabrication of starch nanofibers: electrospinning and non-electrospinning routes and their applications in biotechnology, Applied Biochemistry and Biotechnology 187(1) (2019) 47-74.

[10] J. Xue, T. Wu, Y. Dai, Y. Xia, Electrospinning and electrospun nanofibers: Methods, materials, and applications, Chemical Reviews 119(8) (2019) 5298-5415.

[11] J. Yoon, H.S. Yang, B.S. Lee, W.R. Yu, Recent progress in coaxial electrospinning: New parameters, various structures, and wide applications, Advanced Materials 30(42) (2018) 1704765.

[12] H. Zhang, C. Zhao, Y. Zhao, G. Tang, X. Yuan, Electrospinning of ultrafine core/shell fibers for biomedical applications, Science China Chemistry 53(6) (2010) 1246-1254.

[13] M. Buzgo, A. Mickova, M. Rampichova, M. Doupnik, Blend electrospinning, coaxial electrospinning, and emulsion electrospinning techniques, Core-shell nanostructures for drug delivery and theranostics, Elsevier 2018, pp. 325-347.

[14] L. Weng, J. Xie, Smart electrospun nanofibers for controlled drug release: recent advances and new perspectives, Current Pharmaceutical Design 21(15) (2015) 1944-1959.

[15] S.-F. Chou, D. Carson, K.A. Woodrow, Current strategies for sustaining drug release from electrospun nanofibers, Journal of Controlled Release 220 (2015) 584-591.
[16] S. Chen, X. Huang, X. Cai, J. Lu, J. Yuan, J. Shen, The influence of fiber diameter of electrospun poly (lactic acid) on drug delivery, Fibers and Polymers 13(9) (2012) 1120-1125.
[17] M. Alimohammadi, Y. Aghli, O. Fakhraei, A. Moradi, M. Passandideh-Fard, M.H. Ebrahimzadeh, A. Khademhosseini, A. Tamayol, S.A. Mousavi Shaegh, Electrospun nanofibrous membranes for preventing tendon adhesion, ACS Biomaterials Science & Engineering 6(8) (2020) 4356-4376.
[18] Y. Ding, W. Li, F. Zhang, Z. Liu, N. Zanjanizadeh Ezazi, D. Liu, H.A. Santos, Electrospun fibrous architectures for drug delivery, tissue engineering and cancer therapy, Advanced Functional Materials 29(2) (2019) 1802852.
[19] X. Jiang, S. Wu, M. Kuss, Y. Kong, W. Shi, P.N. Streubel, T. Li, B. Duan, 3D printing of multilayered scaffolds for rotator cuff tendon regeneration, Bioactive Materials 5(3) (2020) 636-643.
[20] J. Hou, R. Yang, I. Vuong, F. Li, J. Kong, H.-Q. Mao, Biomaterials strategies to balance inflammation and tenogenesis for tendon repair, Acta Biomaterialia (2021).
[21] D. Docheva, S.A. Müller, M. Majewski, C.H. Evans, Biologics for tendon repair, Advanced Drug Delivery Reviews 84 (2015) 222-239.
[22] Y. Liu, H. Ramanath, D.-A. Wang, Tendon tissue engineering using scaffold enhancing strategies, Trends in Biotechnology 26(4) (2008) 201-209.
[23] A. Lomas, C. Ryan, A. Sorushanova, N. Shologu, A. Sideri, V. Tsioli, G. Fthenakis, A. Tzora, I. Skoufos, L.R. Quinlan, The past, present and future in scaffold-based tendon treatments, Advanced Drug Delivery Reviews 84 (2015) 257-277.
[24] Y. Bi, D. Ehirchiou, T.M. Kilts, C.A. Inkson, M.C. Embree, W. Sonoyama, L. Li, A.I. Leet, B.-M. Seo, L. Zhang, Identification of tendon stem/progenitor cells and the role of the extracellular matrix in their niche, Nature Medicine 13(10) (2007) 1219-1227.
[25] H.R. Screen, D.E. Berk, K.E. Kadler, F. Ramirez, M.F. Young, Tendon functional extracellular matrix, Journal of Orthopaedic Research 33(6) (2015) 793-799.
[26] A.E. Nichols, K.T. Best, A.E. Loiselle, The cellular basis of fibrotic tendon healing: challenges and opportunities, Translational Research 209 (2019) 156-168.
[27] T. Sakabe, T. Sakai, Musculoskeletal diseases—tendon, British Medical Bulletin 99(1) (2011) 211-225.
[28] Q. Zhang, Y. Yang, L. Yildirimer, T. Xu, X. Zhao, Advanced technology-driven therapeutic interventions for prevention of tendon adhesion: design, intrinsic and extrinsic factor considerations, Acta Biomaterialia (2021).
[29] A. Vinhas, M.T. Rodrigues, M.E. Gomes, Exploring stem cells and inflammation in tendon repair and regeneration, Cell Biology and Translational Medicine, Volume 2 (2018) 37-46.

[30] S.A. Müller, N.P. Quirk, J.A. Müller-Lebschi, P.E. Heisterbach, L. Dürselen, M. Majewski, C.H. Evans, Response of the injured tendon to growth factors in the presence or absence of the paratenon, The American Journal of Sports Medicine 47(2) (2019) 462-467.
[31] D. Tsekes, G. Konstantopoulos, W.S. Khan, D. Rossouw, M. Elvey, J. Singh, Use of stem cells and growth factors in rotator cuff tendon repair, European Journal of Orthopaedic Surgery & Traumatology 29(4) (2019) 747-757.
[32] S.L. Moran, C.K. Ryan, G.S. Orlando, C.E. Pratt, K.B. Michalko, Effects of 5-fluorouracil on flexor tendon repair, The Journal of Hand Surgery 25(2) (2000) 242-251.
[33] B. Kocaoglu, I. Agir, U. Nalbantoglu, M. Karahan, M. Türkmen, Effect of mitomycin-C on post-operative adhesions in tendon surgery: an experimental study in rats, The Journal of Bone and Joint Surgery. 92(6) (2010) 889-893.
[34] Y. Zhou, L. Zhang, W. Zhao, Y. Wu, C. Zhu, Y. Yang, Nanoparticle-mediated delivery of TGF-β1 miRNA plasmid for preventing flexor tendon adhesion formation, Biomaterials 34(33) (2013) 8269-8278.
[35] E.B. Katzel, M. Wolenski, A.E. Loiselle, P. Basile, L.M. Flick, H.N. Langstein, M.J. Hilton, H.A. Awad, W.C. Hammert, R.J. O'Keefe, Impact of Smad3 loss of function on scarring and adhesion formation during tendon healing, Journal of Orthopaedic Research 29(5) (2011) 684-693.
[36] S. Liu, F. Wu, S. Gu, T. Wu, S. Chen, S. Chen, C. Wang, G. Huang, T. Jin, W. Cui, Gene silencing via PDA/ERK2-siRNA-mediated electrospun fibers for peritendinous antiadhesion, Advanced Science 6(2) (2019) 1801217.
[37] A. Suwalski, H. Dabboue, A. Delalande, S.F. Bensamoun, F. Canon, P. Midoux, G. Saillant, D. Klatzmann, J.-P. Salvetat, C. Pichon, Accelerated achilles tendon healing by PDGF gene delivery with mesoporous silica nanoparticles, Biomaterials 31(19) (2010) 5237-5245.
[38] Y. Liu, A. Skardal, X.Z. Shu, G.D. Prestwich, Prevention of peritendinous adhesions using a hyaluronan-derived hydrogel film following partial-thickness flexor tendon injury, Journal of Orthopaedic Research 26(4) (2008) 562-569.
[39] R.E. Ferguson, B. Rinker, The use of a hydrogel sealant on flexor tendon repairs to prevent adhesion formation, Annals of Plastic Surgery 56(1) (2006) 54-58.
[40] G. Yang, H. Lin, B.B. Rothrauff, S. Yu, R.S. Tuan, Multilayered polycaprolactone/gelatin fiber-hydrogel composite for tendon tissue engineering, Acta Biomaterialia 35 (2016) 68-76.
[41] M.Y. Kim, S. Farnebo, C.Y. Woon, T. Schmitt, H. Pham, J. Chang, Augmentation of tendon healing with an injectable tendon hydrogel in a rat Achilles tendon model, Plastic and Reconstructive Surgery 133(5) (2014) 645e-653e.
[42] R. Liu, S. Zhang, X. Chen, Injectable hydrogels for tendon and ligament tissue engineering, Journal of Tissue Engineering and Regenerative Medicine 14(9) (2020) 1333-1348.
[43] P.Y. Chou, S.H. Chen, C.H. Chen, S.H. Chen, Y.T. Fong, J.P. Chen, Thermo-responsive in-situ forming hydrogels as barriers to prevent post-operative peritendinous adhesion, Acta Biomaterialia

63 (2017) 85-95.
[44] Y.L. Zhou, Q.Q. Yang, Y.Y. Yan, C. Zhu, L. Zhang, J.B. Tang, Localized delivery of miRNAs targets cyclooxygenases and reduces flexor tendon adhesions, Acta Biomaterialia 70 (2018) 237-248.
[45] E. Chen, L. Yang, C. Ye, W. Zhang, J. Ran, D. Xue, Z. Wang, Z. Pan, Q. Hu, An asymmetric chitosan scaffold for tendon tissue engineering: In vitro and in vivo evaluation with rat tendon stem/progenitor cells, Acta Biomaterialia 73 (2018) 377-387.
[46] S. Chen, G. Wang, T. Wu, X. Zhao, S. Liu, G. Li, W. Cui, C. Fan, Silver nanoparticles/ibuprofen-loaded poly (L-lactide) fibrous membrane: anti-infection and anti-adhesion effects, International Journal of Molecular Sciences 15(8) (2014) 14014-14025.
[47] W. Wang, N. He, Z. Yao, X. Wang, H. Wang, M. He, Y. Li, Y. Qian, An integrative dual-layer poly-L-lactic acid fibrous membrane prevents peritendinous adhesions, Frontiers in Bioengineering and Biotechnology 8 (2020) 387.
[48] S. Liu, J. Zhao, H. Ruan, T. Tang, G. Liu, D. Yu, W. Cui, C. Fan, Biomimetic sheath membrane via electrospinning for antiadhesion of repaired tendon, Biomacromolecules 13(11) (2012) 3611-3619.
[49] Y.J. No, M. Castilho, Y. Ramaswamy, H. Zreiqat, Role of biomaterials and controlled architecture on tendon/ligament repair and regeneration, Advanced Materials 32(18) (2020) 1904511.
[50] Z. Yin, X. Chen, J.L. Chen, W.L. Shen, T.M.H. Nguyen, L. Gao, H.W. Ouyang, The regulation of tendon stem cell differentiation by the alignment of nanofibers, Biomaterials 31(8) (2010) 2163-2175.
[51] C. Zhang, X. Wang, E. Zhang, L. Yang, H. Yuan, W. Tu, H. Zhang, Z. Yin, W. Shen, X. Chen, An epigenetic bioactive composite scaffold with well-aligned nanofibers for functional tendon tissue engineering, Acta Biomaterialia 66 (2018) 141-156.
[52] Z. Zheng, J. Ran, W. Chen, Y. Hu, T. Zhu, X. Chen, Z. Yin, B.C. Heng, G. Feng, H. Le, Alignment of collagen fiber in knitted silk scaffold for functional massive rotator cuff repair, Acta Biomaterialia 51 (2017) 317-329.
[53] C. Erisken, X. Zhang, K.L. Moffat, W.N. Levine, H.H. Lu, Scaffold fiber diameter regulates human tendon fibroblast growth and differentiation, Tissue Engineering Part A 19(3-4) (2013) 519-528.
[54] S. Liu, C. Hu, F. Li, X.-j. Li, W. Cui, C. Fan, Prevention of peritendinous adhesions with electrospun ibuprofen-loaded poly (L-lactic acid)-polyethylene glycol fibrous membranes, Tissue Engineering Part A 19(3-4) (2013) 529-537.
[55] X. Zhao, S. Jiang, S. Liu, S. Chen, Z.Y.W. Lin, G. Pan, F. He, F. Li, C. Fan, W. Cui, Optimization of intrinsic and extrinsic tendon healing through controllable water-soluble mitomycin-C release from electrospun fibers by mediating adhesion-related gene expression,

Biomaterials 61 (2015) 61-74.
[56] O. Evrova, J. Houska, M. Welti, E. Bonavoglia, M. Calcagni, P. Giovanoli, V. Vogel, J. Buschmann, Bioactive, elastic, and biodegradable emulsion electrospun DegraPol tube delivering PDGF-BB for tendon rupture repair, Macromolecular Bioscience 16(7) (2016) 1048-1063.
[57] S. Liu, M. Qin, C. Hu, F. Wu, W. Cui, T. Jin, C. Fan, Tendon healing and anti-adhesion properties of electrospun fibrous membranes containing bFGF loaded nanoparticles, Biomaterials 34(19) (2013) 4690-4701.
[58] A. Jayasree, S. Kottappally Thankappan, R. Ramachandran, M.N. Sundaram, C.-H. Chen, U. Mony, J.-P. Chen, R. Jayakumar, Bioengineered braided micro–Nano (multiscale) fibrous scaffolds for tendon reconstruction, ACS Biomaterials Science & Engineering 5(3) (2019) 1476-1486.
[59] A.E. Loiselle, G.A. Bragdon, J.A. Jacobson, S. Hasslund, Z.E. Cortes, E.M. Schwarz, D.J. Mitten, H.A. Awad, R.J. O'Keefe, Remodeling of murine intrasynovial tendon adhesions following injury: MMP and neotendon gene expression, Journal of Orthopaedic Research 27(6) (2009) 833-840.
[60] F. Li, C. Fan, T. Cheng, C. Jiang, B. Zeng, Efficient inhibition of fibroblast proliferation and collagen expression by ERK2 siRNAs, Biochemical and Biophysical Research Communications 382(2) (2009) 259-263.
[61] F. Li, H. Ruan, C. Fan, B. Zeng, C. Wang, X. Wang, Efficient inhibition of the formation of joint adhesions by ERK2 small interfering RNAs, Biochemical and Biophysical Research Communications 391(1) (2010) 795-799.
[62] Y. Yang, T. Xu, Q. Zhang, Y. Piao, H.P. Bei, X. Zhao, Biomimetic, stiff, and adhesive periosteum with osteogenic–angiogenic coupling effect for bone regeneration, Small 17(14) (2021) 2006598.
[63] J. Kim, R. Gauvin, H.J. Yoon, J.-H. Kim, S.-M. Kwon, H.J. Park, S.H. Baek, J.M. Cha, H. Bae, Skin penetration-inducing gelatin methacryloyl nanogels for transdermal macromolecule delivery, Macromolecular Research 24(12) (2016) 1115-1125.
[64] N. Kordalivand, D. Li, N. Beztsinna, J.S. Torano, E. Mastrobattista, C.F. van Nostrum, W.E. Hennink, T. Vermonden, Polyethyleneimine coated nanogels for the intracellular delivery of RNase A for cancer therapy, Chemical Engineering Journal 340 (2018) 32-41.
[65] M. Chen, S. Gao, M. Dong, J. Song, C. Yang, K.A. Howard, J. Kjems, F. Besenbacher, Chitosan/siRNA nanoparticles encapsulated in PLGA nanofibers for siRNA delivery, ACS Nano 6(6) (2012) 4835-4844.
[66] D. Cun, D.K. Jensen, M.J. Maltesen, M. Bunker, P. Whiteside, D. Scurr, C. Foged, H.M. Nielsen, High loading efficiency and sustained release of siRNA encapsulated in PLGA nanoparticles: quality by design optimization and characterization, European Journal of Pharmaceutics and Biopharmaceutics 77(1) (2011) 26-35.
[67] P.O. Rujitanaroj, Y.C. Wang, J. Wang, S.Y. Chew, Nanofiber-mediated controlled release of

siRNA complexes for long term gene-silencing applications, Biomaterials 32(25) (2011) 5915-5923.
[68] Y. Yang, Q. Zhang, T. Xu, H. Zhang, M. Zhang, L. Lu, Y. Hao, J.H. Fuh, X. Zhao, Photocrosslinkable nanocomposite ink for printing strong, biodegradable and bioactive bone graft, Biomaterials 263 (2020) 120378.
[69] X. Lu, S. Shi, H. Li, E. Gerhard, Z. Lu, X. Tan, W. Li, K.M. Rahn, D. Xie, G. Xu, Magnesium oxide-crosslinked low-swelling citrate-based mussel-inspired tissue adhesives, Biomaterials 232 (2020) 119719.
[70] O. Evrova, G.M. Bürgisser, C. Ebnöther, A. Adathala, M. Calcagni, E. Bachmann, J.G. Snedeker, C. Scalera, P. Giovanoli, V. Vogel, Elastic and surgeon friendly electrospun tubes delivering PDGF-BB positively impact tendon rupture healing in a rabbit Achilles tendon model, Biomaterials 232 (2020) 119722.
[71] L. Cheng, Y. Wang, G. Sun, S. Wen, L. Deng, H. Zhang, W. Cui, Hydration-enhanced lubricating electrospun nanofibrous membranes prevent tissue adhesion, Research 2020 (2020).
[72] H. Ruan, S. Liu, F. Li, X. Li, C. Fan, Prevention of tendon adhesions by ERK2 small interfering RNAs, International Journal of Molecular Sciences 14(2) (2013) 4361-4371.
[73] J.S. Ribeiro, E.A. Bordini, J.A. Ferreira, L. Mei, N. Dubey, J.C. Fenno, E. Piva, R.G. Lund, A. Schwendeman, M.C. Bottino, Injectable MMP-responsive nanotube-modified gelatin hydrogel for dental infection ablation, ACS Applied Materials & Interfaces 12(14) (2020) 16006-16017.
[74] K. Yue, G. Trujillo-de Santiago, M.M. Alvarez, A. Tamayol, N. Annabi, A. Khademhosseini, Synthesis, properties, and biomedical applications of gelatin methacryloyl (GelMA) hydrogels, Biomaterials 73 (2015) 254-271.
[75] K. Shalumon, C. Sheu, C.-H. Chen, S.-H. Chen, G. Jose, C.-Y. Kuo, J.-P. Chen, Multi-functional electrospun antibacterial core-shell nanofibrous membranes for prolonged prevention of post-surgical tendon adhesion and inflammation, Acta Biomaterialia 72 (2018) 121-136.
[76] Y. Wang, L. Cheng, S. Wen, S. Zhou, Z. Wang, L. Deng, H.-Q. Mao, W. Cui, H. Zhang, Ice-inspired superlubricated electrospun nanofibrous membrane for preventing tissue adhesion, Nano Letters 20(9) (2020) 6420-6428.
[77] J.E. Jackson, Z. Kopecki, P.J. Anderson, A.J. Cowin, Increasing the level of cytoskeletal protein Flightless I reduces adhesion formation in a murine digital flexor tendon model, Journal of Orthopaedic Surgery and Research 15(1) (2020) 1-14.
[78] P. Li, H. Zhou, T. Tu, H. Lu, Dynamic exacerbation in inflammation and oxidative stress during the formation of peritendinous adhesion resulted from acute tendon injury, Journal of Orthopaedic Surgery and Research 16(1) (2021) 1-8.
[79] C.S. Bestwick, N. Maffulli, Reactive oxygen species and tendon problems: review and hypothesis, Sports Medicine and Arthroscopy Review 8(1) (2000) 6-16.
[80] E. Fourniols, J.-Y. Lazennec, M.-A. Rousseau, Salvage technique for postoperative infection and necrosis of the Achilles tendon, Orthopaedics & Traumatology: Surgery & Research 98(8)

(2012) 915-920.
[81] A.A. Shitole, P.W. Raut, N. Sharma, P. Giram, A.P. Khandwekar, B. Garnaik, Electrospun polycaprolactone/hydroxyapatite/ZnO nanofibers as potential biomaterials for bone tissue regeneration, Journal of Materials Science 30(5) (2019) 1-17.
[82] A. Yousefi, F. Sarrafzadeh-Rezaei, S. Asri-Rezaei, A.-A. Farshid, M. Behfar, Fabrication of novel tubular scaffold for tendon repair from chitosan in combination with zinc oxide nanoparticles, Veterinary Research Forum, Urmia, Iran, 2018, p. 105.
[83] M. Vedhanayagam, B. Unni Nair, K.J. Sreeram, Collagen-ZnO scaffolds for wound healing applications: role of dendrimer functionalization and nanoparticle morphology, ACS Applied Bio Materials 1(6) (2018) 1942-1958.
[84] N. Ninan, A. Forget, V.P. Shastri, N.H. Voelcker, A. Blencowe, Antibacterial and anti-inflammatory pH-responsive tannic acid-carboxylated agarose composite hydrogels for wound healing, ACS Applied Materials & Interfaces 8(42) (2016) 28511-28521.
[85] R. Yang, G. Li, C. Zhuang, P. Yu, T. Ye, Y. Zhang, P. Shang, J. Huang, M. Cai, L. Wang, Gradient bimetallic ion–based hydrogels for tissue microstructure reconstruction of tendon-to-bone insertion, Science Advances 7(26) (2021) eabg3816.
[86] J. Yeo, J. Lee, S. Yoon, W.J. Kim, Tannic acid-based nanogel as an efficient anti-inflammatory agent, Biomaterials Science 8(4) (2020) 1148-1159.
[87] J.Y. Lee, H. Lim, J.W. Ahn, D. Jang, S.H. Lee, K. Park, S.E. Kim, Design of a 3D BMP-2-delivering tannylated PCL scaffold and its anti-oxidant, anti-inflammatory, and osteogenic effects in vitro, International Journal of Molecular Sciences 19(11) (2018) 3602.
[88] M. Mehdizadeh, H. Weng, D. Gyawali, L. Tang, J. Yang, Injectable citrate-based mussel-inspired tissue bioadhesives with high wet strength for sutureless wound closure, Biomaterials 33(32) (2012) 7972-7983.
[89] T. Luetragoon, R. Pankla Sranujit, C. Noysang, Y. Thongsri, P. Potup, N. Suphrom, N. Nuengchamnong, K. Usuwanthim, Bioactive compounds in Moringa oleifera Lam. leaves inhibit the pro-inflammatory mediators in lipopolysaccharide-induced human monocyte-derived macrophages, Molecules 25(1) (2020) 191.
[90] X. Xiao, L. He, Y. Chen, L. Wu, L. Wang, Z. Liu, Anti-inflammatory and antioxidative effects of Camellia oleifera Abel components, Future Medicinal Chemistry 9(17) (2017) 2069-2079.
[91] M.W. Bowers, N.S. Turner, D.B. Ryssman, S.L. Moran, Outcomes following treatment of the infected Achilles tendon, Foot & Ankle Orthopaedics 4(2) (2019) 2473011419846943.
[92] T.R. Jildeh, K.R. Okoroha, N.E. Marshall, A. Abdul-Hak, F. Zeni, V. Moutzouros, Infection and rerupture after surgical repair of Achilles tendons, Orthopaedic Journal of Sports Medicine 6(5) (2018) 2325967118774302.
[93] E.A.S. Dimapilis, C.-S. Hsu, R.M.O. Mendoza, M.-C. Lu, Zinc oxide nanoparticles for water disinfection, Sustainable Environment Research 28(2) (2018) 47-56.

[94] X. He, X. Liu, J. Yang, H. Du, N. Chai, Z. Sha, M. Geng, X. Zhou, C. He, Tannic acid-reinforced methacrylated chitosan/methacrylated silk fibroin hydrogels with multifunctionality for accelerating wound healing, Carbohydrate Polymers 247 (2020) 116689.
[95] R. Augustine, H.N. Malik, D.K. Singhal, A. Mukherjee, D. Malakar, N. Kalarikkal, S. Thomas, Electrospun polycaprolactone/ZnO nanocomposite membranes as biomaterials with antibacterial and cell adhesion properties, Journal of Polymer Research 21(3) (2014) 1-17.
[96] R. Augustine, E.A. Dominic, I. Reju, B. Kaimal, N. Kalarikkal, S. Thomas, Investigation of angiogenesis and its mechanism using zinc oxide nanoparticle-loaded electrospun tissue engineering scaffolds, RSC Advances 4(93) (2014) 51528-51536.
[97] R. Augustine, P. Dan, A. Sosnik, N. Kalarikkal, N. Tran, B. Vincent, S. Thomas, P. Menu, D. Rouxel, Electrospun poly (vinylidene fluoride-trifluoroethylene)/zinc oxide nanocomposite tissue engineering scaffolds with enhanced cell adhesion and blood vessel formation, Nano Research 10(10) (2017) 3358-3376.
[98] X. Lv, L. Wang, J. Fu, Y. Li, L. Yu, A one-step tannic acid coating to improve cell adhesion and proliferation on polydimethylsiloxane, New Journal of Chemistry 44(35) (2020) 15140-15147.
[99] D. Lee, H. Hwang, J.-S. Kim, J. Park, D. Youn, D. Kim, J. Hahn, M. Seo, H. Lee, VATA: a poly (vinyl alcohol)-and tannic acid-based nontoxic underwater adhesive, ACS Applied Materials & Interfaces 12(18) (2020) 20933-20941.
[100] A.L. Miller, P.L. Garcia, K.J. Yoon, Developing effective combination therapy for pancreatic cancer: an overview, Pharmacological Research 155 (2020) 104740.
[101] F. Bray, J. Ferlay, I. Soerjomataram, R.L. Siegel, L.A. Torre, A. Jemal, Global cancer statistics 2018: GLOBOCAN estimates of incidence and mortality worldwide for 36 cancers in 185 countries, CA: a Cancer Journal for Clinicians 68(6) (2018) 394-424.
[102] A.B. Lowenfels, P. Maisonneuve, Epidemiology and risk factors for pancreatic cancer, Best Practice & Research Clinical Gastroenterology 20(2) (2006) 197-209.
[103] D.R. Principe, A. Rana, Updated risk factors to inform early pancreatic cancer screening and identify high risk patients, Cancer Letters 485 (2020) 56-65.
[104] J. Kleeff, M. Korc, M. Apte, C. La Vecchia, C.D. Johnson, A.V. Biankin, R.E. Neale, M. Tempero, D.A. Tuveson, R.H. Hruban, Pancreatic cancer, Nature Reviews Disease Primers 2(1) (2016) 1-22.
[105] L. Ireland, A. Santos, M.S. Ahmed, C. Rainer, S.R. Nielsen, V. Quaranta, U. Weyer-Czernilofsky, D.D. Engle, P.A. Perez-Mancera, S.E. Coupland, Chemoresistance in pancreatic cancer is driven by stroma-derived insulin-like growth factors, Cancer Research 76(23) (2016) 6851-6863.
[106] W.J. Ho, E.M. Jaffee, L. Zheng, The tumour microenvironment in pancreatic cancer—clinical challenges and opportunities, Nature Reviews Clinical Oncology 17(9) (2020) 527-540.
[107] C. Qu, Q. Wang, Z. Meng, P. Wang, Cancer-associated fibroblasts in pancreatic cancer: should

they be deleted or reeducated?, Integrative Cancer Therapies 17(4) (2018) 1016-1019.
[108] S. Yachida, S. Jones, I. Bozic, T. Antal, R. Leary, B. Fu, M. Kamiyama, R.H. Hruban, J.R. Eshleman, M.A. Nowak, Distant metastasis occurs late during the genetic evolution of pancreatic cancer, Nature 467(7319) (2010) 1114-1117.
[109] S. Li, H.-X. Xu, C.-T. Wu, W.-Q. Wang, W. Jin, H.-L. Gao, H. Li, S.-R. Zhang, J.-Z. Xu, Z.-H. Qi, Angiogenesis in pancreatic cancer: current research status and clinical implications, Angiogenesis 22(1) (2019) 15-36.
[110] X. Xian, J. Håkansson, A. Ståhlberg, P. Lindblom, C. Betsholtz, H. Gerhardt, H. Semb, Pericytes limit tumor cell metastasis, The Journal of Clinical Investigation 116(3) (2006) 642-651.
[111] J.H. Chang, Y. Jiang, V.G. Pillarisetty, Role of immune cells in pancreatic cancer from bench to clinical application: an updated review, Medicine 95(49) (2016).
[112] P. Goedegebuure, J. B Mitchem, M. R Porembka, M. CB Tan, B. A Belt, A. Wang-Gillam, W. E Gillanders, W. G Hawkins, D. C Linehan, Myeloid-derived suppressor cells: general characteristics and relevance to clinical management of pancreatic cancer, Current Cancer Drug Targets 11(6) (2011) 734-751.
[113] S.F. Valilou, M. Keshavarz-Fathi, N. Silvestris, A. Argentiero, N. Rezaei, The role of inflammatory cytokines and tumor associated macrophages (TAMs) in microenvironment of pancreatic cancer, Cytokine & Growth Factor Reviews 39 (2018) 46-61.
[114] U.L. Katari, J.M. Keirnan, A.C. Worth, S.E. Hodges, A.M. Leen, W.E. Fisher, J.F. Vera, Engineered T cells for pancreatic cancer treatment, HPB 13(9) (2011) 643-650.
[115] A. Roghanian, C. Fraser, M. Kleyman, J. Chen, B cells promote pancreatic tumorigenesis, Cancer Discovery 6(3) (2016) 230-232.
[116] M. Pergamo, G. Miller, Myeloid-derived suppressor cells and their role in pancreatic cancer, Cancer Gene Therapy 24(3) (2017) 100-105.
[117] R. Cui, W. Yue, E.C. Lattime, M.N. Stein, Q. Xu, X.-L. Tan, Targeting tumor-associated macrophages to combat pancreatic cancer, Oncotarget 7(31) (2016) 50735.
[118] M. Overchuk, G. Zheng, Overcoming obstacles in the tumor microenvironment: Recent advancements in nanoparticle delivery for cancer theranostics, Biomaterials 156 (2018) 217-237.
[119] A. Neesse, P. Michl, K.K. Frese, C. Feig, N. Cook, M.A. Jacobetz, M.P. Lolkema, M. Buchholz, K.P. Olive, T.M. Gress, Stromal biology and therapy in pancreatic cancer, Gut 60(6) (2011) 861-868.
[120] K.B. Stopa, A.A. Kusiak, M.D. Szopa, P.E. Ferdek, M.A. Jakubowska, Pancreatic cancer and its microenvironment—recent advances and current controversies, International Journal of Molecular Sciences 21(9) (2020) 3218.
[121] R.F. Hwang, T. Moore, T. Arumugam, V. Ramachandran, K.D. Amos, A. Rivera, B. Ji, D.B. Evans, C.D. Logsdon, Cancer-associated stromal fibroblasts promote pancreatic tumor progression, Cancer Research 68(3) (2008) 918-926.

[122] S.R. Bramhall, The matrix metalloproteinases and their inhibitors in pancreatic cancer, International Journal of Pancreatology 21(1) (1997) 1-12.
[123] T. Armstrong, G. Packham, L.B. Murphy, A.C. Bateman, J.A. Conti, D.R. Fine, C.D. Johnson, R.C. Benyon, J.P. Iredale, Type I collagen promotes the malignant phenotype of pancreatic ductal adenocarcinoma, Clinical Cancer Research 10(21) (2004) 7427-7437.
[124] A. Menke, C. Philippi, R. Vogelmann, B. Seidel, M.P. Lutz, G. Adler, D. Wedlich, Down-regulation of E-cadherin gene expression by collagen type I and type III in pancreatic cancer cell lines, Cancer Research 61(8) (2001) 3508-3517.
[125] Y. Shintani, Y. Fukumoto, N. Chaika, R. Svoboda, M.J. Wheelock, K.R. Johnson, Collagen I–mediated up-regulation of N-cadherin requires cooperative signals from integrins and discoidin domain receptor 1, Journal of Cell Biology 180(6) (2008) 1277-1289.
[126] L. Junliang, W. Lili, L. Xiaolong, L. Xuguang, W. Huanwen, L. Zhiyong, High-molecular-weight hyaluronan produced by activated pancreatic stellate cells promotes pancreatic cancer cell migration via paracrine signaling, Biochemical and Biophysical Research Communications 515(3) (2019) 493-498.
[127] F.C. Kelleher, Hedgehog signaling and therapeutics in pancreatic cancer, Carcinogenesis 32(4) (2011) 445-451.
[128] M.A. Macha, S. Rachagani, S. Gupta, P. Pai, M.P. Ponnusamy, S.K. Batra, M. Jain, Guggulsterone decreases proliferation and metastatic behavior of pancreatic cancer cells by modulating JAK/STAT and Src/FAK signaling, Cancer Letters 341(2) (2013) 166-177.
[129] F. McAllister, M.A.W. Khan, B. Helmink, J.A. Wargo, The tumor microbiome in pancreatic cancer: bacteria and beyond, Cancer Cell 36(6) (2019) 577-579.
[130] L.T. Geller, M. Barzily-Rokni, T. Danino, O.H. Jonas, N. Shental, D. Nejman, N. Gavert, Y. Zwang, Z.A. Cooper, K. Shee, Potential role of intratumor bacteria in mediating tumor resistance to the chemotherapeutic drug gemcitabine, Science 357(6356) (2017) 1156-1160.
[131] S. Pushalkar, M. Hundeyin, D. Daley, C.P. Zambirinis, E. Kurz, A. Mishra, N. Mohan, B. Aykut, M. Usyk, L.E. Torres, The pancreatic cancer microbiome promotes oncogenesis by induction of innate and adaptive immune suppression, Cancer Discovery 8(4) (2018) 403-416.
[132] V. Sethi, G.A. Vitiello, D. Saxena, G. Miller, V. Dudeja, The role of the microbiome in immunologic development and its implication for pancreatic cancer immunotherapy, Gastroenterology 156(7) (2019) 2097-2115. e2.
[133] D. Pagliari, A. Saviano, E. Newton, M. Serricchio, A. Dal Lago, A. Gasbarrini, R. Cianci, Gut microbiota-immune system crosstalk and pancreatic disorders, Mediators of Inflammation 2018 (2018).
[134] J. Rao, Y. Yang, H.P. Bei, C.-Y. Tang, X. Zhao, Antibacterial nanosystems for cancer therapy, Biomaterials Science 8(24) (2020) 6814-6824.
[135] J.P. Neoptolemos, J. Kleeff, P. Michl, E. Costello, W. Greenhalf, D.H. Palmer, Therapeutic

developments in pancreatic cancer: current and future perspectives, Nature Reviews Gastroenterology & hepatology 15(6) (2018) 333-348.
[136] T. Kamisawa, L.D. Wood, T. Itoi, K. Takaori, Pancreatic cancer, The Lancet 388(10039) (2016) 73-85.
[137] C. Springfeld, D. Jäger, M.W. Büchler, O. Strobel, T. Hackert, D.H. Palmer, J.P. Neoptolemos, Chemotherapy for pancreatic cancer, La Presse Medicale 48(3) (2019) e159-e174.
[138] H.r. Burris, M.J. Moore, J. Andersen, M.R. Green, M.L. Rothenberg, M.R. Modiano, M. Christine Cripps, R.K. Portenoy, A.M. Storniolo, P. Tarassoff, Improvements in survival and clinical benefit with gemcitabine as first-line therapy for patients with advanced pancreas cancer: a randomized trial, Journal of Clinical Oncology 15(6) (1997) 2403-2413.
[139] T. Macarulla, R. Pazo-Cid, C. Guillén-Ponce, R. López, R. Vera, M. Reboredo, A. Muñoz Martin, F. Rivera, R. Díaz Beveridge, A. La Casta, Phase I/II trial to evaluate the efficacy and safety of nanoparticle albumin-bound paclitaxel in combination with gemcitabine in patients with pancreatic cancer and an ECOG performance status of 2, Journal of Clinical Oncology 37(3) (2019) 230-238.
[140] M. Ghidini, A. Lampis, M.B. Mirchev, A.F. Okuducu, M. Ratti, N. Valeri, J.C. Hahne, Immune-based therapies and the role of microsatellite instability in pancreatic cancer, Genes 12(1) (2021) 33.
[141] M. Kajihara, K. Takakura, T. Kanai, Z. Ito, Y. Matsumoto, S. Shimodaira, M. Okamoto, T. Ohkusa, S. Koido, Advances in inducing adaptive immunity using cell-based cancer vaccines: Clinical applications in pancreatic cancer, World journal of Gastroenterology 22(18) (2016) 4446.
[142] H. Johansson, R. Andersson, M. Bauden, S. Hammes, S. Holdenrieder, D. Ansari, Immune checkpoint therapy for pancreatic cancer, World journal of Gastroenterology 22(43) (2016) 9457.
[143] M. Katsuda, M. Miyazawa, T. Ojima, A. Katanuma, K. Hakamada, K. Sudo, S. Asahara, I. Endo, M. Ueno, K. Hara, A double-blind randomized comparative clinical trial to evaluate the safety and efficacy of dendritic cell vaccine loaded with WT1 peptides (TLP0-001) in combination with S-1 in patients with advanced pancreatic cancer refractory to standard chemotherapy, Trials 20(1) (2019) 1-11.
[144] X. Huang, L. Ding, X. Liu, R. Tong, J. Ding, Z. Qian, L. Cai, P. Zhang, D. Li, Regulation of tumor microenvironment for pancreatic cancer therapy, Biomaterials 270 (2021) 120680.
[145] J.R. Melamed, R.S. Riley, D.M. Valcourt, E.S. Day, Using gold nanoparticles to disrupt the tumor microenvironment: an emerging therapeutic strategy, Acs Nano 10(12) (2016) 10631-10635.
[146] J. Lu, X. Liu, Y.-P. Liao, F. Salazar, B. Sun, W. Jiang, C.H. Chang, J. Jiang, X. Wang, A.M. Wu, Nano-enabled pancreas cancer immunotherapy using immunogenic cell death and reversing immunosuppression, Nature Communications 8(1) (2017) 1-14.
[147] X. Chen, W. Zhou, C. Liang, S. Shi, X. Yu, Q. Chen, T. Sun, Y. Lu, Y. Zhang, Q. Guo, Codelivery nanosystem targeting the deep microenvironment of pancreatic cancer, Nano Letters

19(6) (2019) 3527-3534.
[148] Y. Kuang, J. Shi, J. Li, D. Yuan, K.A. Alberti, Q. Xu, B. Xu, Pericellular hydrogel/nanonets inhibit cancer cells, Angewandte Chemie 126(31) (2014) 8242-8245.
[149] G. Xia, H. Zhang, R. Cheng, H. Wang, Z. Song, L. Deng, X. Huang, H.A. Santos, W. Cui, Localized controlled delivery of gemcitabine via microsol electrospun fibers to prevent pancreatic cancer recurrence, Advanced Healthcare Materials 7(18) (2018) 1800593.
[150] X. Huang, C. Ou, Y. Shu, Y. Wang, S. Gong, R. Luo, S. Chen, Q. Wu, C. Gong, A self-sustained nanoplatform reverses TRAIL-resistance of pancreatic cancer through coactivating of exogenous and endogenous apoptotic pathway, Biomaterials 272 (2021) 120795.
[151] S. Jiang, P. Song, H. Guo, X. Zhang, Y. Ren, H. Liu, X. Song, M. Kong, Blending PLLA/tannin-grafted PCL fiber membrane for skin tissue engineering, Journal of Materials Science 52(3) (2017) 1617-1624.
[152] S. Calamak, M. Ermis, In situ silver nanoparticle synthesis on 3D-printed polylactic acid scaffolds for biomedical applications, Journal of Materials Research 36(1) (2021) 166-175.
[153] Y.-H. Lee, F.-Y. Cheng, H.-W. Chiu, J.-C. Tsai, C.-Y. Fang, C.-W. Chen, Y.-J. Wang, Cytotoxicity, oxidative stress, apoptosis and the autophagic effects of silver nanoparticles in mouse embryonic fibroblasts, Biomaterials 35(16) (2014) 4706-4715.
[154] E. Barcińska, J. Wierzbicka, A. Zauszkiewicz-Pawlak, D. Jacewicz, A. Dabrowska, I. Inkielewicz-Stepniak, Role of oxidative and nitro-oxidative damage in silver nanoparticles cytotoxic effect against human pancreatic ductal adenocarcinoma cells, Oxidative Medicine and Cellular Longevity 2018 (2018).
[155] J. Dolina, Z. Gončuková, M. Bobák, L. Dvořák, Modification of a hollow-fibre polyethersulfone membrane using silver nanoparticles formed in situ for biofouling prevention, RSC Advances 8(26) (2018) 14552-14560.
[156] Y.Y. Loo, Y. Rukayadi, M.-A.-R. Nor-Khaizura, C.H. Kuan, B.W. Chieng, M. Nishibuchi, S. Radu, In vitro antimicrobial activity of green synthesized silver nanoparticles against selected gram-negative foodborne pathogens, Frontiers in Microbiology 9 (2018) 1555.
[157] S. Liao, Y. Zhang, X. Pan, F. Zhu, C. Jiang, Q. Liu, Z. Cheng, G. Dai, G. Wu, L. Wang, Antibacterial activity and mechanism of silver nanoparticles against multidrug-resistant Pseudomonas aeruginosa, International Journal of Nanomedicine 14 (2019) 1469.